

# TRITIUM RETENTION TECHNIQUES IN THE KATRIN TRANSPORT SECTION AND COMMISSIONING OF ITS DPS2-F CRYOSTAT

Zur Erlangung des akademischen Grades eines  
DOKTORS DER NATURWISSENSCHAFTEN  
von der Fakultät für Physik des Karlsruher Instituts für Technologie  
genehmigte

DISSERTATION

von

**Diplom-Physiker Andreas Kosmider**  
aus Solingen

Erstgutachter: Prof. Dr. G. Drexlin  
Institut für Experimentelle Kernphysik, KIT  
Zweitgutachter: Prof. Dr. Ch. Weinheimer  
Institut für Kernphysik, WWU Münster

Tag der mündlichen Prüfung: 6. Juli 2012



# Contents

<b>1</b>	<b>Introduction</b>	<b>1</b>
<b>2</b>	<b>The Karlsruhe Tritium Neutrino Experiment</b>	<b>17</b>
2.1	High Precision Tritium Beta-Spectroscopy . . . . .	17
2.1.1	MAC-E-Filter Experiments . . . . .	18
2.1.2	Current Neutrino Mass Limits . . . . .	20
2.1.3	Next Generation Implementation . . . . .	21
2.2	The KATRIN Experiment . . . . .	22
2.2.1	General Overview . . . . .	22
2.2.2	Experimental Aims . . . . .	22
2.2.3	The Source . . . . .	23
2.2.4	The Spectrometers . . . . .	25
2.2.5	The Detector . . . . .	27
2.2.6	The Transport Section . . . . .	28
<b>3</b>	<b>Tritium Retention - Technical Principles</b>	<b>29</b>
3.1	Design Criteria Tritium Background . . . . .	29
3.1.1	Calculation of Tritium Activity . . . . .	29
3.1.2	Background through Tritium Decay . . . . .	30
3.2	Principles of Gasflow Reduction . . . . .	33
3.2.1	Parameters and Flow Regimes . . . . .	33
3.2.2	Vacuum Measures . . . . .	34
3.2.3	Turbo-Molecular Pumping . . . . .	35
3.2.4	Sorption & Diffusion . . . . .	39

---

3.2.4.1	Absorption . . . . .	40
3.2.4.2	Diffusion . . . . .	40
3.2.4.3	Adsorption . . . . .	42
3.2.5	Sorption Pumping . . . . .	43
3.2.6	Cryopumping . . . . .	44
3.3	Tritium Gas Flow Reduction in KATRIN . . . . .	47
3.3.1	Gas Flow Reduction in STS . . . . .	47
3.3.2	Gas Flow Reduction in Spectrometers . . . . .	49
3.3.2.1	Pre-Spectrometer . . . . .	49
3.3.2.2	Outgassing . . . . .	49
3.3.2.3	Main Spectrometer . . . . .	50
3.3.2.4	Summary . . . . .	51
3.3.3	Tritium Sorption on Walls . . . . .	52
3.3.3.1	Comparison to Integral Flux . . . . .	55
3.4	Ionized Tritium . . . . .	57
3.4.1	Ion Identification . . . . .	57
3.4.2	Ion Suppression . . . . .	58
<b>4</b>	<b>Tritium Retention - Theoretical Principles</b>	<b>61</b>
4.1	Characterization of Source Output . . . . .	61
4.1.1	Tritium Gas Flux into DPS2-F . . . . .	61
4.1.2	Ion Flux into DPS2-F . . . . .	62
4.1.2.1	Ion Species . . . . .	62
4.1.2.2	Ion-Clusters . . . . .	63
4.1.2.3	Re-neutralization . . . . .	64
4.1.2.4	Summary of expected Ion Load . . . . .	65
4.1.2.5	Impact of Ions on Neutrino Mass Measurement	66
4.2	Gasflow in DPS2-F . . . . .	68
4.2.1	Flow via Calculation of Conductances . . . . .	68
4.2.2	Flow via Single Molecule MC Simulations . . . . .	71



---

4.2.3	Temperature Dependence . . . . .	73
4.2.3.1	Conductance vs Monte Carlo . . . . .	73
4.2.3.2	Temperature effects on Pumping . . . . .	74
4.2.4	Calculations for different Gases . . . . .	75
4.3	Ion Flux in DPS2-F . . . . .	76
4.3.1	Ion detection using FT-ICR . . . . .	76
4.3.1.1	Ion Cyclotron Frequencies . . . . .	76
4.3.1.2	Excitation and detection . . . . .	78
4.3.2	Ion suppression with Dipole Electrodes . . . . .	79
<b>5</b>	<b>The Transport Section</b>	<b>83</b>
5.1	Differential Pumping . . . . .	83
5.1.1	Vacuum Design . . . . .	84
5.1.1.1	Beam Tube Design . . . . .	84
5.1.1.2	TMPs and Differential Pumping . . . . .	85
5.1.1.3	TMPs in magnetic field . . . . .	86
5.1.1.4	Vacuum Analytics . . . . .	87
5.1.2	Magnetic Design . . . . .	88
5.1.2.1	General Design . . . . .	88
5.1.2.2	The Superconductor Circuit . . . . .	89
5.1.2.3	Commissioning Magnet System . . . . .	92
5.1.3	The Ion Analysis and Suppression System . . . . .	93
5.1.3.1	The DPS2-F FT-ICR System . . . . .	94
5.1.3.2	The DPS2-F Dipole System . . . . .	95
5.2	Cryogenic Pumping . . . . .	98
5.2.1	Beam Tube Design . . . . .	99
5.2.2	Magnetic Design . . . . .	100
5.2.3	The Cryopump . . . . .	102
5.2.3.1	Setup of the Cryopump . . . . .	102
5.2.3.2	The Modes of Opeartion . . . . .	102
5.2.3.3	The Argon Frost . . . . .	104
5.2.4	The Getter-Pump . . . . .	106
5.2.5	The Calibration Source . . . . .	107

---

<b>6</b>	<b>Test Experiments at DPS2-F</b>	<b>109</b>
6.1	The Magnetic Geometry Measurements . . . . .	109
6.1.1	Setup of Magnetic Geometry Measurements . . . . .	110
6.1.2	Results of Magnetic Geometry Measurements . . . . .	111
6.2	The Electron-Optics Measurements . . . . .	113
6.2.1	Magnetic Mapping . . . . .	114
6.2.2	Electron Transmission . . . . .	114
6.3	The Ion Suppression Measurements . . . . .	115
6.3.1	Setup of Ion Source and Collector . . . . .	115
6.3.2	Setup of the FT-ICR Modules . . . . .	116
6.3.3	Measurement Scheme . . . . .	117
6.4	The Vacuum Quality Measurements . . . . .	118
6.4.1	Setup of Vacuum Analysis . . . . .	118
6.4.1.1	Volume Assessment . . . . .	118
6.4.1.2	Outgassing Analysis . . . . .	119
6.4.2	Results of Vacuum Analysis . . . . .	120
6.4.2.1	Volume of the primary Vacuum System . . . . .	120
6.4.2.2	Outgassing Values . . . . .	120
6.4.2.3	Mass Spectrum of the residual Gas . . . . .	121
6.5	The Gas Flow Measurements . . . . .	124
6.5.1	Setup of Gas Flow Measurements . . . . .	124
6.5.1.1	The Injection System . . . . .	124
6.5.1.2	The Collection System . . . . .	125
6.5.1.3	Measurement Scheme . . . . .	127
6.5.2	Results of Gas Flow Measurements . . . . .	130
6.5.3	Comparison with Simulations . . . . .	135
6.6	Implications for KATRIN . . . . .	136
<b>7</b>	<b>Conclusion</b>	<b>139</b>

<b>Appendix</b>	<b>141</b>
A.1 Additional Data and Informations . . . . .	141
A.2 FT-ICR Auxillaries & Geometry . . . . .	150
A.3 The SLOW Experiment . . . . .	152
A.4 Design Modifications . . . . .	154
<b>Bibliography</b>	<b>159</b>



# List of Figures

1.1	Medium Base Line Oscillation . . . . .	6
1.2	The Neutrino Mass Hierarchy . . . . .	8
1.3	Neutrino Mass on cosmological Scales . . . . .	10
1.4	Neutrino-less double beta-decay ( $0\nu\beta\beta$ ) Spectrum . . . . .	12
1.5	The $^{163}\text{Ho}$ EC Spectrum . . . . .	14
2.1	Electron spectrum of tritium $\beta$ -decay . . . . .	18
2.2	Fundamental MAC-E Filter Setup . . . . .	20
2.3	The KATRIN Setup . . . . .	23
2.4	The Windowless Gaseous Tritium Source . . . . .	24
2.5	The Source and Transport Section . . . . .	25
2.6	Electric potentials and magnetic fields in KATRIN . . . . .	26
2.7	The Focal Plane Detector System . . . . .	27
3.1	Field-lines in Main Spectrometer . . . . .	31
3.2	Secondary electrons in Main Spectrometer . . . . .	32
3.3	Rotor of a Turbo Molecular Pump . . . . .	36
3.4	Schematic turbo molecular pump . . . . .	37
3.5	Differential pumping, schematically . . . . .	39
3.6	Tritium-Surface Interactions . . . . .	42
3.7	Getter-Pumping Material . . . . .	44
3.8	Tritium suppression in STS . . . . .	48
3.9	Vacuum System in Main Spectrometer . . . . .	50
3.10	Schematic of $\vec{E} \times \vec{B}$ -drift . . . . .	59

---

4.1	Ion and electron density in WGTS . . . . .	66
4.2	Pump Duct DPS2-F for Calculation of Conductance . . . . .	69
4.3	Angular distribution simulated particles . . . . .	71
4.4	Results of Reduction Factor Simulations . . . . .	75
4.5	Schematic Penning Trap . . . . .	77
4.6	Schematic Ion Excitation and Detection . . . . .	79
5.1	The DPS . . . . .	84
5.2	The DPS2-F beam tube . . . . .	85
5.3	The DPS2-F TMPs . . . . .	86
5.4	DPS2-F, Lateral Cut . . . . .	88
5.5	Circuit Diagram of the Protection Diodes . . . . .	89
5.6	Magnet Geometry of DPS2-F . . . . .	90
5.7	Stray field map of DPS2-F . . . . .	91
5.8	The DPS2-F Magnet Modules . . . . .	92
5.9	The Ion Analysis and Suppression System . . . . .	93
5.10	The FT-ICR Penning Trap . . . . .	94
5.11	Dipole Mounting Tools . . . . .	96
5.12	The Ion-Suppression Dipole-Design . . . . .	97
5.13	The CPS . . . . .	98
5.14	CPS beam tube - Cryogenics . . . . .	99
5.15	Assembly of the CPS Magnet System . . . . .	100
5.16	Magnet Geometry of CPS . . . . .	101
5.17	Inside of a CPS beam tube segment . . . . .	102
5.18	Getter Pump in CPS Beam Tube Section 6 . . . . .	106
5.19	Condensed Krypton Source in CPS . . . . .	108
6.1	Setup magnetic z-axis alignment . . . . .	110
6.2	Position of Magnet 5 DPS2-F . . . . .	111
6.3	Magnetic Field Module 5 DPS2-F . . . . .	112
6.4	Electro-Optic Experiment . . . . .	113

---

6.5	Source for the Ion Experiments . . . . .	116
6.6	DPS2-F in Volume Assessment Setup . . . . .	119
6.7	Outgassing Measurements, schematic . . . . .	120
6.8	Outgassing Rates DPS2-F . . . . .	122
6.9	Outgassing Spectrum . . . . .	122
6.10	Injection System Gasflow Experiments . . . . .	125
6.11	Collection System of the Gas Flow Experiments . . . . .	126
6.12	RGA Calibration for Helium . . . . .	128
6.13	DPS2-F in Gas Flow Test Setup . . . . .	129
6.14	Pumping Speed Helium Run #2 . . . . .	131
6.15	Effective capture factor TMPs . . . . .	132
6.16	Reduction factor of DPS2-F and Collection System . . . . .	133
6.17	Reduction factors of DPS2-F . . . . .	134
A.1	Flow Diagram of the DPS2-F of the Vacuum System . . . . .	142
A.2	Pump Port Configuration at DPS2-F . . . . .	143
A.3	Flow Diagram Gas Flow Experiments . . . . .	145
A.4	Modes of Operation of CPS . . . . .	146
A.5	Diffusor for Gas Flow Experiments . . . . .	147
A.6	Data Sheet Steel 316L . . . . .	148
A.7	Data Sheet Steel 316LN . . . . .	149
A.8	Modified FT-ICR Modules . . . . .	151
A.9	The SLOW Experiment . . . . .	152
A.10	Gate Voltage Defect Diode . . . . .	154
A.11	The SC Circuit of DPS2-F . . . . .	155
A.12	Redesign of Diodes . . . . .	157





# List of Tables

1.1	Neutrino Oscillation Parameters . . . . .	7
3.1	Stages of vacuum . . . . .	35
3.2	Hydrogen-diffusion in steel . . . . .	53
3.3	Hydrogen Desorption Energies . . . . .	55
3.4	Ion cyclotron frequencies . . . . .	58
4.1	Probability of Tritium Cluster Formation . . . . .	64
4.2	Ion Flux from WGTS . . . . .	65
4.3	Electron Energies from ionized $\beta$ -Sources . . . . .	67
4.4	Conductances DPS2-F . . . . .	70
4.5	Calculation for Testgases DPS2-F . . . . .	76
4.6	Ion Suppression in DPS2-F . . . . .	81
5.1	Dwelling Time $\tau$ at different Temperatures . . . . .	106
6.1	Volume of the DPS2-F Beam Tube . . . . .	121
6.2	Most Important Fluorine Compounds . . . . .	123
6.3	Calibration Factors for Gas Flow Experiments . . . . .	128
6.4	Effective Capture Factor of TMPs . . . . .	131
6.5	Results Reduction Factor . . . . .	133
A.1	List of Components of the DPS2-F Vacuum System . . . . .	141
A.2	List of Components DPS2-F Vacuum Experiments . . . . .	144
A.3	Auxillary Devices for the Setup of FT-ICR . . . . .	150



# Chapter 1

## Introduction

Neutrinos have strongly influenced the progress of experimental and theoretical physics since their first postulation in a short letter by Wolfgang Pauli in 1930. They are extremely light if compared to their leptonic partners and the quarks, and interact only through the weak force making them very difficult to detect experimentally. Neutrinos are the most abundant fermionic particles in the universe with a present number density of  $336\text{ cm}^{-3}$  in the form of relic neutrinos from the Big Bang [Aba11]. In the Standard Model of Particle Physics, there are three active neutrino types ( $\nu_e$ ,  $\nu_\mu$  and  $\nu_\tau$ ) [ALE06].

Experimental neutrino physics has come a long way since the first detection of a neutrino by Reines and Cowan via the "Poltergeist" series of experiments in 1956 [Cow56]. Since then, highly sophisticated terrestrial neutrino sources and brilliant experimental solutions (e.g. the Goldhaber Experiment 1957, determining the neutrino helicity [Gol58], or the SNO experiment 2001, using a combination of different interactions to assess the "solar neutrino problem" [Aha10]) have marked milestones of experimental neutrino physics [APS04].

### History

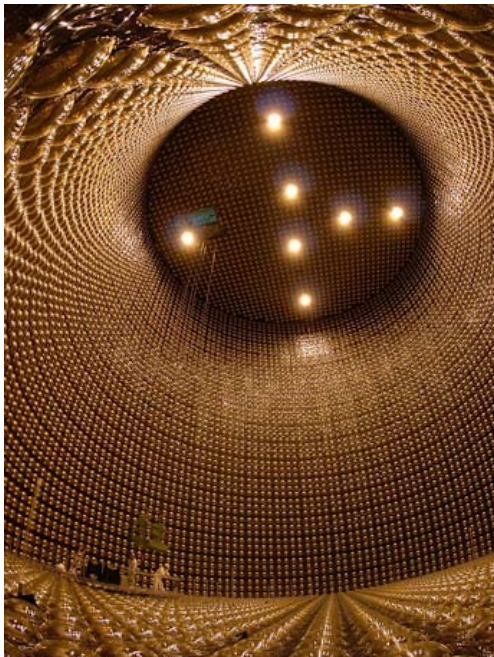
After its postulation, the neutrino and its interactions were coalesced in a coherent theory by E. Fermi in 1933. The neutrino ("the little neutral one") was formulated as a massless, stable, and solely weakly interacting part of the family of leptons. It drew significantly more attention after the first experiments to measure the solar neutrino flux were carried out.

In this context, the famous Homestake Experiment was designed by R. Davis [Dav68] to quantitatively confirm the calculations on the solar neutrino flux carried out by his theoretical colleague J. Bahcall. The experiment thus started out to use neutrinos as messenger particles from the core of the sun, produced by the fusion process  $4\text{ p} + 2\text{ e}^- \rightarrow {}^4\text{He} + 2\nu_e$  there. The fundamental detection process was based on the inverse  $\beta$ -decay of chlorine into argon:

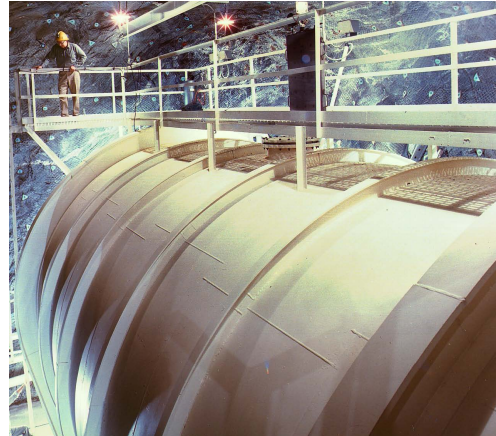
$^{37}\text{Cl} + \nu_e \longrightarrow ^{37}\text{Ar} + e^-$ . To account for this rare charged current (CC) interaction over 615 tons of perchloroethylen were used as a target, and the small number of argon atoms produced had to be extracted by radiochemical means and be counted in small proportional counters [Dav68].

Initial results were presented more than forty years ago. The measurements yielded only 1/3 of the expected solar (electron) neutrino flux, as calculated by Bahcall (based on earlier works by Bethe and Weizsäcker). This "solar neutrino problem" would motivate numerous future experiments, even though the measurements and the calculations were challenged at the time by the community.

In Japan a series of increasingly large water Čerenkov detectors (detecting the characteristic Čerenkov light after elastic  $\nu$ -electron scattering via thousands of photomultipliers) was built in the Kamioka underground laboratory. In 1987 the first one, KamiokaNDE, started data acquisition, confirming a lower than calculated neutrino flux. It measured however, in contradiction to Homestake, a suppression of solar electron neutrinos of about 50 % [Hir91].



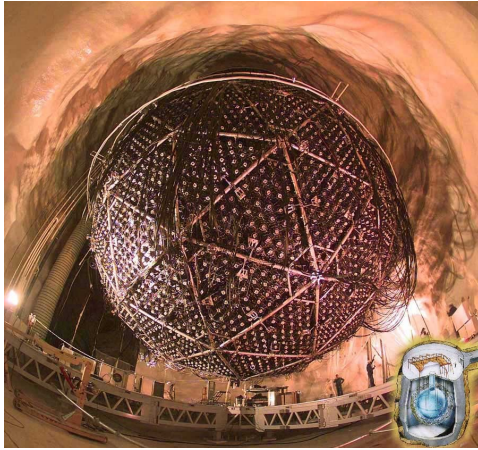
**Inside the Kamiokande Detector**  
source: University of Tokio



**Tank of the Homestake Experiment**  
source: Brookhaven National Labs

It was also Kamiokande II (together with the Irvine-Michigan-Brookhaven detector and the Baksan Neutrino Observatory) that measured cosmic neutrinos emitted by the short (10 s)  $\nu$ -burst from Supernova SN1987, marking the beginning of neutrino astronomy. The analysis revealed the basic validity of our concepts of core-collapse supernovae, and has also been used to put an upper limit on the neutrino mass through time-of-flight analysis [Arn89].

Using data from its successor experiment Super-Kamiokande (a 50 000 t water Čerenkov detector), the Super-Kamiokande Collaboration in 1998 finally presented strong evidence for neutrino mixing and oscillation by measuring atmospheric  $\nu_\mu$  fluxes as a function of their zenith angle [Ash05].



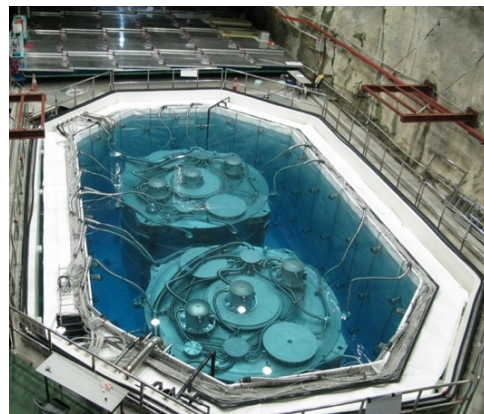
**Main Vessel SNO Experiment**  
source: [SNO homepage](#)

of the subsequent capture process. SNO thus directly demonstrated that flavor transformation of solar neutrinos exist (either by the MSW matter effect [Mik86] or vacuum oscillations), thus rendering strong evidence for neutrinos to be massive.

These advances in neutrino physics motivated new concepts in detector technologies and the exploitation of additional neutrino sources. The solar and atmospheric neutrino experiments have spawned a series of reactor neutrino oscillation experiments. In 2003, the KamLAND experiment has provided the first evidence for the disappearance of reactor anti-neutrinos on the solar  $\nu$ -mass scale, thus providing strong evidence for the Large Mixing Angle solution of the MSW effect to be correct [Abe08].

Current reactor neutrino experiments like Double Chooz, Daya Bay or RENO (since 2011) make use of Gd-doped liquid scintillators to hunt for  $\nu$ -oscillations at the atmospheric  $\nu$ -mass scale [Ard06],[An12],[Ahn10]. For long base-line studies (distance from source on which neutrinos can oscillate), accelerator neutrino experiments like MINOS and OPERA (2005, 2008) were designed, using detection methods optimized for the multi-GeV range [Ada08],[Pes09]. At the same time, next generation solar neutrino observatories like BOREXINO (2007) have expanded the technologies of neutrino physics (or astroparticle physics, in a broader sense) with regard to background levels and suppression into the sub-MeV regime, thus pushing forward to detect individual solar  $\nu$  chains ( ${}^7\text{B}$ ,  ${}^8\text{B}$ , pep) [Bal06].

A final breakthrough concerning the "solar neutrino problem" came from the Sudbury Neutrino Observatory (SNO) in 2001 [Aha10]. Using a spherical detector of 12 m diameter filled with 1000 t  $\text{D}_2\text{O}$ , the SNO Collaboration was able to combine measurements on the pure  $\nu_e$ -flux via CC reactions on the deuteron with neutral current (NC) measurements. In the NC process the deuteron dissociates through neutrino scattering of any flavor. The experimental signature was based on the detection of the neutron from the break-up process and comparison of the characteristic  $\gamma$ -ray signature



**Daya Bay Anti-Neutrino Detectors**  
source: [University of Wisconsin](#)

In summary, a whole variety of experiments, which can not be presented in more detail here, has contributed to the field in the last 15 years, providing evidence for neutrino mixing, and determining the relevant oscillation parameters that will be introduced and explained in the following.

## Neutrino Mixing

After many years of experimental progress it is now established that neutrinos are massive particles and do mix, i.e. the three known flavor states  $\nu_e$ ,  $\nu_\mu$  and  $\nu_\tau$  are quantum superpositions of three light mass states denoted  $\nu_1$ ,  $\nu_2$  and  $\nu_3$ . A corresponding mixing formalism was introduced by Maki, Nakagawa & Sakata [Mak62] as early as 1962<sup>1</sup>. In its current form the PMNS matrix (including Pontecorvo, see next paragraph) can be written as

$$\begin{pmatrix} \nu_e \\ \nu_\mu \\ \nu_\tau \end{pmatrix} = \begin{pmatrix} U_{e1} & U_{e2} & U_{e3} \\ U_{\mu1} & U_{\mu2} & U_{\mu3} \\ U_{\tau1} & U_{\tau2} & U_{\tau3} \end{pmatrix} \cdot \begin{pmatrix} \nu_1 \\ \nu_2 \\ \nu_3 \end{pmatrix}$$

The quantities of this unitary mixing matrix ( $U_{jl}^\dagger = (U_{jl}^*)^T = U_{lj}^*$ ) are usually parametrized as follows:

$$U = \begin{pmatrix} c_{12}c_{13} & s_{12}c_{13} & s_{13}e^{-i\delta} \\ -s_{12}c_{23} - c_{12}s_{23}s_{13}e^{i\delta} & c_{12}c_{23} - s_{12}s_{23}s_{13}e^{i\delta} & s_{23}c_{13} \\ s_{12}c_{23} - c_{12}c_{23}s_{13}e^{i\delta} & -c_{12}s_{23} - s_{12}c_{23}s_{13}e^{i\delta} & c_{23}c_{13} \end{pmatrix} \begin{pmatrix} 1 & 0 & 0 \\ 0 & e^{i\frac{\alpha_2}{2}} & 0 \\ 0 & 0 & e^{i\frac{\alpha_3}{2}} \end{pmatrix}$$

This parametrization can be seen as a superposition of three rotation matrices primarily defined by three mixing angles  $\theta_{ij}$ . The entries of  $U$  are defined through the trigonometric expressions  $c_{ij} = \cos \theta_{ij}$  and  $s_{ij} = \sin \theta_{ij}$ . In  $\nu$ -oscillations, the CP violating phase  $\delta$  (Dirac phase) is of major interest for future experiments, while the two additional Majorana phases  $\alpha_2$ ,  $\alpha_3$  do not influence the oscillation pattern, but are of prime interest for  $(0\nu\beta\beta)$ -experiments.

The neutrino masses and their mixing constitute physics beyond the Standard Model and impose up to nine additional parameters (three mixing angles, three mass states and up to three CP violating phases) on particle physics<sup>2</sup>.

The flavor eigenstates  $|\nu_l\rangle$  with  $l = e, \mu, \tau$  can thus be written as superpositions of the mass eigenstates  $|\nu_j\rangle$  with  $j = 1, 2, 3$ , or vice versa, using the unitary

<sup>1</sup>In the original work by Maki, Nakagawa & Sakata only two weak states ( $\nu_e$ ,  $\nu_\mu$ ) and two "true neutrinos" ( $\nu_1$ ,  $\nu_2$ ) were proposed, connected via a real constant  $\delta$ . The PMNS Matrix was later on expanded to three neutrino states. The reader may notice this rotational parametrisation to be 1 year older than the perhaps better known Cabibbo formalism.

<sup>2</sup>If the Majorana character of neutrinos (i.e.  $\nu_l = \bar{\nu}_l$ ) should be ruled out in the future, the two corresponding phase parameters would have to be dropped.

PMNS Matix  $U$  as

$$\begin{aligned} |\nu_l\rangle &= \sum_j U_{lj} |\nu_j\rangle, \\ |\nu_j\rangle &= \sum_l U_{lj}^* |\nu_l\rangle \end{aligned}$$

In the following we more thoroughly look into the phenomenon of  $\nu$ -oscillation.

## Neutrino Oscillations

In 1957 Bruno Pontecorvo formulated the first theory of neutrino "oscillations." He showed that if different species of neutrinos exist (in his case neutrinos and anti-neutrinos), they might be able to oscillate back and forth between different species. Almost 50 years later the phenomenon of oscillations was finally verified experimentally (see e.g. figure 1.1). Since Pontecorvo's ground-breaking works and ideas, the theory has been further refined over the years.

The fundamental idea can be described as follows: The neutrino mass eigenstates  $m_j$  travel through space with energies

$$E_j = \sqrt{p^2 c^2 + m_j^2 c^4} \approx pc + \frac{m_j^2 c^3}{2p}$$

At this point it is obvious that in the case of  $m_{j'} \neq m_j \neq 0$ ; ( $j' \neq j$ ) the propagation of the mass states through space-time will differ with respect to their mass. The time evolution of these mass eigenstates, as defined above, is then given by

$$|\nu_j(t)\rangle = e^{-iE_j t/\hbar} |\nu_j\rangle.$$

Hence, a pure weak eigenstate, produced at  $t = 0$ , will evolve over time with

$$|\nu_l(t)\rangle = \sum_j U_{lj} e^{-iE_j t/\hbar} |\nu_j\rangle = \sum_{j,l'} U_{lj} U_{l'j}^* e^{-iE_j t/\hbar} |\nu_{l'}\rangle$$

The transition probability of flavor states can now be written through:

$$\begin{aligned} P(\nu_l \rightarrow \nu_{l'}, t) &= |\langle \nu_{l'} | \nu_l \rangle|^2 = \left| \sum_j U_{lj} U_{l'j}^* e^{-iE_j t/\hbar} \right|^2 \\ &= \sum_j |U_{l'j}|^2 |U_{lj}|^2 + 2 \sum_{k < j} |U_{lk} U_{l'k}^* U_{lj}^* U_{l'j}| \cos(\Delta E_{jk} t/\hbar) \end{aligned}$$

If we now consider the highly relativistic case<sup>3</sup>, and introduce the oscillation length  $L$  instead of  $t$  as the relevant parameter, and consider an initially pure

<sup>3</sup>Given the usual case of large kinetic energy and almost vanishing masses, we can assume the relativistic limit of  $p = E$ . Assuming a mass of 1 eV, and considering a 30 MeV  $\nu_\mu$  from  $\pi^+$  decay at rest, we find  $p \cong E \cdot (1 - 4.4 \times 10^{-16})$ .



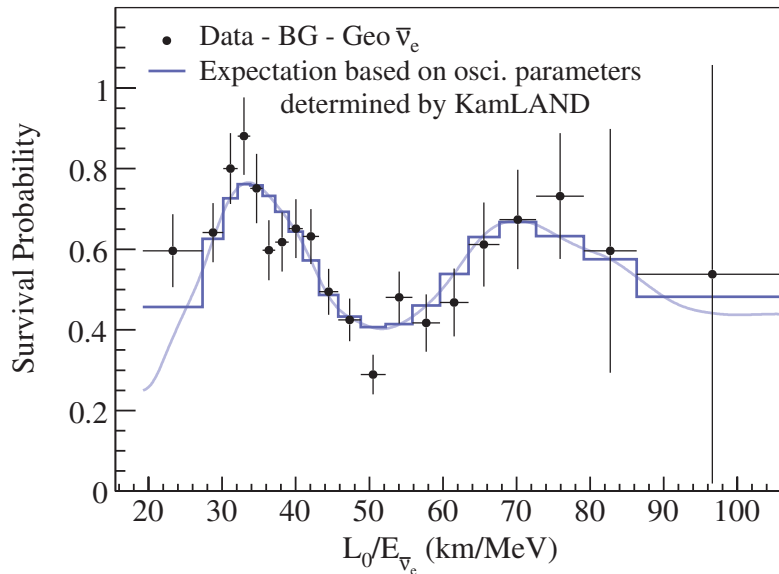


Figure 1.1: **Medium Base Line Oscillation:** Shown are results gained at the KamLAND Reactor Neutrino Experiment very clearly proving an oscillation in the survival probabilities of electron neutrinos with respect to the  $L/E$  ratio. Based on [Abe08].

electron flavor state  $\nu_e$ , we obtain

$$P(\nu_e \rightarrow \nu_e(L/E)) = 1 - \sin^2 2\theta_{13} \cdot \sin^2 \left( 1.267 \frac{\Delta m_{31}^2 L}{E} \right) - \cos^4 \theta_{13} \cdot \sin^2 2\theta_{12} \cdot \sin^2 \left( 1.267 \frac{\Delta m_{21}^2 L}{E} \right)$$

In the last decades considerable experimental efforts were made to determine the oscillation parameters. Table 1.1 sums up the relevant parameters as known by today, also including experimental results which were obtained most recently [PDG10],[Ard06],[An12],[Ahn10].

In general the parameters  $\Delta m_{21}^2$  and  $\theta_{12}$  are referred to as the "solar mixing" parameters (often written as  $\Delta m_{\odot}^2$  and  $\theta_{\odot}$ ), while  $\Delta m_{32}^2$  and  $\theta_{23}$  are known as the "atmospheric mixing" parameters ( $\Delta m_{\text{A}}^2$  and  $\theta_{\text{A}}$ ). This originates from the fact that for solar neutrino oscillations, the  $\nu_e$ , being used to investigate the mixing in the first two generations, is produced in the solar core, whereas for atmospheric neutrinos the  $\nu_{\mu}$  is generated by cosmic muons.

Based on the three flavor oscillation characteristics presented above, the importance of combining complementary experiments with various base lines becomes evident. For example, to measure the small mixing angle  $\theta_{13}$ , indicating genuine three flavor mixing, one needs a detector at a distance  $L \approx 1$  km for MeV energies, so that oscillations driven by  $\Delta m_{\odot}^2$  become negligible. This



Table 1.1: **Neutrino Oscillation Parameters**

The relevant neutrino oscillation parameters are given with their values and errors as of May 2012, together with the relevant experiments.

Parameter	Value	Experiment	Source
$\sin^2(2\theta_{12})$	$0.861 \pm 0.026$	KamLAND + solar	[Aha10]
$\sin^2(2\theta_{23})$	$> 0.92$	Super Kamiokande	[Ash05]
$\sin^2(2\theta_{13})$	$0.092 \pm 0.016_{(\text{stat})} \pm 0.005_{(\text{syst})}$	Daya Bay	[An12]
$\Delta m_{21}^2$	$(7.59 \pm 0.21) \times 10^{-5} \text{ eV}^2$	KamLAND + solar	[Aha10]
$\Delta m_{31}^2$	$(\pm 2.43 \pm 0.13) \times 10^{-3} \text{ eV}^2$	MINOS	[Ada08]

method has very recently been employed successfully by the Daya Bay, RENO and Double Chooz Collaborations [An12],[Ahn10],[Ard06].

From recent solar neutrino data we know the term  $\Delta m_{21}^2 \cos 2\theta_{12} > 0$  [Aha10], [PDG10]. Conventionally, the mass states 1 and 2 of the first two generations are defined so that  $\Delta m_{21}^2 > 0$ . Accordingly, the remaining difference of squared masses  $\Delta m_{23}^2$  is not known at present (see also figure 1.2). With this information from the experimental side, the neutrino mass pattern can be grouped in the following generic cases [Pas05],[PDG10]:

1. Normal hierarchical case:

$$m_1 \ll m_2 < m_3, m_2 \cong (\Delta m_{\odot}^2)^{1/2} \approx 0.009 \text{ eV}, m_3 \cong (\Delta m_{\text{A}}^2)^{1/2} \approx 0.047 \text{ eV}$$

2. Inverted hierarchical case:

$$m_3 \ll m_1 < m_2, m_{1,2} \cong |\Delta m_{\text{A}}^2|^{1/2} \approx 0.047 \text{ eV}$$

3. Quasi-Degenerate case:

$$m_1 \cong m_2 \cong m_3, m_j^2 \gg |\Delta m_{\text{A}}^2|, m_j \gtrsim 0.1 \text{ eV}$$

Cases 1 and 2 are illustrated in figure 1.2. These three possibilities are compatible with all experimental constraints currently known. The generic neutrino mass pattern, either the normal or the inverted hierarchy, can be resolved by very long baseline experiments ( $L > 1000 \text{ km}$ ), exploiting matter enhanced oscillations via the MSW effect [Alb04],[Bar00].

Due to their intrinsic nature as quantum mechanical interference phenomenon, neutrino oscillations are not sensitive to the absolute mass scale. With all mixing angles  $\theta_{ij}$  and mass splittings  $\Delta m_{ij}^2$  now known to rather high precision (apart from  $\delta$ ), it is the absolute mass scale of neutrinos that will be the most decisive parameter for theory to develop a model for  $\nu$ -masses. A successful model of  $\nu$ -masses would impact not only neutrino physics but also elementary particle physics and cosmology.

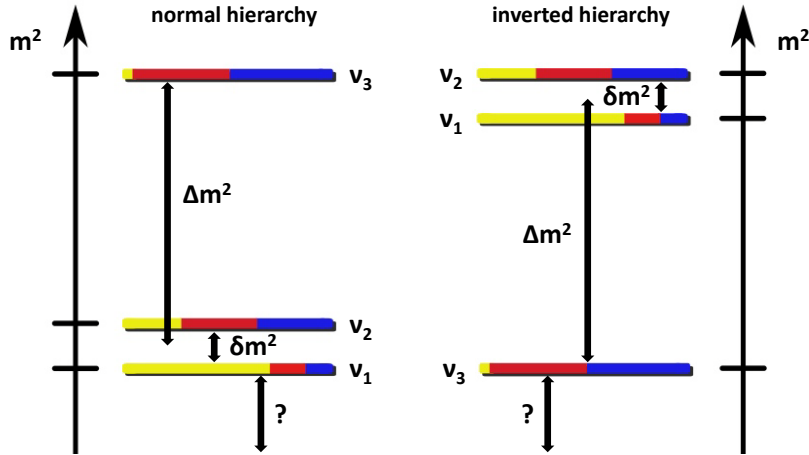


Figure 1.2: **The Neutrino Mass Hierarchy**

Shown are two generic hierarchies of neutrino mass eigenstates. The notations  $\nu_{1,2,3}$  are convention. For higher clarity we have denoted  $|\Delta m_{\text{A}}^2|$  as  $\Delta m^2$  and  $\Delta m_{\odot}^2$  as  $\delta m^2$ . Mixing is indicated through the colors with yellow for electron type, red for muon type and blue for tau type flavor.

### Importance of Neutrino Mass

**Particle Physics beyond the Standard Model** The Standard Model of particle physics describes the neutrino as purely weakly interacting and massless lepton. The determination of the absolute mass scale of neutrinos would therefore be a further important step towards the unraveling of physics beyond the Standard Model. Mass generation in the Standard Model requires a coupling to the Higgs field via the standard Yukawa Lagrangian

$$\mathcal{L}_{\text{Yukawa}} = -y (\bar{\nu}_e, \bar{e})_{\text{L}} \Phi N_{\text{R}} + h.c.$$

with the coupling constant  $y$  and the standard Higgs doublet  $\Phi$  and the non-interacting, right-handed part of the Dirac neutrino  $\nu = \nu_{\text{L}} + N_{\text{R}}$ .

Non-zero couplings of neutrinos to the Higgs field would imply the existence of active, right handed neutrinos. This is however constrained by current experimental results (in terms of the observable helicity) and theory.

To generate  $\nu$ -masses we introduce the following models [Lan95]:

1. simply introduce an active  $\nu_{\text{R}}$  term into  $\mathcal{L}_{\text{Yukawa}}$ , rendering (after symmetry breaking)  $\mathcal{L} = -y\Phi_{0,\text{D}}(\bar{\nu}_{\text{L}}\nu_{\text{R}} + \bar{\nu}_{\text{R}}\nu_{\text{L}})$  with vacuum expectation value  $\Phi_{0,\text{D}}$  of the Higgs doublet field. In this case (which would be the case for Dirac-type neutrinos only) the coupling constant to the Higgs field would have to be tuned to very low values ( $\leq 10^{-12}$ ) from which new questions would arise as to the cause of this value.
2. consider Majorana-type neutrinos ( $N_{\text{R}} = \nu_{\text{R}} = \nu_{\text{R}}^c$ ) and expand the Lagrangian to  $\mathcal{L} = -1/2 y\Phi(\bar{\nu}_{\text{L}}\nu_{\text{R}}^c + \bar{\nu}_{\text{R}}^c\nu_{\text{L}})$ . This expression however does

violate weak iso-spin conservation by  $\Delta I = 1$ , which needs to be compensated by either introducing more complex Higgs models (e.g. a Higgs triplet or two Higgs doublets), or a four-point coupling in the effective field theory approach  $\mathcal{L} = -y\Lambda^{-1}\Phi_0\Phi_0\nu_L^c\nu_L$ . The latter keeps the coupling close to the usual fermionic coupling, however it requires the introduction of a new scale  $\Lambda$  in the range of  $\approx 10^{13}$  GeV.

3. use mixed forms of Dirac and Majorana types rendering a "see-saw model" (numerous varieties of this potential model were proposed so far). In these scenarios, the effective neutrinos are combinations of extremely light (down to  $\approx 10^{-11}$  GeV) and very heavy states (up to  $\approx 10^{16}$  GeV), originating from interactions of different  $y_{\text{Dirac}}$  and  $y_{\text{Majorana}}$  couplings.

Would the absolute values of neutrino masses be known, the field of theoretical neutrino physics would be able to advance rather swiftly, also with regard to understand the generation of fermion masses in general. Along these efforts, clues to solve the hierarchy problem of the mass coupling could be found.

**Cosmological Relevance** Besides fundamental particle physics, also cosmology would benefit significantly from the determination of the absolute  $\nu$ -mass scale. The formation of large-scale structures in the universe is significantly influenced by relic neutrinos, rendering the neutrino mass scale highly important for the further development of cosmological models. The freeze-out of relic neutrinos happened about one second after the Big Bang (at an energy around 1 MeV). Today these neutrinos have a Planck black body temperature of 1.95 K, forming the so called Cosmic Neutrino Background (C $\nu$ B). They are the oldest potential messengers in the cosmos (aside from more speculative gravitational wave echoes from the Big Bang itself), and they are by far the most abundant fermionic particles in the universe.

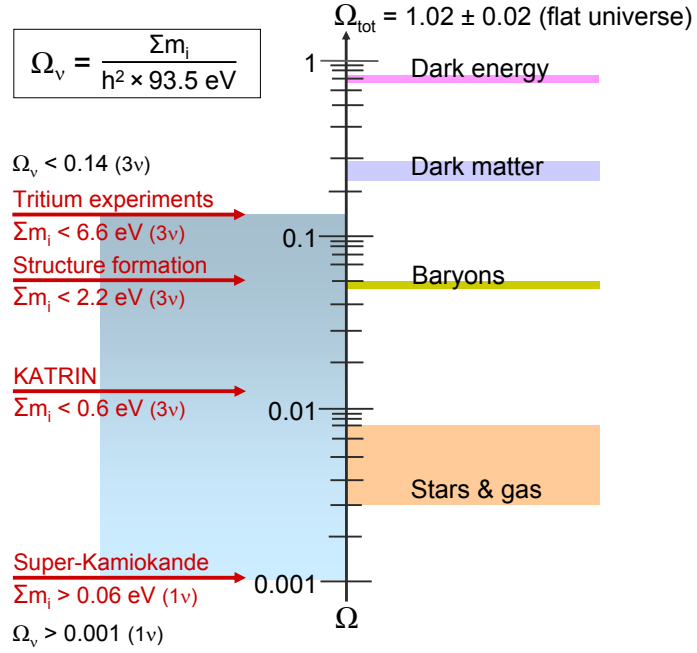
The role of neutrino masses in cosmology is usually parametrized by the fraction  $f_\nu$  of the neutrino mass to the total matter density  $\Omega_m$  in the universe, which is given by [Aba11] through

$$f_\nu = \frac{\Omega_\nu}{\Omega_m} = \frac{\sum m_\nu}{93\Omega_m h^2 \text{ eV}} \cong 0.08 \frac{\sum m_\nu}{1 \text{ eV}}$$

with the numerical factor being given by the latest WMAP7 data for  $h^2\Omega_m$  [Kom11]. As can be seen, even neutrino masses in the sub-eV regime can contribute significantly to the matter budget and thus to structure evolution of the universe (cf. figure 1.3).

Currently there are three independent approaches towards elucidating the absolute neutrino mass scale: cosmological studies, the search for neutrino-less double beta decay ( $0\nu\beta\beta$ ), and finally the precise investigation of single  $\beta$ -decay energy spectra. The general ideas, challenges and up-to-date experimental set-ups will be introduced in the following.

Figure 1.3: **Neutrino Mass on cosmological Scales:** On the right hand side of the  $\Omega$ -ladder the current best estimates of the matter-energy distribution in the universe is shown. Massive neutrinos contribute as hot dark matter. On the left hand side the currently allowed range of contributions from the neutrino mass is shown. As can be seen the neutrino impact currently spans about 2 orders of magnitude. Source: [Eic09]



## Experimental Approaches to the absolute Neutrino Mass

**Cosmological Studies - Structure Formation** As stated above, cosmological models of large-scale structures can be highly sensitive to the sum of the neutrino masses. A summary of the recent developments in this field can be found e.g. in [Han10].

The universe became transparent to neutrinos roughly one second after the Big Bang. The conditions for this freeze-out require the interaction rates for neutrinos to become smaller than the Hubble expansion rate of the universe. This happened at a typical energy scale of the order of 1 MeV. It is to be noted here that neutrinos at this point were highly relativistic, so their mass was not an important parameter at this very early stage (this is also relevant at the CMB freeze-out, see below). At later epochs of the cosmos - the time of structure formation - neutrinos tend to erase structure formation depending on their mass (to paraphrase B. Kayser "the lighter they are, the lumpier it gets" [Kay05]). It is to be noted further that an attempt to determine the neutrino mass from cosmic structure studies of course strongly depends on the model used.

The matter distribution of the universe has been the object of extensive studies in the past years. Especially the measurement of the Cosmic Microwave Background (CMB), e.g. by the WMAP Collaboration [Kom11], has brought important new insights. Based on a seven-year data set, the WMAP Collaboration published an upper limit on the sum of the neutrino masses of  $\sum m_{\nu} < 1.3 \text{ eV}/c^2$  (95 % C.L.).

This value can be combined with other cosmological studies like measurements from Baryon Acoustic Oscillations (BAO), or the measurement of the Hubble constant, which renders again a model-dependent upper limit down to  $\sum m_\nu < 0.44 \text{ eV}/c^2$  (95 % C.L.) [Han10].

Optimistically [Han10], with on-going experiments like the Planck mission, and advances in 21-cm-observations and very large scale lensing surveys, cosmological sensitivities to the neutrino mass may reach down to  $\sum m_\nu < 0.05 \text{ eV}/c^2$  within the next years.

**Supernova Neutrinos** Given their usual ultra-relativistic propagation, a mass determination via a dedicated time-of-flight analysis requires neutrinos to be emitted from a very distant source that is powerful enough to provide a neutrino flux still detectable after long distances.

A Supernova type II can be associated with the core collapse of a massive star. This gravity-driven implosion allows neutron production through electron capture  $p + e^- \rightarrow n + \nu_e$ , and, after the formation of a hot proto-neutron star, thermal  $\nu$ -emission via  $e^+ + e^- \rightarrow \bar{\nu}_l + \nu_l$  [Bri07]. A fraction of 99% of the enormous amount of energy dissipated by the core-collapse (up to over  $10^{59}$  MeV) is carried into space through neutrinos with characteristic kinetic energies of several MeV, rendering an isotropic neutrino emission of  $\approx 10^{58}$  over just a few seconds.

The so far only observation of SN-neutrinos was based on SN 1987A. About a dozens of events associated with the SN-burst were detected by several detectors around the world. SN-based  $\nu$ -mass analysis, like cosmological structure studies, is strongly model-dependent, especially through the many necessary assumptions about the detailed  $\nu$ -emission characteristics of a supernova. Nevertheless, an upper limit on the "electron neutrino mass" of  $m_{\nu_e} < 5.7 \text{ eV}/c^2$  (95 % C.L.) was determined from SN 1987A [Lor02].

In the case of a future galactic supernova, neutrino observatories like ICECUBE and LENA [Ahr04],[Wur12] might yield further insights.

**Neutrino-less double Beta Spectrum** Very interesting insights into the intrinsic properties of neutrinos can be gained through experiments searching for neutrino-less double beta decay ( $0\nu\beta\beta$ ). A genuine detection would not only prove the Majorana nature of neutrinos (i.e.  $\nu = \bar{\nu}$ ), it would also imply lepton number violation and give access to the neutrino mass scale (for a current review see e.g. [Cre10]).

An important characteristic of experimental  $0\nu\beta\beta$ -studies is the specific expected spectral structure (see figure 1.4). Since no energy dissipation by neutrinos is possible, the decay electrons (plus the nuclear recoil) carry away the

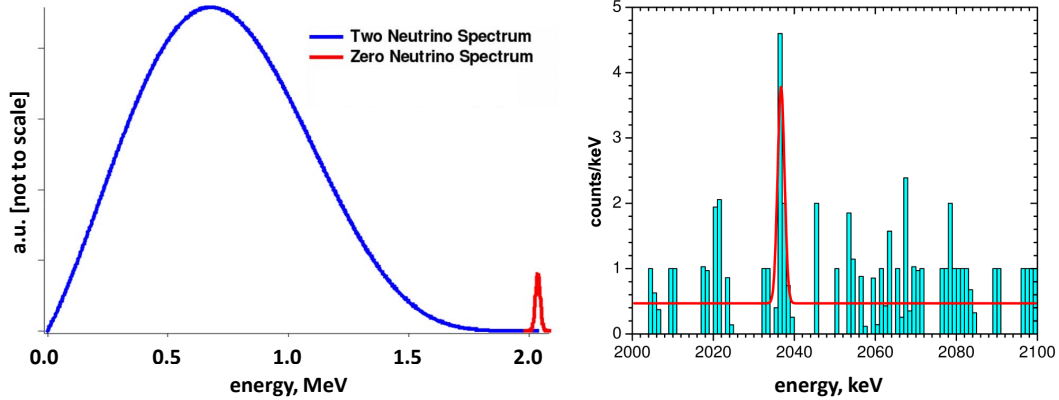


Figure 1.4: **Neutrino-less double beta-decay ( $0\nu\beta\beta$ ) Spectrum**

Shown on the left is a schematic plot of the energy spectrum of double beta-decay. In blue the spectrum for a decay involving two neutrinos, in red the ( $0\nu\beta\beta$ ) spectrum is indicated (not to scale). Based on [Pav10]. On the right the controversial results from  $0\nu\beta\beta$  measurements published by [Kla06] are presented.

entire decay energy, which then can be detected through calorimetric or spectroscopic approaches. From the width  $\Gamma^{0\nu}$  of this decay the effective (Majorana) neutrino mass  $m_{\beta\beta}$  is determined via [Cre10]:

$$\Gamma^{0\nu} = G^{0\nu} |M^{0\nu}|^2 |\langle m_{\beta\beta} \rangle|^2$$

with the phase space integral  $G^{0\nu}$  and the nuclear matrix element  $|M^{0\nu}|^2$ . With  $m_{\beta\beta}$  we denote the effective Majorana neutrino mass which is the "coherent sum" of the mass eigenstates  $m_j$ . The coherent nature of  $m_{\beta\beta}$  allows possible cancellations originating from the (CP violating) Majorana phases  $\alpha_j$ .

$$\langle m_{\nu\beta\beta} \rangle = \sum_j |U_{ej}|^2 m_j e^{i\frac{\alpha_j}{2}}$$

With these potential cancellations the measured effective mass  $m_{\beta\beta}$  will be smaller than the value  $m_\beta$  obtained from the incoherent sum of the pure eigenstates for large non-zero values of  $\alpha_j$ . If combined with direct mass measurements (as will be described below), the study of ( $0\nu\beta\beta$ ) decay allows, at last in principle, for experimental constraints of the Majorana phases.

The controversially discussed results from a sub-group of the Heidelberg-Moscow-Experiment (HDM) show the difficulties in assessing a clear  $0\nu\beta\beta$ -signal (see figure 1.4). It is important to note however that HDM has reached the highest sensitivity so far, using enriched  $^{76}\text{Ge}$  semiconductor detectors from 1990 - 2003. In 2006 [Kla06] a value of  $\langle m_{\beta\beta} \rangle = 0.32(3)$  eV was published.

Several experiments, e.g. SNO+ (filling its large inner sphere with liquid scintillating material and adding 1 t Nd as  $0\nu\beta\beta$ -source), as well as the  $^{76}\text{Ge}$

experiments Majorana and GERDA will scrutinize this result. Other future experiments include CUORE, that will use large amounts (750 kg) of  $\text{TeO}_2$ , which contains the  $\beta\beta$ -active  $^{130}\text{Te}$  at 10 mK, and EXO, which will be (in its final configuration) based on several tons of liquid Xe enriched to 85%  $^{136}\text{Xe}$ , and numerous others, all aiming to verify this rare decay and gain access to the physics behind the  $0\nu\beta\beta$ -decay.

**Single Beta Spectrum** Another strategy to assess the neutrino mass scale is a spectral analysis of the energy spectrum of  $\beta$ -decay electrons close to the  $\beta$ -endpoint of isotopes undergoing single  $\beta$ -decay. For a good differential spectral analysis this requires a low end point energy  $E_0$  to maximize the number of decays detectable close to the endpoint, where the influence of the neutrino mass becomes most apparent. Moreover, the  $\beta$ -decaying isotope should feature a short half-life to provide good statistics.

Currently there are two solid state sources that are being investigated experimentally. They are based on the  $\beta$ -unstable isotopes  $^{187}\text{Re}$  and  $^{163}\text{Ho}$ .

**Rhenium** One promising candidate for these spectral studies is the isotope  $^{187}\text{Re}$ . With  $E_0 = 2.47$  keV, the nucleus  $^{187}\text{Re}$  has the lowest  $\beta$ -endpoint energy known. A drawback is its very long half-life time of  $4.3 \times 10^{10}$  years, which only renders about one Becquerel per milligram of rhenium used.

It is used in  $\beta$ -decay studies of the project "Microcalorimeter Arrays for a Rhenium Experiment" (MARE) [Nuc10]. Also using  $^{187}\text{Re}$  as a  $\beta$ -emitter, the precursor experiment MiBeta of Milano [Nuc02] has published a limit of  $m_{\nu_e} < 15$  eV/ $c^2$  (90% C.L.) [Sis04].

For MARE, the bolometric approach will be further refined, i.e. the energy measurement is based on a precise detection of the decay heat through thermistors designed to record temperature rises on the mK scale. The source here acts as its own detector, with the active crystals ( $^{187}\text{Re}$  bound for example in  $\text{AgReO}_4$ ) scrupulously shielded so that the energy emitted in the decay is measured, except for the part taken away by the neutrino. The thermistor coupled to the crystal transforms the change in temperature into a change in resistivity, which can be read-out with high precision. A rather fast read-out prevents pulse pile-up in the crystal, and thus allows for larger source masses (with good statistics). MARE will deploy arrays of small, separate Rhenium crystals, with single crystal masses of around 0.3 mg being proposed for MARE-I and 1.5 mg for MARE-II. MARE-I aims for an array of 300 Re crystals with an energy resolution of 10 eV. For MARE-II a larger array with up to 100 000 crystals with an energy resolution below 5 eV is envisaged.

Generally speaking, rhenium spectroscopy represents a very interesting approach to neutrino masses, because of its expandability and potentially rather low systematic errors. The set-up and calibration of these large crystal arrays however implies great technical challenges.

**Holmium** Another potentially interesting method is related to the study of the  $^{163}\text{Ho}$  electron capture (EC) decay. The use of Holmium for direct neutrino mass determination was proposed by [Ruj82] in 1982, and has more recently been analyzed by [Gal12]. The decay



produces one electron neutrino and features a remarkably low  $Q$ -value of only around 2.56 keV (comparable with  $^{187}\text{Re}$ ), but combined with a much shorter half-life of 4570 years. Due to the low transition energy, electron capture is only possible for electrons from the M-shell or higher ones. The unique structure of the spectrum arising from the different shells participating in the EC process could enhance the sensitivity towards neutrino mass. As can be seen in figure 1.5 an EC process involving the innermost allowed shell  $M_1$  significantly increases the count rate close to the endpoint.

A new approach to measuring the  $^{163}\text{Ho}$  spectrum and thus determining the neutrino mass influence at the end point is a total calorimetric measurement comparable with the MARE approach to the  $^{187}\text{Re}$  spectrum. It is however important to note that the sensitivity of such experiments to the neutrino mass strongly depends on the absolute  $Q$ -value. With a higher  $Q$ -value, the high-energy tail will smear out and sensitivity will decrease (for  $Q \geq 2.6$  keV the statistical limits with 90% C.L. will hardly reach the  $m_\nu = 0.2$  eV value without undue experimental effort [Gal12]).

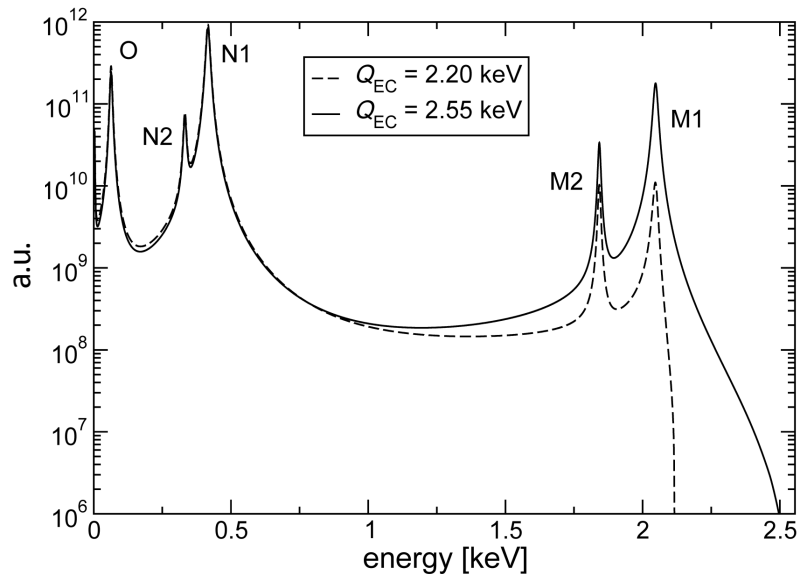


Figure 1.5: **The  $^{163}\text{Ho}$  EC Spectrum:** Shown are two calculated energy spectra of the  $^{163}\text{Ho}$  EC decay. Since the absolute energy ( $Q$ -value) is not yet precisely determined, the count rate at the very end of the spectrum (region of interest for neutrino mass determination) is also not known yet. Source: [Nuc10]



**The ideal  $\beta$ -emitter: Tritium** Tritium with its low end-point energy of 18.6 keV and short half-life of 12.3 years is ideally suited for high precision  $\beta$ -decay studies and the hunt for the  $\nu$ -mass.

Tritium  $\beta$ -spectroscopy in general and the KATRIN-Experiment as a next-generation experiment in particular will be introduced in greater detail in the following section.



## Chapter 2

# The Karlsruhe Tritium Neutrino Experiment

In this chapter we will outline the specific advantages of using tritium for high precision  $\beta$ -spectroscopy for the determination of the neutrino mass (section 2.1). The well-established concept of a MAC-E filter and current upper mass limits will be introduced, as well as the considerable experimental challenges of a next generation MAC-E filter experiment.

The second part of the chapter is dedicated to the KATRIN experiment. Descriptions of the general assembly as well as technical solutions to the various requirements developed by the KATRIN Collaboration are presented in section 2.2.

## 2.1 High Precision Tritium Beta-Spectroscopy

As stated in the introduction, high precision  $\beta$ -spectroscopy is the most promising approach for determining the absolute mass scales of neutrinos in a model-independent way [Thu11]. The most successful approaches so far were carried out by analyzing the kinematics of the tritium  $\beta$ -decay  ${}^3\text{H} \rightarrow {}^3\text{He} + e^- + \nu_e$ .

The study of tritium  $\beta$ -decay (the electron spectrum of this decay is shown in figure 2.1) is ideally suited for the direct measurement of the "electron-neutrino mass".

- The decay  ${}^3\text{H} \rightarrow {}^3\text{He} + e^- + \nu_e$  is a super-allowed nuclear transition, featuring a decay matrix element which is independent of the energy, furthermore simplifying the calculations of energy corrections [Rob88].
- The simple atomic shell structure of tritium and helium allows for exact calculations of electronic or molecular excitations and precise estimations of their relative probabilities [Dos06],[Dos08].

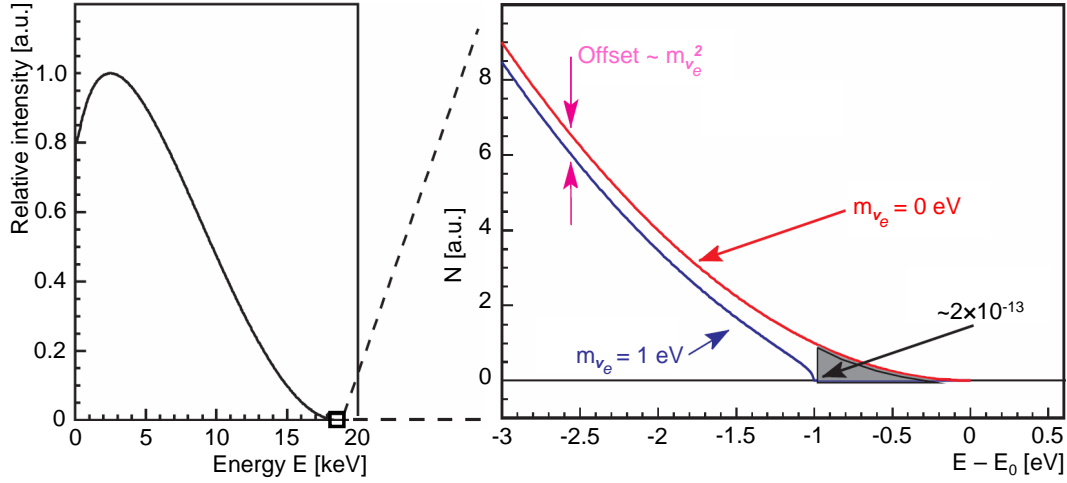


Figure 2.1: **Electron spectrum of tritium  $\beta$ -decay**

Shown on the left is the complete energy spectrum ranging from 0.0 keV up to 18.6 keV. On the right, the energy region close to the endpoint is shown with two distributions, one for a vanishing neutrino mass, the other for a non-zero neutrino mass  $m_{\nu_e} = 1$  eV.

- A gaseous emitter generally has the advantage that no crystal or other solid state effects in the energy signature have to be accounted for.
- It features a relatively low endpoint energy of only  $\approx 18.57$  keV. The low endpoint is preferable in  $\beta$ -spectroscopy, since the retarding potential applied to the large spectrometer must correspond to the maximum kinetic energy. The possibility of vacuum discharge and the stringent requirements on voltage stability lead to technical challenges that are easier to meet with comparably low voltages. The low end point energy also leads to a favorable phase space of the decay. The half-life of 4500(8) d is central to achieving  $\beta$ -intensities in excess of  $10^{10} \text{ s}^{-1}$ .
- Given their low nuclear charge number, tritium and helium feature a very small cross section for inelastic scattering. A large value for this systematic effect would compromise the energy signature for  $m_{\nu_e}$ .

Over the past 25 years tritium  $\beta$ -decay experiments have pushed the model independent sensitivity for the absolute scale of neutrino masses further and further down.

The most promising results were gained using a MAC-E filter setup that will be explained in the following.

### 2.1.1 MAC-E-Filter Experiments

The technique of MAC-E Filters (Magnetic Adiabatic Collimation with an Electrostatic Filter) has been developed in the early eighties. The principle

was first proposed by [Kru83] based on works by [Bea80], and successfully used for tritium  $\beta$ -decay experiments for the first time in Russia in the mid-eighties at Troitsk [Lob85], and, independently in the late eighties at Mainz [Pic92],[Wei93].

MAC-E Filter experiments usually feature the following components:

- A  $\beta$ -decay electron source designed preferably with high intensity and well understood systematic effects (solid-state effects, temperature influences etc.).
- A "transport section", separating the source from the spectrometer, as the spectrometer has to be kept as "clean" as possible. The transport section provides good vacuum conditions and prevents possible  $\beta$ -emitters to decay within the spectrometer.
- The spectrometer, which acts as the MAC-E filter, should feature a precise retarding potential and high energy resolution.
- A detector, which counts the integral  $\beta$ -decay flux which is transmitted through the spectrometer potential<sup>1</sup>.

The principal setup of a MAC-E filter is presented in figure 2.2.

At both ends of the spectrometer vessel two strong superconducting solenoids create an inhomogeneous magnetic field that guides the electrons to be analyzed through the spectrometer. In the middle of the spectrometer, the lowest magnetic field value is reached, defining the so called analyzing plane. The field strength at this mid plane typically is several orders of magnitude lower than in the center of the solenoids.

If a  $\beta$ -decay occurs within the source area of high  $B$ -field, the electrons, generated with an isotropic velocity distribution, are guided by the magnetic field lines and travel on cyclotron paths toward the analyzing plane. Their trajectory is defined by the specific angle between the velocity vector components orthogonal and parallel to the field lines. The drop in local magnetic field strength when entering the spectrometer vessel will force the cyclotron energy part  $E_{\perp}$  of their momentum to be parallelized with respect to the field lines. If designed correctly, without strong field gradients, the magnetic moment  $\mu = E_{\perp}/B$  remains constant. Correspondingly, the shift in momentum occurs adiabatically, resulting in a parallelization of velocity vectors (this is schematically shown in the bottom part of figure 2.2).

With all the velocity vectors being parallelized, a retarding potential is used for integral analysis of the kinetic energy. The potential is generated by applying a high voltage either directly to the spectrometer vessel, or onto electrodes

<sup>1</sup>Advances in detector design, e.g. the use of high energy resolution cryo-bolometers, will likely allow for a differential spectral measurement at some point in the future.

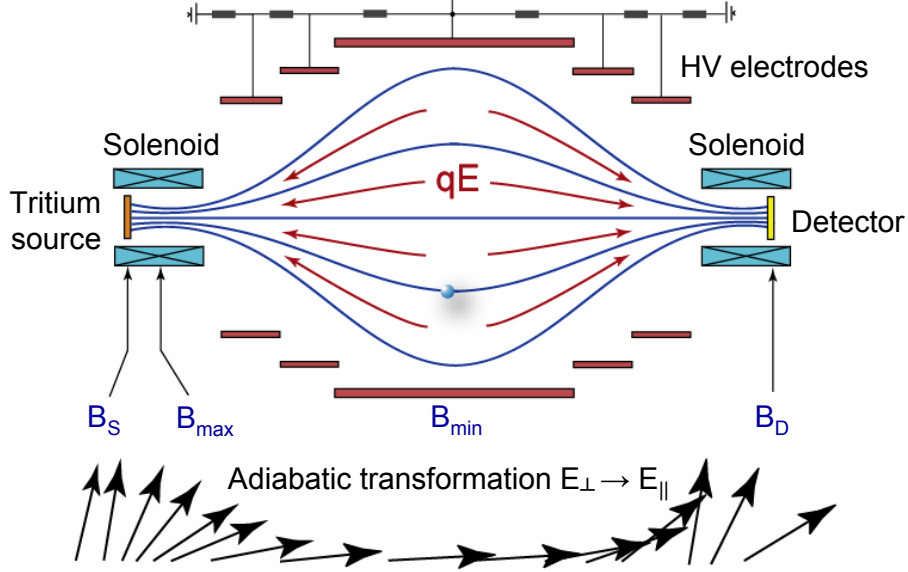


Figure 2.2: **Fundamental MAC-E Filter Setup**

The electrons are created in regions of high magnetic field (at the source; left side). While traveling towards the detector on cyclotron paths along the magnetic field lines, they enter regimes with declining field strength hence orthogonal fractions of the velocity vector are parallelized enabling a precise kinematic discrimination.

constructed within. Electrons with surplus kinetic energy with regard to the retarding potential are counted by a detector on ground potential, installed at the end of the beam line.

This combination of  $E$ - and  $B$ -fields is an essential feature of the MAC-E filter, acting as an integrating high-pass filter. By varying the retarding potential, the shape of the  $\beta$ -spectrum becomes accessible with a high energy resolution  $\Delta E/E$  that is proportional to the ratio of minimal and maximal magnetic fields (corresponding to the analyzing plane and the pinch solenoids):

$$\frac{\Delta E}{E} = \frac{B_{\min}}{B_{\max}} \quad (2.1)$$

With stable source parameters and a precise control of the differences of the electrostatic potential (i.e. between the source and the retarding potential), the narrow spectral region close to the  $\beta$ -decay endpoint of the electron spectrum can be analyzed with great precision.

### 2.1.2 Current Neutrino Mass Limits

The current best values for the effective electron anti-neutrino mass  $m_{\nu_e}^2 = \sum_i |U_{ei}|^2 m_{\nu_i}^2$  were obtained by tritium  $\beta$ -decay studies with the above mentioned MAC-E filter experiments at Mainz and Troitsk.

The Mainz experiment, which used a quench condensed tritium source, has published [Kra05] a result of:

$$m_{\nu_e}^2 = (-0.6 \pm 2.2_{\text{stat}} \pm 2.1_{\text{sys}}) \text{eV}^2/c^4$$

corresponding to an upper limit for the "effective  $\bar{\nu}_e$ -mass" of

$$m_{\nu_e} < 2.3 \text{eV}/c^2 \quad (95\% \text{ CL}).$$

The Troitsk experiment, which uses a gaseous tritium source, has published [Lob03],[Ase11]

$$m_{\nu_e}^2 = (-0.67 \pm 1.89_{\text{stat}} \pm 1.68_{\text{sys}}) \text{eV}^2/c^4$$

resulting in an upper limit for the "effective  $\bar{\nu}_e$ -mass" of

$$m_{\nu_e} < 2.05 \text{eV}/c^2 \quad (95\% \text{ CL}).$$

The current upper limit from the Particle Data Group via combined analysis [PDG10] is set at

$$m_{\nu_\beta} < 2.0 \text{eV}/c^2.$$

### 2.1.3 Next Generation Implementation

As stated above, the past implementations of MAC-E filters for the examination of  $m_{\nu_e}$  were very successful in setting precise upper limits on the  $\nu$ -mass. These experiments, however, can not push forward into the sub-eV regime due to their systematic uncertainties and limited source statistics. Therefore an improved tritium  $\beta$ -decay setup is required to reach smaller  $\nu$ -mass scales. Any next generation experiment with sub-eV sensitivity faces the following challenges:

- A source with highest activity is required, as only a tiny fraction of the order of  $10^{-13}$  of the integral rate carries kinetic energy in the energy range of 1 eV below the end point.
- The column density of the source has to be designed to render highest intensities of unscattered  $\beta$ -decay electrons.
- A high-precision energy analysis calls for a spectrometer with highest energy resolution and background rates as low as possible.

These considerations have been instrumental in designing the KARlsruhe TRI-um Neutrino (KATRIN) experiment which currently is under construction at the KIT, Campus North Site. Its design features will be introduced in the following section.

## 2.2 The KATRIN Experiment

The challenges imposed on the next generation tritium  $\beta$ -decay experiment KATRIN have resulted in the following design:

- The  $\beta$ -source used in KATRIN will feature a luminosity 80 times greater than in the Mainz setup. The source cross section area and column density are significantly enlarged. The source setup is described in section 2.2.3.
- For a good energy resolution alongside an enlarged source area, the analyzing plane and hence the spectrometer cross section area had to be enlarged. KATRIN will feature a spectrometer with an analyzing plane 100 times larger than the one at Mainz (it will be described in further detail in section 2.2.4).
- The spectrometer design will lead to an improvement in energy resolution down to 0.93 eV, which is a factor 4 better if compared to the Mainz setup.
- A reduction of the systematic uncertainty by a factor of 100 is aimed for by numerous means described e.g. in [Kae12] or [KAT04].
- To reduce the statistical error, the tritium scanning time is prolonged to 3 years of net measurement time, which is an increase by a factor of 10.

The global setup as well as the main components of KATRIN will be introduced below.

### 2.2.1 General Overview

The KATRIN design is based on the experiences gained in the Mainz and Troitsk experiments and combines the world-wide expertise in MAC-E based  $\beta$ - spectroscopy in its collaboration. The general setup is shown in figure 2.3.

KIT was chosen as the host site for KATRIN due to its Tritium Laboratory Karlsruhe (TLK), which offers extensive and in-depth experience in handling large amounts of tritium. The KATRIN experimental facilities were thus constructed adjacent to the existent TLK complex.

### 2.2.2 Experimental Aims

The goal of the KATRIN experiment [KAT04] is the model-independent measurement of the "effective electron anti-neutrino mass"  $m_{\nu_e} = \sqrt{\sum_i |U_{ei}|^2 m_{\nu_i}^2}$ .



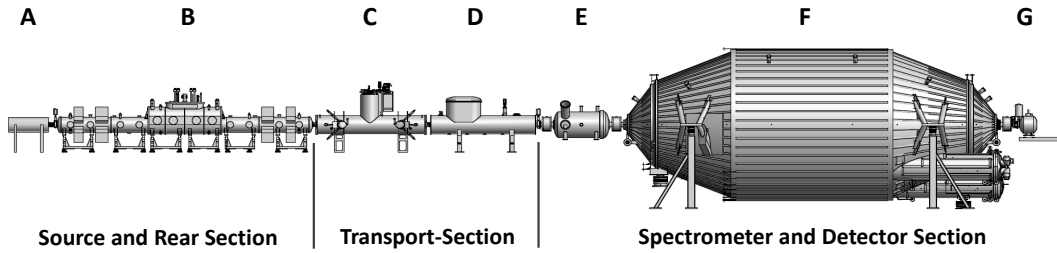


Figure 2.3: **The KATRIN Setup**

Shown are the main components of the KATRIN experiment, based on [Dre12]. The seven large modules are the rear-section (A), the Windowless Gaseous tritium Source (WGTS)(B), the Differential Pumping Section (DPS2-F)(C), the Cryogenic Pumping Section (CPS)(D), the Pre-Spectrometer (E), the Main Spectrometer (F) and the detector system (G). The overall setup measures over 70 meters in length.

The experiment features a discovery potential for the neutrino mass at  $5\sigma$  of  $350 \text{ meV}/c^2$ .

At 90 % CL the sensitivity is  $200 \text{ meV}/c^2$ . This corresponds to an improvement of the present sensitivities on  $m_{\nu_e}$  by one order of magnitude.

To gain enough statistics the experiment will accumulate three years of net measurement time, which will be reached after five calendar years of operation.

### 2.2.3 The Source

The  $\beta$ -decay source of KATRIN is designed as a Windowless Gaseous Tritium Source (WGTS) with a specific activity of  $1.7 \times 10^{11} \text{ Bq}$ . It will deliver a very high rate of  $10^{10}$  signal electrons for analysis in the spectrometers. The importance of systematic effects in the source for the whole experiment can not be overestimated [Kae12].

The WGTS basically consists of a cylindrical beam tube of 10 m length and 90 mm inner diameter which is fed in the middle by a constant inlet of high-purity molecular gaseous tritium (setup is shown in figure 2.4) with the following features:

- To minimize Doppler shifts without actual tritium condensation on the walls, the beam tube is cooled down to 27-30 K using cooling pipes with two-phase neon at its boiling point. The temperature is stabilized over the whole WGTS beam tube to a design value  $\pm 30 \text{ mK}$  or better.
- The desired activity of the source is provided by a constant tritium injection rate of  $1.85 \text{ mbar l s}^{-1}$ . The source gas will have a constant and high (>95%) isotopic purity which is obtained by a dedicated injection system, featuring also a specially developed Laser-Raman-System.

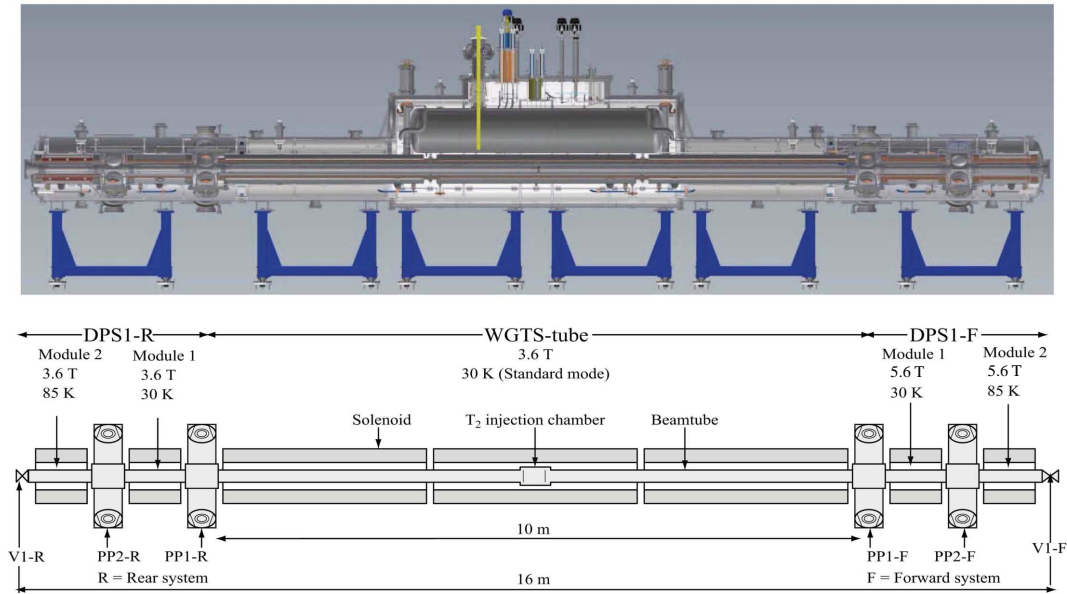


Figure 2.4: **The Windowless Gaseous Tritium Source**

Shown is a cross section through the WGTS cryostat (top) and a schematic of the SC magnet array below. The pump ports at the rear and front end constitute the DPS1-R and DPS1-F.

- A constant tritium pumping rate at both ends of the source tube provides a stable pressure profile with  $p = 3 \times 10^{-3}$  mbar at the injection point, and  $p < 1 \times 10^{-4}$  mbar at the first pump port, rendering a constant source column density of  $\rho \cdot d = 5 \times 10^{17}$  cm $^{-2}$ .
- The beam tube is surrounded by a system of seven superconducting magnets, which create a maximum magnetic field strength of 3.6 T (5.6 T in DPS1-F) at the beamline with a total magnetic flux of  $\approx 230$  T cm $^2$ . For the transport of the  $\beta$ -decay electrons a flux tube of 191 T cm $^2$  is foreseen. The magnetic setup guarantees a maximum emittance angle of 51° with respect to the magnetic field lines for signal electrons to reach the detector (given sufficient kinetic energy).

**The Loop System** The tritium pumped out of the beam tube is handled by a loop system schematically shown in figure 2.5 and described in detail in [Stu10]. It collects the pumped-out tritium molecules leaving the WGTS and DPS cryostats (and CPS during regeneration). It also regulates the injection rate via a pressure and temperature controlled buffer vessel connected to WGTS by a capillary of known conductance.

The tritium gas that is collected by the loops will be cleaned from impurities with palladium membrane filters and merged with tritium gas of high isotopic purity ( $> 98\%$ ) from the Isotope Separation System (ISS) of TLK to compensate for the losses from isotopic separation. The tritium throughput in this

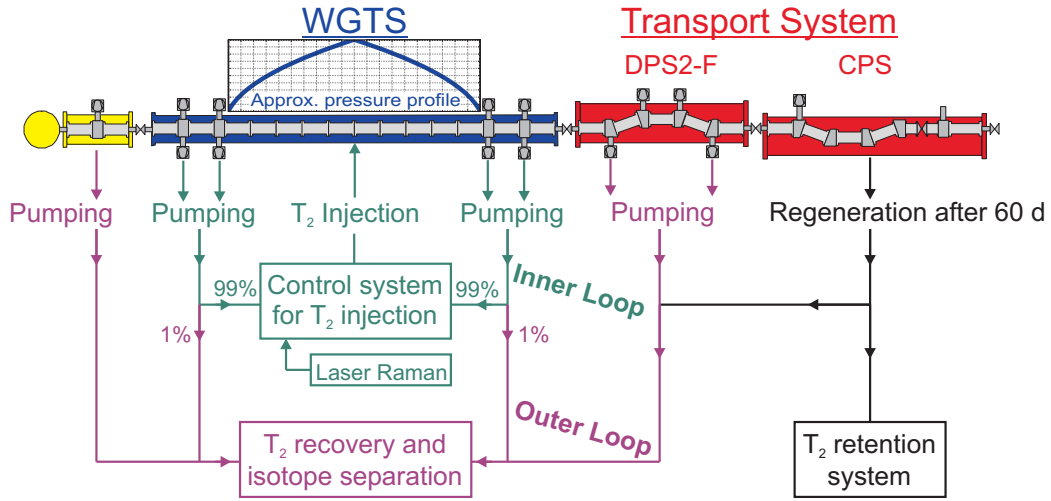


Figure 2.5: **The Source and Transport Section**

Shown are the rear system (yellow) the WGTS (blue) and the transport section (red). The schematics of tritium management are given below. The largest part of the global tritium flow is directly recycled through the inner loop. Lower flow rates and higher impurities are handled by the outer loop.

closed loop system will reach 40 g tritium per day and amount to a value of about 10 kg per year, equivalent to the ITER throughput<sup>2</sup>.

## 2.2.4 The Spectrometers

The KATRIN experiment features two spectrometers of MAC-E filter type. They were manufactured as ultra high vacuum (UHV) recipients from 316LN steel (European steel code 1.4429; see appendix A.7). Both units have already been installed successfully in the KATRIN experimental halls.

**The Pre-Spectrometer** The primary task of the pre-spectrometer is to provide the option to reduce the electron flux into the main spectrometer. Acting as a high pass filter, it can reflect all electrons (and negative ions) with energies  $E \leq 18.3$  keV. The goal of this operating mode is to minimize potential background processes arising from interactions of low-energy electrons with the residual gas in the main spectrometer. The vessel is 3.42 m long and has a diameter of 1.7 m. Its comparably smaller size results in a limited energy resolution of  $\Delta E \approx 70$  eV which is entirely sufficient when acting as a pre-filter.

The pre-spectrometer has so far been commissioned successfully and tested, and is ready for integration in the final KATRIN beamline.

<sup>2</sup>The gas recycling processes require halogen-free exhaust gases to prevent damages of the membranes; the connected gas handling components have to ensure especially the absence of fluorine (cf. section 6.4.2).

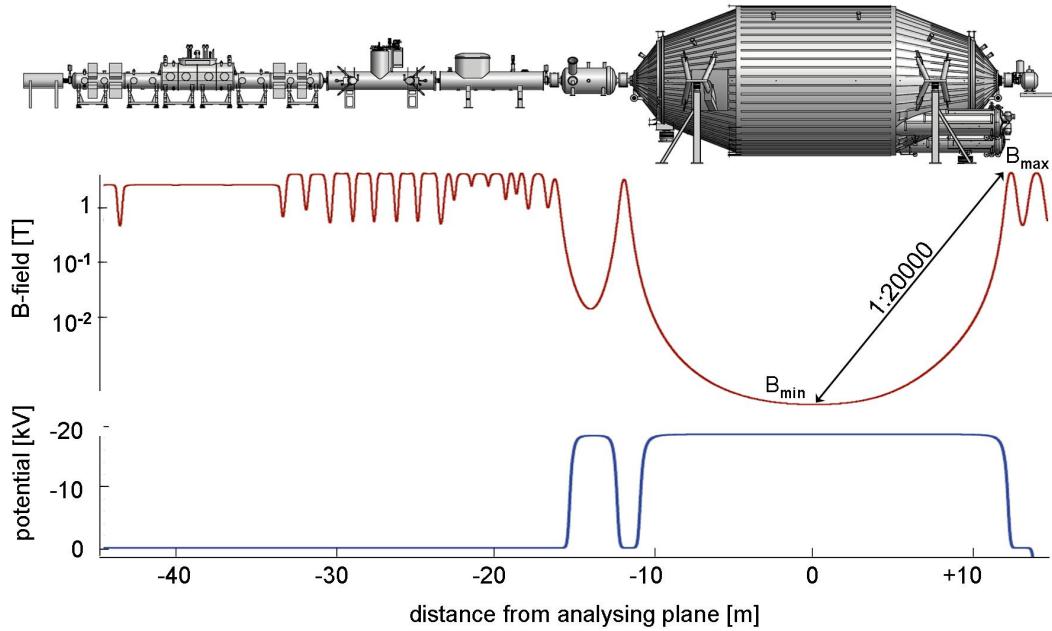


Figure 2.6: **Electric potentials and magnetic fields in KATRIN**

Shown are the values of the electric and magnetic fields over the whole KATRIN setup. The retarding potential and low  $B$ -field values in the spectrometers are characteristic for MAC-filter experiments. Source [Dre12].

**The Main Spectrometer** The largest unit in the entire KATRIN setup is the main spectrometer. With a diameter of 10 m and 23.3 m length it is designed to let the signal-carrying magnetic flux tube expand to a diameter of 9 m. The local field strength in the analyzing plane drops down to 0.3 mT, which is a factor of 20 000 lower than  $B_{\max}$  at the pinch magnet (see figure 2.6). This magnetic scenario allows for an energy resolution of  $\Delta E \approx 0.93$  eV, if inhomogeneities are corrected for.

Within the main spectrometer an inner electrode system is installed. It consists of two layers of steel wires with  $\approx 25$  mm distance between adjacent ones. The 24 000 wires define the retarding potential. It comprises two separate layers covering the whole inner surface of the spectrometer at distances of 15 cm and 22 cm from the walls, respectively.

The inner wire layer is designed to be on a potential of 100 V lower than the outer one and 200 V lower than the wall (e.g.  $U_{\text{wall}} = -18.4$  kV,  $U_{\text{1st layer}} = -18.5$  kV,  $U_{\text{2nd layer}} = -18.6$  kV) to repel electrons emitted from the vessel walls from cosmic muons interacting with the steel. Electron emission from the walls is also due to radioactive decays on the wall surface. The wire system thus adds to the dominant magnetic shielding to prevent background production in the spectrometer.

The scanning of the  $\beta$ -spectrum is carried out by varying the electric potential between WGTS and the spectrometer. Ceramic insulators between DPS2-F (source potential) and CPS (ground potential) as well as between CPS and

pre-spectrometer and between the two spectrometers allow for operation of the beamtube at different potentials.

Surrounding the main spectrometer are two air coil systems, which are installed to compensate the distorting effect of the earth magnetic field (Earths Magnetic Field Compensation System) and to fine-shape the magnetic flux tube in the vessel (Low Field Correction System).

Stable UHV conditions in an absolute pressure regime below  $10^{-11}$  mbar and an ultra-low tritium partial pressure below  $10^{-21}$  mbar are crucial for the spectrometer in order to minimize background events from ionization of residual gas (see the following chapters).

So far the main spectrometer has been vacuum-commissioned successfully. With the wire electrodes having been fully installed by March 2012, a thorough testing of its electro-magnetic properties will start by mid-2012.

## 2.2.5 The Detector

The Focal Plane Detector (FPD) system was specially designed for KATRIN, as shown in figure 2.7.

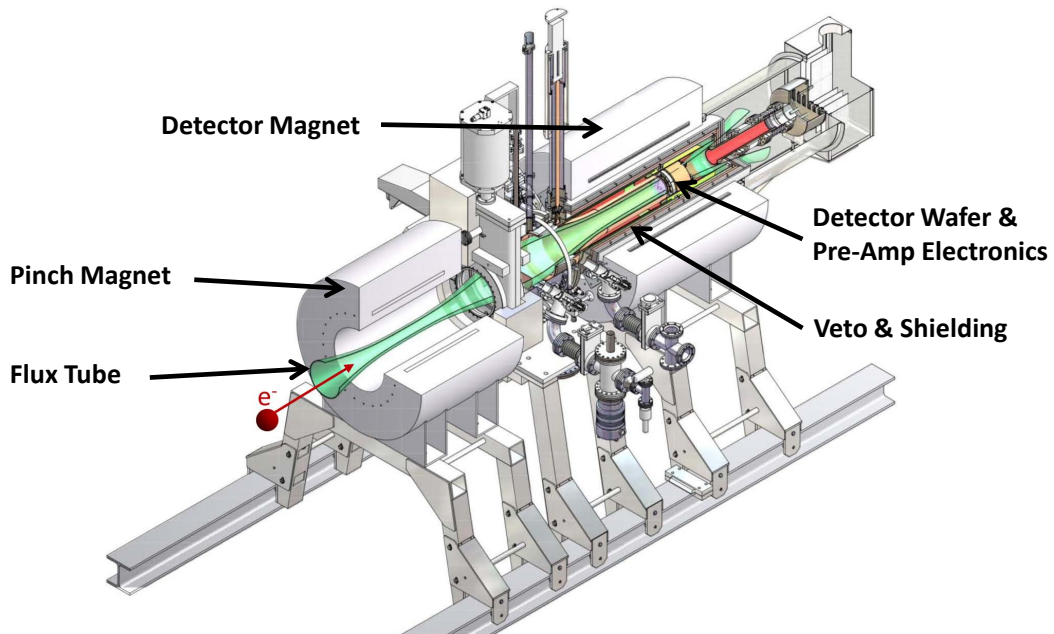


Figure 2.7: **The Focal Plane Detector System**

Shown is the FPD System as it is currently under commissioning at KATRIN. The magnet system and the flux tube carrying the signal electrons is shown as well as the actual detector, its electronics, the shielding and the veto. Based on [Sch12].

Its main components are a silicon PIN-diode array featuring a total of 148 pixels on a 125 mm wafer. The pixels are separated by a distance of  $50\ \mu\text{m}$  and have a dead layer of 100 nm. The signal electrons are guided by two superconducting solenoid magnets: the pinch magnet to be operated at 6.0 T, and the detector magnet to be operated at 3.6 T.

The FPD features numerous electronic components, an UHV system ( $p < 10^{-11}$  mbar), which can be separated from the main spectrometer, a high-vacuum system ( $p < 10^{-6}$  mbar, downstream of the detector wafer), state-of-the-art cooling systems, calibration and monitoring devices, and a custom-made data-acquisition system which are well described elsewhere [Ams12].

The detector system has been successfully commissioned in 2011 and at present is further refined for the upcoming spectrometer tests.

## 2.2.6 The Transport Section

The KATRIN transport section is the central focus of this thesis. It is located between the source and the spectrometers (shown in red on the right side of figure 2.5). It comprises the second and third source-related modules of KATRIN, the Differential Pumping Section 2 and the Cryogenic Pumping Section (DPS2-F and CPS), with a combined length of 14 meters<sup>3</sup>.

The task of the transport section (TS) is the highly effective reduction of tritium gas flow by 14 orders of magnitude. Moreover, the ion flux reduction down to virtually zero is an essential design cornerstone of the TS. To do so, different methods and techniques are combined to provide KATRIN with the vacuum quality and low background levels it requires.

Its other task is the adiabatic guidance of signal electrons from the WGTS to the spectrometers. This guidance is achieved by a system of superconducting magnets surrounding the KATRIN beam line.

As the transport section, with its cryostat modules DPS2-F and CPS, is of major importance for this work, detailed descriptions of these parts of KATRIN will be presented in chapter 5. Before, a thorough introduction to the techniques of tritium retention being implemented (chapter 3), and their mode of operation (chapter 4) will be given.

---

<sup>3</sup>The very first part of the transport section is actually the Differential Pumping Section 1 (DPS1-F), which is, however, incorporated in the the WGTS source cryostat and therefore not denoted as part of the transport section.

## Chapter 3

# Tritium Retention - Technical Principles

In this chapter the technical principles for tritium retention will be introduced in detail. At first the design criteria for the tritium retention factor will be given in section 3.1. Afterwards, in section 3.2, the techniques to achieve these challenging aims are presented. Based on these two sections, in section 3.3 an overview of tritium levels along the whole experiment will be presented. In section 3.4 we finally discuss issues related to ions and review ion-suppression techniques.

### 3.1 Design Criteria Tritium Background

KATRIN will use a tritium source of unprecedented intensity. However, of the envisaged luminosity value of the order of  $10^{11}$  decays per second only a fraction of the order of  $10^{-13}$  will produce electrons in the spectral region-of-interest, resulting in a signal rate at the detector of  $\approx 10$  mHz. To reach the desired sensitivity of 0.2 eV (90% CL) requires a very low background level, which should have a comparable count rate at most.

Circulating the above mentioned enormous quantities of tritium (10 kg per year throughput) in a system with no barrier relative to the spectrometers can result in major systematic effects and huge background rates. Accordingly, KATRIN relies on appropriate countermeasures to reach its physics goals.

#### 3.1.1 Calculation of Tritium Activity

When discussing tritium-related issues, the following constants have been used

- half-life Tritium:  $t_{1/2} = (4,500 \pm 8) \text{ d} \hat{=} 3.888 \times 10^8 \text{ s}$  ([Luc00])

- molar volume of an ideal gas:  $V_{\text{mol}} = 22.414 \text{ l mol}^{-1}$  (DIN, standard conditions)
- volume main spectrometer:  $V_{\text{MS}} = 1.24 \times 10^6 \text{ l}$
- Avogadro constant:  $N_{\text{A}} = 6.022 \times 10^{23} \text{ mol}^{-1}$

To give a first estimate of the huge tritium retention factors required, we assume a tritium partial pressure of  $p = 10^{-20} \text{ mbar}$  in the main spectrometer. This extremely small level would nevertheless result in a substantial  $\beta$ -decay rate  $A_{\text{MS}}$  there, calculated by the following steps:

$$\begin{aligned}
 N(t) &= N_0 e^{-\frac{\ln 2}{t_{1/2}} t} \\
 -\frac{dN}{dt} \Big|_{N_0=1, t=1\text{s}} &= 1.78287 \times 10^{-9} \text{ s}^{-1} \text{ atom}^{-1} \\
 N_{\text{MS}}(p) &= \frac{V_{\text{MS}}}{V_{\text{mol}}} p N_{\text{A}}
 \end{aligned}$$

Now, for a given partial pressure and assuming all tritium bound in HT-molecules (cf. section 3.3.1), we obtain

$$\begin{aligned}
 N_{\text{MS}}(p = 10^{-20} \text{ mbar}) &= 3.33 \times 10^5 \\
 A_{\text{MS}}(p) &= N_{\text{MS}} \left( -\frac{dN}{dt} \right) \\
 A_{\text{MS}}(p = 10^{-20} \text{ mbar}) &= 5.96 \times 10^{-4} \text{ Bq} \\
 &= 51.5 \text{ per day.}
 \end{aligned}$$

The calculated activity  $A_{\text{MS}}$  corresponds to the number of  $\beta$ -decays in the main spectrometer. This value however is only a smaller part of the expected background measured at the detector due to secondary effects as described in the following section.

### 3.1.2 Background through Tritium Decay

**Magnetic Trapping** The setup of the main spectrometer, as described in section 2.2.4, features a design with a magnetic field whose strength drops by more than four orders of magnitude to the middle of the analyzing plane. There, it reaches a strength of  $B_{\text{A}} = 3 \times 10^{-4} \text{ T}$ , while at the pinch magnet (detector-side) it reaches  $B_{\text{P}} = 6.0 \text{ T}$  (cf. figure 3.1), and at the solenoids adjacent to the pre-spectrometer it reaches  $B_{\text{PS-MS}} = 4.5 \text{ T}$ .

As is well known from basic electro-dynamics, the magnetic field-lines between two strong magnets can form a "magnetic bottle", which entraps charged particles. An electron fulfilling the trapping conditions is not able to leave the main spectrometer volume, but will oscillate between the areas of high  $B$ -field. Due



to inelastic collisions with residual gas a potentially high number of secondary electrons will be produced. At some point, the secondaries, which initially are also trapped, will leave the spectrometer and, when hitting the sensitive detector area, cause a background there, which is significantly higher than the primary tritium decay rate.

**Estimation of Tritium induced Background** The storage time of electrons from tritium  $\beta$ -decay in the main spectrometer can reach a time interval of up to several hours, given a residual gas pressure of  $1 \times 10^{-11}$  mbar. Detailed descriptions of these processes and the used values following can be found in [Mer12]. A primary  $\beta$ -decay electron in the few keV range will create  $\langle n_{\text{secondary}} \rangle = 124$  secondary electrons. The number of expected secondaries as a function of the primary energy can be found in figure 3.2.

It is to be noted that not all decay electrons will be trapped. Electrons produced close to the inner surface of the tank can hit the wall due to their large cyclotron radius. Moreover, non-adiabatic processes may break the storage conditions. The probability of trapping over all primary electrons in the main spectrometer is roughly  $\eta_{\text{capture}} = 58\%$ .

This number is decreased further by the following effects. Only a part of the trapped primary electrons are propagating in the "sensitive volume" of the main spectrometer. The outer parts of the magnetic flux tube do form a closed magnetic bottle, but particles produced there usually do not propagate to the sensitive area of the KATRIN detector. The probability for secondary electrons to be produced in the "sensitive volume" is roughly  $\eta_{\text{volume}} = 70\%$ .

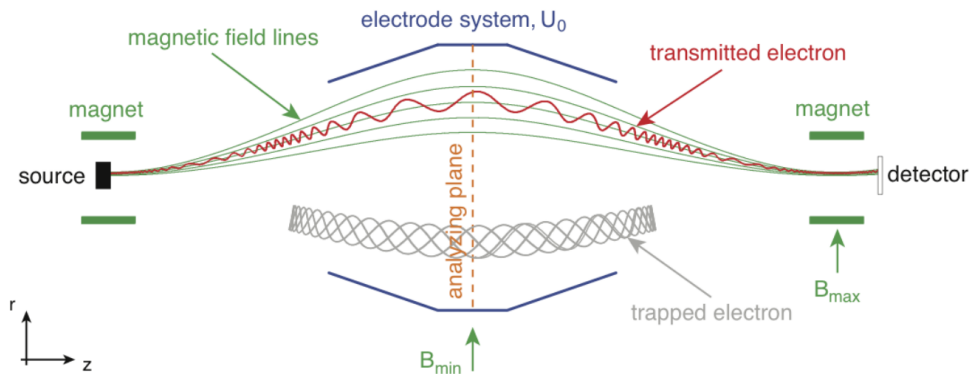


Figure 3.1: **Field-lines in Main Spectrometer**

Electrons produced in the main spectrometer volume can get trapped between the regions of higher magnetic field (grey line). These particles will not leave the spectrometer volume, and collide with residual gas thus losing their energy.

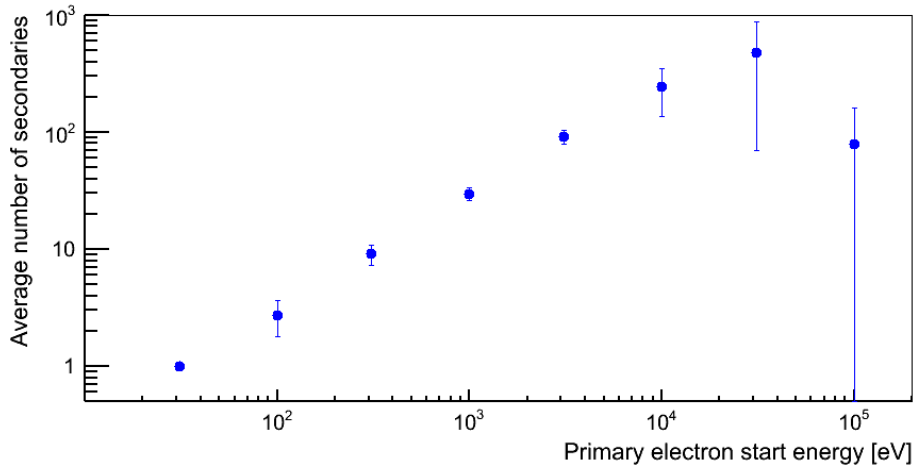


Figure 3.2: **Secondary electrons in Main Spectrometer**

Monte-Carlo simulation of the energy dependence of the production rate of background electrons induced by decay electrons in the volume of the main spectrometer. Simulations are carried out for a residual gas ( $\text{H}_2$ ) pressure of  $10^{-11}$  mbar. Source [Mer12].

At last, one has to take in account that particles can leave the main spectrometer volume on both sides. A perfectly symmetrical spectrometer setup would lead to another reduction of 50%. As the B-field at the detector side, however, is stronger than at the source side, this asymmetry leads to a value of  $\eta_{\text{side}} = 40\%$  of all produced secondaries leaving the spectrometer towards the detector.

After these considerations one estimates for the number of background producing electrons per  $\beta$ -decay:

$$\langle n_{\text{back}} \rangle = \langle n_{\text{secondary}} \rangle \cdot \eta_{\text{capture}} \cdot \eta_{\text{volume}} \cdot \eta_{\text{side}} \quad (3.1)$$

With these calculations, one finds an average background production of 20 detected secondary electrons per single tritium decay in the main spectrometer. To reach KATRIN's goal of measuring the neutrino mass down to 0.2 eV at a 90% confidence level, the background must not exceed 10 mHz (cf. section 2.2.2). This corresponds to a maximum tritium inventory in the spectrometer of less than  $2.8 \times 10^5$  or a partial pressure of less than  $8 \times 10^{-21}$  mbar (assuming HT molecules, cf. section 3.3.1). This challenging goal can only be reached using a tritium retention system of unprecedented efficiency. Moreover, it has to work in a well-defined and safe manner, allowing identical tritium retention over five calendar years. The strategy of reaching this gas suppression factor is described in the following two sections.

## 3.2 Principles of Gasflow Reduction

### 3.2.1 Parameters and Flow Regimes

All further calculations will be based on the following basic definitions, as can be taken for instance from [Wut10].

**Pumping speed:** The pumping speed  $S$  of a vacuum pump is defined as the gas volume conveyed per unit time:

$$S = \frac{dV}{dt}, \quad [S] = 1 \text{ m}^3 \text{ s}^{-1} \quad (3.2)$$

The pumping speed strongly depends on the mass of the pumped gas, as will be further investigated in Section 4.2.1.

**Throughput:** The throughput  $T$  at the suction side of a pump is defined by

$$T = S \cdot p_a = p_a \cdot \frac{dV}{dt}, \quad [T] = 1 \text{ J s}^{-1} = 1 \text{ W} \quad (3.3)$$

**Conductance:** The conductance  $L$  is defined as the inverse of the flow resistance  $W$  analogous to the electrical conductance using the pressure difference  $\Delta p$  as the difference in potential.

$$T = \frac{\Delta p}{W} = L \cdot \Delta p \quad \text{with} \quad [W] = 1 \text{ s m}^{-3} \quad \text{and} \quad [L] = 1 \text{ m}^3 \text{ s}^{-1} \quad (3.4)$$

The known conductance for one gas species with mass  $m_y$  can be used to calculate the value  $L_x$  for any other species with mass  $m_x$  via

$$L_x = \sqrt{\frac{m_y}{m_x}} L_y \quad (3.5)$$

It has to be noted that flow resistances in parallel and series can be calculated analogous to electrical resistances, so that Kirchhoff's Rules can be applied as well.

Another important aspect of vacuum environments and gas flow properties are the different types of gas flow calculations. One differentiates between *laminar flow*, *Knudsen-flow* and *free molecular flow* using Knudsen's number  $K_N$  as follows.

Given a volume  $A \cdot x$  with particle density  $n$  and scattering cross-section  $\sigma$ , the probability  $P$  for a collision of one particle moving through this volume is given by

$$P_{\text{hit}} = \frac{\sigma \cdot n \cdot A \cdot x}{A} = \sigma \cdot n \cdot x \quad (3.6)$$

For  $N$  particles one then finds for the number  $\Delta N$  of scattered particles:

$$\Delta N = N \cdot \sigma \cdot n \cdot x \quad (3.7)$$

or in differential form

$$\frac{\Delta N}{N} = -\sigma \cdot n \cdot x. \quad (3.8)$$

This differential equation is solved by

$$N(x) = N_0 \cdot e^{-\sigma n x} = N_0 \cdot e^{-x/\Lambda} \quad (3.9)$$

with the characteristic mean free path length

$$\Lambda = \frac{1}{\sigma n}. \quad (3.10)$$

Using this free path length<sup>1</sup> one is able to define Knudsen's number  $K_N$  as follows

$$K_N = \frac{\Lambda}{d} \quad (3.11)$$

with  $d$  being the characteristic dimension of the vacuum vessel (e.g. pipe diameter). Based on Knudsen's number the characteristic regimes of gas flow can be defined:

1. *laminar flow* with  $K_N \ll 1$  and  $\Lambda \ll d$ . Depending on Reynold's number, laminar or turbulent flow equations have to be used.
2. *Knudsen-flow* with  $K_N \approx 1$  and  $\Lambda \approx d$ . This is the transfer regime between laminar and free molecular flow.
3. *free molecular flow* with  $K_N \gg 1$  and  $\Lambda \gg d$ . In this regime the intermolecular scattering is negligible. The dominant parameters for calculating particle trajectories are the geometries of the vacuum vessel itself.

### 3.2.2 Vacuum Measures

The term vacuum and its quality stages need to be further specified before introducing the commonly used vacuum measures, as the preferred measure depends on the desired vacuum quality. Table 3.1 gives an overview over the different stages of vacuum and lists some appropriate methods for achieving these levels. The methods listed are not complete, given the wide variety of technical solutions.

The desired KATRIN vacua reach well into the area of ultra high vacuum (UHV), reaching down to  $p < 10^{-11}$  mbar in the main spectrometer. To achieve this goal, a whole variety of vacuum systems will be deployed in KATRIN, the most important of which will be generally described in the following subsections.

---

<sup>1</sup>Rule of thumb: At room temperature and for  $p = 10^{-4}$  mbar one obtains  $\Lambda \approx 1$  m

Table 3.1: **Stages of vacuum:** A general description of the stages of vacuum quality and commonly used methods for reaching these stages.

vacuum level	pressure [mbar]	particle density [cm <sup>-3</sup> ]	pumping method
rough	10 <sup>3</sup> - 1	10 <sup>19</sup> - 10 <sup>16</sup>	piston pump rotary vane pump membrane pump
fine	1 - 10 <sup>-3</sup>	10 <sup>16</sup> - 10 <sup>13</sup>	scroll pump roots pump membrane pump
high (HV)	10 <sup>-3</sup> - 10 <sup>-7</sup>	10 <sup>13</sup> - 10 <sup>9</sup>	diffusion pump turbo molecular pump differential roots pump
ultra high (UHV)	< 10 <sup>-7</sup>	< 10 <sup>9</sup>	turbo molecular pump getter pump cryo pump

### 3.2.3 Turbo-Molecular Pumping

**Basic Principles** Turbo-molecular pumps (TMPs) are the most commonly used pumps for UHV applications. Molecular pumps were first introduced by Gaede in 1913 [Gae13] and since then have been further developed. The main principle of these pumps is based on three ideas:

- Free molecular flow approach: The molecule trajectories, in particular changes in velocity and direction, are purely determined by the geometry of the vacuum vessel. In this case a sufficiently low pressure at the pump outlet is presupposed. Accordingly, TMPs can only be used in combination with a fore-vacuum pump.
- Desorption time: after "hitting" a wall, a molecule is assumed to rest adsorbed on the surface before being desorbed again<sup>2</sup>. The desorption occurs "memory free" i.e. the gas particles desorb with thermal velocity following the cosine law in the rest frame of the blade. In the lab frame the velocity of the wall needs to be added, rendering a directed movement of the desorbed particles.

<sup>2</sup>The retention time varies strongly for different adsorbent materials, adsorption energies, and temperatures, typically between 10<sup>-13</sup> and 10<sup>30</sup> seconds [Wut10]. In the case of TMPs, however, contrary to sorption pumps, high retention times are not a goal.

- Mechanical changes in geometry during desorption time: this is a key feature of molecular pumping. During the retention time, the geometry of the surrounding surfaces is changed in a way to promote one flow direction over the other, thus giving the molecules a higher probability to leave the UHV volume than to return.

TMP-engineering (see figure 3.3) has come a long way during the past decades. The most common design today uses a stator-rotor combination as shown schematically in picture 3.4. There are numerous ways to technically describe TMPs (pumping speed, compression ratio, throughput etc.). In this work the pumping speed and the capture factor  $\alpha$  will be used most frequently. The capture factor is a measure of probability for a gas particle entering the pump volume to get captured, i.e. being pumped by the TMP. It can be calculated via:

$$\alpha = \frac{4 S(M)}{v(M) A} \quad (3.12)$$

The values for the pumping speed  $S$  and the gas velocity  $v$  are temperature dependent and are usually given for room-temperature. The molecular mass  $M$  and the surface area of the entrance flange  $A$  are usually given for each scenario of interest. A comparison of simulated capture factors and experimentally gained pumping speed is a good and easy accessible test for gas-flow Monte-Carlo (MC) simulations (as e.g. described in section 4.2.2).

The design of a complex pumping system such as DPS2-F requires a verified code and hence adequately known capture factors, or a good knowledge of the pumping speed for the pumps to be deployed. Additionally, in the case of

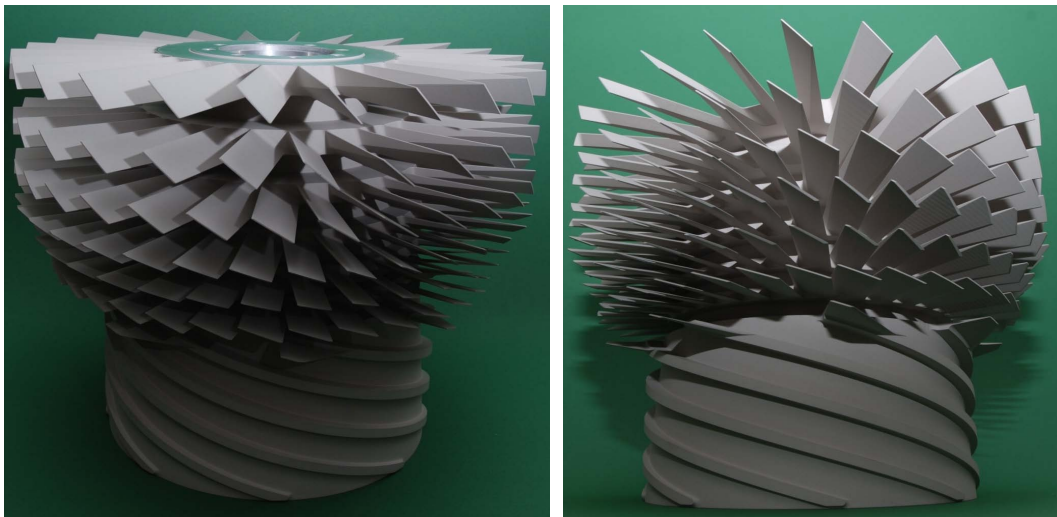


Figure 3.3: **Rotor of a Turbo Molecular Pump**

The rotor of a Leybold MAG-W 2800 TMP, disassembled during vacuum tests at KATRIN. Source [Jan12].

KATRIN, the goal is not only to evacuate a given volume but to deal with a constant gas flow into this volume. The following methods, as introduced by [Mal07], have been used for calculations:

Given a closed vacuum vessel with one TMP, the equilibrium compression ration  $K_0$  is defined as the ratio of the probabilities  $w_{12}$  for a gas particle passing from the vacuum-side to the outside and  $w_{21}$  vice-versa. The vacuum-pressure then reads

$$p_{in} = \frac{p_{out}}{K_0} \quad (3.13)$$

Introducing a steady gasflow into the system the equation is expanded to

$$p_{in} = \frac{Q}{S} + \frac{p_{out}}{K_0} \quad (3.14)$$

rendering for the equilibrium compression ratio

$$K_0 = \frac{p_{out}}{p_{in} - (Q/S)} \quad (3.15)$$

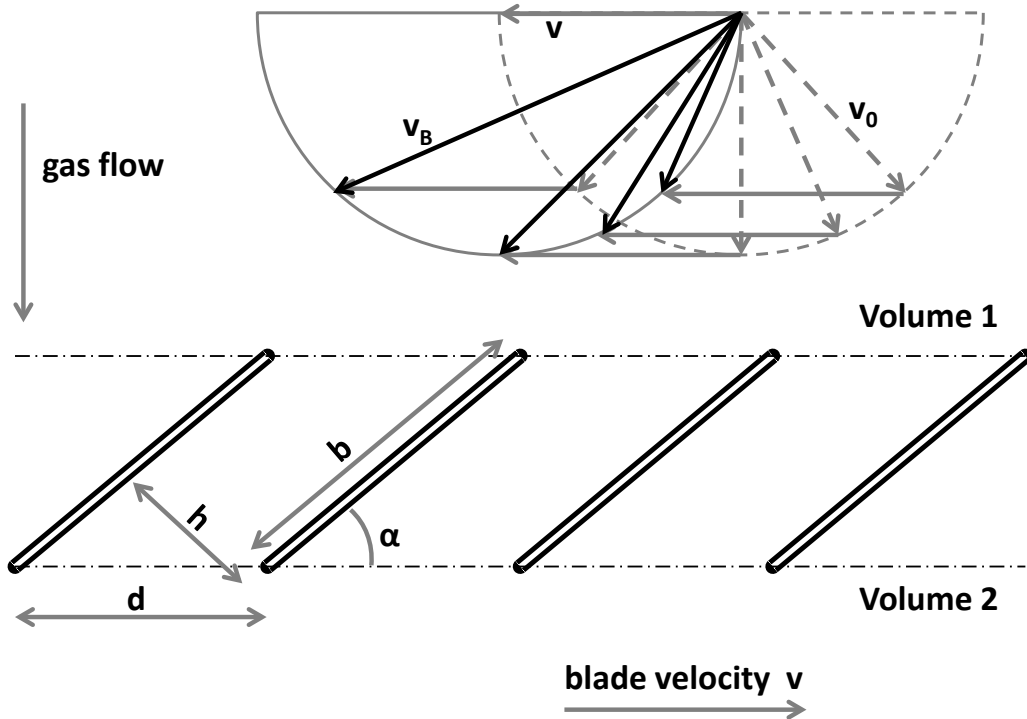


Figure 3.4: **Schematic turbo molecular pump:** The blades turn with velocity  $v$  (gray lines). In the rest-frame of the blades, the original (here isotropically assumed) lab-frame velocity of the gas particles  $v_0$  (dashed gray lines) adds to the inverted blade velocity rendering the velocity  $v_B$  (black lines). This setup renders a passing of the gas particle from volume 1 to volume 2 more likely than vice versa.

The best capture factor  $\alpha_{max}$  possible in this model is equivalent to  $w_{12}$  with no backflow. Taking backflow into account the capture factor is reduced to

$$\alpha = \alpha_{max} - w_{21} \frac{p_{out}}{p_{in}} = \alpha_{max} \left( 1 - \frac{p_{out}}{K_0 p_{in}} \right) \quad (3.16)$$

From this formula it is easy to see the necessity for a low outlet pressure if one wants to reach a significant value for  $\alpha$  at the desired low vacuum pressures. This is generally achieved by combining several pumps to a pumping chain or cascade.

**Cascaded Pumping** To achieve a low final pressure at the outlet it is often useful to cascade (several) TMPs in a row<sup>3</sup>. Given  $n$  identical TMPs in a row (i.e. the outlet of pump  $n$  is connected to the inlet of pump  $n-1$  and so on), and a fore-vacuum pump with ultimate vacuum pressure  $p_{pre}$ , and a pumping speed  $S_{pre}$  one finds for the chain:

$$\begin{aligned} p_0 &= \frac{Q}{S_{pre}} + p_{pre} \\ p_1 &= \frac{Q}{S} + \frac{1}{K_0} \left( \frac{Q}{S_{pre}} + p_{pre} \right) \\ p_2 &= \frac{Q}{S} \left( 1 + \frac{1}{K_0} \right) + \frac{1}{K_0^2} \left( \frac{Q}{S_{pre}} + p_{pre} \right) \\ &\dots \\ p_n &= \frac{Q}{S} \left( \sum_{k=0}^{n-1} \frac{1}{K_0^k} \right) + \frac{1}{K_0^n} \left( \frac{Q}{S_{pre}} + p_{pre} \right) \end{aligned} \quad (3.17)$$

with  $p_0$  as the pressure at the inlet of the pre-vacuum pump and  $p_n$  as the pressure at the inlet of the  $n$ th pump. These methods allow to define a pumping strategy to obtain a minimal pressure at the outlet of a vacuum tube with an already pre-defined maximum pressure at the inlet (as is the KATRIN beamline). To keep the costs to a minimum, detailed differential pumping schemes were developed. In case of differential pumping, the outlet of a pump installed at a location of greater vacuum quality is connected to the vacuum tube at a location of higher pressure, as shown schematically in figure 3.5.

In these arrangements the pressure at the inlet of each on-line pump is given by

$$p_n = \frac{1}{S} \sum_{k=1}^n \frac{\sum_{i=k}^n Q_i}{K_0^{k-1}} + \frac{1}{K_0^n} \left( \frac{\sum_{i=0}^n Q_i}{S_0} + p_{pre} \right) \quad (3.18)$$

<sup>3</sup>There is always an optimal number of pumps, so that the addition of another pump would not decrease the final pressure any further.



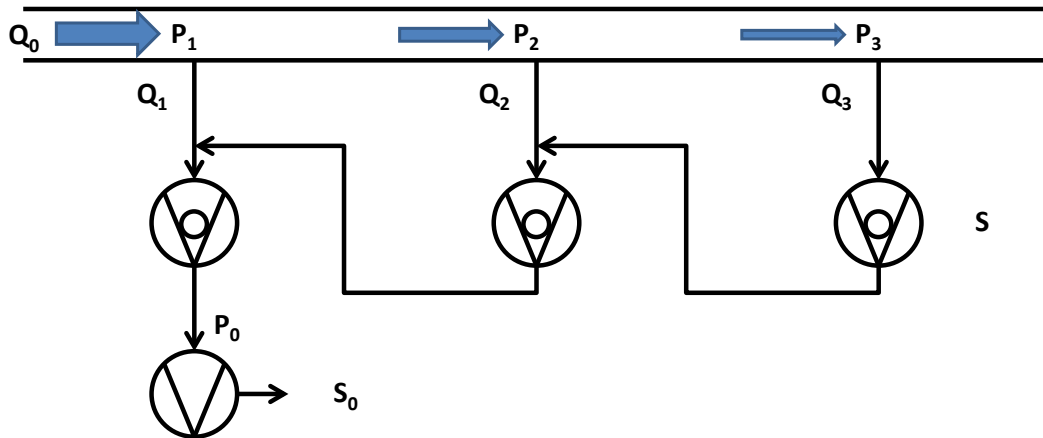


Figure 3.5: **Differential pumping, schematically:** Gas-flow into the system from left to right. For three identical turbo-pumps with pumping speed  $S$  and one pre-vacuum pump with pumping speed  $S_0$  arranged in a way to gain three stages of gas-flow reduction with ascending number of cascaded pumps.

With these considerations a wide variety of TMP combinations is possible to fit the individual need of the given vacuum system. In section 5.1.1 a detailed description of the Differential Pumping System deployed in KATRIN will be given.

It is, however, to be noticed that the conductance of the pipes connecting the inlets and outlets of the cascaded pumps and the outgassing of hydrogen from the walls and the blades of the pumps itself have been neglected. A real hydrogen system, even with a highly sophisticated cascaded pumping, will hardly reach final pressures below  $10^{-10}$  mbar. Lower pressures require different pumping approaches, as for example sorption pumping, which will be described in the following subsection.

### 3.2.4 Sorption & Diffusion

When dealing with low pressure gases, gas interactions with the walls become relevant. Especially in the case of hydrogen (and its isotopes) the processes of adsorption, absorption and permeation can have a great impact on the vacuum performance. The following section will discuss the specific case of hydrogen-steel interactions. The methods introduced in this section will later on be used to explain the techniques of getter- (cf. section 3.2.5) and cryo-pumping (cf. section 3.2.6).

Hydrogen entrapment in steel walls is a commonly known phenomenon in vacuum science and technology. The highly soluble hydrogen (from residual gas or surface-dissolved water) diffuses into metal surfaces rendering a continuous hydrogen background desorbing from the walls in high vacuum environments. The hydrogen concentrations in the metal bulk and on the metal surface de-

pend on temperature and its partial-pressure over the surface. The surface conditions are also of great importance for the hydrogen transport qualities [San05].

When dealing with very low hydrogen (or tritium in the KATRIN case) partial pressures, however, the solubility in the steel tanks can lead to an additional suppression factor.

### 3.2.4.1 Absorption

Absorption processes are based on assumptions concerning the metal bulk, in first order disregarding adsorption processes on the surface. To calculate absorption quantities, the solubility and equilibrium concentrations for the gas and bulk material in question need to be investigated. The concentration  $\chi$  of dissolved hydrogen in equilibrium with gaseous hydrogen can be expressed by

$$\chi = K f^{1/2} \quad (3.19)$$

with the equilibrium factor  $K$

$$K = K_0 e^{\frac{-\Delta H_S}{RT}} \quad (3.20)$$

and  $f$  as the fugacity which can be approximated as the pressure  $p$  for our requirements<sup>4</sup>. The parameter  $K_0$  is the material-dependent equilibrium constant in the high temperature limit, and  $\Delta H_S$  is the heat of solution (see table 3.2).

The validity of equation 3.19 in a very low pressure scenario ( $p < 10^{-9}$  mbar), however, has been questioned [Zar79]<sup>5</sup>. Low-pressure effects will be discussed later on.

### 3.2.4.2 Diffusion

Once dissolved in the metal the hydrogen isotopes will migrate through the steel. After reaching equilibrium concentrations in the surface regions, the dissolved hydrogen will partially diffuse through the metal walls rendering a diffusion flux

$$J_\infty = D \frac{\chi_{inside} - \chi_{outside}}{d} \quad (3.21)$$

---

<sup>4</sup>The fugacity takes in account the co-volumina of real gases within the Van-der-Waals gas equation. The square-root dependence stays nonetheless valid. In the ideal gas case this equation is known as Sievert's law.

<sup>5</sup>The literature evaluating setups at these low pressures and ambient temperature is contradictory. In [LeC83] a strong dependence of the square root validity from the temperature is stated; with lower temperatures lower pressure scales are acceptable (e.g. at 500 K square root dependence down to  $10^{-19}$  mbar).

with the diffusivity  $D$  (see table 3.2), the concentrations  $\chi$  inside and outside of the vacuum system in question and the thickness of the wall  $d$ . The diffusion flux can also be expressed using the equilibrium constant by:

$$J_{\infty} = \frac{DK}{d} f^{1/2} \quad (3.22)$$

The diffusion length is to be calculated via the known formula

$$\Lambda = \sqrt{D\tau} \quad (3.23)$$

with the timescale  $\tau$ , which for our purposes is estimated recursively as half the timescale  $\tau_{\text{eq}}$  after which the equilibrium between residual hydrogen and dissolved hydrogen is reached.

Numerical values for the given parameters can be found in the literature (see table 3.2). Usually hydrogen (protium) values are given, which can (for diffusivity) be transformed to other isotopes via

$$\frac{D_H}{D_{D,T}} = \sqrt{\frac{m_{D,T}}{m_H}} \quad (3.24)$$

This formula can be used in an analogous way for permeability, while solubility, however, is deemed independent of the mass [San06].

Combining solubility and diffusivity, one can gain the equilibrium inventory  $N$  of a given vacuum vessel wall with inner surface area  $A$  by calculating

$$N = \chi A \Lambda \quad (3.25)$$

and finally, the timescale  $\tau_{\text{eq}}$  by dividing  $N$  by the flux into the vessel expressed in tritium atoms per second. The time  $\tau_{\text{eq}}$  then sets a lower limit for the effective pumping time of the vessel itself, neglecting net losses via permeation (i.e. all gas is stored within a thin layer of thickness  $\Lambda$ ). Comparing  $\tau_{\text{eq}}$  to the measurement time of a given experiment will determine whether pumping of the walls will lead to a significant reduction of residual gas (tritium in the KATRIN case).

Estimates for the KATRIN main spectrometer will be given in section 3.3.3.

It is to be noted that the diffusive hydrogen stored and transported via the lattice is not the only trapped form of hydrogen. Entrapment in lattice or surface defects, or alongside oxid-enclosures, can also be important especially when dealing with very low fluxes, as for example given in the KATRIN main spectrometer (see e.g. [Hir84a],[Hir84b]). The binding energies of lattice defects are of the order of  $18 \text{ kJ mol}^{-1}$ , which is significantly lower than the diffusion activation energy (usually above  $50 \text{ kJ mol}^{-1}$ )[Xiu88]. Qualitatively speaking, impurities in the lattice, especially oxides or defects, form *shallow traps*, thus reducing the transport capability (diffusivity and permeability) of the lattice, but will on the other hand greatly increase absorption probabilities.

### 3.2.4.3 Adsorption

Even more important than diffusion-based absorption at very low pressures are adsorption processes. Contaminations on the steel wall (adsorption) can greatly enforce the described retention of hydrogen until these surfaces reach a concentration equilibrium with the residual gas.

In general, adsorption and desorption processes are described via the desorption flux

$$j_{\text{des}} = \frac{dn}{dt} = -\frac{\Delta n}{\tau_0} = \frac{n}{\tau_0} e^{\frac{-E_{\text{des}}}{RT_{\text{wall}}}} \quad (3.26)$$

using the characteristic oscillating time  $\tau_0$ , which for light particles on metal is of the order of  $10^{-13}$  s [Kaz08]. From this oscillating time one can also calculate the (for our estimations) important dwelling time (or sojourn time)  $\tau$

$$\tau = \tau_0 e^{\frac{-E_{\text{des}}}{RT_{\text{wall}}}}. \quad (3.27)$$

The dwelling time corresponds directly to the timescale of adsorption-desorption equilibrium, i.e. the timescale for which the surface will have a net pumping quality.

Besides the hydrogen-metal adsorption, relevant processes are bonding to oxygen-impurities and adsorptions to surface water (see figure 3.6). Oxides are (to some extent) always present when dealing with steel-components in contact with the atmosphere (surface-oxides). During the heating and refinement of the steel, oxygen usually is present as well (via intrinsic oxides).

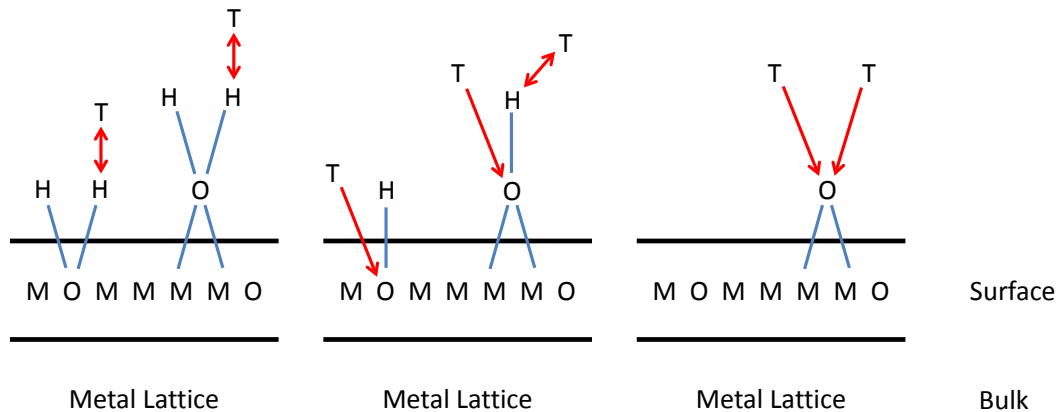


Figure 3.6: **Tritium-Surface Interactions:**

The blue lines indicate bound surface impurities, the red arrows indicate tritium adsorption (adsorption processes with a double headed arrow indicate a Protium desorption). Left: OH<sub>2</sub> type contaminations, mainly isotope exchange. Middle: OH<sup>-</sup> type with isotope exchange and chemisorption. Right: O<sub>2</sub> type with pure chemisorption

Water can bind to the steel walls in multiple ways as well. The water which is bound most weakly is the one physically bound as a result of the contact between the wall and residual water vapor in air. It can easily be removed by purging the vessel. Chemically adsorbed water is covalently bound to the surface and requires heating of the vessel to be removed. Most strongly bound is "structural water", which resides in OH inclusions within the steel. According to [Hir84a] those OH-groups are highly likely to connect with hydrogen from the vacuum.

An ab-initio calculation of the adsorption capability of the surface of a tritium-free vacuum vessel are highly challenging since a detailed a-priori knowledge of the surface composition and cleanliness is usually not given, which leads to a limited knowledge of  $E_{\text{des}}$ . A rough estimate for the relevant KATRIN components will be presented in section 3.3.3.

### 3.2.5 Sorption Pumping

As stated in section 3.2.3, the final pressures of a cascaded turbo-molecular pumping system are limited to pressure ranges between  $10^{-9}$  and  $10^{-10}$  mbar. Additional vacuum quality can be gained by using getter pumps. Getter pumping is a rather old and very well understood vacuum technique. According to Danielson [Dan01], the words originate back to the vacuum components designed to "get" the residual gas in vacuum systems. As stated in various publications, getters can massively improve vacuum systems dealing with hydrogen and result in an improvement in gas-reduction by more than two orders of magnitude (cf. eg. [Poz96]), if compared to solely molecular pumping.

The basic principle is usually a chemical reaction between the getter material (typically a metal) and the residual gas ("chemi-sorption"). In the case of hydrogen (or its isotopologues) it is rather a diffusion process. The hydrogen is captured by the getter surface (see figure 3.7) and migrates into the material thus being bound inside the bulk-material ("physi-sorption").

The basic physical principles are very comparable to those introduced in section 3.2.4. A key feature of the getter material in comparison to steel is its high diffusion length in comparison with desorption energies in the order of  $120 \text{ kJ mol}^{-1}$  [Ich84].

The pumping capacity of the getter pump stays constant until approximately 90 % of its maximum capacity is reached (after that a regeneration via bake-out is needed). This constant behavior allows the definition of a sticking coefficient  $\alpha$  comparable to the capture factor in the case of turbo-pumping.

For the commonly used (also in KATRIN) getter material SAES St-707 excessive studies have been carried out. The KATRIN Collaboration found the sticking coefficient of the deployed material to be  $\alpha = 0.0225(2)$  via simulations, and  $\alpha = 0.0290(4)$  empirically [Day07].

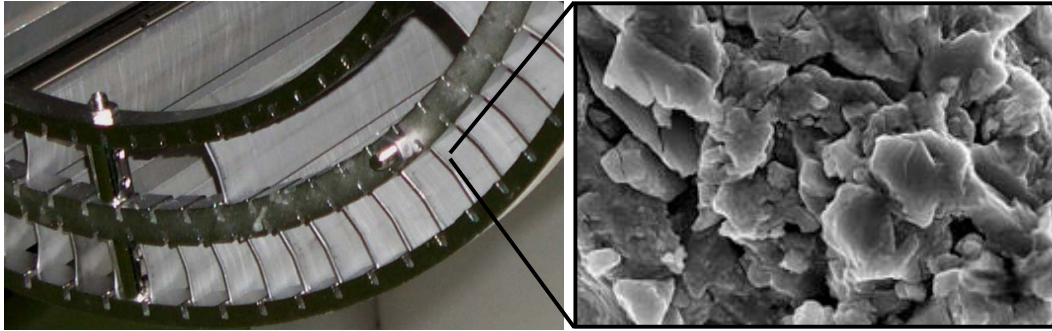


Figure 3.7: **Getter-Pumping Material:**

Shown on the left is a close-up photograph of getter strips used for application in the KATRIN spectrometers. On the right hand side, a microscopic picture of the getter material, taken at the Laboratory for Electron-Microscopy (LEM) at the Faculty for Physics at KIT is shown. The granular surface structure offering a large number of adsorption-sites can be seen in great detail.

Based on this capture factor, calculations can be carried out to estimate the pumping speed and required getter size for deployment in the KATRIN vacuum system, in particular the spectrometers [Day07][Wol12]. A summary of the resulting characteristics of the KATRIN getter pumps is presented in section 3.3.2.

Given its nature a getter pump can only be used as an additional vacuum clean-up in an already very good vacuum ( $p < 10^{-6}$  mbar [Wut10]). In the KATRIN case, i.e. in combination with massive use of turbo-pumping, the conditions are ideal for getter-pump deployment. The main disadvantage of getters in the KATRIN scenario is the presence of trace amounts of radioactive compounds within the getter material. Even in the commonly used low-activity NEG materials, small traces of elements mainly from the actinium series undergo decay and form unstable  $^{219}\text{Rn}$  and  $^{220}\text{Rn}$  atoms. The  $\alpha$ -decay of these short-lived radon isotopes in the vessel itself will lead to an even greater background from electrons than the tritium described above in section 3.1.2. Thorough investigations on these matters have been carried out by the KATRIN Collaboration [Wol12],[Mer12] to find the optimal amount of getter material.

### 3.2.6 Cryopumping

Cryopumping of hydrogen is a process of pure physisorption. The term cryopumping is usually related to the physisorption of gases at temperatures below 120 K. The relatively low energy levels of physisorption are independent of the temperature. By lowering the temperature of the adsorbate, the probability for desorption from the adsorbent is decreasing exponentially.

After randomly hitting the wall the gas particles will lose thermal energy. With a probability  $\alpha$  (analogously to the capture factor introduced in subsection

3.2.3) the gas particle will stick to the surface. In the case of cryo-sorption, the parameter  $\alpha$  is called the sticking coefficient. The adsorbed particle will then either migrate on the cryo-surface, diffuse deeper in the adsorbent material, or desorb from the walls after a characteristic time  $\tau$ , which is comparable to the behavior of gas captured on getter pumps.

The case of low temperature cryo-pumping can be characterized as follows:

- The sticking coefficient  $\alpha$  reaches almost unity ( $\alpha \approx 1$ ). Particles desorbing from a sufficiently large cryo-surface are highly likely to re-adsorb.
- The characteristic energies of physi-sorption on steel are of the order of  $E_{\text{des}} \approx 2 \text{ kJ mol}^{-1}$  or  $\approx 20 \text{ meV}$ , respectively.
- Using again the lattice oscillation time  $\tau_0 \approx 10^{-13} \text{ s}$ , one finds  $\tau$  (using equation 3.27 analogously) to be in the order of  $5.6 \times 10^{11} \text{ s}$  at 4.22 K (boiling point of helium) for adsorption on steel.

The resulting pressure of a vacuum system utilizing a cryo-pump is given by [Rot90],[Wut10], with the following key parameters:

- the rate of adsorption

$$j_{\text{ad}} = \frac{1}{\sqrt{2} \pi k_B} \cdot \frac{\alpha p}{\sqrt{T_{\text{gas}} M}} \quad [\text{s}^{-1} \text{ m}^{-2}]$$

- the rate of desorption

$$j_{\text{des}} = \frac{n_{\text{ad}}}{A} \cdot \frac{1}{\tau_0} \cdot e^{\frac{-E_{\text{des}}}{RT_{\text{wall}}}} \quad [\text{s}^{-1} \text{ m}^{-2}]$$

- the resulting equilibrium pressure, when  $T_{\text{gas}} = T_{\text{wall}} = T$  and  $j_{\text{ad}} = j_{\text{des}}$

$$p_{\text{eq}} = \frac{n_{\text{ad}} \sqrt{T M}}{\alpha A} \cdot \frac{\sqrt{2} \pi k_B}{\tau_0} \cdot e^{\frac{-E_{\text{des}}}{RT}}$$

As can be seen, the parameters of interest for the design of a cryo-pump for a given gas load (corresponds to  $n$  and  $M$ ) and a fixed equilibrium pressure  $p_{\text{eq}}$  are the temperature and the surface. Since temperatures below the helium boiling point for a large area are difficult to achieve, a large adsorbent area is desired. Besides charcoal and other high area materials, the application of condensed gases such as  $\text{CO}_2$  or  $\text{CH}_4$  or noble gases like Ar is possible.

In the case of a condensed gas adsorbent, a high granularity of the "frosting" is desired, leading to a large effective pumping area  $A_0$  (corresponding to a high number of available adsorption spots) as follows [Eic09][Hae89]

$$A_0 = \frac{a_0 F N_A}{M_A} \quad \text{with} \quad F = 3.464 \left( \frac{M}{4\sqrt{2}N_A\rho} \right)^{2/3} \quad (3.28)$$

With  $F$  being the occupied area per adsorbate particle on the adsorbent, assuming tightest packing [Emm37], the parameter  $M_A$  denotes the adsorbends and  $M$  the adsorbates molar mass, and  $\rho$  the adsorbates density. The number  $a_0$  would be the number of adsorbed particles if the whole adsorbent area was covered with one monolayer of adsorbate (which, in reality, will not be reached at temperatures  $> 0$  K) divided by the number of adsorbent particles.

The effect of granularity can be seen in the dependence of grain-size  $\delta$  and the effective pumping area  $A_0$ , which, assuming the grains to be cubicles, is given by [Hae89]:

$$\delta = \frac{6}{A_0 \rho_A} = \frac{6M_A}{\rho_A a_0 F N_A} \quad (3.29)$$

For each adsorbent the grain size  $\delta$  depends strongly on the condensation temperature and condensation rate. Lacking reliable calculation methods, empirical values for the CPS will be given in section 5.2.3.

Lastly, the maximum coverage has to be estimated in order to gain knowledge about the maximum operating time of a cryogenic pumping system [Eic09]:

$$a_{\max} = \frac{(j_{\text{ad}}/A) \cdot t_{\max}}{n_{\text{adsorbent}}} \Leftrightarrow t_{\max} = \frac{n_{\text{adsorbent}}}{j_{\text{ad}}/A} \cdot a_{\max} \quad (3.30)$$

These values have to be handled with care. Comparable to the adsorption to lattice defects, as described in section 3.3.3, the binding energy to the adsorbent can vary due to inhomogeneous adsorbent structure. Holes in the adsorbent lattice, for example, can lead to adsorption sites where the adsorbate is facing up to nine next neighbors, resulting in a stronger bond; these sites will be occupied first. With increasing coverage the average binding energy decreases. When defining the operating time these effects should be kept in mind, and sufficiently large safety margins in coverage (i.e. operating time) should be included.

The cryogenic pumping section (CPS) of KATRIN featuring a large argon-frosted surface at temperatures between 3 and 4.5 K has been designed along these considerations and is described in section 5.2.



### 3.3 Tritium Gas Flow Reduction in KATRIN

In this section the overall KATRIN gas flow will be described. The calculations are based on considerations by J. Bonn and B. Bornschein in 2001 [Bon01], and the KATRIN design report [KAT04]. To estimate the gas flow reduction properties, we use a calculation based on conductance. It is to be noted, that - given the very complex geometry and necessary simplifications - this approach is not as accurate as other methods, nevertheless is accurate enough on the level of engineering and machine-design. Specifically, the overall layout of the KATRIN Transport Section was based on this method. Special attention will be put to the updated value of the CPS reduction factor, values of the spectrometer volume, and to redesigned getter and valve conductivities.

All of the above described gas suppression and vacuum techniques are employed in KATRIN. The following two subsections will give an overview of the whole KATRIN vacuum system, going from rough pumping at the source, pure molecular pumping and cryo-pumping in the transport section down to getter pumping in the spectrometers.

#### 3.3.1 Gas Flow Reduction in STS

The STS will eliminate - to a technical standard - virtually all tritium from the KATRIN beamline. Our goal is to reduce the tritium gas flow from the injected value of  $1.8 \text{ mbar l s}^{-1}$  to a level of less than  $10^{-14} \text{ mbar l s}^{-1}$  when leaving the CPS, as shown schematically in figure 3.8.

The KATRIN gas flow will be reduced by the following stages in the source and transport system:

1. WGTS exit: there, the flux from the source is  $1.8 \text{ mbar l s}^{-1}$   
This flux is fixed by design to allow for a sufficiently high column density, and hence a sufficiently high  $\beta$ -decay rate.
2. DPS1-F reduction factor:  $R_{\text{DPS1-F}} \approx 8 \times 10^2$   
This factor is realized by two stages of molecular pumping, using first four and then two MAG W 2800 TMPs. The estimates given here need to be confirmed during later WGTS commissioning.  
The remaining flow leaving DPS1-F is  $\approx 2 \times 10^{-3} \text{ mbar l s}^{-1}$ .
3. DPS2-F reduction factor:  $R_{\text{DPS2-F}} \approx 1 \times 10^5$  (estimated value)  
Technically, this will be realized by four stages of cascaded molecular pumping using a MAG W 2800 TMP at each port and a buckled beamline (see section 5.1). The experimental investigation of the reduction factor in 2011 as part of this work has rendered a minimum value of  $2.5 \times 10^4$  for  $T_2$ .  
The remaining flow leaving DPS2-F is  $\leq 1 \times 10^{-7} \text{ mbar l s}^{-1}$ .

4. CPS reduction factor:  $R_{\text{CPS}} \geq 3 \times 10^7$

On the hardware side, this will be realized by a fourfold buckled and grooved beamline at 3 - 4.5 K acting as a cryo-pump (see section 5.2). Estimates of this reduction factor are based on experimental data of a test experiment [Eic09], and will be cross-checked during CPS commissioning. The remaining flow leaving CPS is  $\approx 3 \times 10^{-15} \text{ mbar l s}^{-1}$ .

A detailed description of the Differential and the Cryogenic Pumping Sections will be given in chapter 5.

The remaining gas flow leaving the CPS  $q_{\text{CPS} \rightarrow \text{PS}}$  renders a constant input of approximately  $3 \times 10^{-15} \text{ mbar l s}^{-1}$ , i.e.  $7.5 \times 10^4 \text{ molecules s}^{-1}$  into the spectrometer section. We expect this molecular flow to consist mainly of HT molecules. The  $\text{T}_2$  molecules injected in WGTS that have traveled so far downstream will have experienced several collisions with steel components. Those impacts promote the equilibration of all hydrogen isotopologues depending on the local partial pressures. Given the fact that the tritium partial pressure decreases as stated above, the protium pressure will basically be constant due to outgassing from the vast surfaces. This isotope exchange reaction will constantly lower the relative number of  $\text{T}_2$  and increase the number of HT molecules (cf. e.g. [Vas93]). All further calculations for the spectrometer section have hence been carried out for HT.

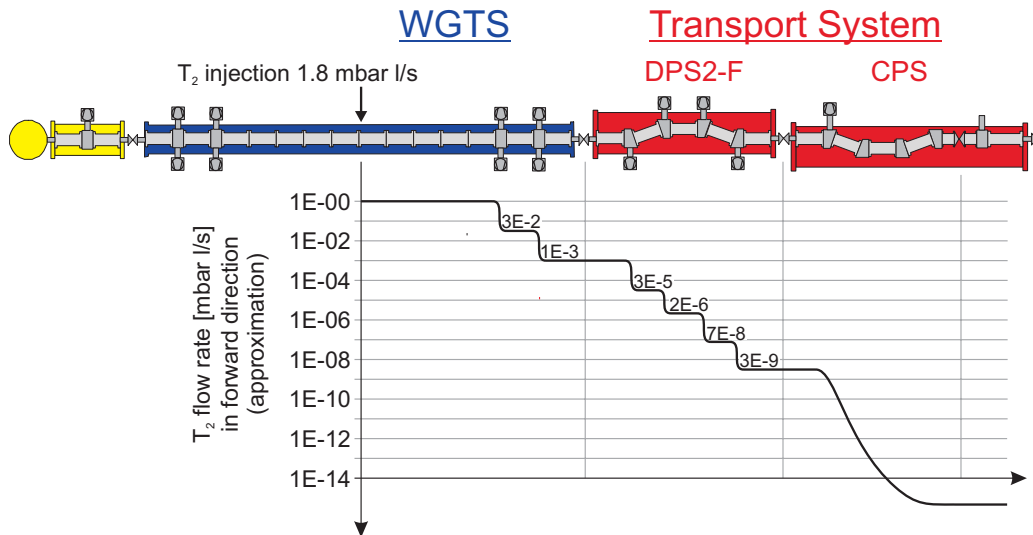


Figure 3.8: **Tritium suppression in STS**

The reduction of tritium flow rate by 14 orders of magnitude. Starting from the injection point in the middle of WGTS through the differential pumping sections down to the exit of the cryogenic pumping section before reaching the spectrometer section.

### 3.3.2 Gas Flow Reduction in Spectrometers

#### 3.3.2.1 Pre-Spectrometer

In the case of an equilibrated gas flow in the pre-spectrometer (which should be reached after several minutes), the number of tritium atoms should remain constant. The partial pressure there is then given by

$$p_{\text{PS}} = \frac{q_{\text{CPS} \rightarrow \text{PS}}}{S_{\text{eff,pre}} + L_{\text{PS} \rightarrow \text{MS}}} \quad (3.31)$$

In this formula the pumping speeds of the TMPs and the getter pumps are combined into  $S_{\text{eff,pre}}$ . Using now (based on this work and [Wol09]) the values

- $q_{\text{CPS} \rightarrow \text{PS}}^{(\text{HT})} = 3 \times 10^{-15} \text{ mbar l s}^{-1}$
- $S_{\text{getter}}^{(\text{HT})} = 4.03 \times 10^4 \text{ l s}^{-1}$
- $S_{\text{TMP}}^{(\text{HT})} = 1.47 \times 10^3 \text{ l s}^{-1}$
- $L_{\text{PS} \rightarrow \text{MS}}^{(\text{HT})} = 530 \text{ l s}^{-1}$

one finds a partial pressure value of

$$p_{\text{PS}}^{(\text{HT})} = 7.2 \times 10^{-20} \text{ mbar} \quad \text{or} \quad n_{\text{PS}}^{(\text{HT})} = 1.51 \times 10^4 \text{ HT - molecules.} \quad (3.32)$$

The pumping speed  $S_{\text{getter}}^{(\text{HT})}$  was calculated based on the simulations carried out by [Day07] for an array of  $2 \times 90 \text{ m}$  of SAES St707 getter strips with a sticking coefficient of 0.029, as introduced in section 3.2.5.

#### 3.3.2.2 Outgassing

As stated in section 3.2.4, the process of outgassing of steel walls is an omnipresent challenge for vacuum containers.

The main spectrometer vessel features a large surface area of  $690 \text{ m}^2$  made from 316LN steel (European steel code 1.4429; see appendix A.7 for further information), which endangers the desired low pressure level needed in the main spectrometer. The outgassing rates of the main spectrometer have been subject to thorough examinations. After a bake-out cycle at  $350 \text{ }^\circ\text{C}$  we found an outgassing rate of  $10^{-12} \text{ mbar l s}^{-1} \text{ cm}^{-2}$  at  $20 \text{ }^\circ\text{C}$ , using the rise of pressure method [Wol09] after pumping for 100 hours. This value fulfills our expectations very well and lies on the lower end of the usually acquired outgassing rates for non-specially treated steels [Moo95]. An analysis of residual gas shows - as expected -  $\text{H}_2$  to be the main residual gas component. Since then, the wire

electrode system (cf. section 2.2.4) and the bearing structure of the getter and cryo-baffles have been installed, adding more than  $530 \text{ m}^2$  to the effective area, leaving an outgassing rate of approximately  $10^{-5} \text{ mbar l s}^{-1}$ . For all further calculations we assume an effective area of  $1300 \text{ m}^2$  steel [Gum12].

To compensate for this enhanced outgassing rate and to achieve the desired vacuum value of  $10^{-11} \text{ mbar}$  in the main spectrometer, one needs a vacuum system with a pumping speed of  $S_{\text{eff}} > 10^6 \text{ l s}^{-1}$ , which will be further described in the following subsection.

### 3.3.2.3 Main Spectrometer

The vacuum system of the main spectrometer is qualitatively comparable to the one deployed in the pre-spectrometer, using again a combination of TMPs (MAG W 2800) and SAES St707 getter strips. Figure 3.9 shows the setup of the vacuum system in one of the pump ports of the main spectrometer.

As can be seen, the TMPs are arranged in two sets of three-fold units at the large pumping ducts at the downstream-side of the spectrometer. Included in those pumping ducts are the large arrays of getter material, featuring a total of 3000 meters of getter strips (see figure 3.7). In front of the getter pumps, cryo-cooled baffles at liquid nitrogen temperature are mounted. Their sole purpose is the reduction of radon background emanating from the getter material. These baffles noticeably decrease the net pumping speed for tritium and hydrogen. The net effect on background reduction however was carefully optimized by the vacuum and background teams (cf. [Goe10],[Mer12],[Wol12]).

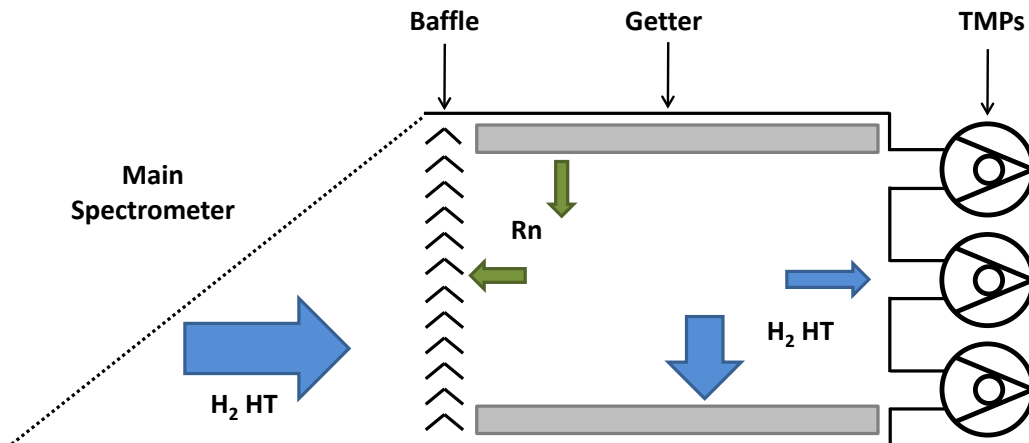


Figure 3.9: **Vacuum System in Main Spectrometer**

The vacuum components used in the two main spectrometer pump ports shown schematically (based on [Goe10]). Residual hydrogen and tritium enter from the main spectrometer volume (blue arrows) and are pumped by the getter and the turbo pumps. Radon emanating from the getter is sticking to the cryo-baffles (green arrows).

Based on the corresponding Monte Carlo simulations [Luo07], and using a sticking coefficient  $\alpha = 0.028$  for the getter strips (cf. section 3.2.5), we find (cf. [Day07][Luo07][Wol09][Wol12]) values of:

- $S_{\text{getter}}^{(\text{H}_2)} = 4.5 \times 10^5 \text{ l s}^{-1}$
- $S_{\text{getter}}^{(\text{HT})} = 3.2 \times 10^5 \text{ l s}^{-1}$
- $S_{\text{TMP}}^{(\text{HT})} = 1.24 \times 10^4 \text{ l s}^{-1}$

Taking into account the tritium gas flow (HT) from the pre-spectrometer into the main spectrometer of

$$\begin{aligned} q_{\text{PS} \rightarrow \text{MS}} &= q_{\text{CPS} \rightarrow \text{PS}} \frac{L_{\text{PS} \rightarrow \text{MS}}^{(\text{HT})}}{S_{\text{total, PS}}^{(\text{HT})} + L_{\text{PS} \rightarrow \text{MS}}^{(\text{HT})}} = 3.80 \times 10^{-17} \text{ mbar l s}^{-1} \\ &= 9.40 \times 10^2 \text{ HT/s} \end{aligned} \quad (3.33)$$

we find a partial pressure of HT in the main spectrometer of

$$p_{\text{MS}} = \frac{q_{\text{PS} \rightarrow \text{MS}}}{S_{\text{total, MS}}} = 1.15 \times 10^{-22} \text{ mbar} \quad (3.34)$$

which corresponds to less than one  $\beta$ -decay per day.

### 3.3.2.4 Summary

The installation of cryo-baffles reduces the net pumping speed of the getter system for hydrogen by 55 % [Goe10] to  $S_{\text{getter}}^{(\text{H}_2)} = 4.5 \times 10^5 \text{ l s}^{-1}$ , which is more than a factor 2 too low for the desired general pressure (mainly composed of hydrogen outgassing from the walls) of  $10^{-11}$  mbar in the main spectrometer. We will try to improve the baking procedure to compensate for this reduced pumping speed<sup>6</sup>.

For tritium, however, the vacuum system is expected to meet all specifications. The already largely reduced flow leaving the transport section is further reduced as follows:

1. Pre-Spectrometer reduction factor (using 180 m NEG strips):  $R_{\text{PS}} \approx 1 \times 10^2$

This value is approximated by simulations [Wol12], and could be upgraded to a value of  $2 \times 10^3$  by using a total of 1000 m NEG strips.

The remaining flow leaving the pre-spectrometer is then found to be  $\approx 3.8 \times 10^{-17} \text{ mbar l s}^{-1}$

---

<sup>6</sup>This slightly higher pressure will still not significantly increase the scattering probabilities of the important signal electrons from the source. It will however increase the production rate of secondary electrons since the production rate per unit time is inverse proportional to pressure [Mer12].

2. Pressure reduction from Pre- to Main Spectrometer  $\approx 6.3 \times 10^2$

This value is again approximated by simulations [Wol12].

The final tritium partial pressure (HT) is then  $\approx 1.1 \times 10^{-22}$  mbar

Using this value together with the calculations for the background originating from tritium  $\beta$ -decay in the main spectrometer (cf. section 3.1.2) we find a tritium (HT) induced background to KATRIN measurements of  $\approx 0.13$  mHz, which is well within the limits defined by our sensitivity goals. Additionally, tritium-wall interactions could significantly lower this value even further, as presented in the following section.

### 3.3.3 Tritium Sorption on Walls

Tritium reaching the main spectrometer vessel does interact with the surface of the vessel as described in section 3.2.4. Given the fact that the main spectrometer is a "fresh" vessel with no tritium inventory and given the very low input of  $\approx 4000$  HT molecules per second, it is important to estimate the time scales on which the steel vessel will reach a concentration equilibrium with the residual gas. Before reaching this equilibrium, the vessel itself acts like an additional tritium pump, reducing the tritium induced background.

**Diffusion** To estimate the maximum uptake before reaching the equilibrium concentration in the main spectrometer vessel by diffusion only, we use equation 3.19 and the values given in table 3.2. We also assume a thermalized gas at 293 K and neglect (for now) surface effects and co-volumina (i.e.  $f = p$ ).

To calculate the integral amount of stored tritium in equilibrium the effective storing volume is needed. The surface area is known to be  $A = 1300 \text{ m}^2$ . The intrusion depth however needs to be estimated. Literature suggests diffusion depths of the order of  $10^{-5}$  m for exposure times of the order of days at room temperature. Calculating the depth for one year ( $3.15 \times 10^7$  seconds) we estimate  $7 \times 10^{-5}$  m, rendering a maximum inventory of  $\approx 2 \times 10^{11}$ .

From this it is easy to calculate the timescale after which a concentration equilibrium will be reached using the flow values as presented in section 3.3.2. For a flux  $q_{PS \rightarrow MS} = 6 \times 10^3 \text{ s}^{-1}$ , as calculated in [Wol12], this concentration would be reached after 800 days (over 2 years), if one assumes that all tritium migrating to the main spectrometer volume is completely absorbed in the walls via diffusion processes. The above calculated flux of  $q_{PS \rightarrow MS} = 9.40 \times 10^2 \text{ s}^{-1}$  renders concentration equilibrium after more than 10 years.

Table 3.2: **Hydrogen-diffusion in steel:**

Solubility, Diffusivity and Permeability of hydrogen (protium) in stainless steel from different studies. Diffusion-length, capacity and equilibrium time were calculated for the KATRIN main spectrometer using the following parameters:  $\tau = 1$  year,  $R = 8.314 \text{ J mol}^{-1} \text{ K}^{-1}$ ,  $p = 5 \times 10^{-26} \text{ MPa}$ ,  $T = 293 \text{ K}$ ,  $A = 1300 \text{ m}^2$ ,  $Q_{PS \rightarrow MS} = 4000 \text{ s}^{-1}$ .

Study	Diffusivity		Solubility			
	$D_0$ [ $\text{m}^2 \text{ s}^{-1}$ ]	$H_D$ [ $\text{kJ mol}^{-1}$ ]	$D$ [ $\text{m}^2 \text{ s}^{-1}$ ]	$K_0$ [ $\text{mol m}^{-3} \text{ MPa}^{-1/2}$ ]	$H_S$ [ $\text{kJ mol}^{-1}$ ]	$K$ [ $\text{mol m}^{-3} \text{ MPa}^{-1/2}$ ]
[San05]	$8.90 \times 10^{-7}$	53.9	$2.19 \times 10^{-16}$	135	5.9	11.98
[Per86]	$2.01 \times 10^{-7}$	49.3	$3.27 \times 10^{-16}$	266	6.86	15.92
[Lou75]	$6.60 \times 10^{-7}$	54.0	$1.56 \times 10^{-16}$	179	5.9	15.89
[Min11]	$1.21 \times 10^{-5}$	63.1	$6.81 \times 10^{-17}$	496	2.58	17.20
[Xiu88]	$4.33 \times 10^{-7}$	50.99	$3.51 \times 10^{-16}$	427	9.67	8.07
[Xiu88]	$5.76 \times 10^{-7}$	53.62	$1.59 \times 10^{-16}$	488	8.65	14.01

Source	Concentration		Diffusionlength		Capacity		Equilibrium-Time	
	$\chi$ [ $\text{mol m}^{-3}$ ]		$A$ [m]		$N$ [atoms]		$\tau_{\text{eq}}$ [d]	
[San05]	$2.68 \times 10^{-12}$		$8.31 \times 10^{-5}$		$1.74 \times 10^{11}$		504.1	
[Per86]	$3.56 \times 10^{-12}$		$1.01 \times 10^{-4}$		$2.83 \times 10^{11}$		818.1	
[Lou75]	$3.55 \times 10^{-12}$		$7.01 \times 10^{-5}$		$1.95 \times 10^{11}$		563.8	
[Min11]	$3.85 \times 10^{-12}$		$4.63 \times 10^{-5}$		$1.40 \times 10^{11}$		403.8	
[Xiu88]	$1.80 \times 10^{-12}$		$1.05 \times 10^{-4}$		$1.49 \times 10^{11}$		430.2	
[Xiu88]	$3.13 \times 10^{-12}$		$7.08 \times 10^{-5}$		$1.74 \times 10^{11}$		502.1	

**Adsorption** As stated in section 3.2.4, the gas-surface interactions in the form of adsorption processes become more important with lower pressures, which is clearly the case in the KATRIN scenario. Exact calculations or even simulations of these processes on a large and widely unknown surface like the one of the KATRIN main spectrometer are very challenging at best.

A rough estimate of the maximum surface concentration and net pumping time however was carried out for the main spectrometer by extrapolating from literature values [Eic09],[Hir84a],[Mor03],[Wut10],[Zar79] as follows.

Studies have shown the sticking probability to be independent of the degree of coverage up to values of 30 % - 40 %. One mono-layer of tritium on the walls of the main spectrometer would correspond to a number of particles of the order of  $10^{21}$ . The overall tritium flux into the vessel over the whole measurement campaign is of the order of  $10^{12}$ , so these marginal degrees of coverage can therefore be neglected.

The sticking time of undissociated HT after equation 3.27 is  $3.7 \times 10^{-10}$  s (given  $E_{\text{des}} = 22$  kJ/mol [Hir84b]), which can be neglected for our time scales. After thus ruling out molecular tritium compounds to be bound directly to the metal as a significant source of tritium retention, atomic (dissociated) hydrogen needs to be investigated. According to Shupe [Shu69], the activation energy for dissociation on a steel surface is  $10.2$  kJ mol $^{-1}$ . Given the well-known formula for process probabilities

$$P_{\text{dis}} = e^{\frac{-E_{\text{dis}}}{RT_{\text{wall}}}} \quad (3.35)$$

we obtain the dissociation probability  $P_{\text{dis}}$ . Assuming free adsorption centers (i.e. neglectable coverage), we write  $P_{\text{dis}} = P_{\text{ads}}$ , which leaves us to calculate the overall adsorption probability  $P_{\text{ads,tot}}$  for dissociated hydrogen. Here, the probability is binomially distributed as follows:

$$P_{\text{ads,tot}} = \binom{n}{k} P_{\text{ads}}^k (1 - P_{\text{ads}})^{n-k}. \quad (3.36)$$

with  $n - k$  being the number of particle-wall interactions without adsorption. Given a most probable velocity of  $1113.3$  m s $^{-1}$  and a characteristic path length in the spectrometer of  $15$  m, we obtain  $n = 223$ . With  $P_{\text{ads}} = 1.52$  % being the adsorption probability for one single hit, we find the overall adsorption probability  $P_{\text{ads,tot}} = 96.7$  %.

The final step towards an estimation of the tritium suppression capability of the vessel walls by adsorption is the calculation of the dwelling time  $\tau$  of the dissociated hydrogen using equation 3.27 and the values given in table 3.3. For a combination of pure iron, nickel and chromium (as in the used steel 316LN), the time scale of adsorption-desorption equilibrium  $\tau$  is expected to be about 10 years at a temperature of  $293$  K.

Combining all these estimations, the tritium suppression factor of the main spectrometer itself would be in the order of 30.



Table 3.3: **Hydrogen Desorption Energies:** Desorption energies of atomic hydrogen from the most relevant metals present in the KATRIN main spectrometer vessel (main components of 316LN steel), all given at 293 K. The values for chromium are not directly measured. The given value there was based on measurements for permeation activation energies. Given the fact that chromium is well known for its hydrogen trapping behavior it is safe to assume its  $E_{\text{des}}$  value to be even higher.

Metal	Source	$E_{\text{des}}$ [kJ mol <sup>-1</sup> ]	$\tau$ s
Iron	[Mor03]	134 kJ mol <sup>-1</sup>	$7.76 \times 10^{10}$ s
Iron	[Wut10]	135 kJ mol <sup>-1</sup>	$1.03 \times 10^{11}$ s
Nickel	[Wut10]	125 kJ mol <sup>-1</sup>	$1.98 \times 10^9$ s
Chromium	[Xiu88]	120 kJ mol <sup>-1</sup>	$2.48 \times 10^8$ s

This very large value has to be handled with some care. Any surface impurities can significantly lower the desorption energies. In this case, tritium, once adsorbed, will migrate into the bulk (as described above), desorb again (with the above illustrated probabilities), or migrate over the surface. The activation energy for hydrogen migration on steel is found to be  $\geq 30$  kJ mol<sup>-1</sup>, which means one adsorbed tritium atom will roughly migrate over  $4 \times 10^7$  adsorption sites on the surface before desorption on a theoretical perfect surface happens.

Depending on the specific surface conditions, the hydrogen will - with specific probabilities - migrate onto impurity-sites. These have desorption energies between 70 kJ mol<sup>-1</sup> (chromiumcarbide impurities), and 180 kJ mol<sup>-1</sup> (grain boundaries) for stainless steel, which corresponds to trapping times between  $3 \times 10^{-1}$  and  $2 \times 10^{19}$  seconds at room temperature [Ber10],[Miz94]. The migration onto oxygen or hydroxid-ions (cf. figure 3.6) is also possible, leading to very tightly bound sub-surface OT- or loosely bound HTO complexes.

The sites with higher binding energy are energetically favored and hence will be occupied first. In general the pumping qualities of the wall will decline over time. Precise estimates on the corresponding time scales, however, are difficult without further knowledge about the exact surface structure and texture.

### 3.3.3.1 Comparison to Integral Flux

The KATRIN measurements are planned to last 3 net years, which corresponds to a tritium flux into the main spectrometer of the order of  $1 \times 10^{11}$  particles. Comparing this value to the maximum surface and in-wall concentrations estimated above, and taking further into account that the main spectrometer

will be baked out every 10 months it is safe to assume that the spectrometer will significantly contribute to the reduction of tritium induced background. The net effect is very difficult to calculate precisely, since the assumptions introduced in section 3.2.4 have never been validated at such low partial pressures and long time scales. By answering these questions during the KATRIN measurements we will contribute uniquely to this field of vacuum physics. The author thus strongly recommends to prepare for high accuracy tritium accounting during the KATRIN start-up in order to utilize these unique possibility to answer interesting XHV questions.

Based on the assumptions and calculations presented in this section, we assume a tritium suppression factor in the sensitive spectrometer-volume (i.e. a suppression factor on the tritium induced background rates) by tritium-wall interaction of  $\geq 30$ . The biggest unknown factor in these assumptions is the concentration of defects with high binding energy.

## 3.4 Ionized Tritium

Ionized tritium will be produced by various processes in the WGTS (see section 4.1.2). The ions are guided by the magnetic field-lines, and hence can not be pumped out like the neutral gaseous tritium. Positive ions will be accelerated to the spectrometers, and, if not stopped before, could cause secondary electrons there, which would lead to a background in the order of several kHz [Win11]. Therefore the flux of tritium ions originating from the source needs to be suppressed or neutralized before reaching the spectrometers.

Two experimental challenges arise from this consideration. One is related to identifying and quantifying the ion flux on-line, the other is related to the question of how to suppress the ion flux without disturbing the signal electron flux. Corresponding experimental solutions are outlined in the following sections, and detailed electro-magnetic calculations are presented in section 4.3, while feasibility studies as well as test experiments are described in sections 6.3 and 6.3.

### 3.4.1 Ion Identification

In general, ions can be identified by their characteristic charge-mass-ratio  $q/m$ . A convenient way to access these values is via measurement of their cyclotron resonance frequency given by:

$$\omega_c = \frac{q}{m} \cdot B \quad (3.37)$$

Ion cyclotron frequencies of the most abundant ion (and ion-cluster) species are given in table 3.4. More detailed descriptions regarding the trap setup and commissioning are given in section 5.1.3. A theoretical approach on ion-analytics via cyclotron frequency is presented in section 4.3.1.

There are numerous technical methods to access and measure the cyclotron frequency of charged particles. Excessive studies have been carried out by our collaborators at the Max-Planck-Institute for Nuclear Physics at Heidelberg (cf. [Bla06][Ubi11]). For our needs a *Gabrielse*-type Penning trap with open endcaps is ideally suited [Gab89]. Its compact duct structure (see figure 5.10) allows an installation without interfering with the electron flux tube.

Two traps will be placed within the KATRIN beamline, one in the first, and another one in the last DPS2-F beam tube segment. Within the trap volume, local spot samples of the constant ion flux will be captured, excited by radio frequency and analyzed repeatedly, providing us with near on-line information on the composition and intensity of the ion flux from the WGTS.

Table 3.4: **Ion cyclotron frequencies** of selected ions and compounds most likely to be detected in the DPS2-F beamline. Calculated for  $B_{\max} = 5.6$  T following [Ubi11]

ion/cluster type	Cyclotron frequency [MHz]
$T_2^+$	12.80
$T_3^+$	8.53
$T_5^+$	5.12
$T_7^+$	3.66
$T^+, {}^3\text{He}^+$	25.59
$H_2^+$	38.39

### 3.4.2 Ion Suppression

The suppression of ions in the KATRIN beamline is a challenging endeavor. Measures have to be taken to not disturb the adiabaticity of signal electrons. Strong electric fields or electrodes within the magnetic flux tube are hence ruled out. We can however take advantage of the fact that ions from the source propagate mainly in a thermal energy range of  $E_{\text{kin}} \approx 10$  meV, which is six orders of magnitude less than the typical energy of the signal electrons. This fact gives rise to the possibility of designing a field trap which confines ions, but can be surpassed by the electrons.

To prevent space charges or even plasma formation, which could lead to electromagnetic disruption of the electron trajectories and energies, the ions need to be eliminated within this field trap.

In the framework of this thesis important conceptual design work on an electrode system covering both functions was performed. An electrostatic mirror will be placed at the end of DPS2-F and through-shaped electrodes will be placed within its beamtube. The mirror will reflect positively charged ions (negatively charged ions are reflected by the retarding potential of the spectrometers), while the through-shaped dipole electrodes will produce a steady  $E$ -field which is orthogonal to the guiding  $\vec{B}$ -field. This in turn will cause an  $\vec{E} \times \vec{B}$ -drift of the passing ions, thereby slowly deflecting the ions out of the flux tube where they can be neutralized, as shown in figure 3.10.

The applied permanent  $E$ -field will originate from a potential not larger than about 100 Volts. The resulting force is in general not strong enough to eliminate all ions from the flux tube after traveling through the dipole field once. Correspondingly, several fly-through cycles of the ions (being reflected by the electrostatic mirror downstream and the high particle density upstream) are necessary for neutralization. We will take advantage of the fact that the  $\vec{E} \times \vec{B}$ -

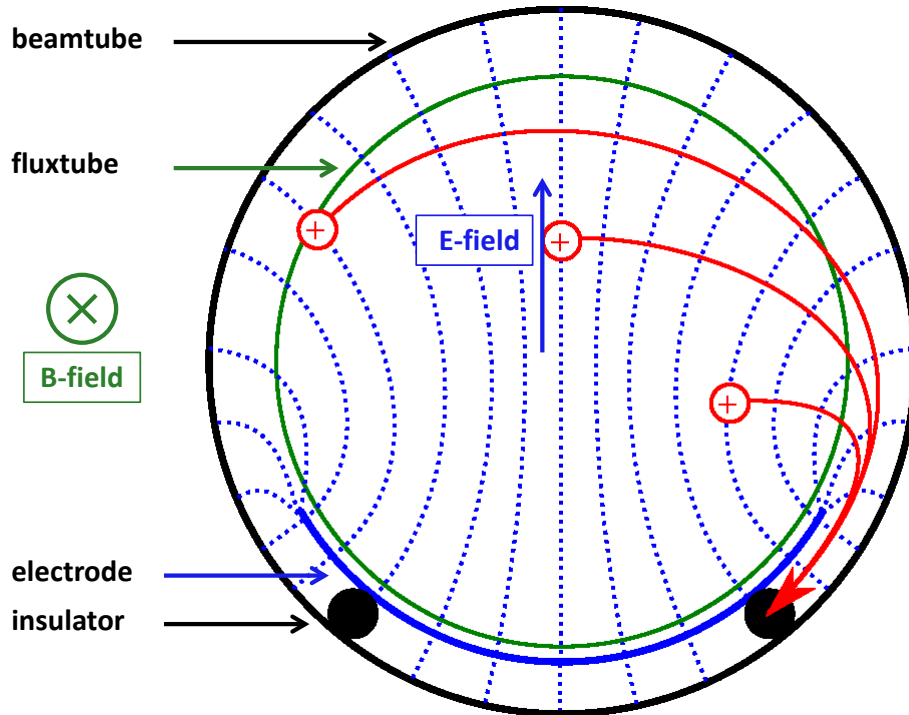


Figure 3.10: **Schematic of  $\vec{E} \times \vec{B}$ -drift**

The dashed blue lines indicate the  $\vec{E}$ -field, the  $\vec{B}$ -field lines are directed up out of the drawing plain. The resulting drift of three (positively charged) exemplary ions is marked in red. Inside the green ring (the KATRIN flux tube demarked by the magnetic flux value of  $191 \text{ T cm}^2$ ) the signal electrons are carried. On the bottom of the beamtube, the electrode setup is shown schematically.

drift is independent of the charge, and hence the direction of fly-throughs. Accordingly, the ion-displacements resulting from each passing-through will add up. A detailed description of the physics of the  $\vec{E} \times \vec{B}$ -drift can be found in section 4.3.2, while a technical description of the proposed installations within DPS2-F is given in section 5.1.3 and the test experiments concerning the dipoles are described in section 6.3.



## Chapter 4

# Tritium Retention - Theoretical Principles

In this chapter we present detailed calculations concerning the output of neutral gas and ions from the source, that the DPS2-F unit has to deal with in standard operation. We also outline theoretical models characterizing tritium fluxes and flow rates in DPS2-F. Finally, we introduce a brief theoretical framework of the proposed ion suppression and analysis systems.

### 4.1 Characterization of Source Output

It is of major importance to estimate the different fluxes leaving the WGTS beam tube, both with regard to the tritium gas flow as well as with regard to the ion flux entering the DPS2-F.

#### 4.1.1 Tritium Gas Flux into DPS2-F

The WGTS tube and the powerful pumping section DPS1-F and DPS1-R have been described on a technical level in section 2.2.3. At this point a closer examination of the gas profile will be given.

The WGTS will be supplied with a continuous gaseous tritium flow of  $1.8 \text{ mbar l s}^{-1}$  (standard conditions) injected at the center of the beam tube. With the given geometry and temperature this renders a pressure at the injection point of  $p_{\text{in}} = 3.37 \times 10^{-3} \text{ mbar}$  [Wol09][Kae12]. Since the beam line itself is closed up to the first pump port, no reduction of flow will occur over the first 5 meters. However, a reduction of pressure, which is expected to be quasi-linear down to the DPSF-1, will take place. Corresponding simulations reveal (cf. [Luo05], see also section 4.2.2) a reduction factor in the tritium flow of  $R_1 \approx 34$  and  $R_2 \approx 24$  for the two pumping stages of DPS1-F. Combining

these values with the bifurcation of the injected flow (almost 50 % will travel to the rear pumping section) to a value of  $0.9 \text{ mbar l s}^{-1}$  we obtain a gas load streaming into DPS2-F of

$$Q_{\rightarrow \text{DPS2-F}} = \frac{Q_{\text{in}}}{R_1 \cdot R_2} = 1.103 \times 10^{-3} \text{ mbar l s}^{-1}. \quad (4.1)$$

It is to be noted that the gas flow into DPS2-F comprises the effect of "molecular beaming", i.e. the gas particles not pumped out by the six TMPs of DPS1-F stream down the beam tube in an aligned movement. In this case any additional pumping from the sides of a straight beam tube would be greatly impaired. This is the primary motivation behind the  $20^\circ$  tilting of adjacent DPS2-F beam tube modules. The beaming effect is thus abolished at the first pump port and can therefore be neglected in the further calculations on gas flow suppression (see section 4.2).

## 4.1.2 Ion Flux into DPS2-F

The main decay process in the WGTS is usually written<sup>1</sup> as the transition  $\text{T} \xrightarrow{\beta} {}^3\text{He}^+ + e^- + \bar{\nu}_e$ . Since the source gas injected in the WGTS is high-purity molecular tritium ( $\text{T}_2$ ), the ionized compound  $({}^3\text{HeT})^+$  is produced. As presented in [Ott06], according to quantum-chemical calculations, 57.4 % of the daughter molecules will be in a  $({}^3\text{HeT})^+$  ground state, the remaining ones in an excited state rendering primarily  ${}^3\text{He}^+$  and  $\text{T}^+$  (see [Jon99] for details)<sup>2</sup>. Secondary processes and interactions with the  $\beta$ -decay and secondary electrons will, in general, lead to more complex ion structures and even cluster formation, which will be discussed below.

### 4.1.2.1 Ion Species

As stated above, an ensemble of different ion species and ion clusters needs to be considered when estimating the ion load that the beam line elements of DPS2-F have to deal with. As part of an overall investigation, the questions of ion interactions with neutral tritium, the re-neutralization of ions via slower source-related electrons as well as ionization of tritium molecules by collision with decay electrons need to be accounted for. The following estimations are based on considerations reported in [Glu10].

<sup>1</sup>For better readability of chemical formulas we will use the notation T instead of  ${}^3\text{H}$  for tritium.

<sup>2</sup>According to Wexler [Wex59] 5.5 % of  $\text{T}_2$  directly dissociates to  ${}^3\text{He}^+$  and  $\text{T}^+$  while 94.5 % undergo the above described transition. The resulting ion flux in the WGTS, however, is not significantly affected by the different ways of dissociation. There are plans within the KATRIN collaboration to perform a test experiment on this issue [Bod12].



**Interaction with neutral tritium:**

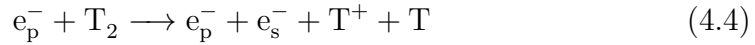
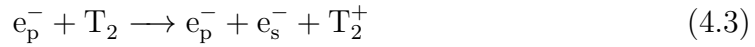
The mean tritium gas density, as given in 4.1.1, yields a high probability for the dissociation of the initially formed  $({}^3\text{HeT})^+$  compound. The transition



renders an energetically optimal combination, and correspondingly, virtually all  $({}^3\text{HeT})^+$  molecules undergo this transition after  $\approx 1$  mm path length.

**Ionization:**

The main ionization processes caused by primary  $\beta$ -decay electrons  $e_p^-$  are:

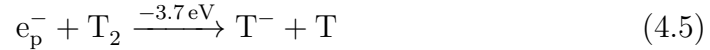


In these cases, secondary electrons  $e_s^-$  are produced. This non-dissociative process is dominant with a 94.5 % probability [Wex59].

On average the large e- $\text{T}_2$  scattering cross section implies that about 15 ionizing collision per  $\beta$ -decay electron will occur within the WGTS column.

**Negative ions:**

A small amount of negative ions will also be produced in the WGTS beam tube. The formation following



is, however, an endothermic reaction requiring an amount  $\Delta E = 3.7$  eV of energy. Given the fact that the thermalization cross section for the secondary source electrons is three magnitudes higher than the cross section of this reaction, only a comparably small amount of  $\text{T}^-$  ions will be produced. We expect that only a fraction  $< 2$  % of the overall produced ions will be negative ions (cf. table 4.2). Nevertheless, due to the larger endpoint energy of a  $\text{T}^-$   $\beta$ -decay, this species is of major importance for KATRIN (cf. section 4.1.2.5).

**4.1.2.2 Ion-Clusters**

Another important tritium  $\beta$ -decay active species are ion-clusters. These entities form in the WGTS via a combination of charged and neutral tritium molecules and ions [Pau95],[Smi10]. The primary processes are



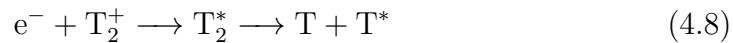
Odd-numbered, singly ionized tritium compounds ( $\text{T}^+$ ,  $\text{T}_3^+$ ,  $\text{T}_5^+$  ...) have a rather high likelihood of forming larger clusters when colliding with neutral

tritium gas at low temperatures [Pau95]. It is to be noted that the cluster-formation depends on the Ortho-Para-ratios of the injected tritium gas. Since these values are still under investigation for KATRIN, the standard Ortho-Para-ratios ("normal", or n-T<sub>2</sub>) were used for the following calculations<sup>3</sup>. It will nevertheless be shown in section 5.1.3, that the ion-suppression-techniques developed in the framework of this thesis will work effectively over a wide range of cluster concentrations. The probabilities for cluster-formation are presented in table 4.1.

#### 4.1.2.3 Re-neutralization

Given the fact that the WGTS contains rather high electron densities, re-neutralization processes lowering the overall ion density have to be considered as well. These processes tend to be dissociative by using the neutralization energy to break up cluster or quasi-molecular compounds (cf. [Mit90]).

The generic recombination process in this case is:



Apart from this ion-electron process, recombination between positive and negative ions will occur as well.

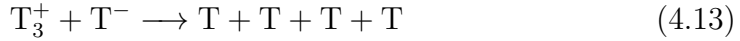
Table 4.1: **Probability of Tritium Cluster Formation**

Given in the general form  $[T_i^+] + 2 [T_2] \xrightarrow{k_3} [T_{i+2}^+] + [T_2]$  for standard ortho-para-ratio(n-T<sub>2</sub>) [Pau95].

cluster type	association coefficient $k_3$ [cm <sup>6</sup> s <sup>-1</sup> ]	dissociation time $\tau_{diss}$ [ns]
T <sub>3</sub> <sup>+</sup>	1.5 ± 0.5 · 10 <sup>-28</sup>	0.39
T <sub>5</sub> <sup>+</sup>	2.5 ± 0.5 · 10 <sup>-28</sup>	0.74
T <sub>7</sub> <sup>+</sup>	9.0 ± 3.0 · 10 <sup>-28</sup>	2.80
T <sub>9</sub> <sup>+</sup>	3.0 ± 1.0 · 10 <sup>-27</sup>	9.90
T <sub>11</sub> <sup>+</sup>	1.0 ± 0.5 · 10 <sup>-26</sup>	34.00
T <sub>13</sub> <sup>+</sup>	1.0 ± 0.5 · 10 <sup>-26</sup>	35.00
T <sub>15</sub> <sup>+</sup>	8.0 ± 5.0 · 10 <sup>-27</sup>	28.2

<sup>3</sup>The question of Ortho-Para-ratios is of even greater importance concerning the final state distribution of the tritium- $\beta$ -spectrum. Compare for example [Dos06].

The predominant recombination processes in the WGTS are listed below:



The recombination coefficients<sup>4</sup>  $\alpha$  of these neutralizations are energy-dependent quantities following roughly an  $E^{-1}$  power law and feature characteristic values of  $\alpha = 10^{-7} \text{ cm}^3 \text{ s}^{-1}$  [McG79]. The recombination processes reduce the ion current leaving the WGTS beam tube from an initial value  $I_{\text{ion}} \approx 144 \text{ nA}$  to  $I_{\text{ion}}^{\text{exit}} \approx 27 \text{ nA}$  (cf. table 4.2).

#### 4.1.2.4 Summary of expected Ion Load

Taking in account all these processes, the approximated flux of charged particles leaving the WGTS beam tube into the upstream end of the transport section is given in table 4.2, while a corresponding density profile is presented in figure 4.1.

This ion load traveling downstream into DPS2-F can result in a build-up of space charges that, in the worst case, would be able to influence the adiabaticity of the signal  $\beta$ -decay electrons. The evolution of charge over time in the DPS2-F is given by the relation:

$$\frac{dQ}{dt} = I_0 - \frac{q}{\tau} \quad (4.14)$$

Table 4.2: **Ion Flux from WGTS**

Estimated ion flux leaving the WGTS beam tube. The values take into account electron-ion recombination and follow [Glu10]

ion/cluster type	flux
$T_3^+$	19 nA
$T_5^+$	6.5 nA
$T^+$	1 nA
${}^3\text{He}^+$	0.25 nA
<b>positive ions</b>	<b>27 nA</b>
$T^-$	2 nA

<sup>4</sup>The recombination coefficient  $\alpha$  is given in units of  $\text{cm}^3 \text{ s}^{-1}$  and can be seen as the product of the cross section  $\sigma$  given in  $\text{cm}^2$  and a velocity  $v$  given in  $\text{cm s}^{-1}$ . The recombination rate  $R$  per unit volume and time then follows the relation  $R = \rho_{\text{ions}} \cdot \rho_{\text{electrons}} \cdot \alpha$ .

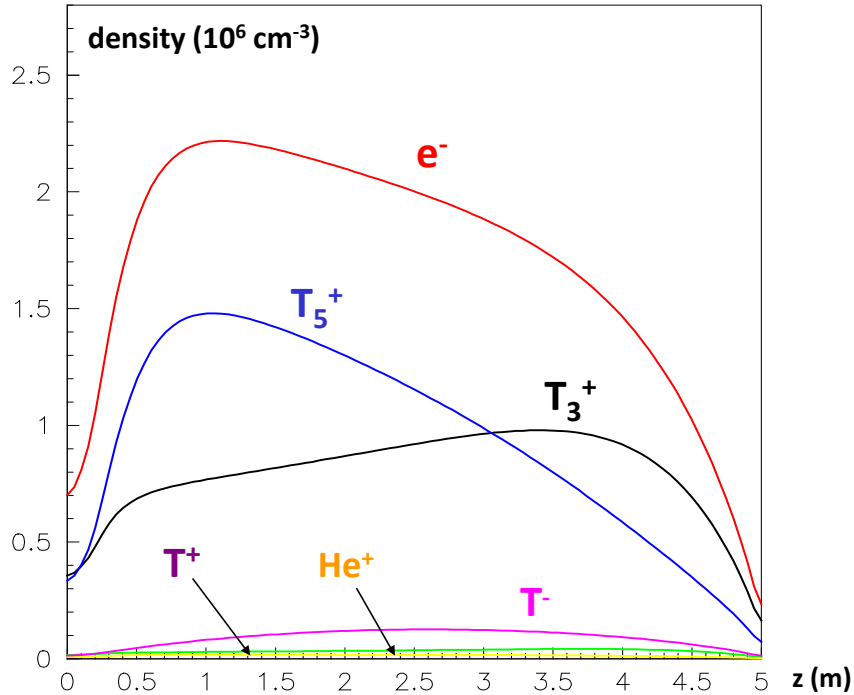


Figure 4.1: **Ion and electron density in WGTS**

The density of electrons and the most important ion species in the WGTS over the length measured for the injection point in m. Source [Glu10].

with the ion-flux  $I_0$  and the live time  $\tau$  of ions in the DPS2-F. This equation is solved by the ansatz:

$$Q(t) = I_0 \tau \left(1 - e^{-\frac{t}{\tau}}\right) \quad (4.15)$$

As can be seen, the charge density rises continuously for large values of  $\tau$  and stays on a constant level for small of  $\tau$ . Our calculations call for a value of  $\tau$  to be smaller than 10 seconds, to avoid a significant build-up of space charge [Win11]. Studies on the expected mean live-time of ions in the DPS2-F beam line are presented in section 4.3.2.

#### 4.1.2.5 Impact of Ions on Neutrino Mass Measurement

If we would neglect the ion formation within the source volume, thus allowing for the build-up of higher ion densities, it would be necessary to account not only for a build-up of space charge but also for  $\beta$ -electrons emitted from ions. These would differ significantly in terms of end-point energy, thus imposing a systematic error onto the KATRIN measurements.

In table 4.3 the endpoint energies for relevant ions and charged clusters are presented. It is obvious that the  $T^-$  ions entail the greatest threat, given their

Table 4.3: **Electron Energies from ionized  $\beta$ -Sources**

Estimated endpoint energies of charged tritium species.  $\Delta Q$  is always given relative to the  $Q$ -value of a standard molecular  $T_2$  decay. Sources: [KAT04], [Tit03]

ion/cluster type	Energy $\Delta Q$
T atomar	-8.1 eV
$T^+$	-48.9 eV
$T_2^+$	-32.4 eV
$T_3^+$	-18.6 eV
$T^-$	+15.7 eV

ability to emit electrons with energies above the molecular end point energy to be measured by KATRIN.

Studies carried out by the Collaboration [KAT04] show that the relative concentration of  $T^-$  with regard to  $T_2$  must be kept below a ratio of  $10^{-6}$  in order not to cause a systematic error larger than  $\Delta m_\nu^2 = 0.01 \text{ eV}^2$ .

In a conservative approach, using a  $T^-$ -flux of 2 nA, an integral tritium amount of  $5 \times 10^{19}$  molecules, and tightening the concentration requirements down to  $\leq 10^{-8}$ , we calculate a maximum survival time for the  $T^-$  ions in the order of 10 s (see section 4.3.2).

## 4.2 Gasflow in DPS2-F

Inside the DPS2-F beam tube there is a pressure gradient from the entry value of  $10^{-3}$  mbar to the  $10^{-9}$  mbar exit level. In a pressure range below  $10^{-3}$  mbar the Knudsen number is sufficiently low to assume free molecular flow in first approximation [Wut10]. Two different approaches for the estimation of gas flow will be shown in the following two subsections.

### 4.2.1 Flow via Calculation of Conductances

Calculations based on the macroscopic quantity of the conductance offer a rather fast approach to estimate the gas flow suppression factor of DPS2-F. For this reason, the vacuum design of the DPS2-F was based on this method [Bon03]. The terms used below were briefly introduced in section 3.2.1. In the case of the beam tube elements of DPS2-F we can make the following assumptions concerning the gas flow reduction.

According to [Wut10], the conductance of a constructional element is given by the product of an orifice with the same clearance  $C_O$  and the passing probability  $P$ :

$$C = C_O \cdot P. \quad (4.16)$$

The passing probability for a circular tube follows from

$$P = \frac{14 + 4\frac{l}{d}}{14 + 18\frac{l}{d} + 3\left(\frac{l}{d}\right)^2} \quad (4.17)$$

for a pipe of the length  $l$  and the diameter  $d$ . In the case of a long pipe ( $l \gg d$ ) the formula is simplified to

$$P = \frac{4d}{3l}. \quad (4.18)$$

The orifice conductance is given by the relation

$$C_O = \frac{\bar{v}}{4} \cdot A \quad (4.19)$$

with the clearance area  $A$  and the mean particle velocity  $\bar{v}$ . The dependence of  $C_O$  from temperature  $T$  and the particle mass  $m_p$  is proportional to

$$C_O \propto \sqrt{\frac{T}{m_p}}. \quad (4.20)$$

To calculate the gas flow suppression capability of DPS2-F, we consider four equivalent pumping stages, each being a combination of a pump port, a linear (pipe) beam tube segment, and a pump duct with attached TMP. The conductance  $C_T$  of each beam tube segment can be approximated by a single, long,

and circular tube with inner diameter  $d_{\text{eff}}$ <sup>5</sup>. The pump-duct-approximation is more complicated and schematically shown in figure 4.2. The geometry there features three separate segments and the effective pumping speed is calculated for the point in the pump duct, where the effective capture factor of the pump will be measured later on (cf. section 6.5.2).

First, the passing probability  $P$ , depending on the entrance areas  $A_i$  for the three pump duct segments has been calculated via [Wut10]

$$P_{1,N} = \left( A_1 \cdot \sum_{i=1}^N \frac{1}{A_i} \cdot \left( \frac{1}{P_i} - 1 \right) + \sum_{i=1}^{N-1} \left( \frac{1}{A_{i+1}} - \frac{1}{A_i} \right) \cdot \delta_{i,i+1} + 1 \right)^{-1}. \quad (4.21)$$

with  $\delta_{i,i+1} = 1$  for  $A_{i+1} < A_i$  and  $\delta_{i,i+1} = 0$  otherwise. Afterwards the effective conductance of the whole duct was calculated. In combination with the pumping-speed this renders the pumping-speed perceived at the pump port  $S_{\text{PP}}$  through

$$S_{\text{PP}} = \left( \frac{1}{S_{\text{eff}}} + \frac{1}{C_{\text{duct}}} - \frac{4}{\bar{v} \cdot A_{\text{duct}}} \right)^{-1}. \quad (4.22)$$

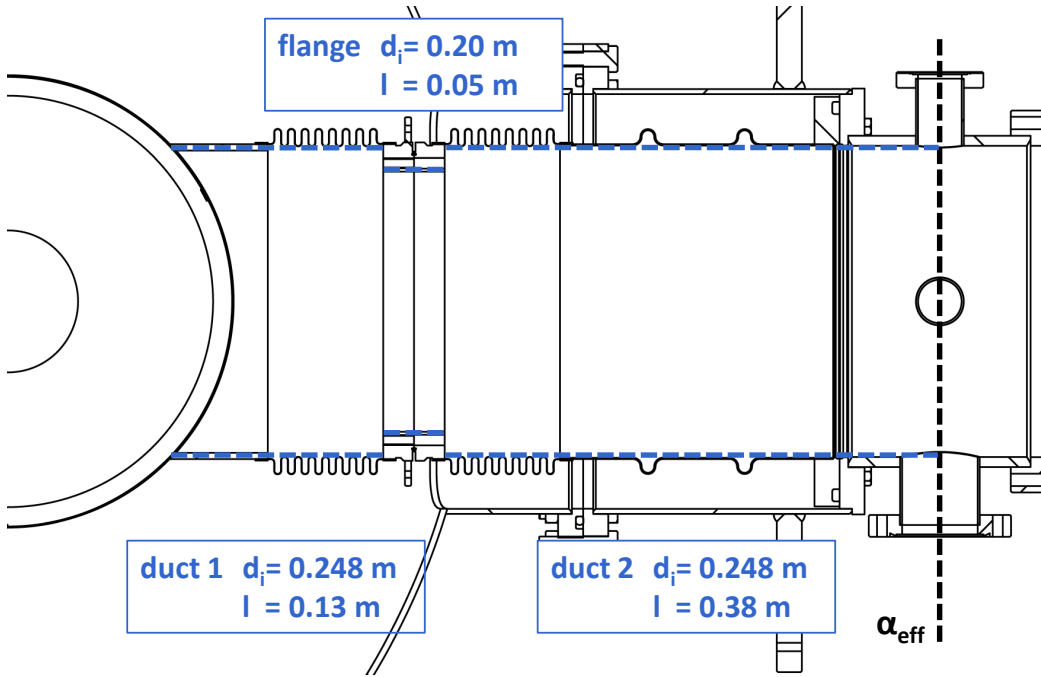


Figure 4.2: **Pump Duct DPS2-F for Calculation of Conductance**  
Highlighted in blue are the approximations for the parts. The inner diameters are 248 mm for the bellows and pipes and 200 mm for the connector flange. Marked in dashed black is the effective pumping area.

<sup>5</sup>In case of a DPS2-F beam tube element the geometrical diameter would have to be reduced due to the bellow in the middle of the beam tube segment but also enlarged due to the large cones at the entrances of the tube. We therefore assume therefore  $d_{\text{eff}} = d_{\text{geo}} = 0.086$  m.

The gas flow suppression capability  $X$  for each stage is then given by

$$X = \frac{S_{PP} + C_T}{C_T} \quad (4.23)$$

and the overall reduction factor calculated through conductances  $R_C$  of the DPS2-F is thus the combination of the four elements via

$$R_C = X^4 \quad (4.24)$$

neglecting backstreaming into WGTS (which can be incorporated in the suppression factor for DPS1-F). The calculated values are summarized in table 4.4. The formulas are only valid for a uniform temperature; see section 4.2.3 for a discussion on temperature influences.

The values in table 4.4 are in good agreement with the estimates carried out in [Bon03] and [Luo06a], taking into account the increase in beam tube diameter due to design changes since then.

The study of the vacuum characteristics of DPS2-F via the method of macroscopic quantities such as the conductance is highly sensitive to variations of the actual geometry and therefore is perfectly suited for general design-strategies. Especially complex components like bellows and valves, but also the non-trivial geometry of the segments and pump-ports complicate the calculations, however. An alternative and usually more accurate approach is offered by microscopic Monte-Carlo-Simulations which will be introduced in the following section.

Table 4.4: **Conductances DPS2-F**

Given are the calculated values that are relevant for the conductance-based calculations of the reduction factor of DPS2-F given for  $T_2$  at room temperature.

<b>Component</b>	$l$ [m]	$d_{\text{eff}}$ [m]	$P$	$C$ [ $\text{ls}^{-1}$ ]
1. duct	0.13	0.248	0.664	8152.2
flange	0.05	0.2	0.803	6413.9
2. duct	0.38	0.248	0.414	5086.2
total pump duct	-	-	0.261	3201.0
TMP	-	-	0.196	2405.0
beam tube	1.07	0.086	0.091	134.1
	$S_{PP}$ [ $\text{ls}^{-1}$ ]	$X$	$R$	
pumping stage	1546.0	12.53	$2.46 \times 10^4$	



### 4.2.2 Flow via Single Molecule MC Simulations

A microscopic approach to solving the flow characteristics of DPS2-F is based on the simulation of single molecule trajectories using Monte Carlo methods. Single particle simulations are usually only valid for high vacuum i.e. regimes with free molecular flow and sufficiently high Knudsen-Number (no collisions between gas particles). This method has been used for over 40 years [Smi66] and is subject to constant development. Commonly used today is the MOLFLOW+ code [Ker09]. The underlying principles are:

- Straight trajectories are assumed for each injected, reflected or diffused particle. The surface from which the particle departs has no influence on further tracking.
- The direction of each starting particle is fixed by randomly choosing parameters  $X$  and  $Y$  that render the particles spherical start angles via

$$\theta = \arccos\left(\sqrt{1-X}\right) \quad \text{and} \quad (4.25)$$

$$\phi = 2\pi Y. \quad (4.26)$$

$X$  and  $Y$  are chosen from the Interval  $[0,1]$ , thus forming an isotropic spherical distribution as shown in figure 4.3.

- The vacuum containment to be investigated needs to be discretized. Usually this task is based on CAD models which are transformed into a mesh

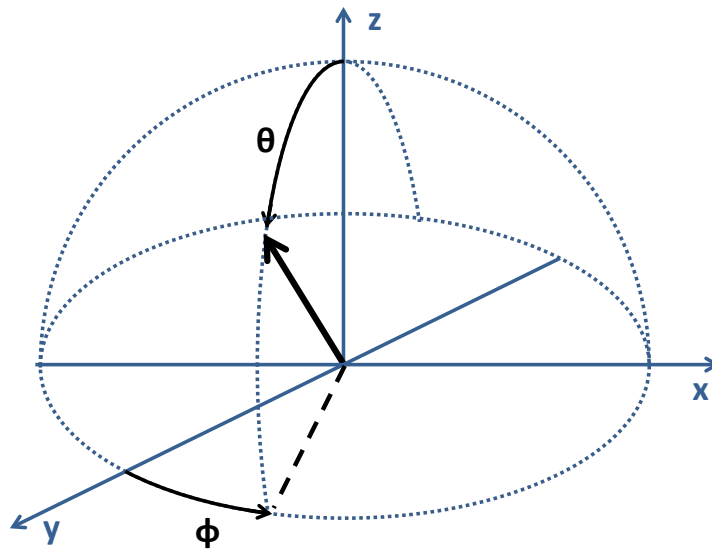


Figure 4.3: Angular distribution simulated particles

of polygonal facets. The fidelity of this discretization is crucial for the quality of the later simulation. On the other hand a too high granularity leads to excessive computing times.

- The most important question usually is: On which surface areas do the simulated particles leave the vacuum systems? Usually these surfaces represent inlet or outlet flanges or pumps. For a realistic simulation those surfaces are parametrized by a capture factor  $\alpha$  ( $\alpha \in [0, 1]$ ). This capture factor is usually not known a priori, hence these simulations go hand in hand either with a direct measurement of  $\alpha$ , or conductance-based calculations.

In a system like DPS2-F the question at hand is: what flow rates are to be expected at the outlet with respect to the flow at the inlet? These two surfaces together with the four TMPs leave us with the study of transport probabilities between six relevant surfaces. A priori the simulations are carried out for either an assumed capture factor of the pumps, or (as will be shown exemplarily in section 4.2.4) for a whole range of values for  $\alpha_{\text{TMP}}$ .

The transport probabilities between an ensemble of  $n$  surfaces are usually given by an  $n \times n$ -Matrix  $\mathbf{W}$ . The single entries of  $\mathbf{W}$  are defined by

$$w_{i,j} = \frac{A_i}{G_j} \quad (i, j \in \{1, \dots, n\}) \quad (4.27)$$

with  $A_i$  denoting the number of particles absorbed (eliminated) on surface  $i$ , and correspondingly  $G_j$  the number of those generated (started, reflected) on surface  $j$ . Obviously the sum over all elements  $w_{i,j}$  needs to be normalized to unity. Also, the net flow rate over all boundaries is zero.

We now define the net flow  $Q_i$  emitted from surface  $i$  into the volume through the injected flow  $s_i$  less the captured (i.e. not reflected) part  $\alpha_i$  of the incoming flow  $f_i$ .<sup>6</sup>

$$Q_i = s_i - \alpha_i f_i \quad (4.28)$$

Since the injection rates  $s_i$  and the capture factors  $\alpha_i$  are known parameters, we need to investigate the parameters  $f_i$  as follows.

Using the entries of the transport matrix we can describe the incoming flow by

$$f_i = \sum_{j=1}^n w_{i,j} (s_j + (1 - \alpha_j) f_j) \quad (4.29)$$

which yields a system of  $n$  equations for  $n$  unknown values and hence can be solved exactly.

---

<sup>6</sup>Note, that we neglect desorption in this case. Otherwise, the desorption flow can be included in  $f_i$ .

Applying these relations and quantities to the DPS2-F setup we have to consider

- Six relevant surfaces:  $n = 6$
- Injection solely from surface 1:  $s_1 = s$ ,  $s_{2,3,4,5,6} = 0$
- No reflection of incoming gas at the entrance  $\alpha_1 = 1$ , equivalent capture factors at the TMP-surfaces  $\alpha_{2,3,4,5} = \alpha$ , and a fixed, yet to be experimentally determined capture factor of the (CPS-) surface 6: ( $0 < \alpha_6 = \alpha_{\text{CPS}} < 1$ )

For the reduction factor  $R_{\text{MC}}$  of DPS2-F we thus obtain the relation:

$$R_{\text{MC}} = -\frac{Q_6}{s - f_1} = \frac{\alpha_{\text{CPS}} \cdot \left( s + \sum_{j=2}^6 w_{6,j} (1 - \alpha_j) f_j \right)}{s - f_1} \quad (4.30)$$

Note that these considerations are completely temperature-independent (see section 4.2.3), and that for real predictions of the DPS2-F reduction factor the effective capture-factors of the TMPs and of the CPS are yet to be determined. Predictions over a wide parameter range of the parameter  $\alpha$  can be found in section 4.2.4.

For the KATRIN beamline the MOVAC3D code, developed at the Institute of Technical Physics at KIT, was used [Luo06a].

## 4.2.3 Temperature Dependence

### 4.2.3.1 Conductance vs Monte Carlo

The seeming discrepancy between the thermal dependence of the reduction-factor  $R_{\text{C}}$  for conductance-based calculations and  $R_{\text{MC}}$  obtained by non-thermal-dependent MC simulations is to be explained as follows:

MC simulations focus solely on the transport probabilities of individual particles. The codes in use do not examine the transport velocities. Calculations of conductances however inquire how much volume is being transported per unit time. In the case of falling temperatures the gas particles lose velocity, hence the conductances fall, and the trajectories imposed by MC are paced in longer time spans.

For reduction factors (i.e. ratio number of particles in to number of particles out) of interest here, transport velocities are irrelevant. For the MC method this is quite obvious since the principles presented in section 4.2.2 do not change with temperature. Nevertheless, calculations based on conductance are also still valid if we focus on the number of particles and not on the  $pV$ -flow.

In free molecular flow and a system with different local temperatures particle densities and pressure experience *thermal transpiration* [Wut10] leading to:

$$\frac{n_1}{n_2} = \sqrt{\frac{T_2}{T_1}} \quad \text{and} \quad \frac{p_1}{p_2} = \sqrt{\frac{T_1}{T_2}} \quad (4.31)$$

implying that in the colder area the pressure drops and the particle density rises with  $\sqrt{T}$ .

As shown in section 4.2.1 the conductance falls with  $\sqrt{T}$  as well and the  $pV$ -flow  $Q$ , that is defined by

$$Q = C \cdot p \quad (4.32)$$

falls proportional to  $T$ . If we now consider the basic fundamentals of gas-theory we find the correlation between particle numbers and  $pV$ -amount to

$$N = \frac{p \cdot V}{k_B \cdot T} \quad (4.33)$$

which is inversely proportional to  $T$ , thus canceling out evenly the reduction in  $pV$  transport.

The calculations of conductance thus do remain valid for all experimentally relevant changes in temperature or temperature gradients along the system to first order.

#### 4.2.3.2 Temperature effects on Pumping

In the case of the DPS2-F cryostat, the beam tube is thermally decoupled from the TMPs that stay at room temperature. The capture factor of the pumps should therefore be stable for all beam tube temperatures. Considering however the basic principles of gas flow reduction via turbo-pumping, as presented above in section 3.2.3, we nevertheless found the capture factor of the pump to be dependent on the gas temperature when entering the rotor-stator volume of the pump (cf. equation 3.12).

It can be assumed that a certain amount of the tritium gas propagating from the DPS2-F beam tube to the pump is not yet thermalized when entering this volume. This effect will lead to a direct increase of  $\alpha_{\text{TMP}}$  and an increase in the reduction factor  $R_{\text{C,MC}}$  (this fact holds for calculations based on conductance and for MC simulations). The extent and thus the importance of this effect, however, is difficult to quantify. None of our available models offers a local distribution of the gas velocity. Nonetheless, even very conservative estimations of a 5% increase in  $X$  would enlarge the reduction factor by over 20%.

To answer these more advanced questions further experiments on the gas flow characteristics with the DPS2-F at operational temperatures have to be carried out.

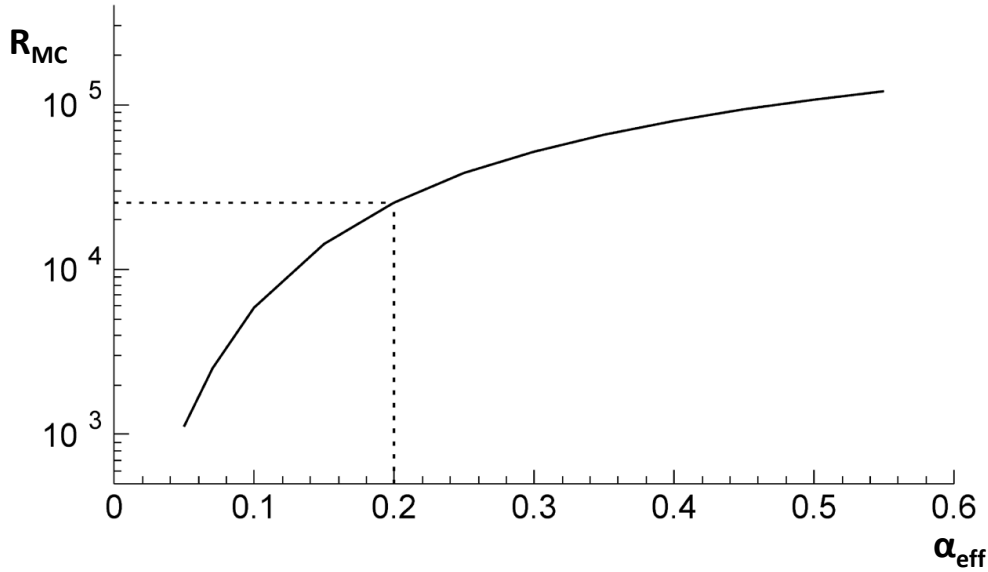


Figure 4.4: **Results of Reduction Factor Simulations**

Based on the updated (as delivered) symmetries and carried out with MOLFLOW+. The dashed lines indicate the expected value for tritium. Source [Luk12]

#### 4.2.4 Calculations for different Gases

Before reporting on the direct measurements of the gas flow reduction factor (see chapter 6) it is useful to calculate first the expected values. Figure 4.4 shows the results of the latest simulations carried out for the DPS2-F beam tube and pumping system (featuring all hitherto geometry modifications). The figure displays the expected reduction factor for tritium as a function of the later on measured capture factor of the TMPs  $\alpha_{\text{eff}}$ . The simulations were carried out using the above described MOLFLOW+ code [Luc00].

The curve highlights the strong dependence of  $R_{\text{MC}}$  on the parameter  $\alpha_{\text{eff}}$ .

During the initial experimental test campaign with the DPS2-F cryostat, the  $\beta$ -active tritium gas was not available due to the regulations applying to this specific isotope. Several other gas species, including hydrogen isotopologues, were used instead (see chapter 6).

In table 4.5 values for the pumping-speed  $S_{\text{PP}}$ , the stage reduction  $X$ , and the DPS2-F reduction factor  $R$  for the relevant test gases are given. These calculations were conductance-based at room temperature, as described above in section 4.2.1. In this case, the values for the pumping speeds are not estimated but taken from measurements (see section 6.5.2).

Table 4.5: **Calculation for Testgases DPS2-F**

The values for the pumping-speed  $S_{PP}$ , the stage reduction  $X$ , and the DPS2-F reduction factor  $R$  have been obtained by conductance-based calculations for the relevant test gases at room temperature.

<b>Testgas</b>	$S_{PP}$ [ $\text{l s}^{-1}$ ]	$X$	$R$
He	2440	10.28	$1.12 \times 10^4$
D <sub>2</sub>	2368	10.11	$1.04 \times 10^4$
Ne	2074	22.07	$2.37 \times 10^5$
Ar	1672	28.49	$6.59 \times 10^5$
Kr	1336	37.88	$2.06 \times 10^6$

## 4.3 Ion Flux in DPS2-F

### 4.3.1 Ion detection using FT-ICR

The ion concentration and the composition of the ion flux can be measured on a near-on-line basis using Fourier Transform-Ion Cyclotron Resonance (FT-ICR) devices. These units, developed at the Max-Planck-Institute for Nuclear Physics at Heidelberg, Germany, discriminate ions by detecting differences in Ion Cyclotron frequencies as they occur in the strong B-fields (values around 5 T) governing the KATRIN beamline, as described in section 3.4.1.

#### 4.3.1.1 Ion Cyclotron Frequencies

Figure 4.5 shows the schematic setup of a Penning trap, which is a central design feature of these FT-ICR units. To understand the ion cyclotron frequency and its experimental measurement, the fundamental relations governing the equations-of-motion of trapped particles need to be investigated (the following summarizes works by [Bro86] and [Ubi11]).

Assuming a hyperbolic trap (as shown on the left side of figure 4.5), the potential  $V$  can be written in cylindrical coordinates by

$$V(\rho, z) = \frac{U}{2d^2} \left( z^2 - \frac{\rho^2}{2} \right) \quad (4.34)$$

where  $U$  denotes the trapping potential and  $d$  is the trapping scale defined by

$$d = \frac{1}{2} \left( z_0^2 + \frac{\rho_0^2}{2} \right). \quad (4.35)$$

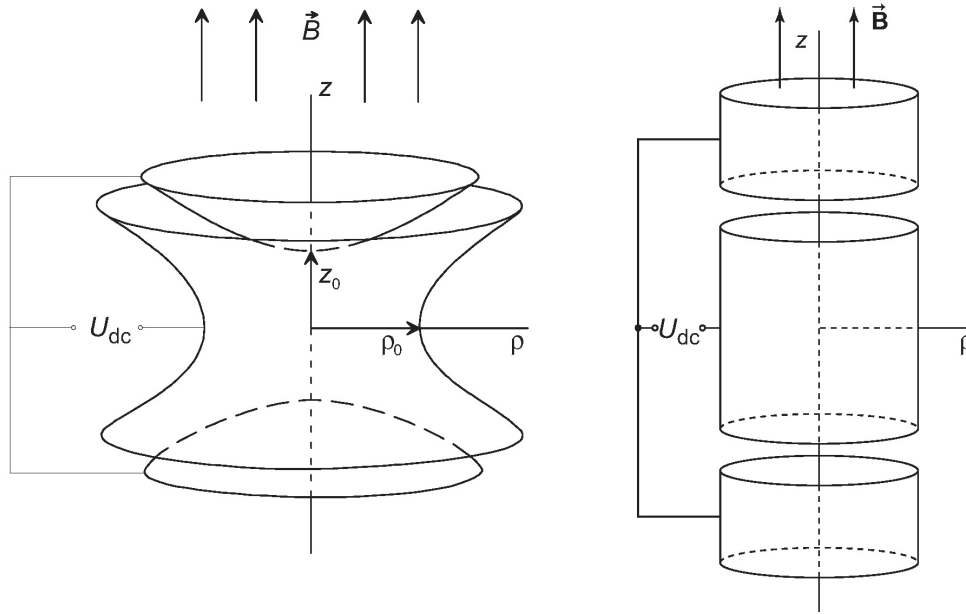


Figure 4.5: **Schematic Penning Trap**

A hyperboloidal Penning trap (left picture) and cylindrical Penning trap (right side) taken from [Bla06]. The  $\vec{B}$ -field is purely in  $z$  direction providing the radial confinement. The endcaps are set to a potential providing the axial confinement.

In this case,  $z_0$  and  $\rho_0$  denote the shortest distance from the trap center to the end caps and the ring electrode. With the Lorentz-force

$$\vec{F}_L = q \left( \vec{E} + \vec{v} \times \vec{B} \right) = q \left( -\vec{\nabla}V + \vec{v} \times \vec{B} \right) \quad (4.36)$$

we gain the differential equations

$$\begin{aligned} \ddot{x} &= \frac{qU}{2md^2} x + \frac{qB}{m} \dot{y} \\ \ddot{y} &= \frac{qU}{2md^2} y - \frac{qB}{m} \dot{x} \\ \ddot{z} &= -\frac{qU}{md^2} z \end{aligned} \quad (4.37)$$

Combining and solving these equations<sup>7</sup> leaves us with four frequencies of physical meaning: the already introduced pure cyclotron frequency  $\omega_c$  (cf equation 3.37), the axial oscillation frequency  $\omega_z$  defined by

$$\omega_z = \sqrt{\frac{qU}{md^2}} \quad (4.38)$$

<sup>7</sup>We use the complex variable  $u = x + iy$  to acquire  $\ddot{u} + i\omega_c\dot{u} - 1/2\omega_z^2U = 0$ . The solvability to non-imaginary values gives boundary conditions for the trap design (see [Bro86]).

and the eigen-frequencies  $\omega_{\pm}$  defined by

$$\omega_{\pm} = 1/2 \left( \omega_c \pm \sqrt{\omega_c^2 - 2\omega_z^2} \right). \quad (4.39)$$

The eigen-frequency  $\omega_-$  denotes the frequency of circular magnetron motion in the  $x$ - $y$ -plane of the trap, and the eigen-frequency  $\omega_+$  denotes the modified cyclotron frequency (which will actually be measured later on). They can be approximated as

$$\omega_- = \frac{U}{2d^2B} \quad \text{and} \quad \omega_+ = \omega_c - \frac{U}{2d^2B}. \quad (4.40)$$

The trajectory of the trapped ions is thus defined by the superposition of the axial oscillation ( $\omega_z$ ), the magnetron drift ( $\omega_-$ ) and the modified cyclotron motion ( $\omega_+$ ).

#### 4.3.1.2 Excitation and detection

There are numerous ways to excite and detect ion clouds trapped in an electrode system. We will focus below on the dipolar excitation using narrow frequency bands and the detection via the induced image charge. The schematic setup is shown in figure 4.6. When the driving field is oriented in  $x$ -direction it is defined by

$$\vec{E}_x = \frac{U_d}{a} \cos(\omega_d t + \phi_d) \vec{e}_x \quad (4.41)$$

with the driving voltage  $U_d$ , the electrode radius  $a$ , the excitation frequency  $\omega_d$  and the phase constant  $\phi_d$ .

The phase constant is responsible for the breaking of isotropic symmetry in the  $x$ - $y$ -plane. The phase shift between circulating ions and the excitation field forces the ions to bundle up laterally into a localized charge cloud circling the main axis.

The excitation frequency  $\omega_d$  can - with the use of advanced Fourier-Transformation-electronics - be narrow-banded to excite only a specific ion-species, or be broad-banded [Mar98].

After a characteristic excitation time ( $\sim B/U$ ; of the order of ms) the ion bundle is well focused ( $\omega_+ \approx \omega_c$ ) and circles within the trap volume. This circling induces image charges on the detection electrodes, which can be approximated via

$$\Delta Q = 2q \frac{\cos(\omega t) r}{a}. \quad (4.42)$$

When differentiating with respect to time we obtain the image current as

$$I = \frac{d\Delta Q}{dt} = -2 \frac{qr\omega}{d} \sin(\omega t). \quad (4.43)$$

The induced image current can then be amplified and further be analyzed after Fourier transformation to frequency space.



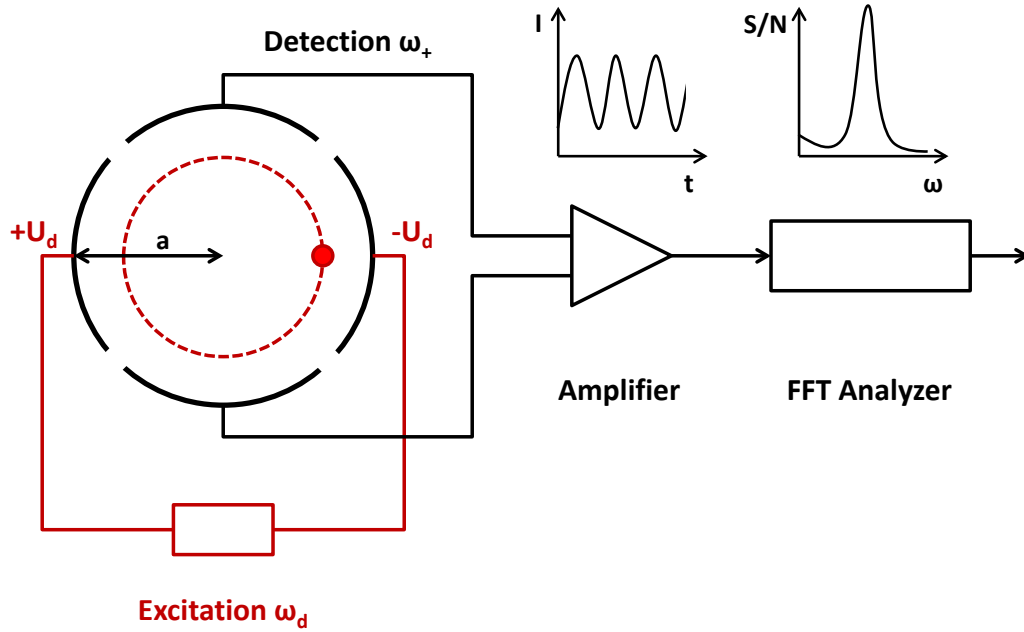


Figure 4.6: **Schematic Ion Excitation and Detection**

Shown is a schematic setup of an FT-ICR analysis using dipolar excitation. The function generator (excitation circuit in red on the bottom) stimulates the chosen characteristic frequencies. After excitation the cyclotron frequencies are detected and transformed (analysis circuit in black on the right). Based on [Ubi11].

### 4.3.2 Ion suppression with Dipole Electrodes

While the FT-ICR units provide excellent monitoring and analysis capabilities, they do not eliminate the trapped ions in the beam line. This can only be achieved by an  $\vec{E} \times \vec{B}$ -drift (as briefly introduced in section 3.4.2) that should, however, not influence the high-energy signal electrons.

To derive an understanding of the  $\vec{E} \times \vec{B}$ -drift principle, we start out again with the Lorentz force of an  $\vec{E}$ -field (see equation 4.36). The magnetic field is assumed to be directed purely in  $z$ -direction, while the electric field shall be free in all three dimensions. We obtain the differential equations

$$\begin{aligned}
 m\ddot{x} &= qE_x + qyB \\
 m\ddot{y} &= qE_y + qxB \\
 m\ddot{z} &= qE_z
 \end{aligned}
 \tag{4.44}$$

which can be solved by

$$\begin{aligned}
 x(t) &= \frac{v_{\perp} m}{qB} \sin\left(\frac{qB}{m}t\right) + \frac{E_y}{B}t + x_0 \\
 y(t) &= \frac{v_{\perp} m}{qB} \cos\left(\frac{qB}{m}t\right) - \frac{E_x}{B}t + y_0 \\
 z(t) &= \frac{qE_z}{2m}t^2 + v_{\parallel}t + z_0
 \end{aligned} \tag{4.45}$$

with  $v_{\parallel}$  and  $v_{\perp}$  defined by their orientation with respect to the magnetic field (i.e. to the  $z$ -axis). Within these equations of motion we can identify the gyration motion with the cyclotron-frequency  $\omega_c = \frac{qB}{m}$  (given by the first terms in equation array 4.46), but also an additional term causing motion in the  $x$ - $y$ -plane. These additional terms cause an  $\vec{E} \times \vec{B}$ -drift which can be described as

$$\vec{v}_{\text{drift}} = \frac{1}{|\vec{B}|^2} \vec{E} \times \vec{B}. \tag{4.46}$$

This drift is not influenced either by the particle mass, the sign of particle charge or the particle motion with respect to either field. The drift is solely proportional to the strength of the electric field and inversely proportional to that of the magnetic field. The strength  $|\vec{B}|^2$  of the  $\vec{B}$ -field in our scenario is fixed, so we can only adjust the electric field strength within some boundaries.

Let us now reconsider the case of through-formed dipole electrodes, as proposed in section 3.4.2, to establish this drift-generating  $\vec{E}$ -field. By solving for this special capacitor geometry<sup>8</sup> we find the correlation between field and voltage in the middle of the beam tube to be

$$E = \frac{2.6}{r_D} U_D. \tag{4.47}$$

with the dipole voltage  $U_D$  and the dipole-electrode radius  $r_D$ . The quality factor of this ion-suppression technique is given by the time required to eliminate ions from the beam line. First we calculate the sojourn-time  $\tau_D$  of an ion in the respective area of length  $L_D$  through

$$\tau_D = L_D \sqrt{\frac{m_{\text{ion}}}{q U_D}} \tag{4.48}$$

assuming  $q U_D \gg E_{\text{kin}}$  (i.e. ion at rest before acceleration). The dislocation  $R$  of the ion after passing the electrode is then given by

$$R = v_{\text{drift}} \tau_D = \frac{2.6 \cdot L_D}{r_D \cdot B} \sqrt{\frac{m_{\text{ion}} U_D}{q}}. \tag{4.49}$$

---

<sup>8</sup>We have to solve  $U = \int \vec{E}(\vec{r}) d\vec{r}$  for a cylindrical capacitor setup with the inner electrode only covering  $120^\circ$ .

If we define the length of the ion trajectory in the azimuthal and radial plane from its starting point to the boundaries of elimination (see section 5.1.3.2)  $b$ , we find the important elimination time  $\tau_{\text{elim}}$  to be

$$\tau_{\text{elim}} = \frac{b}{v_{\text{drift}}} = b \cdot B \frac{r}{2.6U_{\text{D}}} = n \cdot L_{\text{D}} \sqrt{\frac{m_{\text{ion}}}{qU_{\text{D}}}}. \quad (4.50)$$

with  $n$  denoting the number of passings through the dipole-section which are calculated through  $b = \lambda/L_{\text{D}}$  with the mean free path length  $\lambda$ .

These calculations are strongly simplified to clarify the fundamental principles. In particular the assumption of the ions propagating only in the middle of the beam tube does not hold for the real ion load. Therefore, extensive simulations of ion trajectories have been carried out in the framework of KASSIOPEIA [Win11].

The estimated correlation  $\tau \propto U_{\text{D}}^{-0.5}$  was simulated and fitted against  $\tau = a \cdot U_{\text{D}}^b$ . The simulated values come close to the assumed ones in the simplified assumptions and are given in table 4.6. The characteristic elimination times, the number of transits and the resulting build-up of space-charge are also presented for various ion species.

As a result of these estimations it is obvious that our dipole proposal for ion suppression meets the necessities of KATRIN, as presented in section 4.1.2.4. The life time of ions is expected to be smaller than 20 ms, which is a factor 500 shorter than the (conservatively estimated) upper limit of 10 s.

Table 4.6: **Ion Suppression in DPS2-F**

The fit-parameters for  $\tau = a \cdot U_{\text{D}}^b$ , the mean free path length  $\lambda$ , the elimination time  $\tau$ , the number of transits and the resulting build-up of space-charge  $U_{\text{SC}}$  in the middle of the beamline for the most relevant ions are calculated for a dipole voltage of 100 V. The results are taken from [Glu10],[Win11].

ion species	a	b	$\lambda$ [m]	$\tau$ [ms]	n	$U_{\text{SC}}$ [mV]
${}^3\text{He}^+$	211	-0.59	14.95	6.73	13.87	-1.03
$\text{T}^+$	215	-0.60	15.01	6.76	13.98	-4.17
$\text{T}_3^+$	217	-0.58	8.91	4.01	15.27	-86.55
$\text{T}_5^+$	220	-0.60	6.67	3.00	14.30	-27.72



# Chapter 5

## The Transport Section

The major importance of a highly efficient transport section for the KATRIN experiment, as well as the theoretical foundations for the tritium and ion-suppression and suitable techniques have been established in the previous sections. Now we discuss the large-scale application of these techniques in the KATRIN beamline. The two cryostats DPS2-F and CPS forming the KATRIN transport section have been contracted to an industrial partner, ASG Superconductors<sup>1</sup>. A detailed description of the DPS2-F and CPS, specifically from a machine-physics point of view, will be presented in this section.

### 5.1 Differential Pumping

The DPS2-F is the second module of the Source and Transport Section (STS) of the KATRIN experiment. As mentioned previously, the DPS1-F and the DPS1-R are mechanically included in the WGTS module. The DPS2-F cryostat is 6.96 m long, and features a cascaded differential pumping system with four large turbo-pumps plus support pumps, a fourfold buckled beam line, and a superconducting magnet system to guide the signal electrons towards the CPS and the spectrometer sections.

The operating temperature of the beamtube is 77 K, while the turbo pumps, which are mounted on pump ducts on the outside of the vacuum vessel, are operated at room-temperature.

The DPS2-F module was originally designed to reach a tritium flow reduction factor of  $R \approx 1 \times 10^5$ . Due to redesign issues (extension of beam tube diameter) this factor currently only reaches a value of  $\approx 2.5 \times 10^4$ .

The cryostat was the first KATRIN main component of the STS that was successfully commissioned in 2010/11. The following section will introduce this main component and describe the most important technical issues based on [KAT04],[Noe03] and assessments performed in the framework of this thesis.

---

<sup>1</sup>ASG Superconductors S.p.A., C.so F. M. Perrone 73r, 16152 Genova, Italy

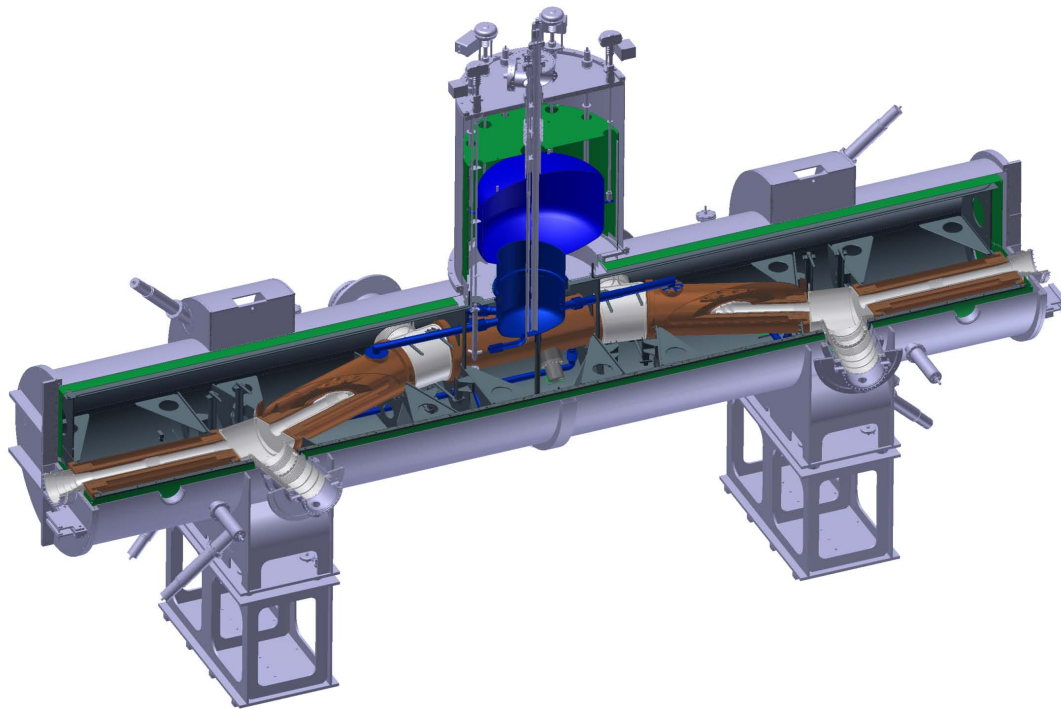


Figure 5.1: **The DPS2-F**

Shown is a quarter cut through the DPS2-F cryostat. The tritium flow and signal electron trajectories are directed from left to right. Within the radiation shield (green) the liquid helium cooling system (blue) and the magnet system (brown) partially surrounding the beam tube itself (silver) can be seen.

## 5.1.1 Vacuum Design

### 5.1.1.1 Beam Tube Design

The DPS2-F beam tube consists of five beam tube segments with overall length of 1070 mm each. Single elements are manufactured from welding together two identical straight sections with an inner diameter of 86 mm and one bellows in between, to compensate for contractions during the cool-down. The bellows are 90 mm long and have an inner diameter of 81 mm. Between the five tube segments, four pumping ports are installed. The pumping ports are cylindrical chambers and cut wedge-shaped, which results in the desired 20° buckling between the tube segments. The four main turbo molecular pumps are attached to DN 250 CF flanges, which are connected to the pumping chambers via pump ducts of 670 mm length and 250 mm diameter. The geometry of the DPS2-F beam tube alignment is shown in figure 5.2

Large VAT gate valves are installed before the TMPs to disconnect the beam tube from the outer vacuum system. The considerable length of the pump ducts was chosen to minimize the effect of thermal radiation from the pumps

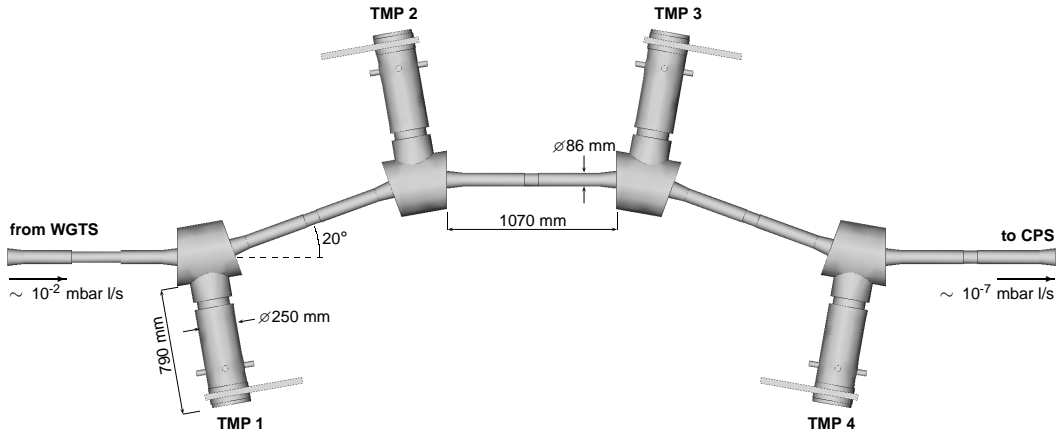


Figure 5.2: **The DPS2-F beam tube**

Shown is the beam tube and the four pump ports forming the inner vacuum-system and primary tritium containment.

(which are operated at room-temperature) onto the beam tube (which is kept at 77 K) and to minimize the magnetic field strength at the location of the TMPs. This is important, as the (electrically conductive) rotor of the TMPs will heat up due to induced eddy-currents, if operated in high fields (see section 5.1.1.3 and [Jan12] for further information).

To further weaken the thermal coupling, the pump ducts are constructed in a double-walled manner with the inner wall coupled to the outer flange through two 112 mm long bellows connected by a flange of 207 mm inner diameter.

All beam tube components (except the bellows) are manufactured from austenitic 316L steel (see appendix A.6). The integral leak tightness was required to be  $\leq 10^{-8}$  mbar l s<sup>-1</sup>. This value was met, as proven during commissioning, thus performed in the framework of this thesis.

### 5.1.1.2 TMPs and Differential Pumping

The primary pumps used at the DPS2-F beam tube (cf. figure 5.2) are four TURBOVAC MAG W 2800 DN 250 CF by Leybold Vacuum<sup>2</sup>, one at each pump port. The experimentally obtained final pressure of  $\approx 6 \times 10^{-10}$  mbar came close to the manufacturer-claimed final pressure of  $10^{-10}$  mbar. Important TMP parameters such as pumping-speed and other characteristics were investigated as part of this thesis (see chapter 6).

To implement the desired cascaded pumping setup (cf. section 3.2.3) and greater compression ratios for each stage, the outlet of the downstream turbopumps is connected to the pump duct of an upstream pump. The outlet of TMP #3 was then connected to the inlet of TMP #1, and the outlet of TMP

<sup>2</sup>Oerlikon Leybold Vacuum GmbH, Bonner Strasse 498, 50968 Cologne, Germany

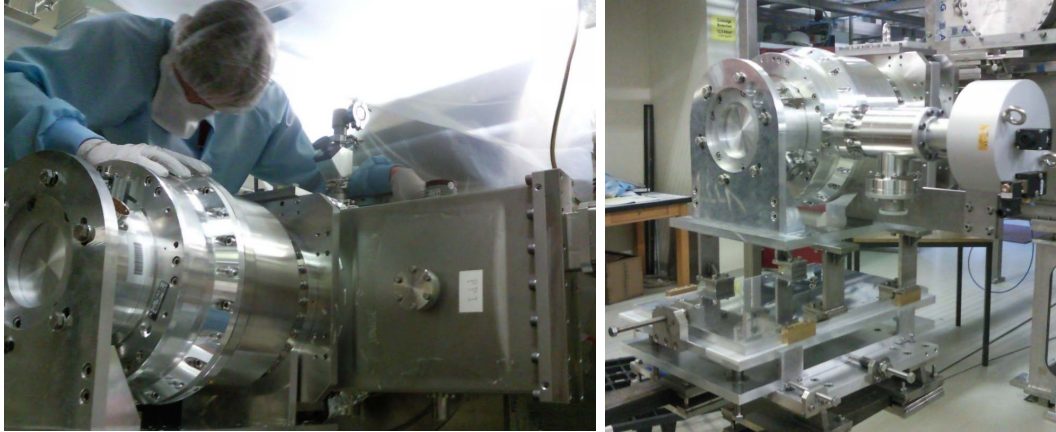


Figure 5.3: **The DPS2-F TMPs**

Right: a pre-assembled pump group comprising the large TMP and gate valve as well as support structure, mounted onto a special-designed assembly unit. Left: the author during mounting of a pump group onto the DPS2-F.

#4 to the inlet of TMP #2. The outlets of the TMPs #1 and #2 are then connected to a 2nd (3rd) stage TMP (Pfeiffer TMU 200 MP), which finally is connected to a roughing pump (Leybold SC15D, scroll pump). The cascaded pumping setup is presented in full detail in appendix A.1.

### 5.1.1.3 TMPs in magnetic field

The combination of high magnetic fields and TMPs running at high revolution speeds poses non-trivial additional challenges. The magnetic fields induce Eddy-currents at the rotor whose temperature will rise accordingly. These phenomena were thoroughly investigated by the KATRIN collaboration [Jan12].

The maximum rotor temperature ensuring full life-time of the TMP is limited to 90 °C, while 120 °C is the maximum (short-term) temperature for full operation, but strongly decreases the guaranteed life-time of the pump.

For a MAG W 2800 without significant gas load ( $p_{\text{in}} \leq 10^{-5}$  mbar) this temperature is reached in magnetic fields of  $B_{\text{max}\perp} = 3$  mT [Jan12], with  $B_{\perp}$  defined as the part of the field orthogonal to the TMP axis.

Parallel fields relative to the TMP axis will not induce substantial currents, but can - when increased over a critical field strength - dislocate the rotor in its magnetic bearing, thus severely damaging the pump. The KATRIN Collaboration assessed this value to be  $B_{\text{max}\parallel} = 12.5$  mT for external fields parallel to the bearing field, and  $B_{\text{max}\parallel} = 21.2$  mT for external fields anti-parallel to the bearing field.

In the case of the DPS2-F vacuum system (or other equivalent KATRIN setups such as WGTS, CPS, or the spectrometers), these values are often met or



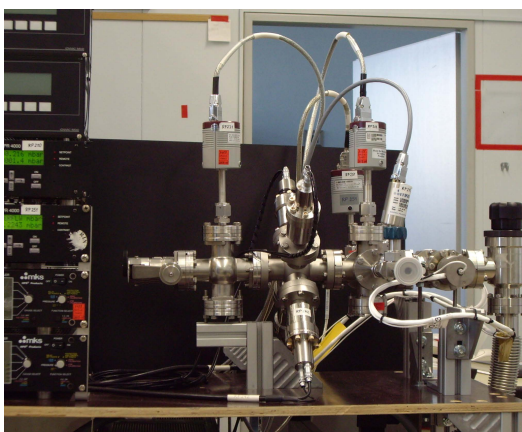
even exceeded. In these cases a suitable shielding - usually manufactured from soft iron - has to be installed. As can be seen in the field map in figure 5.7, no critical values of parallel fields are reached. The strength of the orthogonal field parts do however reach the critical values at pump port 1 and 4. Accordingly, soft iron shielding of 3 mm strength has been installed for all four MAG W 2800 at the DPS2-F.

To further optimize the operational temperature, the pumps are water-cooled at the base with an inlet temperature of 15 °C. Temperature measurements using the built-in sensors have not yielded evidence for an increase in base temperature of more than 2 K after field ramp-up during the commissioning of DPS2-F.

#### 5.1.1.4 Vacuum Analytics

Each pump port of the DPS2-F system is equipped with four auxiliary ports (DN CF40 and CF63) for flexible sensor mounting and electrical feed-throughs. A detailed scheme of primary instrumentation (as used for all measurements described in this work) is given in appendix A.2.

Two of the auxiliary ports at each pump port are equipped with vacuum sensors (cf. equipment list A.1 in the appendix). Cold cathode vacuum sensors are mounted at each port. The two upstream ports also feature capacity sensors, while hot cathode sensors for XUV applications are mounted at the two downstream ports.



**Various Pressure Sensor during Pre-Calibration Tests**

The capacity sensors are well calibrated ex factory. Our testing showed an absolute error in the order of  $10^{-5}$  mbar [Luk11b], but the ionizing gauges (cold and hot cathodes) need calibration after linking with the read-out system.

All sensors were thoroughly tested and finely calibrated, as explained in [Luk11b]. The calibration factors were implemented into the instrumentation and control electronics (ICE) system, which, for the test measurements described in this work, was based on LabView. In later

KATRIN operations the global ICE system will be based on a Siemens PCS7 system. After migration of all systems and the full re-commissioning of DPS2-F the sensor calibration should be redone.

## 5.1.2 Magnetic Design

### 5.1.2.1 General Design

Being part of the KATRIN transport section, an important feature of DPS2-F is its magnet system that has to adiabatically transport the signal  $\beta$ -decay electrons to the spectrometer section for energy analysis. The key features of the DPS2-F magnet design have been defined in [Noe03]. They include the following aspects:

- Transport of a magnetic flux tube of  $191 \text{ T cm}^2$  within a minimum margin of 10 mm from the walls of the inner vacuum system (i.e. the beam tube and the pump ports).
- The magnetic alignment has to guarantee the matching of field-lines at the entrance and the exit parts with a margin of 1 mm laterally, and a parallel alignment with a margin of  $0.5^\circ$ .
- The minimal field strength within the flux tube must be  $\geq 0.5 \text{ T}$  to guarantee full electron adiabaticity (see section 2.2.6 and [Wei03a]).

The design of the supplier ASG has successfully met these requirements with a total of 15 superconducting magnets, which are grouped in 5 modules, each one composed of a main coil and two correction coils in a single overall cryostat. The modules rest in a liquid helium reservoir connected to a main helium-supply vessel, rendering a total helium reservoir of 415 liters. Cold helium is

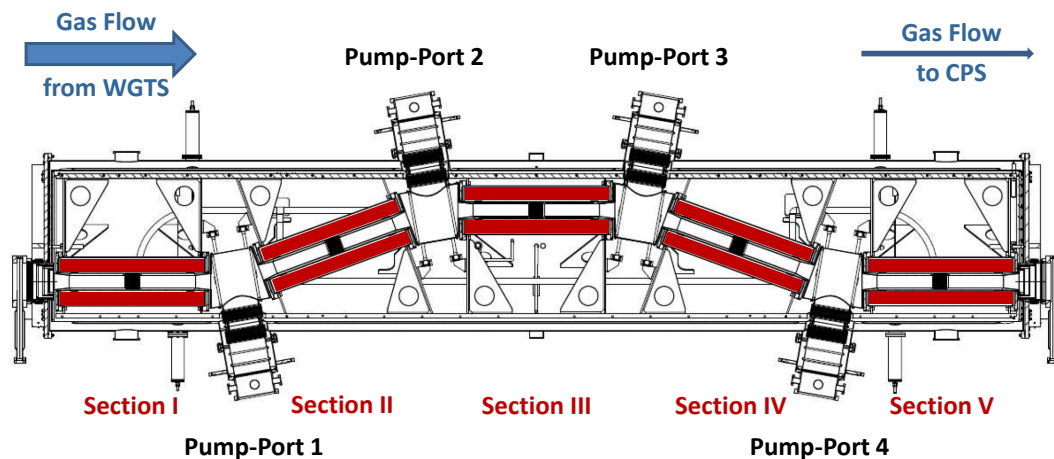


Figure 5.4: DPS2-F, Lateral Cut

Shown is a lateral cut through the DPS2-F cryostat. Gas, ions and electrons enter from the left after leaving the WGTS unit. The pump ports and beam tube sections are labeled in ascending order. Colored in red are the superconducting magnet modules.

supplied from an external Linde TCF 50 refrigerator. In standard operation mode, supercritical helium is condensed directly in the main supply vessel via a Joule-Thompson valve. The stand-alone time of the cryostat was designed to be 36 hours, but measured to be around eight hours only in a worst case scenario. In total the DPS2-F cryosystem has to cope with a heat load of  $(30.4 \pm 2.4) \text{ W}$  [Put11]. A constant supervision of the cryo-system is thus required, which is carried out by cryo technicians from the Institute of Technical Physics at KIT.

The number of intrinsic windings is 3700 for the correction coils, and 17 225 for the main coils. The operational current was designed to be 200 A, thus rendering a current density of  $132.75 \text{ A mm}^{-2}$  for the correction coils, and  $132.75 \text{ A mm}^{-2}$  for the central solenoids. The magnetic geometry is given in figure 5.6, while a stray field map is provided in figure 5.7.

The validity of the design drawings, in particular with regard to the actual positioning of the magnets, was tested as part of the commissioning in this work. Methods and results are presented in section 6.1.1. Additionally, more detailed examinations of the magnetic fields are planned to assess the field profile at the inlet and outlet via systematic analysis making use of a small-scale Hall-probe (cf. section 6.2.1). The overall pellucidity for the signal bearing flux tube of  $191 \text{ T cm}^2$  will be checked by measuring the transmission of electrons emitted at various radial positions, thereby focusing on the edge of the flux tube (cf. section 6.2.2).

### 5.1.2.2 The Superconductor Circuit

The magnet modules of DPS2-F have been designed by the manufacturer to quench safely with no dump of stored energy to external resistors. Accordingly,

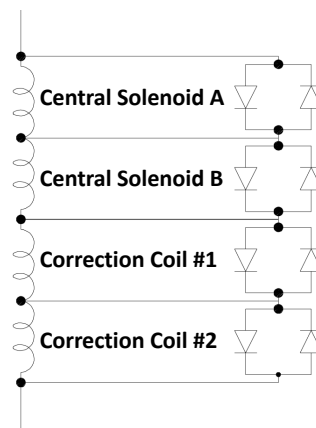


Figure 5.5: **Circuit Diagram of the Protection Diodes:** Eight protection diodes for each one of the five magnet modules. At liquid helium temperatures, the diodes feature a characteristic forward voltage between 0.7 and 1.4 V.

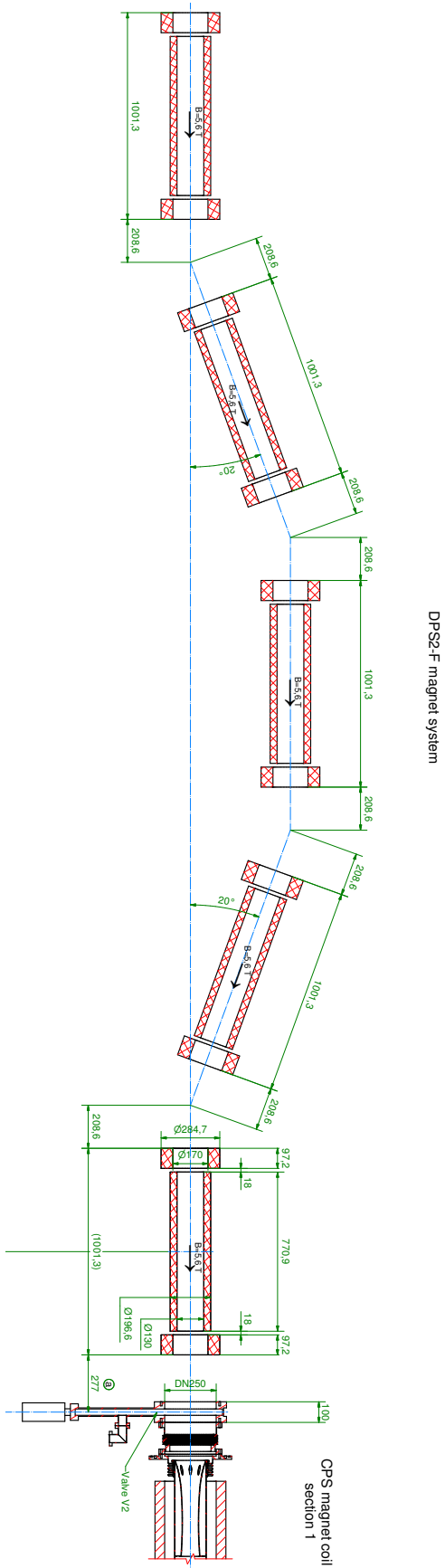
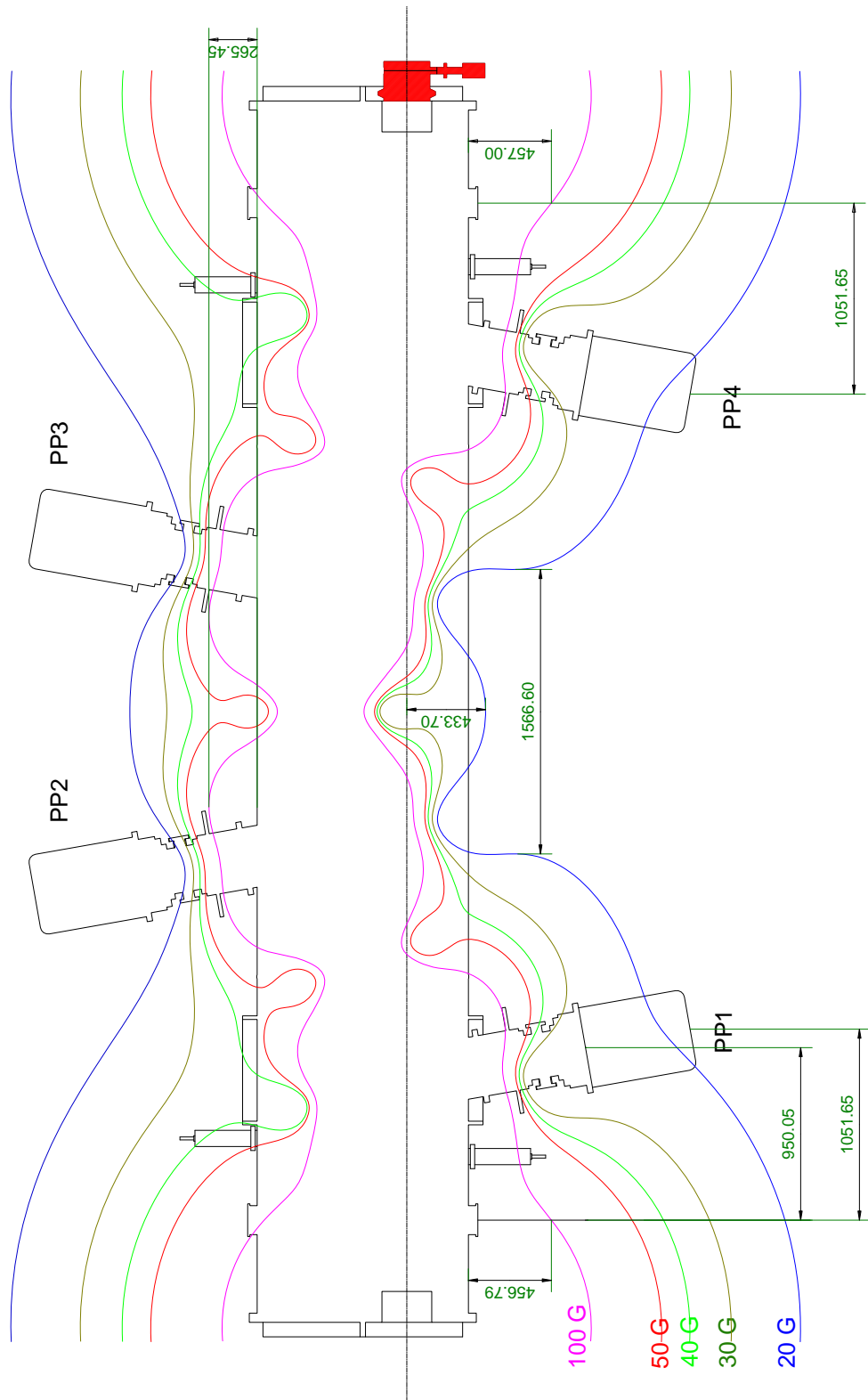


Figure 5.6: **Geometry of the superconductors deployed in DPS2-F**  
 Shown is the geometry of the super-conducting magnets deployed in DPS2-F taken from the suppliers final documentation [Dor11].



5 Gauss at 4.5 m from the cryostat cylinder outer shell

**Figure 5.7: Stray field map of DPS2-F**  
 Shown is a map of the magnetic stray fields at DPS2-F simulated for the maximum field value of  $B_{\max} = 5.6 \text{ T}$  envisaged for final operations.

the superconductor circuit is protected (as usual for these kinds of applications) via Schottky-diodes connected in parallel as can be seen in figure 5.5. Each module is electrically sub-divided into four sections, with each section being protected by diodes. There is one section for each correction coil, and two for the central coil. This design enables the DPS2-F magnets to be driven in both polarities, therefore the diodes are always placed in groups of two, one in forward direction of the current, and one in reverse. Besides offering protection, the diodes limit the charging voltage to approximately 1.4 V at operational temperature. As shown in figure 5.8, the diodes (eight per module) are fixed directly onto the magnet module inside the helium chamber.

The magnet circuit also features a superconductive switch to operate the magnet modules in persistent mode. It is located in the main helium vessel in the turret. It is closed by default and can be opened by heating the copper part of the switch.

A sketch of the superconducting circuit including the diodes and the superconducting switch is given in appendix A.11.

### 5.1.2.3 Commissioning Magnet System

During the commissioning works at the end of 2010, noticeable deviations of the as-built cryostat dimensions from the design values became obvious. Specific

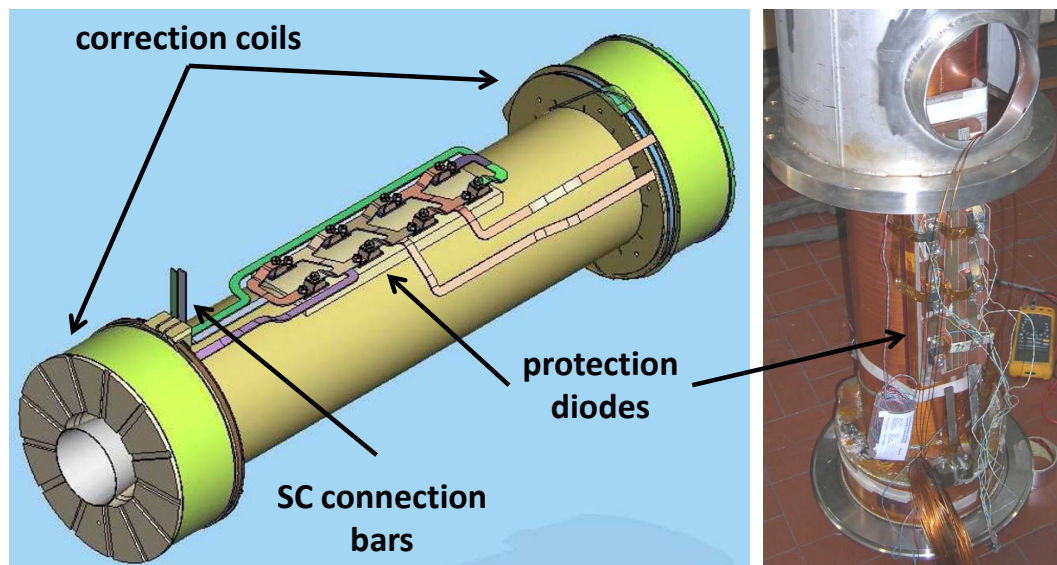


Figure 5.8: **The DPS2-F Magnet Modules**

Shown is one of the five magnet modules of the DPS2-F magnet system. Identified are the two correction coils at the ends and the connector circuit including the eight protection diodes. On the right side, magnet module #2 is shown during assembly. Based on [Dor05],[Dor11].

flaws of the cryogenic system lay-out were however manageable and have been described elsewhere [Put11].

The performance of the magnet system, however, turned out to be not as good as expected. The above mentioned nominal current of 200 A at 70 % of the maximum current capacity of the magnet-system was not met. The highest current reached without quench was 195 A. Subsequent to these investigations, a commercial and technical agreement was reached to limit the operational current to 185 A and to abstain from bake-out of the primary vacuum system to minimize thermal stress on the modules.

Following these activities, in summer 2011 a major malfunction of the above mentioned SC circuit occurred, which is described in more detail in Appendix A.4. This malfunction has limited the scope of test procedures foreseen for the DPS2-F cryostat at this point.

### 5.1.3 The Ion Analysis and Suppression System

The principles of ion species analysis and ion suppression were introduced in section 4.3. The technical realization features two three-pole Penning traps provided by *Stahl-Electronics*<sup>3</sup>, and twelve through-shaped dipole-electrodes. The traps will be placed in beam tube sections I and V, while the dipole system will be located in section II - IV (three groups of four electrodes), as schematically shown in figure 5.9.

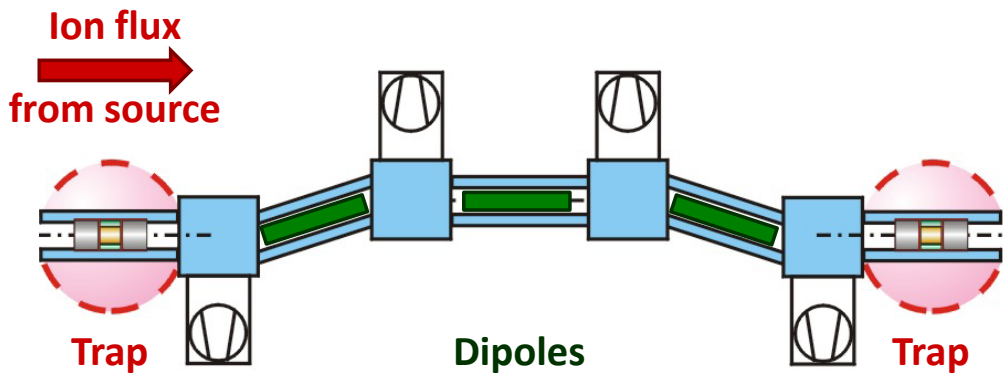


Figure 5.9: The Ion Analysis and Suppression System

Shown is a schematic of the ion analysis and suppression system. The FT-ICR traps (red) are located at the outer beam tube sections, the dipole electrodes used to create the  $\vec{E} \times \vec{B}$ -drift displacing the ion flux (green) are located within the three inner beam tube sections.

<sup>3</sup>STAHL-ELECTRONICS, Dr. Stefan Stahl, Kellerweg 23, 67528 Mettenheim, Germany.



### 5.1.3.1 The DPS2-F FT-ICR System

Based on the FT-ICR ion-analysis principles described in section 4.3.1, specific FT-ICR modules, shown in figure 5.10, were developed. The technical realization and a proof-of-functionality have been thoroughly described in [Ubi09].

An FT-ICR module consists of two endcap-electrodes for trapping, and a central ring electrode, which is split into four segments for ion excitation and for image charge detection, as described in section 4.3.1.2.

The length of the module is 310 mm, the inner diameter is 71 mm. The latter parameter is sufficient - in regions of high B-field - to let the entire KATRIN flux tube pass, thus not restricting or influencing the propagation of signal electrons. Approximately one third of the module has an outer diameter of 83 mm, while two thirds have been narrowed down to an outer diameter of 79 mm, providing a reduced diameter to fit into the bellow in the middle of the beam tube (see appendix A.2).

The outer support-structure is manufactured from a magnesium-aluminum alloy. The inner electrodes are made out of 1 mm thick oxygen-deprived copper, first coated with 50  $\mu\text{m}$  silver, then with 1  $\mu\text{m}$  gold to prevent oxidation to ensure good conductivity. All insulators are made of PEEK (Polyetheretherketone), a plastic which can be vacuum-applicable (outgassing tests at MPIK Heidelberg were carried out successfully [Ubi09]). Mounted onto the support-structure are a DC filter and a preamplifier.

The mass resolution  $\Delta m/m$  of the FT-ICR unit reaches down to several  $10^{-6}$ . The measured detection threshold was found to be  $\approx 6000$  trapped ions for  $\text{He}^+$  and  $\approx 1000$  trapped ions for  $\text{H}_2\text{O}^+$ , which is several orders of magnitude below the expected levels in DPS2-F (cf. section 4.1.2).

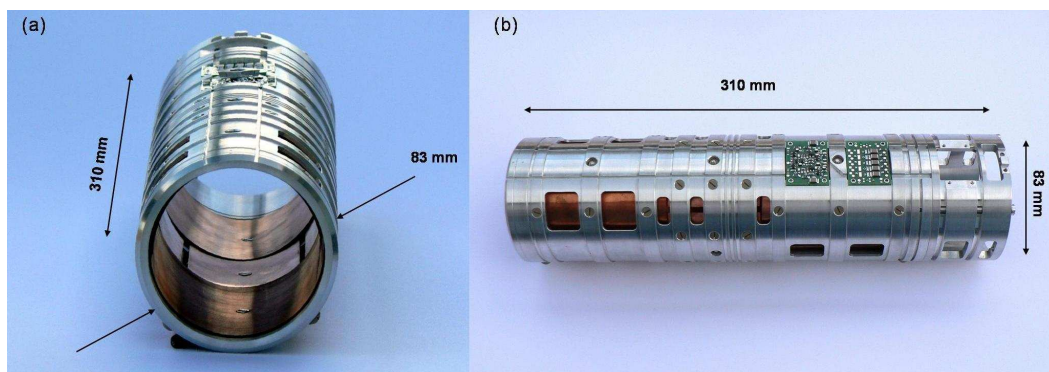


Figure 5.10: **The FT-ICR Penning Trap**

Shown is a functional prototype of the FT-ICR system foreseen for installation in the DPS2-F. The final traps will have a slightly modified bearing structure (see text). Both, electrodes and electronics design, are final as shown here.



The FT-ICR modules will be inserted into the DPS2-F beam tube through the pump ports #1 and #4 with the help of specific tools, since the entrance- and exit-valves are not accessible at that point anymore.

A list of required auxiliary electronics is given in appendix A.2

### 5.1.3.2 The DPS2-F Dipole System

The proposed exploitation of the  $\vec{E} \times \vec{B}$ -drift described in section 4.3.2 calls for a suitable through-formed electrode, as well as auxiliary components and applicable methods of installation. After a series of specific design-studies (e.g. [Rei09],[Win11]), partially guided by the author, it was decided to implement the design presented in figure 5.12.

The dipole electrodes are manufactured from stainless steel and are gold-plated. The outer ones have a length of 178 mm, while the inner ones are 30 mm longer to protrude over the beam tube bellow. Each element covers a radial angle of  $120^\circ$ . The electrodes are separated from ground potential by 4 mm thick  $\text{Al}_2\text{O}_3$ -ceramic tubes. For easier mounting, better contact to the DPS2-F beam tube and protecting the beam tube bellows in the case splintering of a ceramic tube, the electrodes and tubes rest on carrier-plates manufactured from stainless steel with a length of 184 mm. Each of two adjacent carriers is interlocked so that access to the inner electrodes remains.

The radial geometry is strongly influenced by the magnetic flux tube. As stated above, a flux tube of  $191 \text{ T cm}^2$  will transport the signal  $\beta$ -decay electrons towards the spectrometers. The minimum inner diameter of the electrode setup thus is calculated to be  $\geq 75 \text{ mm}$  [Rei09].

During regular tritium measurements, ions will drift towards the  $\text{Al}_2\text{O}_3$ -ceramic tubes, as described in sections 3.4.2 and schematically shown in figure 3.10. The use of an insulator (or rather poor conductor) is mandatory so that the field-lines not to hit the eliminating surface orthogonally, which would obviously hinder the  $\vec{E} \times \vec{B}$ -drift. However, the use of a "real" insulator imposes new problems, namely the build-up of surface charges arising from accumulated ions on the insulator.

To solve this generic problem it was decided to coat the surface of the  $\text{Al}_2\text{O}_3$ -ceramic tubes with a layer of high electric resistivity. The coating is chosen in a specific way to guarantee a current of  $I_{\text{min}} = 10 \mu\text{A}$  for each tube, but also to limit the global heat development to 1 W, thus rendering a maximum current of 100 mA for the total of all tubes (given a potential of 100 V). These requirements leave us with a resistance-corridor of  $100 \text{ k}\Omega - 2.5 \text{ M}\Omega$  at the operational temperature of 77 K for each tube.

Several tests to process industry-coated tubes to produce custom-tailored coatings of desired conductivity have been carried out [Kos09]. Our aim was the

production of under-stoichiometric titanium dioxide surfaces by controlled oxygen migration. Previous studies in the literature (e.g.[Die03],[Ohm91]) show a strong dependence of the conductivity of  $\text{TiO}_X$  from oxygen concentration ( $1.55 < X < 1.9$ ) and a good stability at low temperatures. The corresponding setup is briefly described in Appendix A.3.

Even though experiences in surface processing were gained, the trials for on-site production of these surfaces was resulting in rather high costs and expenditure of time. Since acceptable solutions are commercially available at moderate prices, a strategic decision was made in favor of industry-manufactured coatings.

The final connection as well as the installation of the electrodes will be carried out through the nearest pump ducts. Special tools for installation and alignment of the electrodes and their carriers have been developed and successfully tested at a mock-up in the course of this work [Win11]. An example is shown in figure 5.11

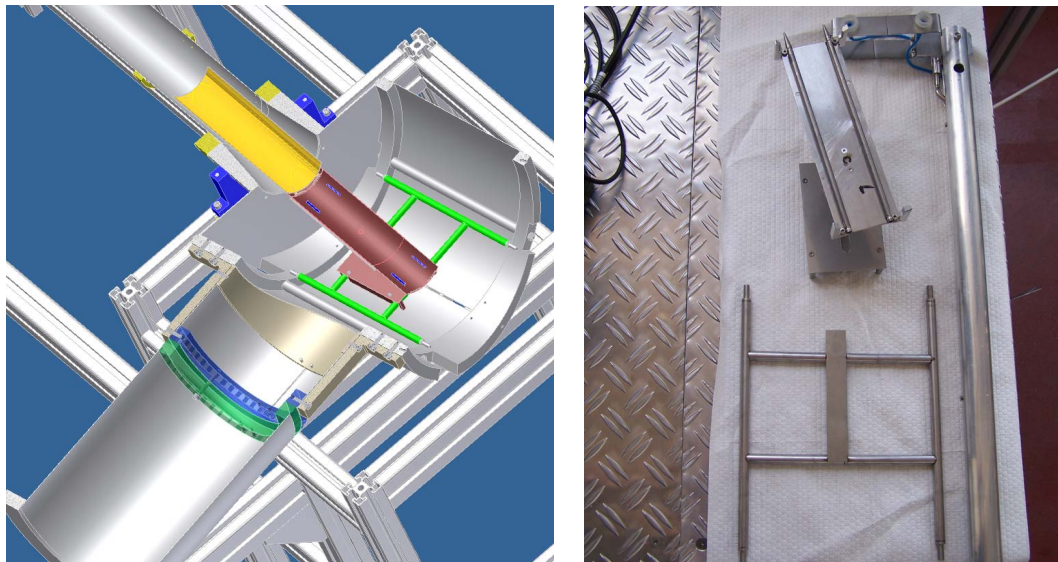


Figure 5.11: **Dipole Mounting Tools**

Shown on the right hand side is a mounting rack and a translation tool utilizing suction cups, which is used to align the dipole carriers in the pump ports. Deployment of this mounting rack within the beam tube is drafted on the left hand side in a construction scheme. Additional tools for transversal movement and electrical connection have been developed as well.

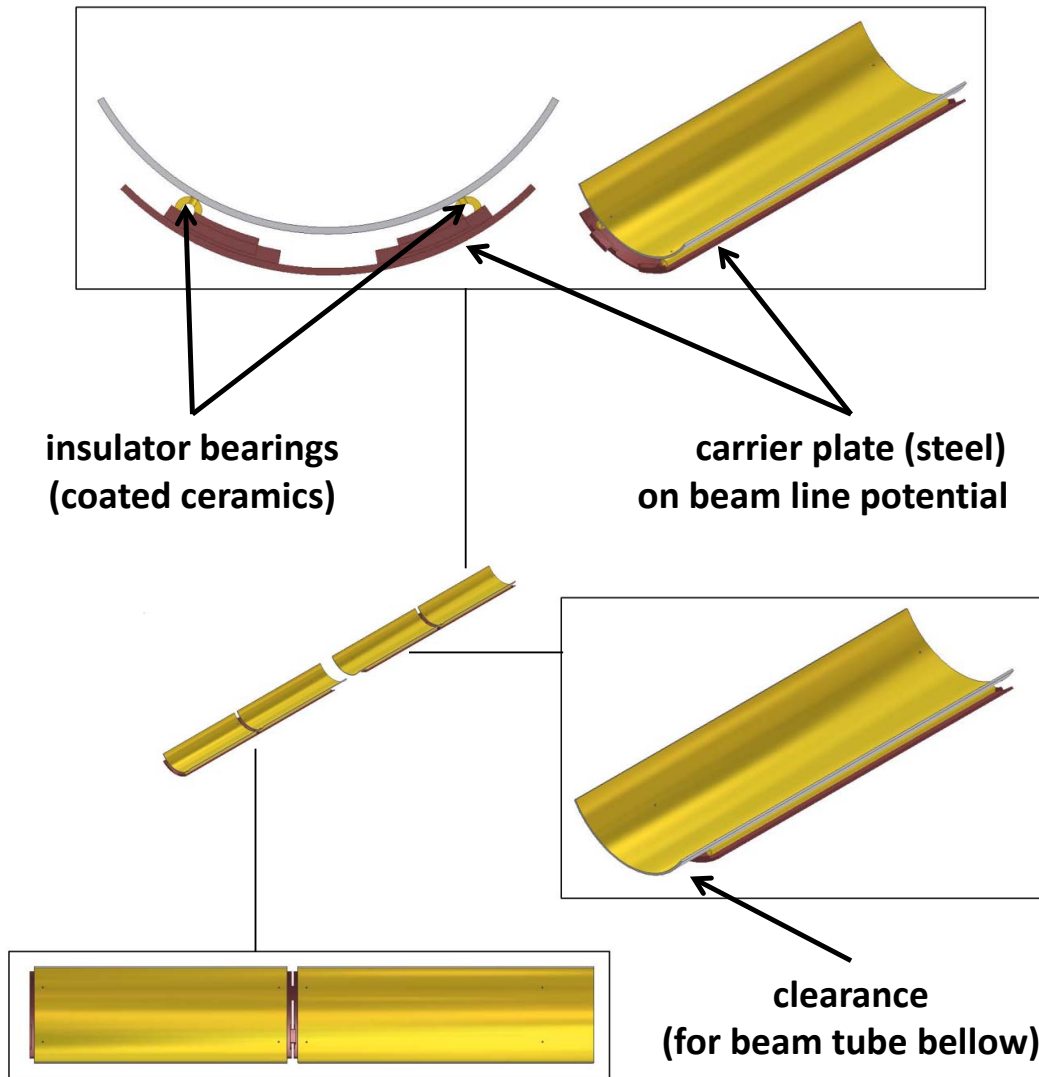


Figure 5.12: **The Ion-Suppression Dipole-Design**

Shown is the arrangement of four dipole-electrodes in one beam tube segment based on [Win11]. Since the beam tube features a bellow of reduced diameter in the middle, two electrodes have to be inserted from each side. The carrier plates are designed to leave a clearance for this bellow. The electrodes rest on  $\text{Al}_2\text{O}_3$ -ceramic tubes of 4 mm diameter that are coated with a high-resistive material to prevent a steady current while allowing for neutralization of the impinging ions.

## 5.2 Cryogenic Pumping

The Cryogenic Pumping Section (CPS) is the last module of the Source and Transport Section (STS) of the KATRIN experiment. It features a large-area cryo-pumping system based on argon snow frosted onto gold-plated steel as adsorbent. Further elements are a fourfold buckled beam line (comparable to DPS2-F) and a superconducting magnet system to guide the signal electrons toward the spectrometer sections. The CPS is designed to guarantee a tritium flow reduction factor of  $\geq 3 \times 10^7$ . The beam tube operational temperatures in this module will range from room temperature down to 3 K at the frost pump, with other distinct operational modes at 77 K (liquid nitrogen cooled), 40 K (argon capillaries) and 6 K (the desired temperature for argon-frost preparation). The following section will outline the general design features of this unique apparatus. The details are based on [Eic09],[KAT04],[Kle08].

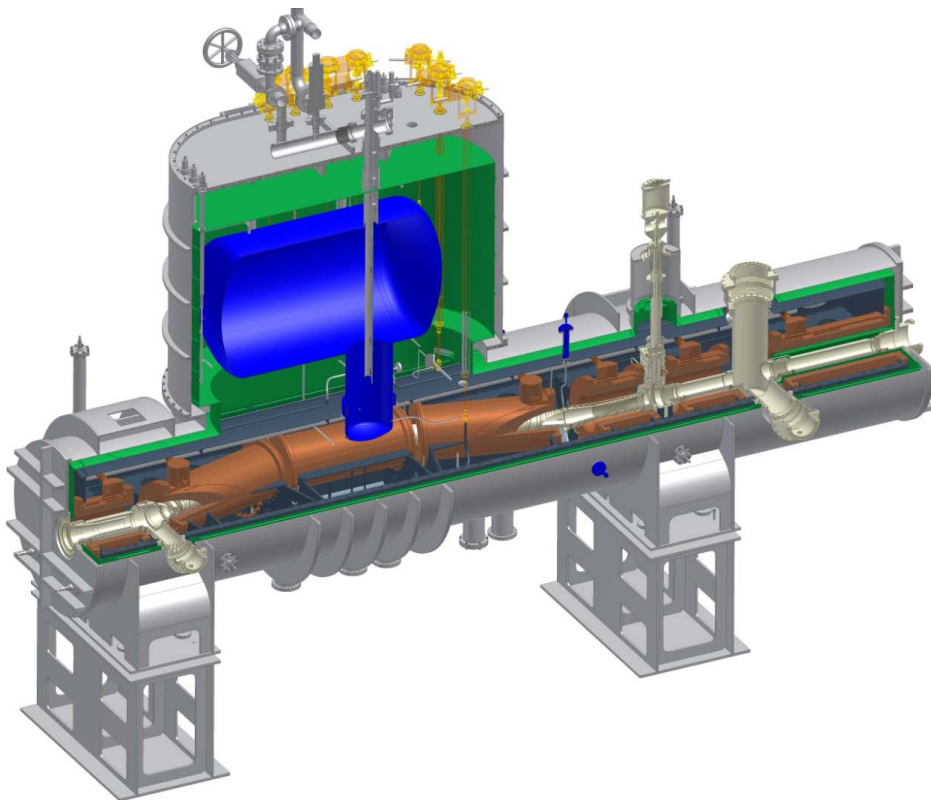


Figure 5.13: **The CPS**

Shown is a quarter cut through the CPS cryostat; flow direction from left to right. Within the radiation shield (green) the liquid helium system (blue) and the magnet system (brown) and the beam tube itself (silver) can be seen. Source: [Dre12]

### 5.2.1 Beam Tube Design

The CPS cryostat features an even more complex beam tube design than DPS2-F. The beam tube is segmented into 7 sections as shown in figure 5.14.

The first sections form the cryo-pumping section of CPS.

- Section 1 acts as a thermal transition part from the CPS-facing end of the DPS2-F. It is 655 mm long and kept at liquid nitrogen temperature (77 K). With a diameter of 148 - 152 mm it is wider than the other sections. This additional space allows for the installation of an alternative condensed  $\beta$ -emitting source (to be used to cross check systematics arising from the source and transport section). During standard operations it will be deployed with cylindrical, coated inserts of high thermal absorption coefficient ( $> 0.9$ ) to shield the following cryo-pumping sections from thermal radiation emitted by the DPS2-F beam tube and the gate valve between DPS2-F and CPS.
- Sections 2 - 5 form the actual cryopump. They have an inner diameter of  $\approx 75$  mm and are, comparable with the beam line elements in the DPS2-F, tilted by  $15^\circ$  with respect to the antecedent one. To enlarge the inner area of the  $\approx 1100$  mm long (688 mm for section 5) segments, the inner wall features a fin-structure as can be seen figure 5.17. Perforated capillaries running along the inside of the tube sections 2-4 allow the transfer of the argon adsorbent into the cryopumping section.
- Section 6 is also designed as a thermal transition part kept at 77 K. It is  $\approx 734$  mm long, has an inner diameter of 112 - 114 mm and is coupled upstream onto a specially developed cold gate valve. The cold gate valve will close in case the cryogenic pumping is interrupted to

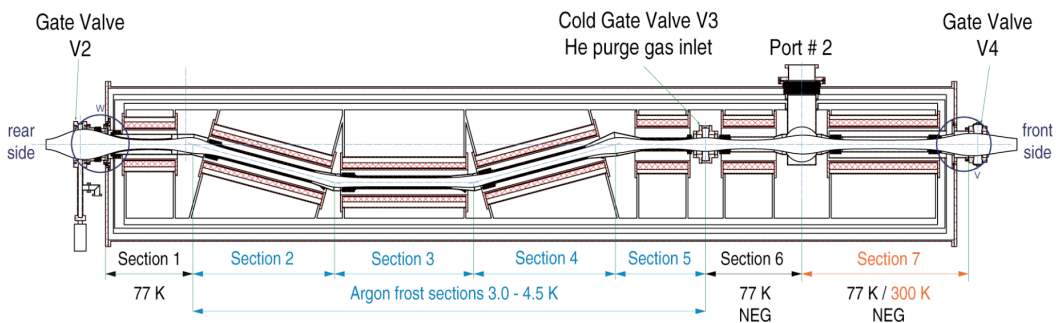


Figure 5.14: CPS beam tube - Cryogenics

Shown is an overview of the 7 segments of the CPS beam tube with specifications about the local temperatures at standard operation. The cryo-pumping sections are to be found in sections 2 - 5 (marked blue). NEG stands for Non evaporative getter (cf. section 3.2.5). Taken from [Kle08].



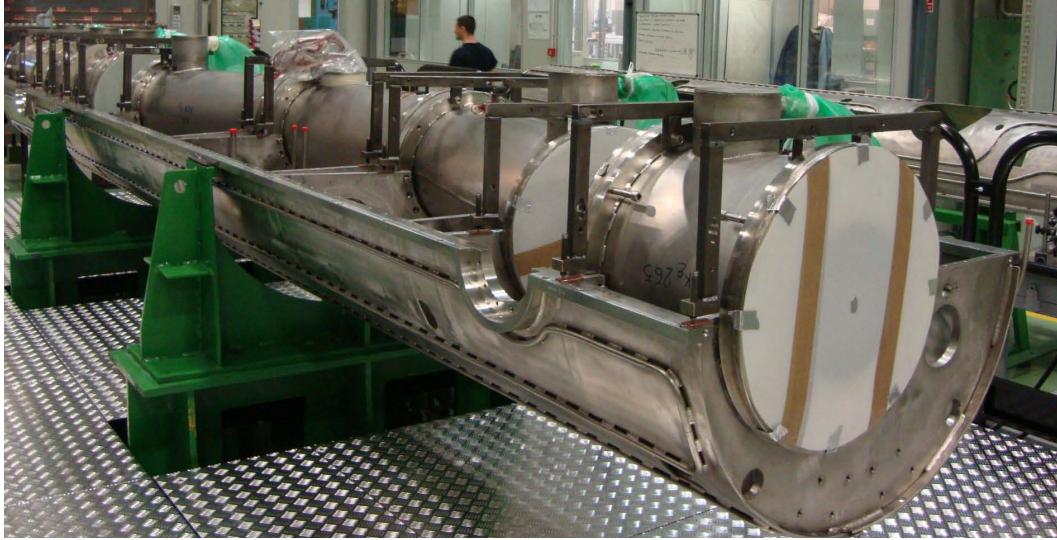


Figure 5.15: **Assembly of the CPS Magnet System**

Shown is the cold support mass for the helium containers of the magnets system during assembly in May 2011.

prevent tritium from migrating to the downstream components. Section 6 itself is equipped with non evaporative getter (NEG) strips.

- Section 7 is  $\approx 1274$  mm long, has an inner diameter of 112 – 114 mm and will be kept at room temperature during standard operations. Between sections 6 and 7 a DN250 CF and a DN200 CF flange are included to provide access for a  $^{83m}\text{Kr}$  calibration source and a detector for monitoring the source. These components are needed during commissioning and calibration of the whole KATRIN setup.

### 5.2.2 Magnetic Design

As is the case for all KATRIN modules, the CPS magnetic design has to guarantee the adiabatic downstream transport of the signal electrons. As described above for DPS2-F (cf. section 5.1.2), superconducting solenoids surround each of the seven beam tube segments. The SC-current for standard operations is planned to be 200 A with a current density of  $118.6 \text{ A mm}^{-2}$ , creating a magnetic field of  $B_{\text{max}} = 5.6 \text{ T}$ . The design also guarantees the transport of the  $191 \text{ T cm}^2$  magnetic flux tube within a margin of  $d = 2 \text{ mm} + 4 \text{ T mm}/B$  (3 mm minimum) from the inner mechanical structure. To ensure adiabaticity, the minimal field may not drop below  $B_{\text{min}} \geq 0.4 \text{ T}$ .

As in DPS2-F, the solenoids are cooled in a liquid helium bath at 4.5 K and were initially foreseen to be operated in persistent mode during standard operation. The magnetic geometry is displayed in figure 5.16. As can be seen, for CPS no correction coils are required.

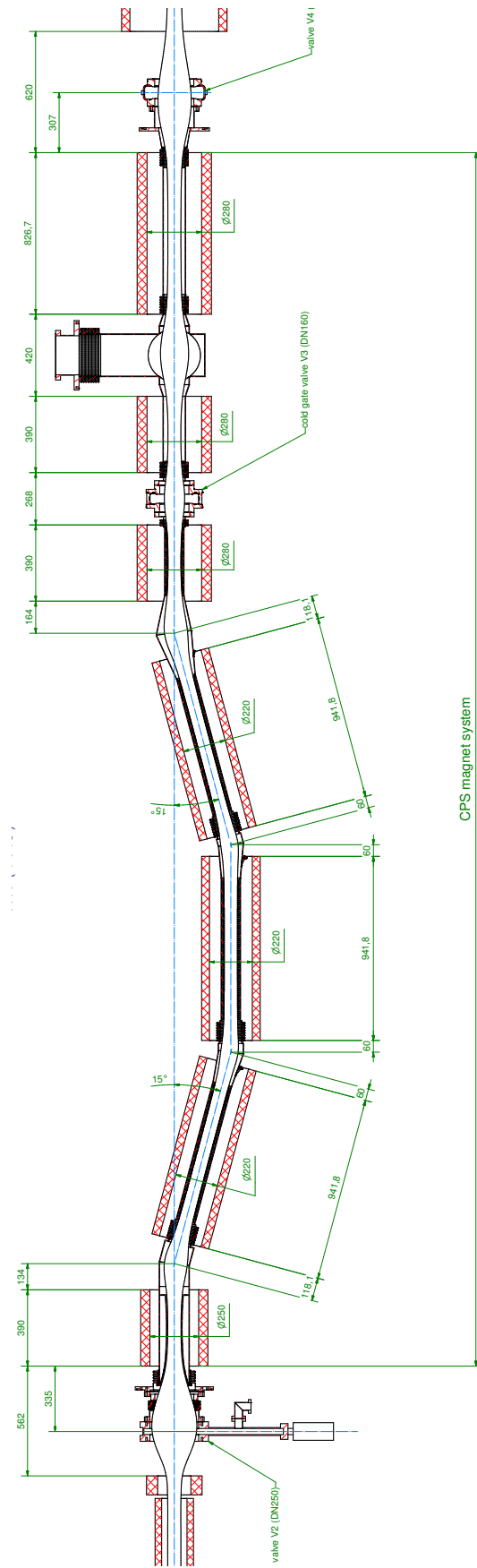


Figure 5.16: Geometry of the superconducting magnets deployed in CPS  
 Shown is the geometry of the superconducting magnets to be deployed in CPS provided by the supplier during the design phase.

### 5.2.3 The Cryopump

#### 5.2.3.1 Setup of the Cryopump

As stated above, the beam tube sections 2 - 5 form the actual cryopump within the CPS cryostat. The segments have an overall length of approximately 4 m and an inner diameter of 95 mm. To increase the surface, fins are honed into the cylindrical segments (as shown in figure 5.17). All together the active cryopumping surface amounts to an area of approximately 3.08 m<sup>2</sup>.

To prevent residual contamination of the walls by tritium absorption (cf section 3.2.4), the inner surface of the beam tube segments will be plated with gold.

On top of the gold-plated fin-structure, the actual cryo-adsorbent in the form of argon frost is applied through porous capillaries into beam tube sections 2 - 4.

#### 5.2.3.2 The Modes of Operation

After commissioning, bake-out and NEG activation, the CPS will cycle through several modes of operation, which will be introduced in the following (a tabular overview can be found in Appendix A.4).

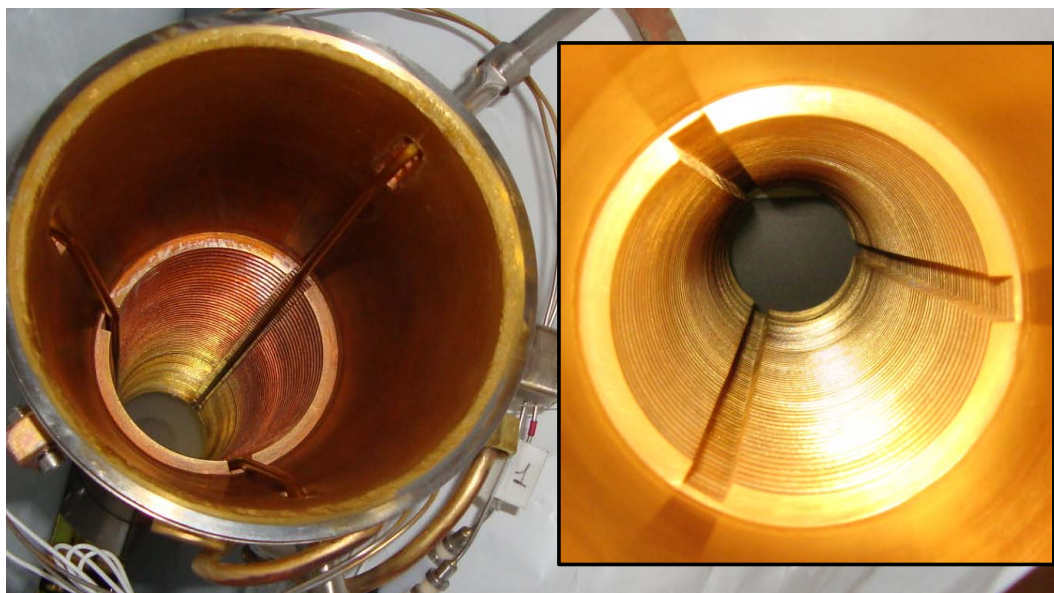


Figure 5.17: **Inside of a CPS beam tube segment**

Shown is the beam tube section 3 during earlier stages of CPS construction. The grooves providing an enlarged area for the frosted argon and three capillaries for argon injection can be seen. Inserted on the right is a photograph of the newly gold-plated beam tube section 2.



- 1. Cool Down:** At the beginning of each cycle of operation the CPS magnets and beam line have to be cooled down to operational temperatures. Section 1 and 6 will be cooled down to 77 K, and sections 2 - 5 to 3.0 - 4.5 K. Section 7 will be kept at room temperature (its magnet is shielded by an additional liquid nitrogen radiation shield between the magnet container and the beam tube). All seven solenoids are cooled via a central cooling system using liquid helium at approximately 1.3 bar and 4.5 K. This cool-down procedure has to be achieved in less than one week.
- 2. Argon Preparation:** The optimal temperature to create an argon frost layer of small to medium sized crystallites is approximately  $(6 \pm 0.5)$  K. This requires that segments are reheated up to this temperature. The capillaries, which are used for the transport of liquid argon, are heated from inside up to 40 K to prevent blockage due to argon freezing before reaching the fin surface. The other sections are kept at their respective operational temperature.

The time period required for the argon preparation mode is estimated to be several hours. Additional tests for the optimal frosting time are yet to be carried out.
- 3. Standby:** This is the default mode prior and subsequent to data taking periods. All subsystems are at operational temperature and pressure. The cold gate valve between sections 5 and 6 is closed. The argon frost layer is already prepared and data acquisition can start immediately. There should be no time restraints on the duration of standby mode.
- 4. Standard Operation:** This is the standard KATRIN measuring mode. All subsystems are at operational temperature and pressure. The cold gate valve V3 between sections 5 and 6 is open and small amounts of tritium enter from the source side through the gate valve V2. The individual data collecting cycles are intended to last 60 days.
- 5. Regeneration:** After each data collection cycle the CPS has to be regenerated. The amount of adsorbed tritium then has reached up to  $8.5 \times 10^{-5}$  mol, corresponding to an activity of 2.47 Ci (an amount that should be handled with care). For a slow and controlled outflow of the argon together with the adsorbed tritium, gaseous helium of 100 K is purged through the cryopumping segments of CPS. To ensure a one-way transport in an optimal manner the gate valve is closed, and warm helium gas is inserted into the beam tube in section 5 through a flange at the gate valve. Later on it is extracted via the pump port upstream of section 2 as well as through an auxiliary pump port downstream of the entrance valve which will be closed as well. The regeneration mode always starts from the standby mode (see above). After successful regeneration, the CPS is reset to standby mode unless insufficient purging or high residual contamination requires a bake-out of the beam tube.

The time for regeneration is also estimated to last several hours. As for the optimal argon-preparation time, specific tests to determine the optimal regeneration time, are yet to be carried out.

The usual CPS cycle during KATRIN operation will proceed in the steps 1-3-2-3-4-3-5-3. The cold gate valve downstream of the cryopump is closed at all times, except during data collection.

### 5.2.3.3 The Argon Frost

**Argon Frost Coverage and Granularity** The cryopumping capability and performance of the CPS strongly depends on the quality of the preparation of the argon frost on the inside of the CPS beam tube. As stated in section 3.2.6, there is an optimal preparation temperature for a given cryo adsorbent leading to high granularity and hence a large surface. For argon the minimal grain size  $\delta$ , which leads to the greatest values for the inner surface  $A_0$ , and hence the maximum mono-layer capacity  $a_0$ , is reached at a formation temperature of  $T_{\text{opt}} = 6.0 \text{ K}$  (cf. [Abe79]).

The optimal crystallite size of argon reached at a condensation temperature of 6.0 K is  $\delta = 60 \text{ nm}$  [Nep05] which renders a mono-layer capacity between  $a_0 = (5.8 - 6.0) \times 10^{-2} \text{ mol H}_2/\text{mol Ar}$  [Hae89],[Abe79].

Following the calculations for surface-density presented in section 3.2.6, we estimate a value  $A_0 = 1.08 \times 10^5 \text{ m}^2 \text{ kg}^{-1}$ . This number is in accordance with the experimentally obtained value of  $A_0 = 1.38 \times 10^5 \text{ m}^2 \text{ kg}^{-1}$  reported in [Bec72].

Previous studies ([Tem70],[Tem71]) suggest the possibility of a further increase in mono-layer capacity by allowing for a helium atmosphere of approximately 0.1 mbar during the condensation process, which was claimed to result in a slight increase in granularity of the frost. This effect could be explored during CPS commissioning tests.

Another important aspect of the argon layer preparation is the desired thickness of the adsorbent. Several different studies show a decrease in mono-layer capacity with increase of the adsorbent layer above its ideal value (cf. [Tem70] and [Sch71])<sup>4</sup>. This effect can be explained by an increase in temperature with an increasing distance from the cold wall.

On the other hand, as mentioned above, the desired high granularity of the adsorbent is accompanied by an increase in porosity. Measurements show an 85 % degree of coverage for a single layer of argon condensed on silver [Nep05],

<sup>4</sup>Both, Tempelmeyer [Tem70] and Schulze [Sch71], studied the capacities of carbon dioxide for the cryogenic pumping of hydrogen. Schulze reached a value  $a_0 = 0.33 \text{ mol H}_2/\text{mol CO}_2$  on 1000 nm of  $\text{CO}_2$  adsorbent, whereas Tempelmeyer published a value of only  $a_0 = 0.22 \text{ mol H}_2/\text{mol CO}_2$  on 29 000 nm.

leaving a significant part of the cold structure uncovered. For full coverage we assume the preparation of at least 5 layers of frozen condensate to be necessary.

Based on these considerations, we propose a thickness of the argon layer between 300 - 3000 nm.

Unfortunately, the actual thickness of the condensate layers for a large cryopumping surface is difficult to infer. The test experiment TRAP (which is a scaled down version of the cryopumping part of the CPS by a factor of ten) has shown adequate results for an approximated thickness in the order of 1500 nm [Eic09], confirming our recommendations.

Combining these findings with the estimated cryopumping area of approximately  $3\text{ m}^2$ , the amount of argon to be injected into CPS (the only controllable parameter concerning thickness) should be in the order of 16.5 grams<sup>5</sup>, providing us with the theoretical capacity to adsorb  $N = 0.024$  mol of hydrogen isotopes.

As stated in section 3.3.1, the flow of HT into the CPS will be approximately  $4 \times 10^{-7} \text{ mbar l s}^{-1}$ . An amount of 1% of the theoretical maximum capacity will be reached after  $1.5 \times 10^7 \text{ s}$  (approximately half a year). After the planned pumping-cycle of 60 days an activity of  $9.13 \times 10^{10} \text{ Bq}$  or 2.47 Ci will be stored on the argon frost, occupying, however, only  $3.5 \times 10^{-3}$  of the calculated monolayer capacity.

**Dwelling Time on the Argon Frost** Now we calculate the dwelling time of tritium on the argon frost with respect to the operational temperature using the methods described in section 3.2.6 and hydrogen/argon data from [Hae89]. For an adsorption of hydrogen on argon the binding energy is  $E_B \approx 440 \text{ J mol}^{-1}$  between one hydrogen molecule and one argon atom [Hae89]. To estimate the expected number of binding partners, the crystal structure of argon has to be taken into account. Argon crystals feature a face-centered cubic structure (fcc lattice). This leaves a growth surface with either octahedral (111) or cubic (100) faces, rendering three or four nearest neighbors.

Calculations of the dwelling time  $\tau = \tau_0 e^{\frac{E_B}{RT_{Ar}}}$  for temperatures of 4.22 K and for 3 K are summarized in table 5.1. The values presented emphasize the importance of decreasing the cryopumping temperature below 4 K. It is to be noted that the migration of adsorbed particles will lead to a (slow) accumulation of the adsorbed tritium on the (100)-sites from where the possibility of further migration at 3 K is virtually excluded.

Decays of tritium stored on the argon layer will locally damage the frost structure. In addition, externally induced concussions could also cause significant tritium migration. These influences should be assessed later on using the techniques developed in the framework of the TRAP Experiment [Eic09].

<sup>5</sup>Assumed is an overall area of  $3.08 \text{ m}^2$ , an average layer-thickness of 3000 nm, and a density of solid argon of  $1.77 \text{ g cm}^{-3}$  [Dob58].

Table 5.1: **Dwelling Time  $\tau$  at different Temperatures**

Given are values for the dwelling time of hydrogen on argon with respect to the operational temperatures of CPS and with respect to the possible growth faces of the argon crystals.

Temperature	$\tau$ on (111)-surface	$\tau$ on (100)-surface
4.22 K	$2.16 \times 10^3$ s	$6.02 \times 10^8$ s
3.00 K	$9.49 \times 10^9$ s	$4.33 \times 10^{17}$ s

### 5.2.4 The Getter-Pump

As stated above, the insides of sections 6 and 7 of the CPS beam tube are equipped with NEG-strips, as shown schematically in figure 5.18.

In standard operation mode, technically no tritium should leave the cryopumping sections of CPS. Hence, these comparably small getter pumps are not considered part of the primary vacuum system. They do however come into use in the case of system malfunction. Its two main tasks are:

1. to prevent the build-up of residual gas when the cold gate valve is closed. The downstream side of the gate valve, if closed, would be at approximately 10 K. Accordingly, residual gas from the spectrometer side would condense there, which could disrupt further valve function.
2. to act as a "last resort barrier" in the case of a sudden cryopumping failure and corresponding excessive tritium release. As the large gate

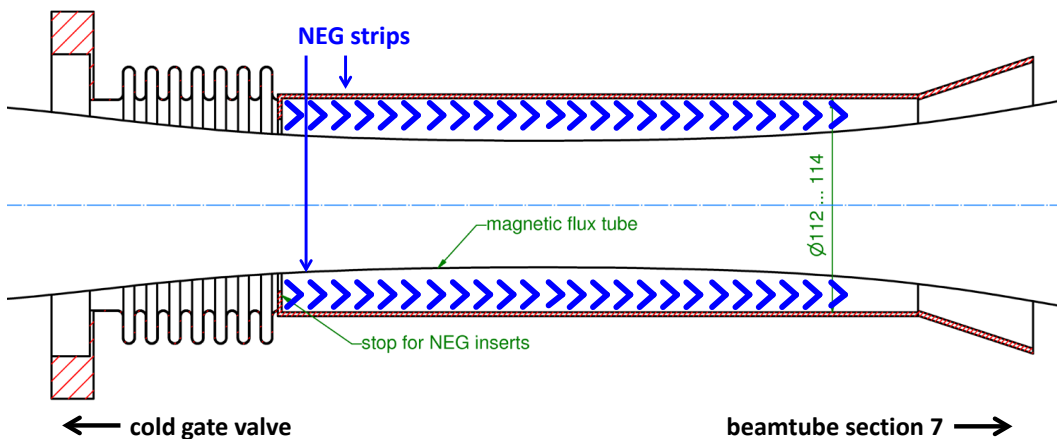


Figure 5.18: **Getter Pump in CPS Beam Tube Section 6**

Shown is a schematic view of beam tube section 6. Indicated in blue are the NEG-strip cartridges covering the wall of the beam tube. The figure is based on [Mul08].

valve needs a time period of over 15 seconds for full closure, tritium could escape during this time span towards the spectrometer section, thereby causing contamination. The NEG strips will mitigate this scenario.

Besides these safety-related tasks, the getter pump also guarantees for an adequate vacuum during calibration (cf. next section).

The getter pumps in segment 6 are operated at 77 K and in section 7 at room temperature (standard operation). They will provide a pumping speed of  $\approx 300 \text{ l s}^{-1}$ . Their exact length and geometry are yet to be determined, but experience gained during the commissioning of other KATRIN getter pumps (cf. chapter 3) will be used as input.

### 5.2.5 The Calibration Source

To map out the spectrometer filter characteristics over the entire transported flux tube, it is planned to use a calibration source, which is located close to the spectrometers. For adequate access of such a system, a large DN250 flange between the CPS beam tube sections 6 and 7 is foreseen.

We will use a  $^{83}\text{Rb}/^{83m}\text{Kr}$  system as  $\beta$ -emitter, with  $^{83m}\text{Kr}$  quench-condensed onto a highly oriented pyrolytic graphite (HOPG) substrate at approximately 30 K. The metastable isotope  $^{83m}\text{Kr}$ , produced by the decay of the  $^{83}\text{Rb}$  mother isotope, features distinct conversion lines close to the relevant energies of KATRIN. The energies from the preferred conversion lines (the "K-32" and the "L3-32") were estimated to be  $E_K = 17824.3(5) \text{ eV}$  and  $E_{L3} = 30472.3(5) \text{ eV}$  [Zbo11].

The condensed Krypton source is currently under construction at the University of Münster [Bau11]. A design study is shown in figure 5.19.

The source system consists of a zeolite container placed on top of CPS, in which  $^{83}\text{Rb}$  is stored. The  $^{83}\text{Rb}$  mother isotope decays into metastable  $^{83m}\text{Kr}$  atoms which emanate from the zeolite and are guided via a capillary into the beam tube of CPS and condensed onto the HOPG substrate.

To avoid a deterioration of the substrate by residual gases coming from the CPS beam tube, and to provide a more stable operating temperature, it is housed in a copper jacket which also collimates the conversion electrons to some degree.

As a result of the coil geometry at this position, the magnetic field lines widen between the beam tube elements 6 and 7, as can be seen in figure 5.16. By positioning the source in this regime, it is possible to transport an electron beam of then only  $1 \text{ mm}^2$  to the detector which enables us to check the transmission function of the spectrometer for each detector pixel individually.

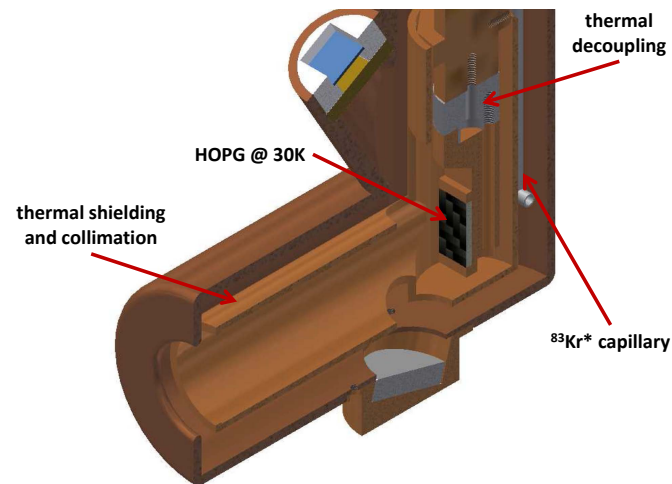


Figure 5.19: **Condensed Krypton Source in CPS**

Shown is a lateral cut through the condensed Krypton source as designed by [Bau11]. The  $^{83m}\text{Kr}$  isotope is guided through a steel capillary (on the right, only partially shown) to the HOPG (black, in the middle), where it condenses.

The calibration mode of CPS is essentially the standby mode of operation (see section 5.2.3.2), but with beam tube section 7 cooled to 77 K. The cold gate valve remains closed, and the source is inserted through the large duct behind section 6.

## Chapter 6

# Test Experiments at DPS2-F

The DPS2-F cryostat was delivered from the manufacturer ASG to KIT in July 2009. After successful installation and mounting the extensive commissioning works began in 2010. Detailed technical results of these initial tests on the level of acceptance tests can be found in the reports of the manufacturer [Par11]. In April 2011 the cryogenic system, the beam tube and cryostat vacuum, as well as of the superconducting magnet system were successfully commissioned. This thesis has contributed substantially to these works. After the validation of the basic functionality parameters of the system, we were able to investigate the physics performance of the DPS2-F cryostat. In this regard, a detailed test program of DPS2-F was designed in the framework of this thesis. The portfolio of experimental tests is presented in this chapter. The scientific aims, the corresponding setup and the results of the experiments are presented. In section 6.1 the tests concerning magnetic geometry are presented at first, section 6.2 then discusses electron-optical experiments. The scope of the ion suppression experiments is introduced in section 6.3. Then two sections are dedicated to vacuum tests. Investigations of general vacuum qualities are documented in section 6.4. In section 6.5 we finally present the most important experiments and results, which deal with the gas flow characteristics. The current state of DPS2-F and the implications of our measurements for the KATRIN experiment are summarized in section 6.6.

### 6.1 The Magnetic Geometry Measurements

The exact knowledge of the position and geometry of the superconducting magnet system is crucial for calculating local field strengths and assessing the electromagnetic transport characteristics of the beam line. Relying only on the manufacturer's documentation is viable as first order approximation only. As the KASSIOPEIA code allows an in-depth study of the electromagnetic system, more thorough magnet geometry tests revealing the as-built characteristics of

the system have to be carried out at DPS2-F.

The information obtained during this phase is vital to calculate mechanical forces between the modules (relevant for system integrity), for precision field mapping & understanding of the details of the electro-magnetic optics (relevant for signal electron transport). Additionally, the B-field stability (relevant for the estimation of systematic error) and stray field (relevant for the interaction with auxillary electronics) characteristics have to be investigated.

### 6.1.1 Setup of Magnetic Geometry Measurements

In the course of this work the magnetic field at DPS2-F magnet module 5 was investigated as follows.

The magnetic field strength was measured with a 1-dimension Hall-probe of the type MMA-2536-WL manufactured by LakeShore<sup>1</sup>. As read-out system a Gauss-meter from LakeShore was used. The probe was carried by a PVC tube, and an image of this device is shown in figure 6.1. To stabilize the temperature at the sensitive tip of the probe during the gradual insertion into the 80 K beam tube, warm gas at room temperature was led through the PVC tube to the Hall-probe.

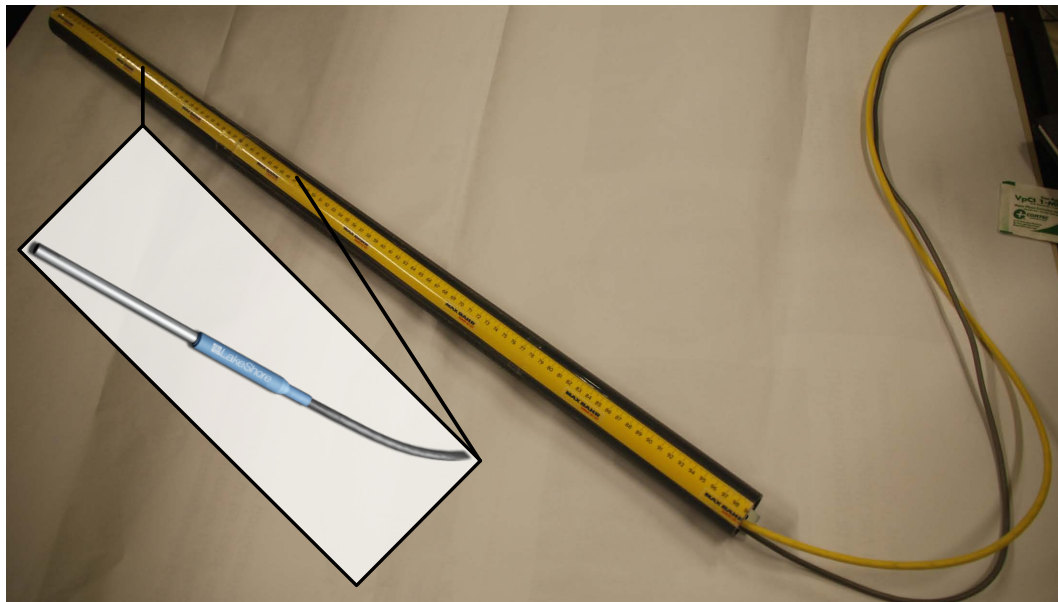


Figure 6.1: **Setup magnetic z-axis alignment**

The LakeShore Hall-probe is fixed inside a PVC tube which is inserted into a steel tube flange on axis of magnet module 5.

<sup>1</sup>For detailed information see: <http://www.lakeshore.com/products/hall-probes/axial-probes/Pages/Specifications.aspx>



The measurement of the local B-field was performed by pushing the PVC tube, and therefore the Hall-probe as well, through a blind flange with an attached tube of 1 meter length. The steps were varied between 1 mm and 1 cm, as can be seen in the measured data. To measure the step size, a millimeter scale on the PVC-Tube was used.

### 6.1.2 Results of Magnetic Geometry Measurements

In figure 6.2 the measured B-field values are juxtaposed to corresponding simulation data. The center of the module was found at an intrusion depth of 734.0 mm, measured from the outer face of the limiting flange, while the original design called for a depth of 731.5 mm. This corresponds to a discrepancy of 2.5 mm (cf. section 5.1.2, [Gil12b],[Kos11a]), which, however, is only slightly above the design tolerances.

We believe the displacement of the magnet module can be explained by a global shift of the whole DPS2-F magnet system, rather than by a displacement in relation to the other modules. The latter could have limiting consequences with regard to the transport capability of the unit, cf. section 6.2. This assumption is backed by studies of the thermal shielding carried out during the commissioning DPS2-F, which suggested a global shift of the inner radiation shield (which is borne by the same support structure as the magnets) by several

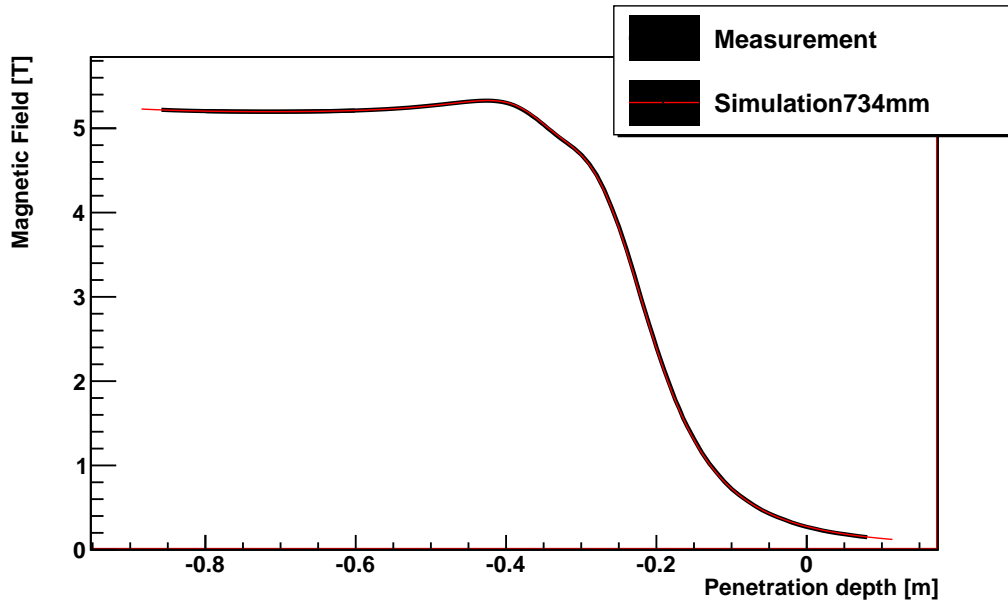


Figure 6.2: **Position of Magnet 5 DPS2-F**

Measured position of SC Magnets in Module V of DPS2-F. Comparison of measured B-field values and modified simulation over the intrusion depth measured from the outer side of the final flange in meter.

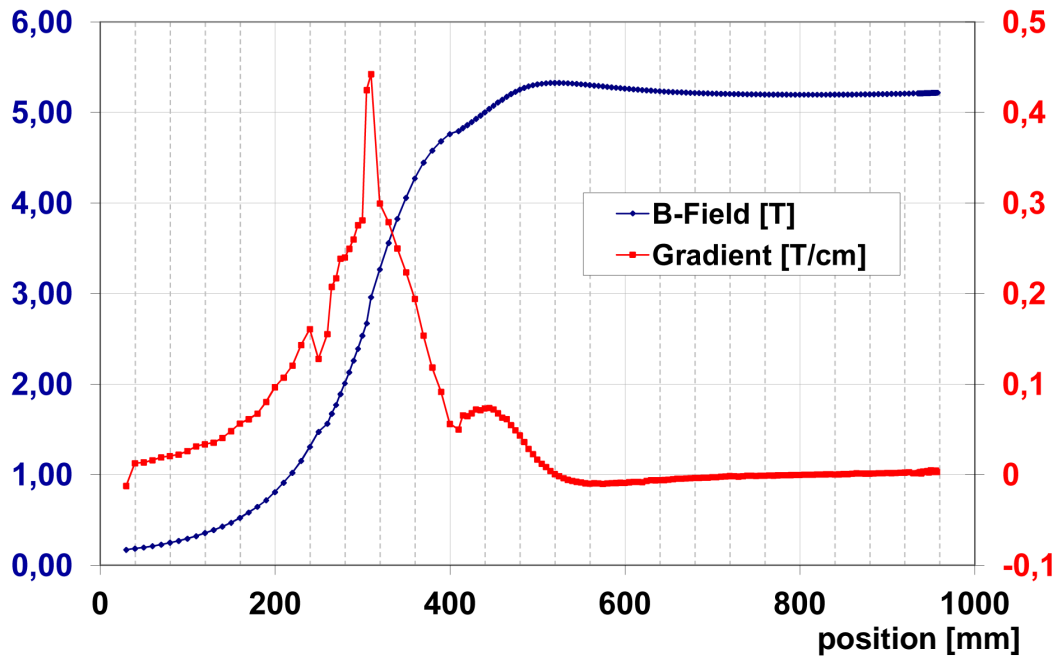


Figure 6.3: **Magnetic field and its gradient in Module 5 of DPS2-F**  
 The absolute strength of the on-axis B-field is plotted in blue (left axis), the gradient of the B-field along the z-axis is plotted in red (right axis) over the intrusion depth measured from the outer side of the final flange in mm.

millimeters, thus also decreasing the insulation quality of the cryostat [Put11]. Nevertheless, the measured discrepancy underlines the need for thorough electro-optic studies to ensure the optimal transport capabilities of DPS2-F.

Additional information on the magnet system in its as-built status were gained by the study of the absolute field values and the field gradient on axis, as given in figure 6.3. These field values will be used as a benchmark for the radial field studies that will be carried out within the framework of the electron-optical experiments (see the next section).

## 6.2 The Electron-Optics Measurements

A prime objective of the test program is to demonstrate that the DPS2-F is capable of transporting the signal bearing electrons from the source towards the spectrometer without changing their energy or momentum vector (in case of identical B-field strength). The goal of the electron-optical tests is thus to verify that the DPS2-F magnet and beam line geometry are suited to transport the full flux value of  $191 \text{ T cm}^2$  for  $18.6 \text{ keV}$  electrons without losses. First proposals for these electro-optical (or Beam Alignment Measurements) were made in [Ste10]. They can be grouped into two parts: the confirmation of the correct flux positioning, and the actual test of the intrinsic DPS2-F transport properties.

A setup using a vacuum feed-through manipulator was chosen, as schematically shown in figure 6.4. A small-scale Hall-probe is mounted onto the manipulator (e.g. a Hositrad RPLR manipulator), allowing a measurement precision better than 1%. The precision of positioning of the probe will be  $\leq 1 \text{ mm}$  in  $z$ -direction, while the azimuthal precision still has to be determined.

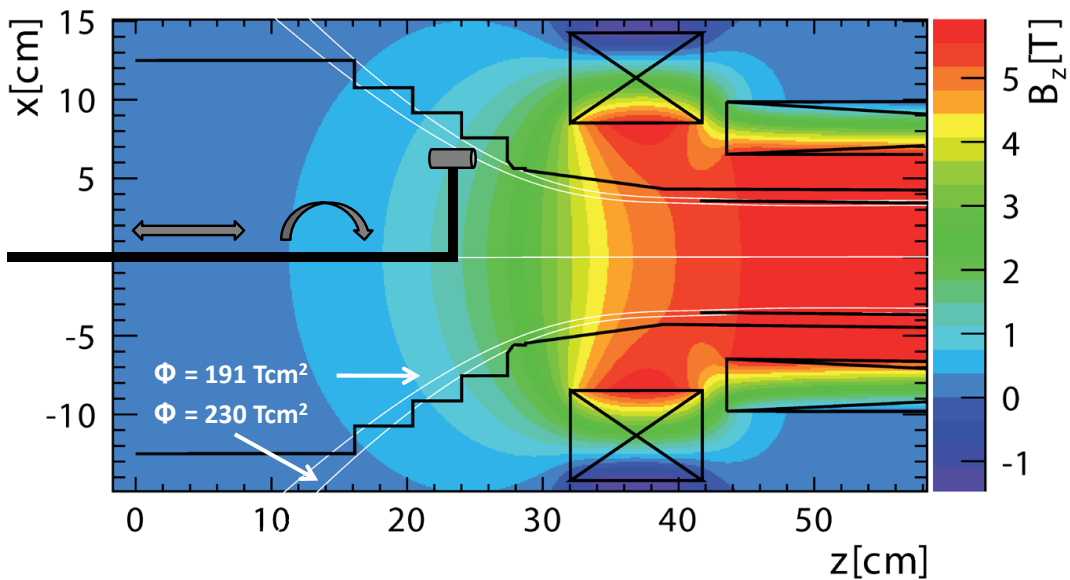


Figure 6.4: **Electro-Optic Experiment**

Shown is a simulated field map of the entrance area of DPS2-F. Marked in white are the flux tube edges, the inner one demarcating the important  $191 \text{ T cm}^2$  area. Placed in this area is a Hall-probe on an axially and azimuthally movable manipulator to verify the field geometry. For the transmission tests, the probe will be replaced by an electron source. Based on [Ste10].

### 6.2.1 Magnetic Mapping

The magnetic mapping has to be carried out first, to assess the exact local field strengths at the inlet and outlet of DPS2-F. The geometrical positioning of the electron source used later on has so far only been determined via simulations based on KASSIOPEIA. Since the investigations regarding the magnet positioning revealed distinct deviations between the documentation and the as-built geometry of the order of a few millimeters [Kos11a] (which is larger than the required accuracy for source positioning), detailed investigations regarding geometry and the validity of the  $B$ -field simulations have to be carried out.

### 6.2.2 Electron Transmission

On the edge of the DPS2-F flux tube, whose position has been determined beforehand, a solid  $^{83}\text{Rb}/^{83m}\text{Kr}$  (implanted in platinum) electron source will be placed and moved onto various azimuthal positions. It is housed in a 14 mm casing with a 1 mm aperture and will provide an activity in the order of 200 kBq. To provide adequate protection for the beam tube, a mechanical safety clearance of 5 mm will be ensured via suitable interlocks.

In the course of these measurements, a detector as described in [Sch10] is placed at the downstream exit of DPS2-F. It is designed with a front plate covering the whole flux tube and comprises 14 silicon PIN diode detectors of  $9 \times 9$  mm cross section by Hamamatsu. Twelve diodes are arranged in an outer circle to cover a "flux ring" with an inner edge of  $170 \text{ T cm}^2$  and an outer edge of  $230 \text{ T cm}^2$ . Three surface mounted Hall-probes and two Pt1000 temperature sensors as additional analytic tools are also placed on the detector holders' main surface. The unit is cooled indirectly by the DPS2-F beam tube, which is kept at 77 K.

The detector will be installed on-axis in the middle of the the DPS2-F exit flange, held by a manipulator providing on-axis mobility. Displacement along the  $z$ -axis, away from the DPS2-F flange, will give access to lower flux values. Taking into account both the detector and source efficiency, the small aperture of the source casing and magnetic mirroring in the DPS2-F beam line, a count rate between 1 and 10 transmitted electrons per second is expected.

The two main objectives of these investigations are the examination of the overall transmission probability, and, later on, to investigate any azimuthal displacement of the electrons.

These tests should be carried out as the very last preparative step before data taking. After proving an electron transmission factor of unity no further changes to the DPS2-F beam tube related parameters of the unit should be made.

## 6.3 The Ion Suppression Measurements

The design of the ion analysis and suppression system has been introduced in section 5.1.3. Since a complete mock-up of the DPS2-F beam line and magnet system was impossible to implement with reasonable effort, the first tests of functionality have to be carried out using the DPS2-F unit itself. Our aims in this experimental campaign are:

- Demonstrate the functionality of the FT-ICR analysis system.
- Investigate the quality and stability of the dipole system.
- Acquire optimal field (voltage) values for the ion suppression.

The original ion flux analysis and ion suppression system, featuring the two Penning traps and twelve through-shaped dipole-electrodes, as described in section 5.1.3, are installed as they will be later in the KATRIN standard operation mode.

### 6.3.1 Setup of Ion Source and Collector

**The Ion Source** An important task of the preparation of these experiments was the development of a suitable ion source to mimic the ion flux emitted later on from the WGTS (cf. section 4.1.2). Again, for safety reasons, tritium was not used at this point. Our ion source was therefore designed to allow for a series of tests with different (ionized) test gases.

The ion source Elliot III has been developed by our team in 2008 (previous to this work) and was tested at MPIK Heidelberg in 2009. A thorough technical description is given in [Zol09], while commissioning and scientific examination is described in [Luk11a]. It is depicted in figure 6.5.

Elliot III produces the required ion flux through the process of electron impact ionization of the residual gas inside a barrel-shaped electrode grid. The electrons are produced by illuminating a photo-cathode with UV-light emitted from a deuterium light source. The design of the ionization volume is based on highly efficient electron trapping (with multiple ionizations per primary electron), leading to a significant ion yield of up to 20 nA, which is comparable with the WGTS output. This allows to operate with residual gas pressures of  $<10^{-4}$  mbar, which is comparable with the pressure level in DPS2-F. The energy of the produced ions is typically several tens of eV, while the diameter of the ion beam is approximately 3 cm.

The source was designed for operations in high magnetic fields (corresponding tests were carried out at field values up to 4.7 T). Finally the source can be

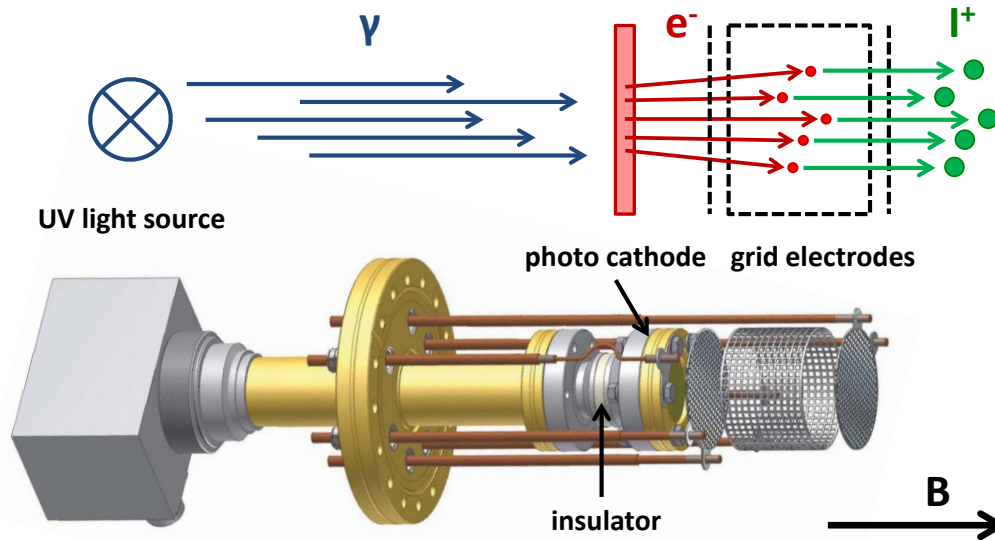


Figure 6.5: **Source for the Ion Experiments**

Shown is the Elliot III Ion Source. A UV-light source back-illuminates a gold-plated photo-cathode, from which electrons are emitted and captured in the barrel-shaped electrode grid put on positive potential so that they can ionize residual gas within. Based on [Luk11a].

used, due to its negligible heat dissipation, in an environment with cryogenic operating temperatures of 77 K.

The experimental combination of this source together with the FT-ICR analysis tools has also been tested successfully [Ubi09].

**The Ion-Collector** For a direct measurement of the produced ion flux a Faraday-Cup is used. This unit consists of a stainless steel plate acting as a cathode and a grid electrode to prevent a discharge of the electron flux from the plate. Two Faraday-Cups have been tested in Heidelberg during the commissioning of the source and the FT-ICR modules. These units are available now for KATRIN. They will cover the relevant magnetic flux-tube and can be interlocked with the frame of the FT-ICR modules. One of these cups will be used for the ion suppression test described here. It is installed at the downstream end of beam tube section 5 behind the downstream FT-ICR module. With this Faraday-Cup we are able to measure the ion flux (2 - 20 nA) that reaches the downstream end of DPS2-F.

### 6.3.2 Setup of the FT-ICR Modules

The FT-ICR module (as described in section 5.1.3.1) usually takes measurements via the following steps:

1. Ramp up the end cap potential to close the Penning trap and capture ions in the sensitive volume.
2. Apply the excitation frequency  $\omega_d$  in narrow-banded mode (of the order of several 100 kHz) to excite only a specific ion species, or in broad-banded mode (up to 20 MHz) for different species as described in section 4.3.1.2.
3. Measure, amplify and analyze the induced characteristic signal of the coherent ion movement, as depicted in figure 4.6.
4. Release the trapped ions by zeroing the end cap voltage.

As stated above, the FT-ICR modules and the ion source have been tested in combination. The separation of helium and deuterium ( $\Delta m/m = 6.25 \times 10^{-6}$ ) was successfully proven after an excitation time of several seconds only.

### 6.3.3 Measurement Scheme

After the installation of the two Penning trap-based FT-ICR units and the twelve through-shaped dipole electrodes, as described in section 5.1.3, and the initial evacuation and cool-down procedure of the DPS2-F, the following measurement scheme is proposed for the gas species hydrogen, deuterium, helium and neon:

1. The ideal pressure and the parameters of the electrostatic potential for the source are identified by measuring the transported ion flux reaching the Faraday-Cup in beam tube section 5. For this fine-tuning step the dipole electrodes and the Penning traps are offline and kept on beam tube potential (grounded). The aim is to measure a constant ion current of  $I_0 \geq 20$  nA.
2. The downstream end-cap electrode of the FT-ICR module in section #5 is put on potential. All ions produced are reflected here and again upstream at the barrel electrode of the source (comparable to the later on KATRIN scenario).
3. After some equilibration time of the order of some minutes the undisturbed, reflected ion density is measured with the FT-ICR modules.
4. The dipole voltage is increased by steps (the size of which still to be defined). The captured ion density is then recorded as a function of dipole voltage. The measurements should be repeated several times for each dipole voltage to check the stability of the suppression.

## 6.4 The Vacuum Quality Measurements

When commissioning and understanding a new vacuum system, it is always crucial to determine the volume, the outgassing rates and the composition of the residual gas. The corresponding tests concerning these qualities are described in this section.

Since the commissioning of DPS2-F revealed an inherent tendency of the magnet system for spontaneous quenching (see section 5.1.2.3) when operated close to the design current of 200 A, the strategic decision was made to refrain from activating the beam tube heaters for a bake-out cycle. To operate the vacuum system without bake-out makes the requirement for scrutinizing the outgassing characteristics of the primary vacuum containment reported here even more pressing.

Of particular interest in this context are fluorine compounds, because fluorine can damage the permeator membranes in the outer loop system of the closed tritium cycle (cf. section 2.2.3), once the DPS2-F is connected to it. Fluorine is typically found in the passivation layer of stainless steel surfaces in the form of compounds with iron and chrome where it is tightly bound. Further spots include areas where cleaning and welding chemicals have remained in the beam tube.

### 6.4.1 Setup of Vacuum Analysis

#### 6.4.1.1 Volume Assessment

The first objective of the test measurements was to estimate the volume of the primary vacuum system of the DPS2-F system by static expansion.

At first the vacuum system is evacuated using TMP #1. All other pumps and the collection system are decoupled from the beam tube. Different gases are then expanded from a buffer vessel of volume  $V_0 = 15.41(2)$  l (as can be seen in figure 6.6) into the DPS2-F primary vacuum containment immediately after closing the gate valve at pump port #1.

Special care is required for the setting of the expansion speed. In case of a too large expansion speed, the process of adiabatic cooling will occur. This in turn will lower the measured pressure and cause a heightened value for  $V_{BT}$ . On the other hand, for too low expansion speeds the contributions from the outgassing of compounds in the beam tube vacuum will render a reduced volume value. From fine-tuning investigations an optimum expansion time of approximately 2 minutes was found for this procedure.

Then a total of three expansion runs using neon, and a further three runs using argon were carried out.



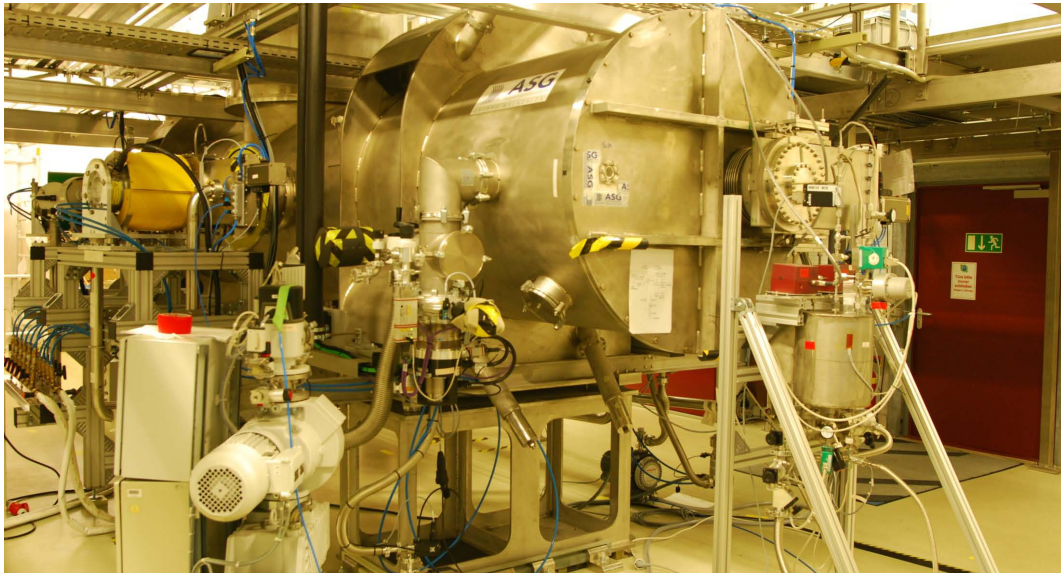


Figure 6.6: **DPS2-F in Volume Assessment Setup**

Shown is the DPS2-F module fully instrumented for volume assessment. On the right-hand side the injection system with the buffer vessel used for the controlled gas expansion can be seen.

#### 6.4.1.2 Outgassing Analysis

To thoroughly study the residual gas background, as well as global outgassing rates, several tests have been carried out. An overview of the vacuum system setup is shown in figure 6.7. The tests were carried out as follows [Kos10b].

**Measurement of the Outgassing Rate** After evacuation of the beam tube and pump-down with one Leybold MAG 2800 turbomolecular pump (VP231) for about 5 hours, the gate valve towards the pump (AV231) was closed, and the subsequent pressure rise was monitored over a time period of 12 minutes. Then the valve was opened again and the accumulated residual gas was pumped out. This procedure was repeated three times. During the second and third test, the mass spectrum of the residual gas was recorded with a Residual Gas Analyzer, and absolute pressure values were taken with four identical MKS IM 422 cold cathode vacuum sensors (RP 2X2).

**Measurement of the Residual Gas Spectrum** After the gate valve was closed, the mass spectrum of the residual gas up to mass values of 100 a.m.u. was cyclically recorded five times during equal time intervals. The scan speed was 1 s per mass unit, and the next scan started immediately after the completion of the previous one. Thus the difference between successive spectra represents the mass spectrum of the accumulated gas during 100 s. Because of large pressure differences in the system during the pumping with the MAG

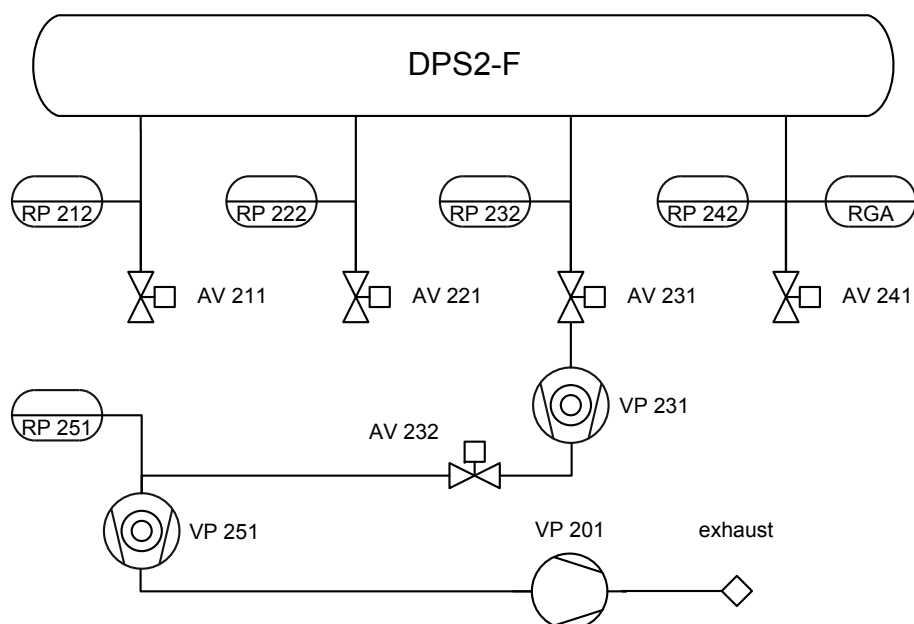


Figure 6.7: **Outgassing Measurements, schematic**

Shown is the setup of the outgassing measurements of the primary vacuum containment of DPS2-F (beam tube, pump ports, ducts etc.). The pressure gauges used are MKS cold cathode vacuum sensors, the RGA is a Pfeiffer QMS200 Prisma.

pump, the gas redistributes in the system for quite some time after closing the valve. After approximately 150 s the pressure readout in all four pump ports reached the same level, i.e. within the readout tolerances of the cold-cathode sensors.

## 6.4.2 Results of Vacuum Analysis

### 6.4.2.1 Volume of the primary Vacuum System

The results of the volume calibration are given in table 6.1. Six independent assessments of volume were carried out, three thereof using neon and argon each. After taking into account the buffer vessel volume of 15.41 l and neglecting outgassing effects (which are of the order of  $10^{-5}$  mbar), we conclude a value of  $V_{BT} = 329.36(77)$  l.

### 6.4.2.2 Outgassing Values

After evacuating the DPS2-F via the turbomolecular pump VP 231 (see figure 6.7) for approximately 5 hours, the absolute pressure in the DPS2-F reached values between  $2.2 \times 10^{-6}$  mbar at pump port 1, and  $9.5 \times 10^{-7}$  mbar at pump

Table 6.1: **Volume of the DPS2-F Beam Tube**

The values are measured via two sets with three different runs each using argon and neon at operational temperature ( $\approx 77$  K). Given are the mean values for each gas and the corresponding standard deviations, as well as the total mean value for all measurements.

run	pressure [mbar]	Volume [ $\ell$ ]
Ne 1	8.37	330.05
Ne 2	13.86	330.15
Ne 3	31.24	329.37
$\langle \text{Ne} \rangle$		$329.86 \pm 0.35$
Ar 1	46.32	327.83
Ar 2	26.83	329.19
Ar 3	17.94	329.55
$\langle \text{Ar} \rangle$		$328.85 \pm 0.74$
total mean		$329.36 \pm 0.77$

port #4. At pump port #3, through which the vessel was evacuated, an absolute pressure of  $7.7 \times 10^{-8}$  mbar was found before equilibration. For the estimation of the overall outgassing rate, the pressure values from all four pump ports (RP 212, 222, 232 and 242) were averaged.

Figure 6.8 shows the pressure rise in the DPS2-F beam tube over time. The errors displayed are estimated in units of standard deviation. The beam line volume was estimated to  $V_{\text{BT}} = 329.36(77)$  l, while the beam line surface amounts to an area of approximately  $A_{\text{BT}} = 1.0 \times 10^5$  cm<sup>2</sup>. Taking into account these values, the overall outgassing rate is calculated to  $Q_{\text{BT}}^{\text{out}} = 8.42 \times 10^{-6}$  mbar ls<sup>-1</sup>, corresponding to a value of  $8.42 \times 10^{-11}$  mbar ls<sup>-1</sup> cm<sup>-2</sup> per unit area.

#### 6.4.2.3 Mass Spectrum of the residual Gas

Figure 6.9 shows the differences of the mass spectra in cycles #5 (started 400 s after closing the valve) and #3 (started 200 s after closing the valve). The major groups of peaks correspond to common components of the residual gas: hydrogen (H<sub>2</sub>) at mass 2, water (H<sub>2</sub>O) at masses 16-20, nitrogen (N<sub>2</sub>) at masses 28, 29, 14 and 15, carbon monoxide (CO) mainly influencing the mass peak at 28 and carbon dioxide (CO<sub>2</sub>) at masses 44 and 12, also contributing to the peaks at masses 28 and 16. The high relative intensity of the peak at mass 32 from O<sub>2</sub><sup>+</sup> might be due to the relatively short pumping time before the test, since oxygen is usually removed from vacuum vessels much faster than nitrogen

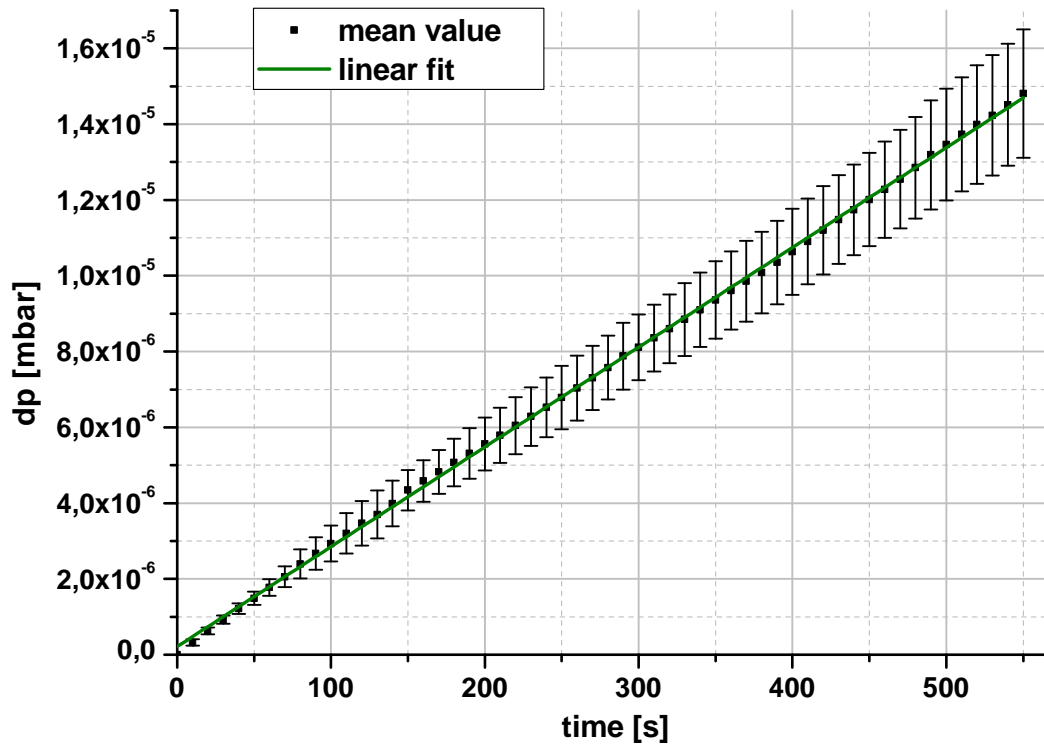


Figure 6.8: **Outgassing Rates DPS2-F**

Evaluated on basis of test run #3 with the closed primary vacuum system (beam tube and pump ducts; gate valves closed). Errors are given by standard-deviation

or water. The intensity of this peak should be rechecked in an outgassing test after the instrumentation of the beam line is complete.

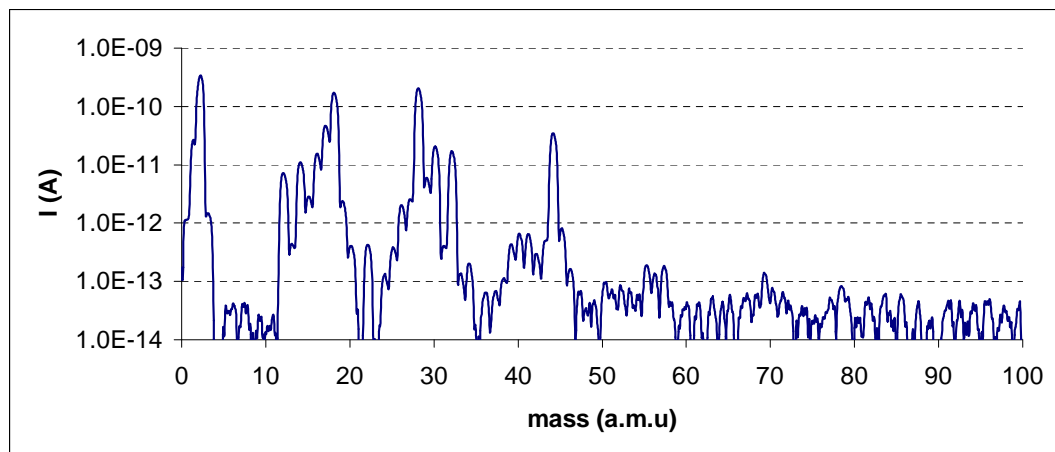


Figure 6.9: **Outgassing Spectrum**

Mass spectrum of the residual gas accumulated in the DPS2-F beam tube over 200 seconds.

**Fluorine** Interestingly, potential peaks corresponding to ions and ion fragments of fluorine compounds were all at the level of the background. Since fluorine is very reactive, also fluorine compounds with carbon and nitrogen were analyzed as well as  $F_2$ . The species  $F^+$  and  $HF^+$  ions were not analyzed since the peaks at corresponding masses (19, 20) contain strong contributions of water.

The analyzed peaks of the fluorine compounds are summarized in table 6.2. Only traces ( $\leq 1.0 \times 10^{-9}$  mbar  $l s^{-1}$  for each species) of all these compounds could be detected. The total rate of fluorine containing compounds was estimated to be below a value of  $1.0 \times 10^{-8}$  mbar  $l s^{-1}$ , judging from the ratio of the intensities of the potentially fluorine containing peaks to the sum of major peaks in the spectrum<sup>2</sup>.

Table 6.2: Most Important Fluorine Compounds

m/q	Compound	Ion
38	$F_2$	$F_2^+$
69	$CF_4$ , $CHF_3$ , $C_2H_2F_4$ ...	$CF_3^+$
51	$CHF_3$	$CHF_2^+$
50	$CHF_3$ , $CCl_2F_2$	$CF_2^+$
85	$CCl_2F_2$	$C(^{35}Cl)F_2^+$
87	$CCl_2F_2$	$C(^{37}Cl)F_2^+$
52	$NF_3$	$NF_2^+$
33	$NF_3$ , $C_2H_2F_4$	$NF^+$ , $CH_2F^+$
75	$FeF_3$ , $FeF_2$	$FeF^+$
94	$FeF_3$ , $FeF_2$	$FeF_2^+$
71	$CrF_3$	$CrF^+$
90	$CrF_3$	$CrF_2^+$

<sup>2</sup>Intensities of the major peaks were weighted by the inverse of the corresponding ionization probability. Relative ionization probabilities were taken from Leybold Vacuum [Ley98].

## 6.5 The Gas Flow Measurements

The measurements related to the precise gas flow analysis in DPS2-F form the experimental cornerstone of this thesis. They were carried out by the STS vacuum group in 2010 and 2011 and are thoroughly described and published in [Luk12].

The main goal of these experiments was the measurement of the gas flow reduction factor  $R_{\text{exp}}$  of DPS2-F thus confirming the earlier values obtained by calculations ( $R_C$ ) and simulations ( $R_{\text{MC}}$ ) as described in section 4.2. In the course of this work a thorough calibration of the vacuum sensors connected to the DPS2-F was carried out as well [Luk11b].

### 6.5.1 Setup of Gas Flow Measurements

The full setup for assessing the volume, gas flow and reduction factor measurements is shown schematically in Appendix A.3. The experimental setup of the vacuum studies can be grouped in three units:

- the DPS2-F vacuum system itself (part numbers with leading 2).
- the injection system upstream of DPS2-F for finely tunable gas loads (part numbers with leading 1).
- the collection system downstream of DPS2-F, which mimics the CPS influences and contains the most relevant analysis tools (part numbers with leading 3).

#### 6.5.1.1 The Injection System

The injection system for DPS2-F allows for a controlled and stable gas flow injection into the beam tube volume corresponding to the loads expected from the WGTS (i.e. the DPS1-F). The setup is shown in detail in figure 6.10.

The injection system is connected to the beam line via the upstream gate valve of DPS2-F. Its central element is a buffer vessel of volume  $V_0 = 15.41(2)$  l with a gas supply stream (highlighted in blue) connected to a gas cabinet. The test gases utilized (D, He, Ne, Ar, Kr) had a purity of 99.99% or better.

The flow controller RV 101 (an MKS flow controller with a range of  $10^{-4}$  -  $10^{-2}$  mbar l s<sup>-1</sup>; see Appendix A.2) is used to keep the pressure in the buffer-vessel constant, while slowly injecting test gases through the gas distribution stream (highlighted in green) into the DPS2-F beam tube.

The pressure in the buffer vessel is monitored via the high pressure gauge RP 102. The flow into the DPS2-F system is controlled by the RV 102 component

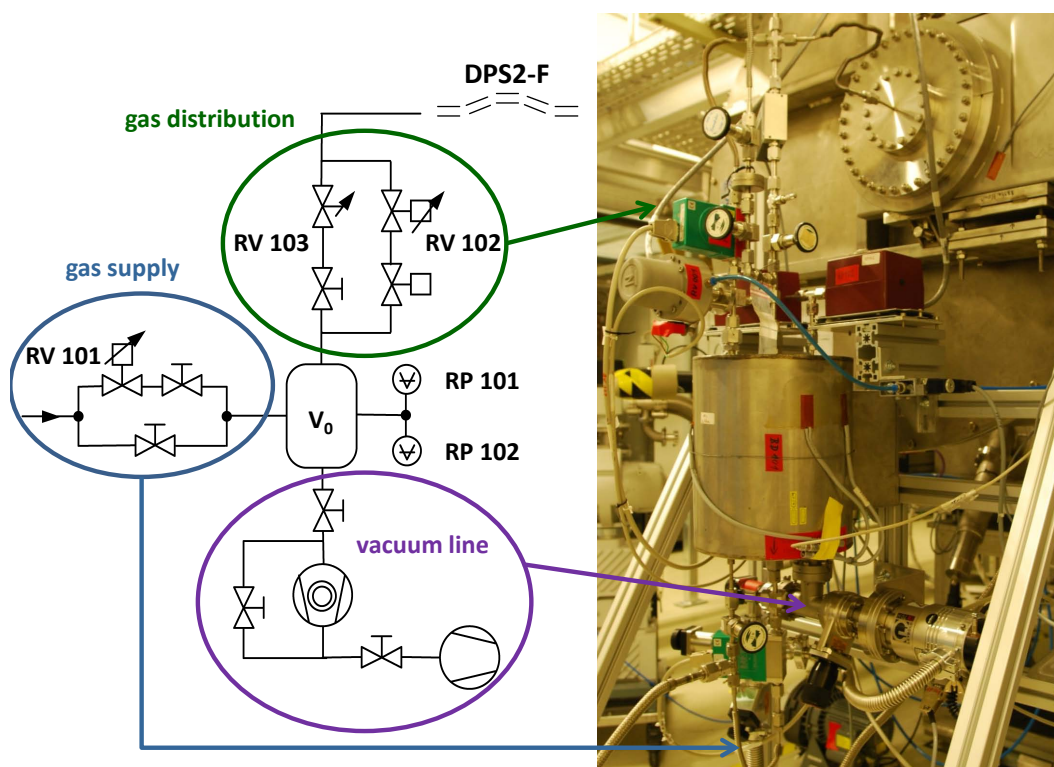


Figure 6.10: **Injection System Gasflow Experiments**

Highlighted are the gas distribution streams into DPS2-F (green), the gas supply stream connected to a gas cabinet (blue), and the evacuation line (purple).

(in case of low flow rates), or the manual needle valve RV 103 (high flow rates). The injection system can be evacuated separately from the DPS2-F beam tube over a TMP roughing pump combination (highlighted in purple).

### 6.5.1.2 The Collection System

The collection system is designed and built to analyze the remaining gas flow after passing through DPS2-F. The setup is shown in figure 6.11.

The collection system is connected to the downstream gate valve of DPS2-F. It features a large cryopump ( $800\text{ l s}^{-1}$  for nitrogen; highlighted in blue), which, in combination with a TMP, provides vacuum conditions comparable with the downstream CPS setup later on. All vacuum preparations and regenerations of the cryopump are carried out by a TMP-roughing-pump-combination installed in parallel.

Given the very low partial pressures of the test gases at this point (of the order of  $10^{-7}\text{ mbar l s}^{-1}$ ), and the potential systematics related to outgassing of residual gases, a mass selective quantitative study of the remaining gas flow is necessary. This is realized by incorporating a residual gas analyzer (a Pfeiffer



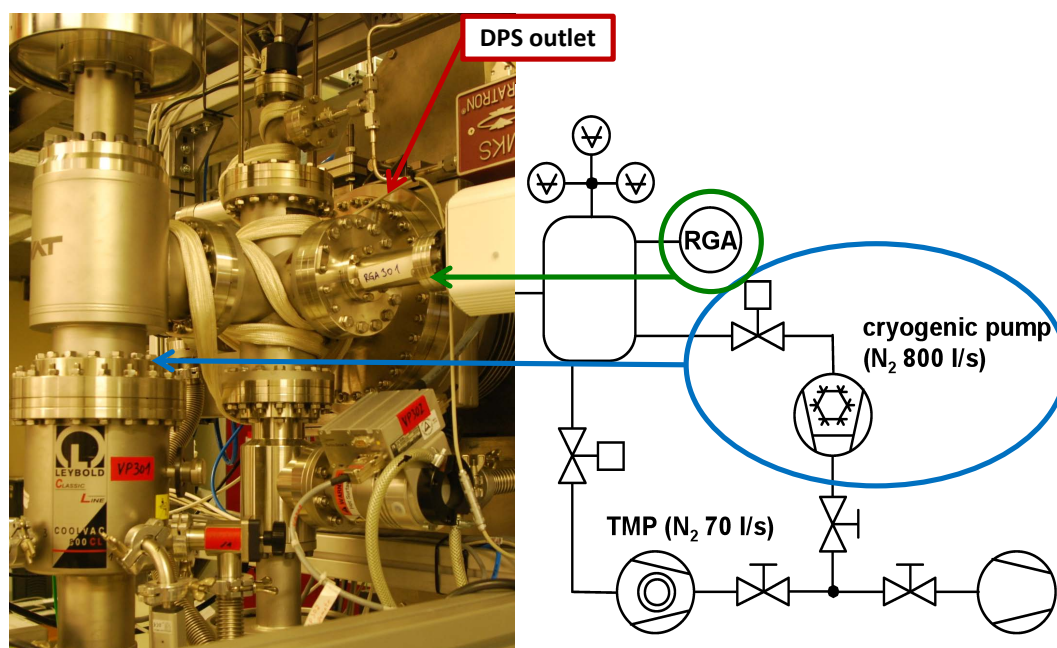


Figure 6.11: **Collection System of the Gas Flow Experiments**

The cryopump, providing an effective pumping speed comparable to the CPS, and the residual gas analyzer are visible, both on the left-hand side photograph, as well as on the schematic overview on the right-hand side. The connection to the DPS2-F beam line via the downstream valve, located in the back.

Prisma M200, highlighted in green; see appendix A.2). This unit can, after adequate calibration, be used for quantitative studies.

The thermodynamic parameters of pressure (integral) and temperature are monitored by an array of sensors mounted onto the volume between the beam line and the cryopump.

**Calibration of the Collection System** The use of a residual gas analyzer for accurate quantitative studies requires a thorough calibration beforehand. The goal of the calibration is to establish a constant conversion factor between the gas flow (i.e. the particle density) on the one hand and the RGA-generated ion current on the other hand, which can be assumed to be constant for a constant gas flux in the free molecular regime.

Given its nature, the calibration had to be performed with all relevant components in the same setup as later on during the "real" experiments, and also with the gases used later on. Accordingly, the configuration of the injection and collection system was used as described in the previous section. These units were connected via a CF-250 gate valve, identical to the ones used at the upstream and downstream end of DPS2-F. To provide a homogeneous distribution of the injected gas over the whole area of the entrance flange of the collection system (which is comparable to the distribution of gas after passing



through the DPS2-F beam tube), a custom-made diffuser was installed between the injection system and the gate valve. The diffuser was designed and manufactured as a cylindrical deepening in a blind flange covered with a steel plate with 1400 holes of 1 mm diameter, as schematically depicted in figure A.5 in the Appendix.

Since the expected gas flow after passing the DPS2-F (hence the calibration gas flow) is of the order of  $10^{-7}$  mbar l s<sup>-1</sup>, commercially available flow controllers could not be used, given their rather large inaccuracy at these low flow rates and pressures. Instead a metal disc of 0.7 mm strength with an 0.1 mm drilled orifice was installed between the buffer vessel of the injection system and the diffuser (parallel to the injection streams, marked in green in figure 6.10). This disk featured a very small conductance of  $L_{\text{He}} = 2.67(6) \times 10^{-4}$  l s<sup>-1</sup>, which was measured by recording the pressure rise in the collection system, while keeping the pressure in the injection system stable at values between 0.6 - 0.8 mbar. The value of this gas dependent conductance can be adapted when dealing with other test gases using equation 3.5.

The completed setup allowed for an accurate regulation of gas flow rates in the range from  $10^{-6}$ - $10^{-8}$  mbar l s<sup>-1</sup> by controlling the pressure in the buffer vessel. For each flow rate value, the corresponding RGA current is recorded, and subsequently the calibration factor  $k$  is determined via the relation:

$$k_{\text{gas}} \cdot I_{\text{RGA}} = Q = L_{\text{gas}} \cdot p_{\text{buffer}}. \quad (6.1)$$

The calibration measurements were carried out over the entire pressure range mentioned above, thus covering two orders of magnitude. The resulting ion current generated by the RGA was recorded and showed excellent linearity. Exemplary calibration curves can be found in figure 6.12. The calibration factors  $k$  obtained are given in table 6.3.

In spite of the very satisfying calibration results, a conservative systematic error of 10 % was assigned for the later measurements. This was based on the rather poor reproducibility of the measurements<sup>3</sup>, and in view of the necessary disassembly, relocation and recommissioning of the measurement setup from the test laboratory to DPS2-F, and finally owing to the fact that several calendar months passed between calibration and final measurements.

### 6.5.1.3 Measurement Scheme

**Pumping Speed** For the empirical study of the effective pumping speed  $S_{\text{eff}}$  of the TMPs (representing the fundamental and most important factor for the gas flow MC simulations; cf. section 4.2), we use only the first pump port with

<sup>3</sup>Over four weeks, several measurements for helium were carried out in the same setup. A spread between the calibration factor of 12 % for filament 1 and 5 % for filament 2 of the RGA was recorded (cf. [Win10]).

Table 6.3: Calibration Factors for Gas Flow Experiments

Measurement of the calibration factors  $k$  for the residual gas analyzer used in the reduction factor test experiments at DPS2-F. A total of two RGA filaments and five different gases were experimentally assessed. For the further calculations we assume a relative error of 10%.

Gas	$k$ Filament 1 [mbar l A <sup>-1</sup> s <sup>-1</sup> ]	$k$ Filament 2 [mbar l A <sup>-1</sup> s <sup>-1</sup> ]
D <sub>2</sub>	$8.2 \times 10^5$	$7.4 \times 10^5$
He	$1.4 \times 10^6$	$1.1 \times 10^6$
Ne	$2.1 \times 10^6$	$1.2 \times 10^6$
Ar	$8.1 \times 10^5$	$3.1 \times 10^5$
Kr	$1.6 \times 10^6$	$5.1 \times 10^5$

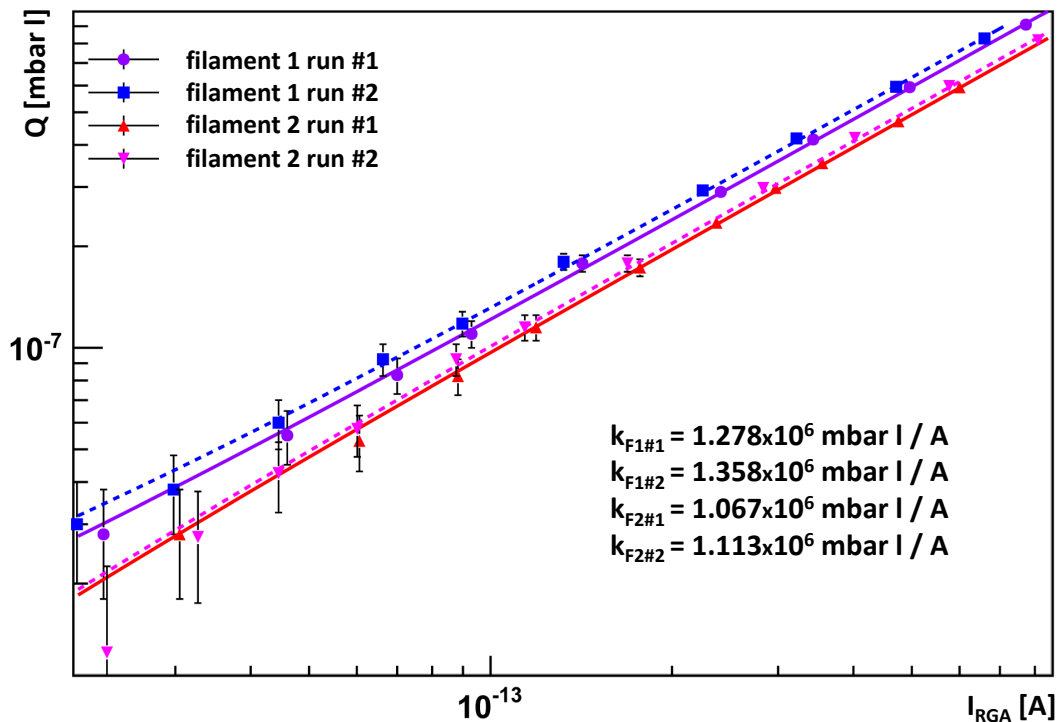


Figure 6.12: RGA Calibration for Helium

An exemplary calibration curve for Helium is presented. Displayed with the gas flow rates over the resulting ion current measured with the RGA at the corresponding mass peak. Also given are the resulting calibration constants  $k$  as used in equation 6.1. The variations over time, as described in section 6.5.1.2, can also be noticed. Based on [Win10].

TMP #1 running, while the gate valves of the three remaining ones are closed to prevent a net gas flow downstream of pump port 1. The collection system is decoupled as well.

The strategy of these measurements is to deduce  $S_{\text{eff}}$  by measuring the flow  $Q$  into DPS2-F and the corresponding pressure  $p$  in pump duct #1 for several different flow rates and gases. As stated in sections 3.2 and 4.2, the pumping speed can be deduced via the  $Q/p$ -ratio. This is not directly possible for the bare pump itself, but for the theoretical pumping area at the location of the pressure measurement. Thus the measurement renders not  $S_{\text{TMP}}$ , but the already discussed parameter  $S_{\text{eff}}$ .

In our case the pressure  $p$  was measured with a calibrated Baratron gauge RP 211 (see Appendix A.1) in the upper CF40 flange of the pumping duct at a distance of 230 mm from the TMP flange.

The gas loads are distributed into the beam tube through the manual needle valve RV 103 in the injection system. The corresponding flow rate can be calculated through the pressure drop in the injection buffer  $Q = V\dot{p}_{\text{buffer}}$ . The pressure  $p_{\text{buffer}}$  is measured via the gauge RP 102 (figure 6.10). For a short measurement time and a relatively low pressure drop rate, the flow rate, which is proportional to  $\dot{p}$ , can be assumed to decrease linearly. The setup was designed for a limited pressure gradient of  $< 1 \times 10^{-4} \text{ s}^{-1}$ .



Figure 6.13: DPS2-F in Gas Flow Test Setup

Shown is the DPS2-F module, fully assembled and instrumented for gas flow studies. On the left side the collection system is visible. On the right side two of the four large TMPs with their shielding (in green and yellow) can be seen.

The accuracy of the flow determination by means of this method can be cross-checked by direct comparison with the mass-flow meter RV 101, which determines the compensating gas flow into the buffer vessel. The systematic error of this procedure is assumed to be of the order of 1 %, arising from the combined uncertainties of the pressure gauges, the volume of the buffer vessel, and the mass-flow meter for the cross-check. The corresponding results are presented in section 6.5.2.

**Reduction Factor** Finally we address the reduction factor measurements themselves. These were performed at room temperature for a variety of flow rates ranging between 0.0018 - 0.020 mbar l s<sup>-1</sup> for deuterium, and 0.0025 - 0.028 mbar l s<sup>-1</sup> for the four noble gases investigated.

The previous calibration of the RGA allowed for a conversion of the RGA current signals into output flow rate values, thereby rendering the reduction factors for the DPS2-F in this test setup. The measured reduction factors, however, are not identical to the ones in the final KATRIN setup. Inevitably, the capture factor of CPS will differ from the one of the collection system used in this work. These corrections and the final results are presented below.

## 6.5.2 Results of Gas Flow Measurements

**Capture Factor** The effective capture factor  $S_{\text{eff}}$  for each test gas is derived by calculating the  $Q/p$ -ratio for various flow rates. An exemplary evaluation is depicted in figure 6.14.

The figure shows the effective pumping speed  $S$  (highlighted in red and purple), and the gas flow rate  $Q$  as a function of the measurement time given in seconds. This graph corresponds to the helium run #2 carried out at pump port #1 at room temperature.

Results for the measurement of the effective capture factors  $S_{\text{eff}}$  for all test gases are presented in table 6.4.

The uncertainties of  $S_{\text{eff}}$  arise mainly due to the scattering of  $p_{\text{buffer}}$  from which  $Q$  is calculated. As is shown in figure 6.14, the parameter  $Q$  is particularly sensitive to instabilities of the pressure signal. Therefore a series of approximately 300 pressure values taken at a rate of 1 s<sup>-1</sup> were used to minimize this uncertainty.

In figure 6.15 the obtained capture factors  $\alpha_{\text{eff}}$  are plotted over the logarithm of molecular mass. The observed logarithmic dependence is in good agreement with values reported in the literature and previous studies by the KATRIN Collaboration [Mal07]. A slightly higher capture factor for neon (if compared to the other species) has been observed in several studies without satisfying explanation. Since neon is of no further importance for KATRIN, and the

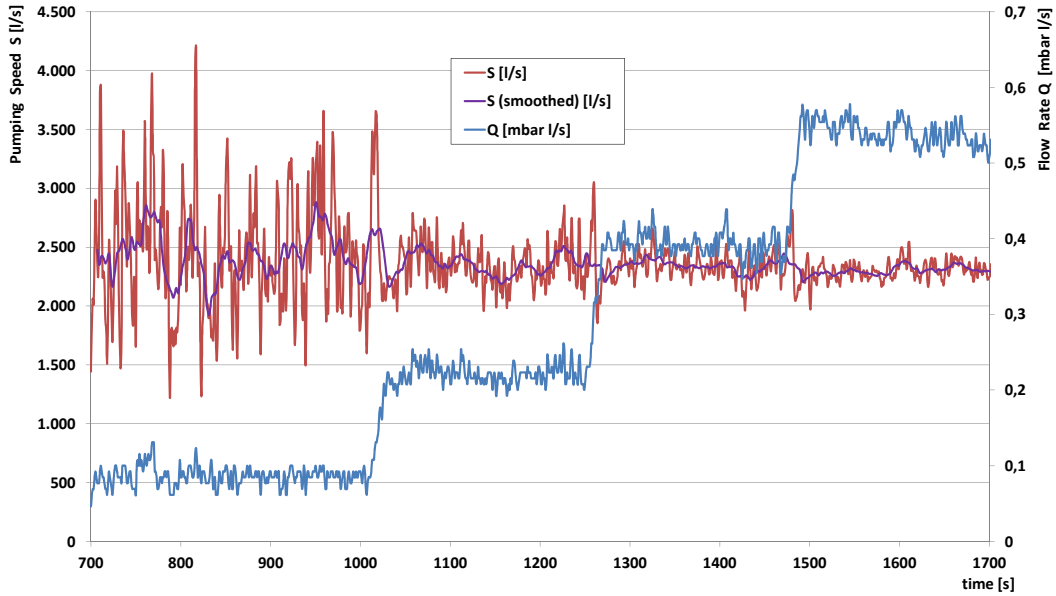


Figure 6.14: **Pumping Speed Helium Run #2**

Plotted are the measured flow rate of helium (blue) and the resulting effective pumping speed (red; smoothed in purple) of the TMP #1 at room temperature.

deviation is rather small, no follow-on investigations concerning this effect have been carried out.

The data displayed in figure 6.15 was fitted with the functional dependence  $\alpha = a_0 + a \cdot \ln(M)$ . After linear regression we obtain fit values of  $a = 0.0822(33)$  and  $a_0 = 0.0485(10)$ . Based on these values, a capture factor for tritium  $\alpha_{\text{eff}}^{(\text{T}_2)} = 0.196(8)$  was interpolated.

As stated in section 4.2.3.2 the values based on room temperature measurements will be improved when the beam tube is operated at its nominal op-

Table 6.4: **Effective Capture Factor of TMPs**

Given are the measured effective pumping speeds and capture factors for  $\text{D}_2$ , He, Ne, Ar and Kr at room temperature.

Gas	Mass [a.m.u.]	$\bar{v}$ [m s <sup>-1</sup> ]	$S_{\text{eff}}$ [l s <sup>-1</sup> ]	$\alpha_{\text{eff}}$
He	4	1246.0	2440(36)	0.162(2)
D <sub>2</sub>	4	1246.0	2368(41)	0.157(3)
Ne	20	557.2	2074(52)	0.308(8)
Ar	40	394.0	1672(42)	0.351(9)
Kr	84	271.9	1336(13)	0.407(4)

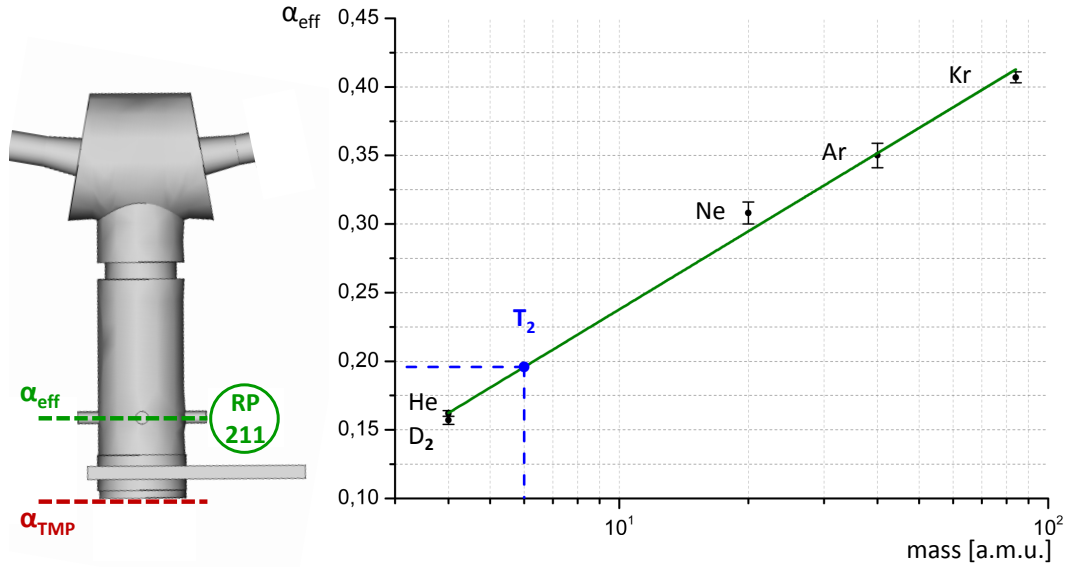


Figure 6.15: **Effective capture factor TMPs**

Plotted are the measured effective capture factors for D<sub>2</sub>, He, Ne, Ar and Kr at room temperature. Interpolated (marked in blue) is the room temperature value of  $\alpha_{\text{eff}}$  for tritium.

erational temperature. On the other hand, cold gas coming from the 77 K beam tube will then be thermalized very quickly on its way to the pump when hitting the thermally decoupled pump ducts, or at the first rotor of the TMP, thus reducing this effect. Nevertheless we expect a measurable increase of  $\alpha_{\text{eff}}$  of the order of several percent. Further testing at operational temperature, after the repair of DPS2-F, is therefore highly recommended.

**Reduction Factor** Using the setup described in section 6.5.1.3, and the calibrations described in section 6.5.1.2, the reduction factor of DPS2-F in combination with the collection system  $R_{\text{CS}}$  was evaluated for the test gases via direct measurement. These important results are summarized in table 6.5 and displayed graphically in figure 6.16.

To obtain a value for the reduction factor that is more comparable with the standard KATRIN operation mode, modifications related to the CPS were carried out as follows.

Even though the collection system was designed to mimic the CPS properties as close as reasonably possible, there remains a small difference between the capture factors  $\alpha_{\text{CS}}$  and  $\alpha_{\text{CPS}}$ . Qualitatively speaking, if the capture factor of the CPS exceeds the one ( $\alpha_{\text{CS}}$ ) of the collection system, the reduction factor  $R_{\text{final}}$  of DPS2-F would be lower than  $R_{\text{CS}}$  due to smaller value of  $w_{i,6}$  resulting from a decreased probability of gas particles streaming back into the DPS2-F beam tube (cf. section 4.2.2). Both  $\alpha$ -values are not known a priori.

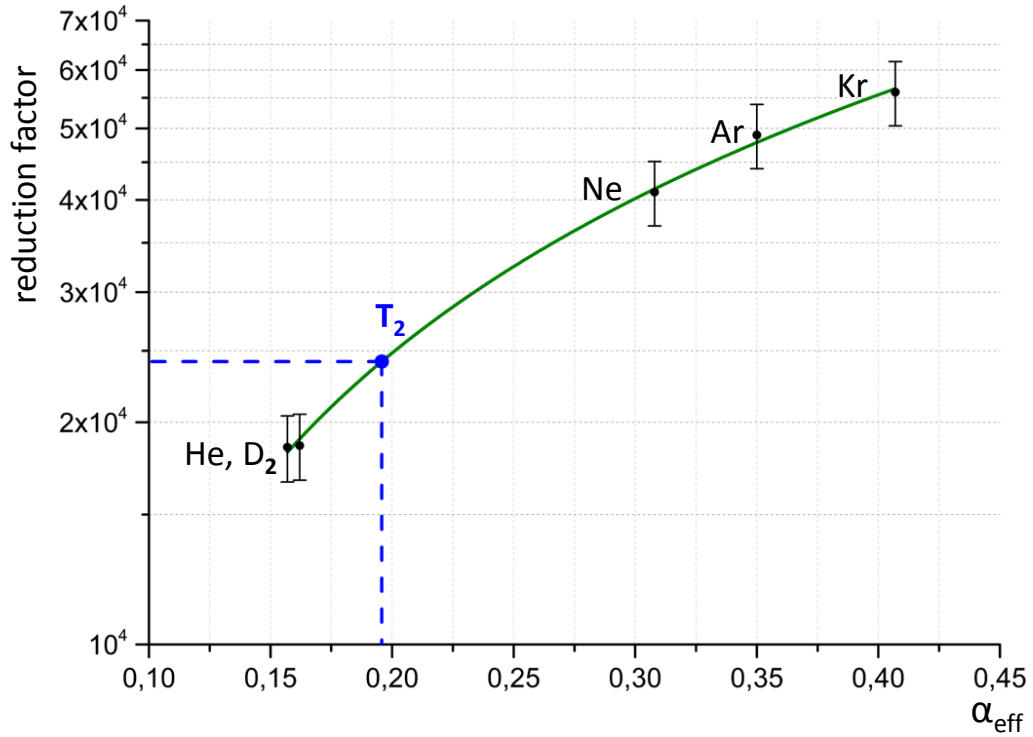


Figure 6.16: **Reduction factors of DPS2-F and Collection System**

Based on the measured values and interpolations without the calculated correction of CPS attached. The Value for Tritium (blue) was interpolated after fitting.

The capture factor of the collection system  $\alpha_{\text{CS}}$  was assessed as was  $\alpha_{\text{eff}}$  of the TMPs (see previous section). However, given the very low pressures in the collection system, the RGA units had to be used to determine the  $Q/p$ -ratio

Table 6.5: **Results Reduction Factor**

Given are measured values of the capture factors of the collection system  $\alpha_{\text{CS}}$ , of the DPS2-F reduction factors with the downstream collection system  $R_{\text{CS}}$  and of estimated DPS2-F reduction factors in the KATRIN standard setup  $R_{\text{CPS}}$ .

Gas	$\alpha_{\text{CS}}$	$R_{\text{CS}}$	$R_{\text{final}}$
He	0.077(9)	$1.86(19) \times 10^{-4}$	$1.66(19) \times 10^{-4}$
D <sub>2</sub>	0.099(12)	$1.86(19) \times 10^{-4}$	$1.81(19) \times 10^{-4}$
Ne	0.111(9)	$4.10(41) \times 10^{-4}$	$4.10(41) \times 10^{-4}$
Ar	0.113(10)	$4.9(5) \times 10^{-4}$	$4.9(5) \times 10^{-4}$
Kr	0.116(10)	$5.6(6) \times 10^{-4}$	$5.7(6) \times 10^{-4}$

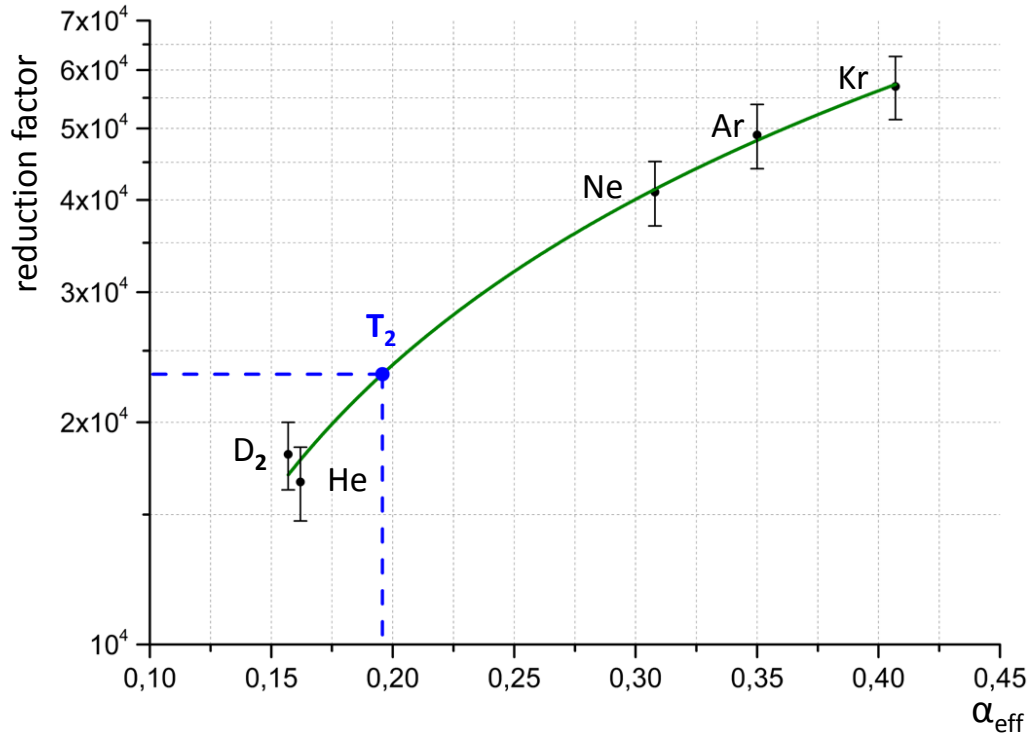


Figure 6.17: **Reduction factors of DPS2-F**

The value for tritium was interpolated after fitting the calculated reduction factors for the test gases. The quoted values are the empirical values corrected by the modified downstream capture factor (i.e. for a configuration with CPS instead of the collection system).

(instead of performing a direct pressure measurement, as in the case of the beam line TMPs), which rendered an uncertainty of over 10%. The values were cross-checked with the updates MC simulations using the experimentally deduced values for  $\alpha_{\text{eff}}$  of the beam line TMPs. The estimated values for  $\alpha_{\text{CS}}$  are included in table 6.5.

The sticking probabilities of the cryo section of CPS have been studied elsewhere [Luo08]. Using the same MC methods as for the DPS2-F an estimation of the capture factor of CPS was possible. The calculations rendered a value of  $\alpha_{\text{CPS}}(\text{T}_2) = 0.1055(15)$ .

Now all necessary parameters are at hand, and we are finally able to estimate the unknown reduction factors of DPS2-F for the test gases used. The results are also listed in table 6.5.

The empirical dependence between  $R_{\text{final}}$  and  $\alpha_{\text{eff}}$  was determined by a fit to the data, as shown in figure 6.17. This method differs from our previously published approach [Luk12], which was solely based on simulations and rendered slightly larger values for  $R_{\text{T}_2}$ . The results presented in [Luk12] also featured an overestimation of the reduction factors for the heavier gases in use. The de-



viation between  $D_2$  and He in figure 6.17 can be explained by the considerable difference in sticking probability of the two gases in the cryo section of CPS.

Based on the empirical inter-dependences, an interpolation to the reduction factor for tritium was possible with an estimated value of

$$R_{T_2} = (2.32 \pm 0.23_{\text{sys}} \pm 0.09_{\text{fit}}) \times 10^4.$$

This value is about a factor 4 smaller than the corresponding value of the KATRIN design report [KAT04]. The deviation is caused by design changes of the beam tube and by temperature influences, that have already been discussed above. A discussion of necessary corrections and an estimation of the the final KATRIN value will be given in the following section.

### 6.5.3 Comparison with Simulations

The corresponding predictions for  $R_{T_2}$  based on calculations of conductances (cf. section 4.2.1) and our previously published (simulation-based) values [Luk12] are consistent with the experimental values for the reduction factor of this work within the margins of error. The largest deviation is approximately 7%.

From the analysis of the macroscopic conductance value we predict a factor  $R_C = 2.43 \times 10^4$ , and a factor  $R_{MC} = 2.50 \times 10^4$  from the simulations based on  $\alpha_{\text{eff}}$  [Luk12]. The experimental values gained here, result in a more conservative estimation of  $R = 2.32 \times 10^4$ .

The reasons for the discrepancy between the experimental value and the estimated ones can be found in the challenges of the simulation for the complex geometry of components such as bellows and valves, and in the rather large uncertainties of the RGA measurements and the necessary interpolations to tritium values.

Given the complexity of the system, the achieved coherence of results is very satisfying and makes a reduction factor (for the current setup at room temperature) of  $2.4 \times 10^4$  an important input parameter for obtaining the overall tritium retention factor of the Transport Section.

## 6.6 Implications for KATRIN

The wide variety of tests proposed and outlined above were planned to be carried out over the entire calendar year 2011. Shortly after the measurement of the reduction factor at room temperature, however, a malfunction of the superconductor circuit (cf. section 5.1.2) occurred. Apparently, one of the protective diodes "burned out". After copious considerations it was decided to shut down the DPS2-F unit for repair to prevent damage to the superconducting magnet system in the case of further quenches. At present the SC circuit is undergoing a complete redesign to ensure fail-safe operation or fast repair options for the protection diodes during the later tritium measurements. Details of this incident and its implications can be found in Appendix A.4.

With the DPS2-F module undergoing a major redesign phase lasting more than one calendar year, the test experiments concerning the ion suppression and the electro-optics as well as gas flow tests at operational temperature had to be postponed and could not be included in this thesis.

The most important measurements - the experimental confirmation of the gas flow reduction factor of DPS2-F - were however carried out successfully. In addition several smaller experiments investigating the exact geometry of the magnetic field as well as volume calibration and outgassing analysis were carried out. All results obtained in the course of these measurements were presented above.

Finally we discuss the implications of our measurements for the long-term neutrino mass measurements. The following points are important in that aspect:

- The Monte Carlo simulations used to predict the reduction factors and transmission properties of the vacuum system [Luo06a], [Luo06b] yield sufficiently correct values. The tests of DPS2-F described above have validated the predictions, thus confirming their applicability for the vacuum components of the KATRIN experiment. A detailed knowledge of the geometry is however required for more accurate MC predictions. The yet-to-be-determined temperature influences (warm pump, cold gas) may however affect the MC reliability to some extent.
- Conductance-based predictions also yield remarkably good predictions for a system of this complexity. The consequences for the vacuum qualities of the DPS2-F unit due to future modifications can therefore be estimated rather quickly and reliably using this method for first estimates. As for MC simulations, the temperature influences in studies on conductance of the DPS2-F system are yet to be determined.
- The reduction factor of  $R \approx 2.4 \times 10^4$  is significantly lower than the value  $R = 1 \times 10^5$  aimed for in the very first design phase [KAT04]. The value obtained in this work will however be modified when the DPS2-F is

fully equipped with its beam tube instrumentation. The corresponding reduction of the beam tube diameter by inclusion of dipoles and FTICR modules plus beam tube delimiters will increase  $R$  by approximately a factor of 2. The operation with a cold beam line, i.e. cold gas, will add roughly another 20%<sup>4</sup>. At this point we predict  $R_{\text{operational}} \geq 5.5 \times 10^4$ . This value is within a factor of two of the design specification. With regard to the expected excellent tritium retention characteristics of the CPS unit (cf. the assessments in section 5.2.3.3), this factor 2 between design value and actual performance of DPS2-F will not influence the neutrino mass measurements of KATRIN.

Nevertheless, it will be crucial to determine the reduction factor of the DPS2-F at operational temperatures, as well as of the DPS-CPS combination before starting tritium scanning with the entire setup.

- With the commissioning and dedicated experimental tests of the primary vacuum system of DPS2-F, a first major milestone in the setup of the KATRIN experiment and its Transport Section has been concluded successfully.

To summarize the above statements, we can conclude that the tritium retention by active differential pumping is a highly efficient method of reducing the tritium flow rate by more than four orders of magnitude. The DPS2-F cryostat is thus an essential and important design cornerstone to successfully operate the closed KATRIN tritium cycle. Without its proven tritium retention characteristics a throughput of 10 kg per year would not be possible.

Apart from its central design feature of active tritium retention, the DPS2-F cryostat fulfills many important further requirements and will be essential for ion diagnostics and ion suppression. In view of the complex systematic effects associated with ions, this is a major task, and this thesis has, apart from giving proof-of-principle of the tritium retention capacities of DPS2-F, also contributed significantly to developing the advanced beam tube instrumentation required to control and minimize the impact of ions for the long-term neutrino mass measurements.

---

<sup>4</sup>We base this assumption on first rough observations on the development of pressures in the pump ports with the beam line cooled down. As stated above, coherent studies are still pending.



## Conclusion

The KATRIN experiment is currently being set up at the Tritium Laboratory Karlsruhe at the KIT. To reach its design sensitivity KATRIN relies on a tritium source of unprecedented intensity ( $10^{11}$   $\beta$ -decays per second) and stability ( $10^{-3}$  for the column density). To limit the systematic effects from tritium  $\beta$ -decays in the large electrostatic spectrometers of KATRIN a large-scale tritium retention system comprising active pumping by turbomolecular pumps and passive pumping by cryo-sorption with an unprecedented tritium retention factor of over 14 orders of magnitude will have to be operated continuously over a time period of five calendar years. Recent advances in the understanding of background processes associated with trapped keV-range electrons in the electrostatic spectrometers of KATRIN call for an even better tritium retention factor.

In the course of this thesis work a comprehensive overview of the relevant tritium retention techniques is given. Only by carefully designing the interplay between active pumping by TMPs, passive cryo-sorption on condensed argon frost, and finally pumping by getters, while also considering interactions with the spectrometer walls can we obtain an overall reduction of the tritium flow by a factor of  $10^{22}$  over the entire beam length of 70 m.

A central element in the different tritium retention techniques to be used at the KATRIN experiment is the DPS2-F cryostat, which arrived on site in July 2009. In the framework of this thesis, the almost 7 m long complex cryostat was commissioned successfully. Its beam line consists of five 1 m long elements, separated by four pump ports and surrounded by a complex superconducting magnet system which has to guide the signal  $\beta$ -electrons through an  $\Omega$ -shaped chicane, where beam elements are tilted by  $20^\circ$  to prevent beaming effects.

The central aspect of this thesis was to investigate the tritium retention factor of the DPS2-F, both experimentally and by calculation. In the latter case we have carried out a macroscopic ansatz based on conductances, and also followed a microscopic approach based on MC simulations. Both methods agree remarkably well with each other. Most importantly, there is also excellent agreement with the experimental value for tritium of  $R_{T_2} = 2.4 \times 10^4$  obtained after carefully designing a gas inlet and a gas capture system at the DPS2-F cryostat. The experimental investigations for the technique of (cascaded)

differential pumping of tritium (as well as for other gas species) demonstrate the excellent tritium retention characteristics of the unit. Further increases in tritium retention can be expected after the beam tube instrumentation is completed and the system is at operating temperatures of 77 K.

This thesis has also contributed in a major way to advance the important beam tube instrumentation. These elements consist of an FT-ICR system for ion diagnostics as well as of through-shaped electric dipole elements to oust ions from the beam tube via an induced  $\vec{E} \times \vec{B}$  drift without influencing the adiabatic transport of signal electrons.

Finally, this thesis has resulted in a complete plan for a thorough test measurements campaign to access the electro-optic properties of the superconducting magnet guiding system as well.

Due to a malfunction of one of the protective diodes of the magnet system only the important tritium retention factor could be determined experimentally. At present the magnet protection scheme is undergoing a complete redesign with the goal to implement a fail-safe system which will allow the continuous operation of the DPS2-F cryostat over the entire measurement time of KATRIN of five calendar years. Once the ongoing repair works are finished successfully, the DPS2-F will be re-commissioned and tested following the procedures derived in the framework of this thesis.

Apart from experimental work related to the commissioning and initial testing, this thesis has also been focused on investigations related to a better theoretical understanding of different tritium retention techniques. In the case of cryogenic pumping this was related to an investigation of the dwelling time of hydrogen on argon. Further important studies were carried out with respect to a better understanding of the complex tritium-wall interactions, most importantly in the large main-spectrometer, where an additional reduction factor of 30 was calculated.

To conclude, the two central elements of the KATRIN Transport Section, the DPS2-F cryostat and the CPS unit, will be instrumental in reducing the tritium flow to the required level. This will allow the KATRIN experiment to operate the WGTS tritium source at highest intensity, while at the same time keeping the spectrometers almost unaffected by  $\beta$ -decays of migrating HT molecules. These two facts are essential cornerstones for KATRIN to reach its design  $\nu$ -mass sensitivity of 200 meV. This will allow to measure the fundamental mass scale of neutrinos, and to fix their role as hot dark matter in the universe while at the same time advancing our understanding of mass generation for elementary particles.

# Appendix

## A.1 Additional Data and Informations

In this Appendix, specific data are given for the instrumentation used for the setup during the test measurements of DPS2-F.

Table A.1: **List of Components of the DPS2-F Vacuum System**

The part numbering scheme corresponds to the flow charts given below. Pressure ranges are taken from the supplier and do not necessarily reflect reality.

Number	Component	Type	Supplier
VP2X1	Turbomolecular Pump	MAG 2800 W	Leybold
VP251	Turbomolecular Pump	TMU 200 MP	Pfeiffer
VP201	Roughing Pump	SC15D	Leybold
AV2X1	Automatic Gate Valve	10848-CE24	VAT
AV2X2	Automatic Valve	57036-GE44	VAT
RP201, 210	Vacuum Probe	722A13TCE2FA	MKS
RP211, 221	Vacuum Probe ( $1.3 - 10^{-3}$ mbar)	Baratron 626B.1 MBE	MKS
RP251	Vacuum Probe ( $1.3 - 10^{-3}$ mbar)	Baratron 626A.1 MBE	MKS
RP2X2	Vacuum Probe ( $10^{-2} - 1.3 \times 10^{-11}$ mbar)	IM422	MKS
RP231, 241	Vacuum Probe ( $10^{-4} - 2 \times 10^{-12}$ mbar)	Ionivac IE514	Leybold
RP243	Residual Gas Analyzer	Prisma M200	Pfeiffer

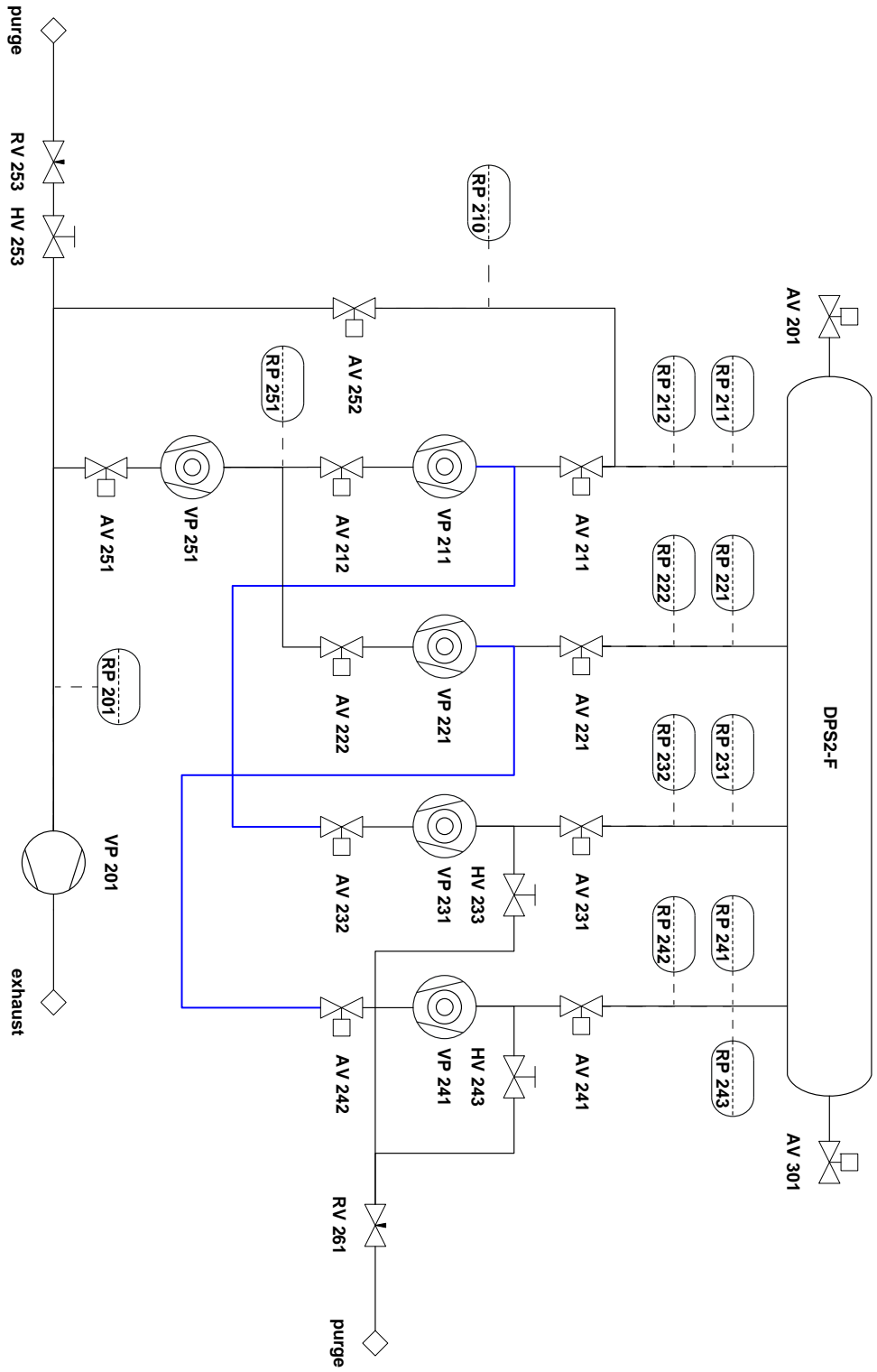


Figure A.1: **Flow Diagram of the DPS2-F Vacuum System**  
 Gas flow from left to right. Highlighted in blue is the cascading stream connecting the exhausts of the downstream TMPs (VP 231 & VP 241) with the inlets of the upstream TMPs (VP 211 & VP 221). This setup renders three-stage pumping for the first two and four-stage pumping for the last two beamline TMPs.



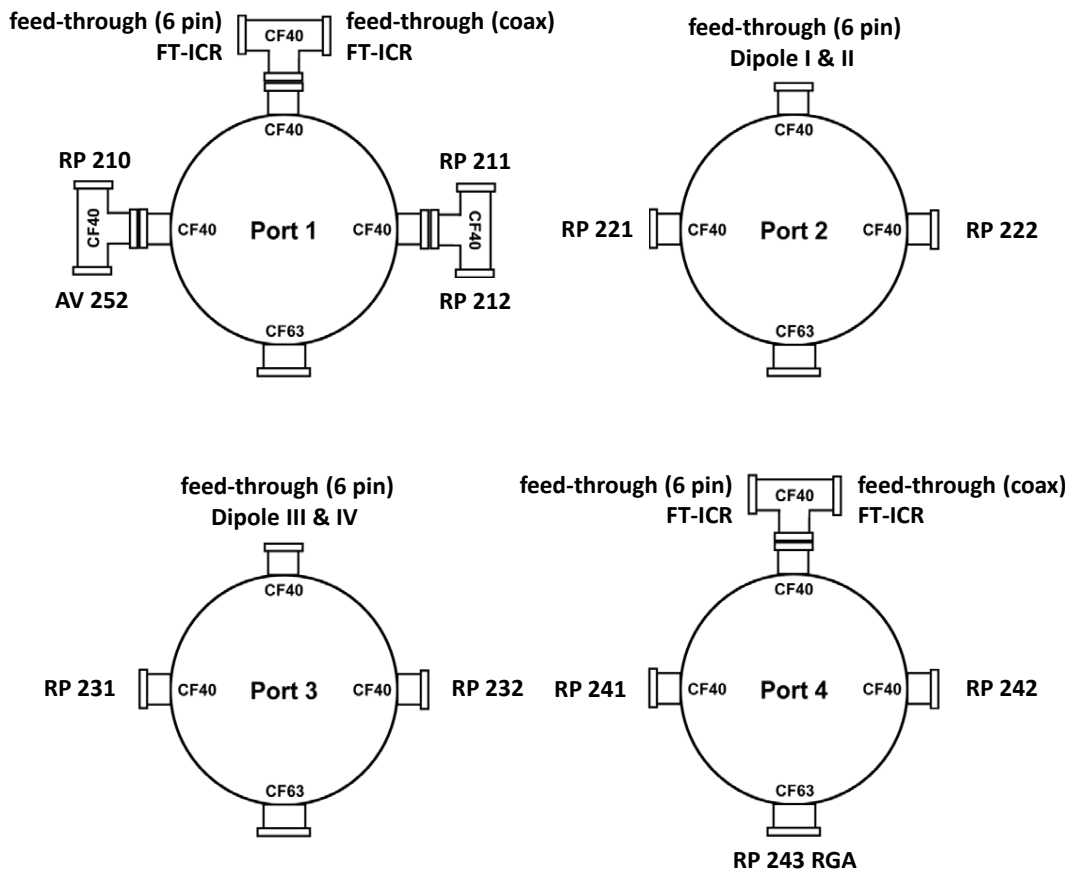


Figure A.2: **Pump Port Configuration at DPS2-F**

A schematic display of the occupation of the auxiliary ducts at the four main pump ports of DPS2-F vacuum system. The part numbering is as referenced in table A.1

Table A.2: **List of Components DPS2-F Vacuum Experiments**

The part numbering corresponds to the flowcharts given below. The upper half contains the parts of the injection system, the lower half those of the collection system.

Number	Component	Type	Supplier
BD101	Buffer Vessel 15.4 l	-	FZKA
VP101	Turbomolecular Pump	TW70	Leybold
VP102	Roughing Pump	ACP 15	Alcatel
AV101	Automatic Valve	SS-4BG-V51-3C	Best
RV101	Flow Controller	M200-02C4V2A	MKS
RV102	Flow Controller	M200-02C4V1A	MKS
RV103	Needle Valve	$\leq 100$ sccm	MKS
RP101	Vacuum Probe ( $1.3 - 10^{-5}$ mbar)	Baratron 690A01TRA	MKS
RP102	Vacuum Probe ( $1300 - 10^{-2}$ mbar)	Baratron 690A13TRA	MKS
RT101	Temperature Sensor	PT100	Jumo
VP301	Cryo Pump	COOLVAC 800CL	Leybold
RT302	Temperatur Sensor	Si-Diode (incl in VP 301)	
VP302	Turbomolecular Pump	TW70	Leybold
VP303	Roughing Pump	SC15D	Leybold
VP304	Turbomolecular Pump	TURBOVAC SL80	Leybold
AV301	Automatic Gate Valve	10848-CE24	VAT
AV302	Automatic Valve	57040-GE44	VAT
AV303	Automatic Valve	57036-GE44	VAT
RP301	Vacuum Probe ( $1.3 - 10^{-5}$ mbar)	Baratron 690A01TRA	MKS
RP302	Vacuum Probe ( $1300 - 10^{-2}$ mbar)	Baratron 690A13TRA	MKS
RP303	Vacuum Probe ( $10^{-4} \text{ } \text{œ} \text{ } 10^{-9}$ mbar)	RP27	Leybold
RP304	Vacuum Probe ( $1000 - 5 \times 10^{-4}$ mbar)	Thermovac TR212	Leybold
RGA301	Residual Gas Analyzer	Prisma M200	Pfeiffer
RT301	Temperature Sensor	PT100	Jumo

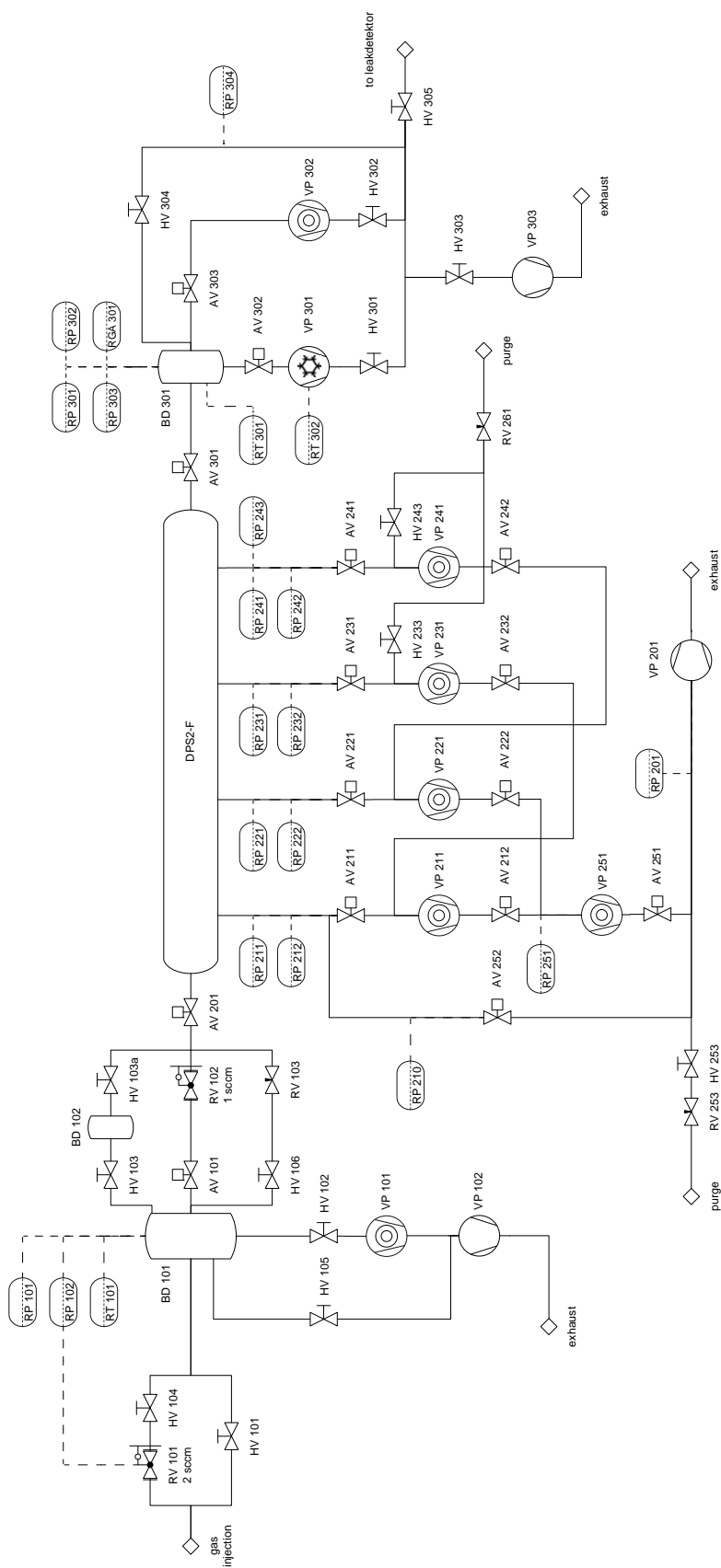


Figure A.3: Flow Diagram Gas Flow Experiments  
 Shown is the full flow diagram of the gas flow experiments carried out in the course of this work. The part numbering corresponds to table A.2.

<b>Mode of Op.</b>	<b>Bake-Out &amp; NEG Activation</b>	<b>Cool-Down</b>	<b>Argon – Preparation</b>	<b>Standby</b>	<b>Standard Operation</b>	<b>Regeneration</b>	<b>Warm-Up</b>	<b>CKrS-Calibration</b>
<b>Component</b>	<b>Temp. K</b>	<b>Temp. K</b>	<b>Temp. K</b>	<b>Temp. K</b>	<b>Temp. K</b>	<b>Temp. K</b>	<b>Temp. K</b>	<b>Temp. K</b>
Outer Radiation Shield	300 ± 20	300 → 77	77 + 5	77 + 5	77 + 5	77 + 5	77 → 300	77 + 5
Solenoids	300 ± 20 <sup>a)</sup>	300 → 4.5	4.5 ± 0.1	4.5 ± 0.1	4.5 ± 0.1	4.5 ± 0.1 <sup>b)</sup>	4.5 → 300	4.5 ± 0.1
Beam Tube Section 1	500 ± 20	300 → 77	77 + 10	77 + 10	77 + 10	> 100	77 → 300	77 + 10
Port #1	500 ± 20	300 → 77	77 + 10	77 + 10 <sup>c)</sup>	77 + 10 <sup>c)</sup>	> 100	77 → 300	77 + 10 <sup>c)</sup>
Beam Tube Section 2 - 5	500 ± 20	300 → 4.5	6 ± 1	3.0 - 3.5	3.0 - 3.5	Transient 3 → 100	> 100 → 300	3.0 - 3.5
Inner Argon Gas Injection Capillaries	500 ± 20	300 → 4.5	> 40 <sup>d)</sup>	~ 3.5	~ 3.5	Transient 3 → 100	> 100 → 300	3.0 - 3.5
Cold Gate Valve body	500 ± 20	300 → 4.5	6 - 10	4.5 ± 0.1	4.5 ± 0.1	Transient 4.5 → 100	> 100 → 300	4.5 ± 0.1
Beam Tube Section 6 (24 h)	620 ± 20 (24 h)	300 → 77	77 + 10	77 + 10	77 + 10	77 + 10	77 → 300	77 + 10
Port #2	< 620	300 → 77	77 + 10	77 + 10	77 + 10	77 + 10	77 → 300	77 + 10
Beam Tube Section 7 (24 h)	620 ± 20 (24 h)	~ 300	~ 300	300 ± 20 <sup>e)</sup>	300 ± 20 <sup>e)</sup>	~ 300	~ 300	77 + 10
Inner Radiation Shield	300 - 400	300 → 77	77 + 5	77 + 5	77 + 5	77 + 5	77 → 300	77 + 5
<b>Mode of Op.</b>	<b>Bake-Out &amp; NEG Activation</b>	<b>Cool Down</b>	<b>Argon – Preparation</b>	<b>Standby</b>	<b>Standard Operation</b>	<b>Regeneration</b>	<b>Warm Up</b>	<b>CKrS-Calibration</b>
<b>Status</b>	<b>Status</b>	<b>Status</b>	<b>Status</b>	<b>Status</b>	<b>Status</b>	<b>Status</b>	<b>Status</b>	<b>Status</b>
Argon Gas Injection	Injection OFF	Injection OFF	Injection ON Argon	Injection OFF	Injection OFF	Injection OFF	Injection OFF	Injection OFF
Purge Gas Injection	Injection OFF	Injection OFF	Injection OFF	Injection OFF	Injection OFF	injection ON Helium	Injection OFF	Injection OFF
Magnetic Field Status	OFF	OFF	OFF / ON	ON	ON	OFF / ON	OFF	ON
Cold Gate Valve Status	CLOSED	CLOSED	CLOSED	CLOSED	OPEN	CLOSED	CLOSED	CLOSED

## Remarks

- <sup>a)</sup> The solenoids need to be protected against the heat from the beam tube by helium gas flow.
- <sup>b)</sup> The additional heat load from the beam tube heaters must be considered for the cooling of the solenoids.
- <sup>c)</sup> Liquid nitrogen cooled baffles at the pump duct are required.
- <sup>d)</sup> The heaters inside the argon injection capillaries are on, additional heat load to the beam tube has to be taken into account.
- <sup>e)</sup> Permanent beam tube heating may be required to stabilize the beam tube temperature.

## Figure A.4: Modes of Operation of CPS

An overview of the different modes of operation of CPS with regard to the temperatures of the subsystems, taken from [Kle08]

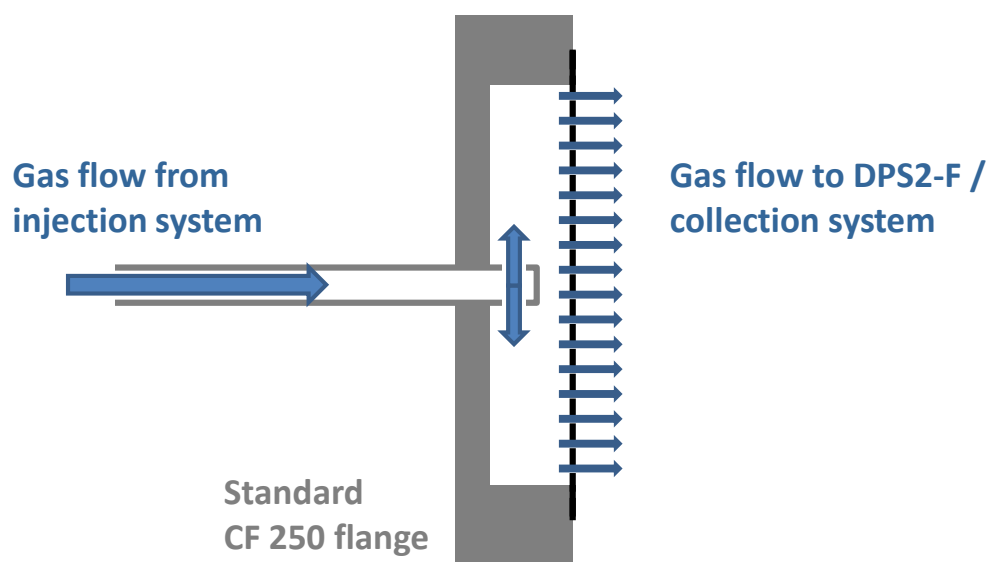



Figure A.5: **Diffuser for Gas Flow Experiments**

This unit guarantees a homogeneous distribution of the injected gas flow from the injection system towards the collection system during calibration, and towards the DPS2-F beam tube system during the experimental campaign.

Alloys 316 / 316L



www.finetubes.com

e142 August 2011

## Stainless Steels

### Alloys 316/316L (UNS S31600/UNS S31603)

Grade 316 is the standard molybdenum-bearing grade, second in overall volume production to 304 amongst the austenitic stainless steels. The molybdenum gives 316 better overall corrosion resistant properties than Grade 304, particularly higher resistance to pitting and crevice corrosion in chloride environments.

Grade 316L, the low carbon version of 316 and has very high immunity from sensitization (grain boundary carbide precipitation). It is extensively used in the oil and gas and chemical industries for its cost effective corrosion resistance and ease of

fabrication. There is commonly no appreciable price difference between 316 and 316L stainless steel. The austenitic structure also gives these grades excellent toughness, even down to cryogenic temperatures. Compared to chromium-nickel austenitic stainless steels, 316L stainless steel offers higher creep, stress to rupture and tensile strength at elevated temperatures.

These alloys may be considered for a wide variety of applications where one or more properties are important.

#### Available tube product forms

- STRAIGHT
- COILED
- SEAMLESS
- SEAM WELDED AND COLD REDRAWN
- SEAM WELDED, COLD REDRAWN AND ANNEALED

#### Typical Applications

- PROCESS ENGINEERING
- CONTROL LINES
- UMBILICALS
- HIGH PERFORMANCE LIQUID CHROMATOGRAPHY (HPLC)
- HEAT EXCHANGERS
- CONDENSERS
- SEMICONDUCTORS
- MEDICAL IMPLANTS (INCLUDING PINS, SCREWS AND IMPLANTS)

#### Typical manufacturing specifications

- ASTM A213    ● ASME SA213
- ASTM A269    ● NFA 49-117
- ASTM A312    ● BS 10216
- ASTM A632

Also individual customer specifications.

#### Industries predominantly using this grade

- OIL AND GAS
- CHEMICAL PROCESSES
- HIGH PERFORMANCE
- COMMERCIAL

#### Technical Data

Temper	Mechanical Properties			
	Annealed		Cold worked (approx. 20%)	
Material	316	316L	316	316L
Tensile Rm	75	70	102-131	ksi (min)
Tensile Rm	515	485	700-900	MPa (min)
R.p. 0.2% Yield	30	27	73-102	ksi (min)
R.p. 0.2% Yield	205	182	500-700	MPa (min)
Elongation (2" or 4D gl)	35		40	
			% (min)	

Physical Properties (Room Temperature)		
Specific Heat (0-100°C)	500	J.kg-1.°K-1
Thermal Conductivity	16.3	W.m-1.°K-1
Thermal Expansion	15.9	mm/m.°C
Modulus Elasticity	19.3	GPa
Electrical Resistivity	7.4	μohm/cm
Density	7.99	g/cm³


Element	Chemical Composition (% by weight)			
	316		316L	
	Min	Max	Min	Max
C	-	0.08	-	0.035
Mn	-	2	-	2
Ni	10	14	10	15
Cr	16	18	16	18
Mo	2	3	2	3
S	-	0.03	-	0.03
Si	-	1	-	1
P	-	0.045	-	0.045

www.finetubes.com

Disclaimer: The information contained within this data sheet is for guidance only and is not intended for warranty of individual application - express or implied.

Figure A.6: **Data Sheet Steel 316L**  
 Data sheet of the steel used for the beam tubes of the KATRIN transport section. European steel code 1.4435. Source [Fin11]

Alloy 316LN



www.finetubes.com

e141 August 2011

## Stainless Steels

### Alloy 316LN (UNS S31653)

316LN (UNS S31653) is a lowcarbon, nitrogen-enhanced version of Type 316 molybdenum-bearing austenitic stainless steel. The Type 316 alloys are more resistant to general corrosion and pitting/crevice corrosion than the conventional chromium-nickel austenitic stainless steels such as Type 304. They also offer higher creep, stress-rupture and tensile strength at elevated temperature. The nitrogen in Type 316LN adds additional resistance to sensitization in some circumstances.

The nitrogen content of Type 316LN stainless steel also provides some solid solution hardening, raising its minimum specified yield strength compared to Type 316L stainless steel. Like Types 316 and 316L, the Type 316LN alloy also offers good resistance to general corrosion and pitting/crevice corrosion.

#### Available tube product forms

- STRAIGHT
- COILED
- SEAMLESS
- SEAM WELDED AND COLD REDRAWN
- SEAM WELDED, COLD REDRAWN AND ANNEALED

#### Typical Applications

- ORTHOPAEDIC IMPLANTS
- TRAUMA NAILS
- NEUROLOGICAL APPLICATIONS
- SURGICAL INSTRUMENTS

#### Typical manufacturing specifications

- ASTM F138
- ASTM F2181

Also individual customer specifications.

#### Industries predominantly using this grade

- MEDICAL
- CHEMICAL PROCESSES
- HIGH PERFORMANCE LIQUID CHROMATOGRAPHY (HPLC)

#### Technical Data

Temper	Mechanical Properties	
	Annealed	Cold worked
Tensile Rm	75 ksi (min)	125 ksi (min)
Tensile Rm	515 MPa (min)	860 MPa (min)
R.p. 0.2% Yield	30 ksi (min)	100 ksi (min)
R.p. 0.2% Yield	205 MPa (min)	690 MPa (min)
Elongation (2" or 4D gl)	35 % (min)	15 % (min)

Chemical Composition (% by weight)		
Element	Min	Max
C	-	0.03
Mn	-	2
Ni	13	15
Cr	17	19
Mo	2	3
S	-	0.1
Si	-	0.75
P	-	0.25

Physical Properties (Room Temperature)		
Specific Heat (0-100°C)	485	J.kg <sup>-1</sup> .°K <sup>-1</sup>
Thermal Conductivity	16.3	W.m <sup>-1</sup> .°K <sup>-1</sup>
Thermal Expansion	16.5	mm/m.°C
Modulus Elasticity	200	GPa
Electrical Resistivity	7.4	μhm/cm
Density	7.99	g/cm <sup>3</sup>

www.finetubes.com

Disclaimer: The information contained within this data sheet is for guidance only and is not intended for warranty of individual application - express or implied.

Figure A.7: Data Sheet Steel 316LN

Data sheet of the steel used for the KATRIN main spectrometer. European steel code 1.4429. Source [Fin11]

## A.2 FT-ICR Auxillaries & Geometry

### Auxillary Components:

The subsequent list summarizes the hardware devices required to perform FT-ICR at the KATRIN setup inside the DPS2-F cryostat. It states the amount of units required and their present hardware status [Ubi12].

Comments about Table A.3:

- **Fast high voltage switches:** At this moment (May 2012) the switches needed for the KATRIN traps are being built by Stahl Electronics, and they should be delivered the latest in mid-2012.
- **Flange amplifiers:** The components needed for building the two flange amplifiers that will be used in KATRIN are available and ready to be mounted.
- **Vacuum cables:** The required overall length of cables is yet to be defined by MPIK Heidelberg. KIT will provide single-strand kapton-insulated cables, that already have been used for several KATRIN ap-

Table A.3: **Auxiliary Devices for the Setup of FT-ICR**

List of required devices for the installation of the FT-ICR detection system at KATRIN and their status (SE for Stahl Electronics).

Device	Ammount	Status/Comment
Traps (complete setup)	3	✓
Control PC	1	✓
FFT analyzer	1	✓
Downconverter	1	✓
Pulse delay generator	1	✓
Fast high voltage switches	4	to be provided by SE
Flange amplifier (DN CF 40)	2	✓
Cryoamplifier	2	✓
Rf-filters	2	✓
Feedthroughs (DN CF 40)	2	to be provided by SE
Vacuum cable		kapton-coaxial by SE kapton-single-strand by KIT
Function generator	1	✓
Power supply	1	✓



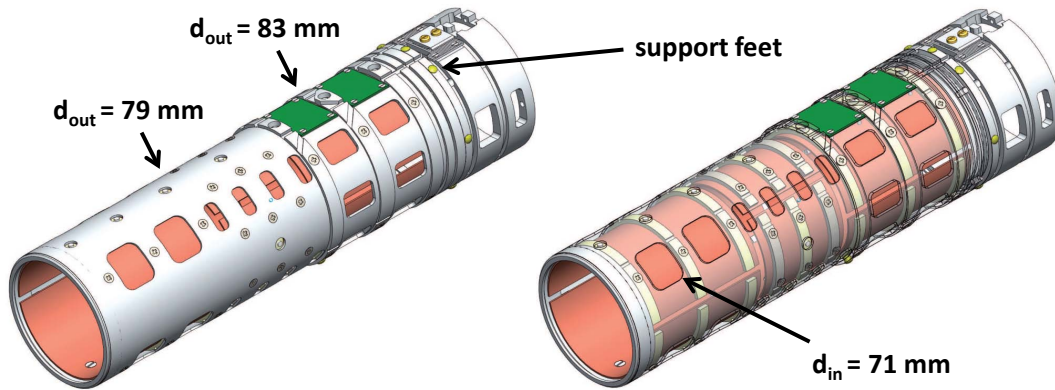


Figure A.8: **Modified FT-ICR Modules**

The modified support structure of the FT-ICR modules, based on [Ubi11]. Note the narrowed outer diameter so that the trap can be positioned over the bellows in the middle of the DPS2-F beam tube sections. All relevant other parts remain unchanged [Ubi09].

plications. Stahl Electronics will provide suitable coaxial-cables for the ICR signals.

All devices (except the kapton-insulated single-strand vacuum cables) will be delivered in one single and complete shipping by Stahl Electronics. The DPS2-F team will inform Stahl Electronics about a suitable delivery date after repair and re-commissioning of DPS2-F.

#### Updated Design:

The FT-ICR traps were initially designed for an overall inner diameter of the DPS2-F beam tube of 86 mm with bellow groves extending to the outside of the tube. This design was changed by the DPS2-F manufacturer to a bellow extending into the beam tube thereby reducing the inner diameter to 81 mm. As a result, the FT-ICR modules had to be modified.

A photograph of the (at this point already built) modules is given in figure 5.10, and a sketch of the re-design is given above in figure A.8. All components relevant to the functionality (electrodes, pre-amplification etc.) remained unchanged.

### A.3 The SLOW Experiment

The dipole system proposed to eliminate ions inside the DPS2-F beam tube volume calls for special coatings of the  $\text{Al}_2\text{O}_3$ -ceramic tubes separating the dipole electrodes from beam tube potential. Several materials were investigated. We decided on under-stoichiometric aluminiumoxide. Stoichiometric  $\text{TiO}_2$  is an electrical insulator. Studies show, however, that the reduction of oxygen content in  $\text{TiO}_x$ , with  $1.55 < X < 1.9$ , leaves a material stable at low temperatures and in an oxygen-deprived atmosphere (as given in DPS2-F). In that case, it behaves like an n-doped semi-conductor with variable electric resistivity [Ohm91],[Pad87] including the increase of conductivity at lower temperatures.

To process these kinds of coatings, we designed and commissioned the SLOW (Study on Low-Conductivity Overlays in a Wide Temperature range) experiment, as depicted in figure A.9.

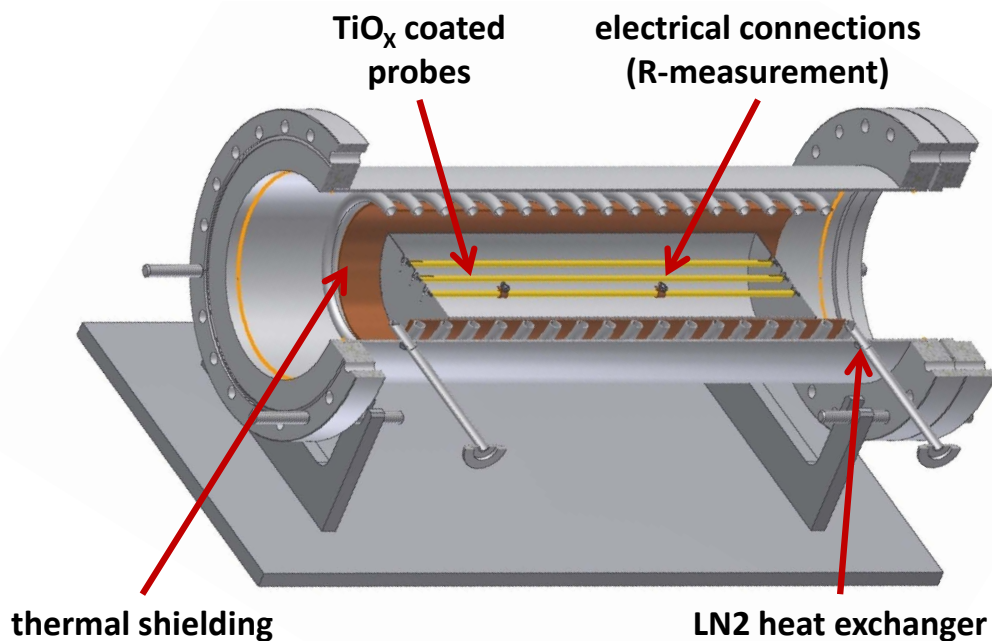


Figure A.9: **The SLOW Experiment**

Based on [Win11]. Inside the vacuum container a copper radiation shield and a coiled steel tube that can be fed with liquid nitrogen provide the cooling. Inside, a carrier through bears the coated ceramic tubes on steel wires. Temperature measurements are realized by placing a PT-100 sensor on to an uncoated reference tube. Heating is realized with heating strips on the outside and purging with pre-heated gas through the coil. A gas control system (not shown) allowed for an online manipulation of the atmosphere in the container (primarily high-vacuum or an atmosphere of several mbar of He).

By heating of the probe in vacuum or under low pressure helium, the oxygen concentration on the surface should fall, and the conductivity would rise correspondingly [Ear42].

SLOW allows access to a wide temperature range from 77 - 800 K. Heating and cooling are possible in the same containment, primarily to prevent contact of the heated coatings to atmospheric oxygen before cool-down. Up to half a dozen different coatings of the original ceramic tubes can be processed simultaneously. The unprocessed coatings were industry-fabricated<sup>1</sup>.

The desired effect was indeed measured [Kos10a]. In particular, a drop in resistivity by a factor of 20 (best case) was acquired after heating for 70 hours at approximately 600 K. With a resistivity (calculated for the dipole tube geometry) in the range of several  $G\Omega$  it was still significantly larger (by an order of magnitude) than the desired conductivity-corridor of  $100\text{ k}\Omega$  -  $2.5\text{ M}\Omega$  (cf. section 5.1.3.2) at the operational temperature of 77 K. After re-exposure to atmosphere and repeated measurements, the obtained surface-conductivity returned close to the original values. Several different heating strategies and different unprocessed probes were unsuccessfully tested.

We then investigated coatings with a thin layer of pure titanium ( $\approx 100\text{ nm}$  in between two layers of  $\text{TiO}_2$ ) and tried to promote migration of oxygen from the surface into the bulk material (as described e.g. in [Fra08]). Also a fine-tuning of the thickness of the surface  $\text{TiO}_2$ -layer would have rendered a fitting tunnel-probability for charge carriers between the conducting Ti-layer and the surface.

The manufacturing of these "sandwich" coatings however turned out to be very expensive. Also, our contractors were not able to reproduce surface thicknesses exactly. More advanced surface analysis tools would have been required for a detailed study of the dependence of layer thickness, tunnel-probability and effective surface conductivity. After some considerations and a successful search for other contractors who were able to manufacture coatings for our special needs<sup>2</sup>, it was decided to proceed along an industrial solution.

---

<sup>1</sup>Sputtered by NTTF-COATINGS GmbH, Maarweg 32, D-53619 Rheinbreitbach

<sup>2</sup>offered for example by NTG Neue Technologien GmbH & Co. KG, Gelnhausen, Germany

## A.4 Design Modifications

**The DPS2-F Malfunction** During the initial DPS2-F test campaign under the aegis of the author a major malfunction of the DPS2-F superconducting magnet system occurred. On July 14th, 2011 the magnet module #2 quenched during ramp-up. After approximately 30 seconds the quench heaters were fired, forcing the remaining current into the diodes to be dissipated.

During the next attempt to charge up the magnet system on July 18th, 2011, an abnormal behavior of magnet module # 2 was observed. The source-side correction coil (highlighted in red in figure A.11) did not charge in the same manner as the other solenoids [Gil11].

Careful investigation of the malfunction revealed a short-circuit of the correction coil. Follow-up investigations were carried out [Kos11b] using a frequency generator and oscilloscope (AC mode due to the SC-coil being in parallel) with peak-to-peak voltages of  $1.0\text{ V} \leq U_{F,p-p} \leq 8.0\text{ V}$ . The frequencies were chosen around 1 kHz, thus rendering an inductive impedance of roughly  $12\text{ k}\Omega$ .

In figure A.10 exemplary graphical results are given. For a diode in normal operating conditions without any short circuit, only the parts of the sinusoidal voltage with values  $U \geq U_{\text{gate}}$  will pass, as shown on the left side of the figure. In the case of a short-circuit diode, the entire sinusoidal voltage will pass, only being damped by the residual resistance (as shown on the right of figure A.10, and measured over the impaired module).

Due to an inconsistent documentation of the coil circuit and the voltage taps, additional tests to measure the inductance of the remaining coils had to be

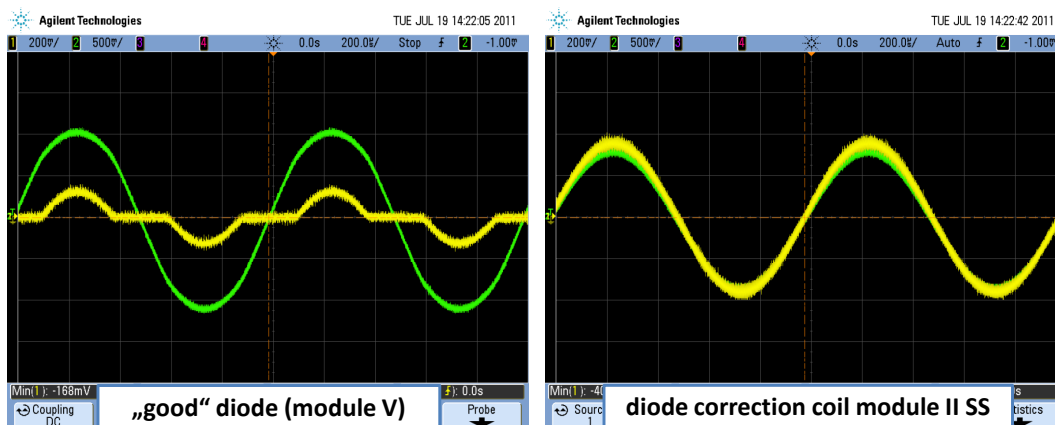


Figure A.10: Gate Voltage Defect Diode

Screen shots of oscilloscope measurements on a well functioning coil-diode combination (left side) and the malfunctioning coil-diode pair (right side) which belongs to the source-side correction coil of module #2 [Kos11b].

carried out [Kos11b]. In the course of these measurements we assessed the phase shift between current and voltage to determine the resonance frequencies (here roughly 17 Hz for the main coils). In doing so, we could prove the damage to be located at the correction coil (older documentations pointed to the main coil).

Finally, a detailed analysis of the short circuit was performed. It revealed a current-selective behavior. Interestingly, we obtained a value of the ohmic resistance of the short fused diode of  $R_{\text{eff}} \approx 0.14 \text{ m}\Omega$  for  $I < 10 \text{ A}$ , and  $R_{\text{eff}} \approx 1.80 \text{ m}\Omega$  for  $I > 10 \text{ A}$ . So far there is no viable explanation for this unexpected phenomenon.

With this specific diode not working in a regular way, a potential future quench in the affected coil would not be detectable via voltage measurements, thus

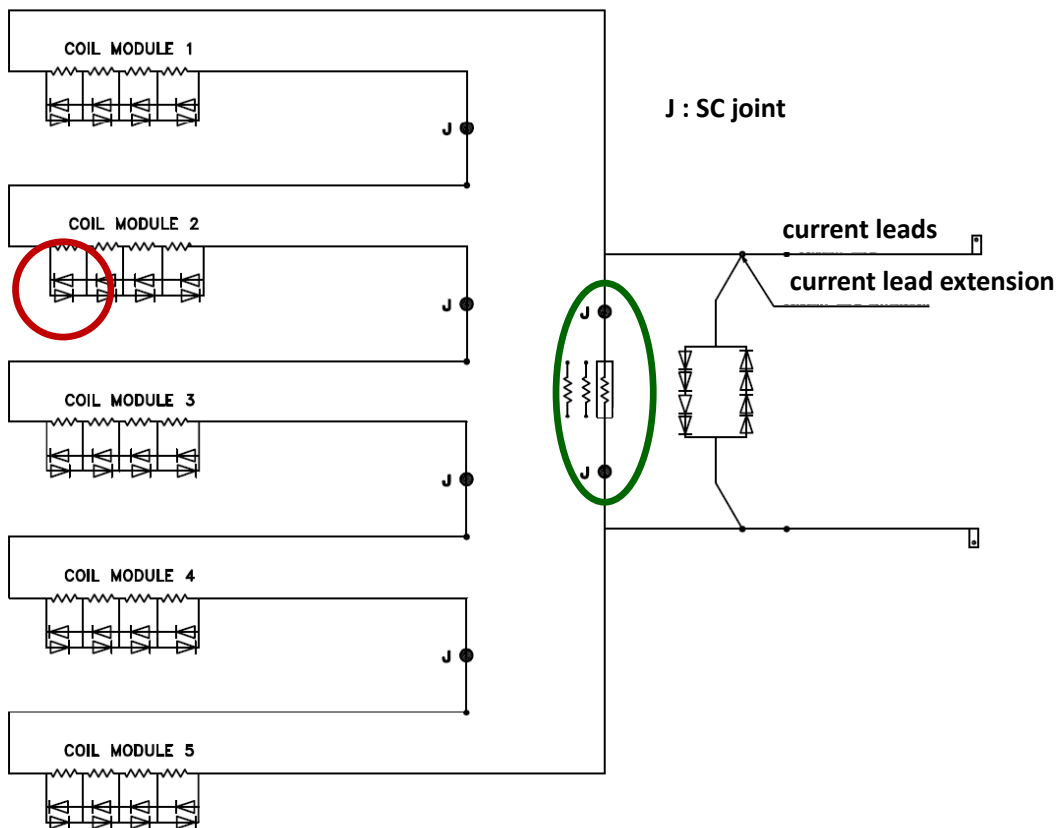


Figure A.11: **The SC Circuit of DPS2-F**

This simplified scheme of the SC circuit of DPS2-F is based on the manufacturer's documentation [Dor11]. Highlighted in green is the superconducting switch (placed in the turret of DPS2-F), and highlighted in red is the malfunctioning diode pair which belongs to the source-side correction coil of module #2.

leaving the safety of the SC in this module significantly impaired with the high risk of permanent damage of the coil<sup>3</sup>.

The cause of this malfunction to occur is not known yet. The effective heat-load ( $\int I^2 dt$  of the order of  $0.2 \text{ MA s}^2$ ) on the damaged diode circuit during the quench on July 14th was almost two orders of magnitude lower than maximal heat loads on other diodes in the system during quenches before. Potential explanations for the burn out include:

- The diode affected is simply a "bad" diode. In the case of mass-produced electronic products, small fractions of sub-standard quality components have to be taken into account. In this context it is important to note that before DPS2-F assembly the diodes have not all been tested at operational temperatures (LHe environment) by the contractor.
- A general insufficient thermal connection to the heat sink. In particular, the recommended mounting procedure of the diode manufacturer has not been followed by ASG. Moreover, the geometry of the diode bearing (see [Dre11] or [Kos11b] for details) is not well designed for good heat transport.
- Mechanical instabilities at low temperatures. After multiple cold-warm-cycles, the connection of the diode to the heat sink, as well of the diode to its epoxy casing might be impaired.

The Schottky-type diodes used, and in particular their mounting procedure as well as the heat sink dimensions were considered unacceptable for long-term KATRIN operations after this incident [Dre11]. A "simple" exchange of the broken diode as proposed by the manufacturer, would have left the project in the permanent risk of a failure in the future. Consequently, a complete redesign of the protection circuit of DPS2-F, as well as that of CPS, was initiated.

**Current Status of Redesign** Since the cryotechnic functionality of DPS2-F and its tritium retention capabilities was proven with this work, the redesign studies for a better diode circuit are carried out for the CPS cryostat first. The actual status of the new design strategy (by May 2012 [Gil12a]) include the following features:

- Replacement of all Schottky-diodes with liquid helium temperature tested Semikron p-n diodes type SK240 (as used in the WGTS), and reconfiguration of the copper heat sinks to obtain a better thermal operating stability at 4.5 K (see figure A.12).

---

<sup>3</sup>At this point it should be noted that also a short fuse of the SC bus connectors at the very entrance and the exit of the coil would lead to this kind of behavior. This possibility was however ruled out by the contractor, based on the winding scheme.

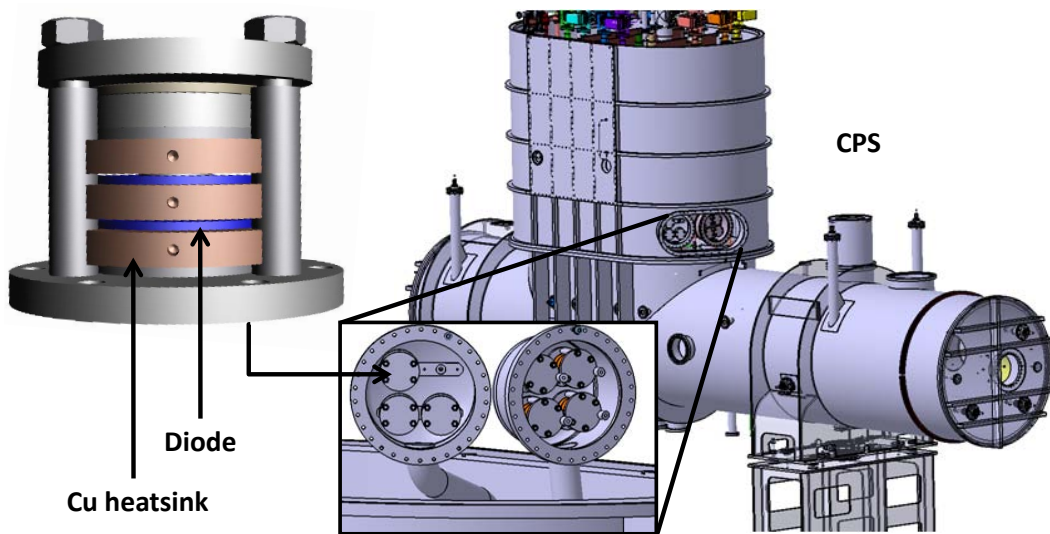


Figure A.12: **Redesign of Diodes**

Shown are the proposed diode stacks (left side) with the diode chips clamped between massive gold-plated copper heat sinks. As shown, the actual proposal foresees the diode stacks to be placed in domes mounted within the turret structure, connected to the main helium vessel yet leaving accessibility from the outside. Not shown are the bus bars connecting the diode stacks to the magnet modules down in the main cryostat. Based on [Gil12a].

- Accessibility to diodes from the outside. In case of a future malfunction of a diode, which can never be excluded *ab initio*, an exchange of the diode in question can be carried out without major hardware works. Accordingly, the diodes will be placed at the dome of CPS, adjacent to the main helium reservoir (see figure A.12).
- There will be major re-arrangement of the bus bars in the existing system to connect the magnets with the diodes. Accordingly, a re-enforcement of the bus bars will be implemented to carry high heat loads in the case of a quench.
- For a more compact design, and with regard to new operating principles (see below), the CPS magnets will be operated in one direction only, thus reducing the number of diodes required by 50%. The final direction will be anti-parallel to the earth magnetic field.
- In the future, all superconducting systems will be operated in the driven mode (i.e. without SC-switch, but with the use of an ultra-stabilized PSU).

With an integral conductance of  $L = 177$  H, and rendering a total stored energy of 3.54 MJ, the CPS cryostat houses the most energetic of all KATRIN magnet

systems. A design considered safe for CPS will, after testing, be developed analogously for DPS2-F and WGTS.

The remodeling and complete new assembly of the CPS superconducting circuit is planned to be completed in spring 2013. After successful implementation of this task, corresponding modifications of the DPS2-F protection system are scheduled. These extensive redesigns of the SC system of the Transport Section will be finished by mid-2014, allowing a start of the long-term tritium scanning by 2015.



# Bibliography

- [Aba11] K. N. Abazajian et al. *Cosmological and Astrophysical Neutrino Mass Measurements*, arXiv:1103.5083 v1
- [Abe79] H. Abe, W. Schulze *The Sorption Capacity of Solid Rare Gas Layers*, Chem. Phys. (41), pp. 257-263, 1979
- [Abe08] S. Abe et al. (KamLAND Collaboration) *Precision Measurement of Neutrino Oscillation Parameters with KamLAND*, Phys. Rev. Let. (100), 221803, 2008
- [Ada08] P. Adamson et al. (MINOS collaboration) *Measurement of Neutrino Oscillations with the MINOS Detectors in the NuMI Beam*, Phys. Rev. Let. (101), 131802, 2008
- [Agu01] A. Aguilar et al. (LSND collaboration) *Evidence for neutrino oscillations from the observation of  $\bar{\nu}_e$  appearance in a  $\bar{\nu}_\mu$  beam*, Phys. Rev. D (64), 112007, 2001
- [Aha10] B. Aharmim et al. (SNO collaboration) *Low-energy-threshold analysis of the Phase I and Phase II data sets of the Sudbury Neutrino Observatory*, Phys. Rev. C (81), 055504, 2010
- [Ahn10] J. K. Ahn et al. (RENO collaboration) *RENO: An Experiment for Neutrino Oscillation Parameter  $\theta_{13}$  Using Reactor Neutrinos at Yonggwang*, arXiv:1003.1391 v1, 2010
- [Ahr04] J. Ahrens et al. (IceCube collaboration) *Sensitivity of the IceCube detector to astrophysical sources of high energy muon neutrinos*, Astropart. Phys. (20), pp. 507-532, 2004
- [Alb04] C. Albright et al. *Neutrino Factory and Beta Beam Experiments and Development*, arXiv:physics/0411123 v2, 2004
- [ALE06] ALEPH, DELPHI, L3, OPAL, SLD Collaborations, LEP Electroweak Working Group, SLD Electroweak and Heavy Flavour Groups *Precision electroweak measurements on the Z resonance*, Physics Reports (427), pp. 257-454, 2006

- [Ams12] J. F. Amsbaugh et al. *Prototype focal-plane detector system for the KATRIN experiment*, to be published in 2012
- [An12] F.P. An et al. (Daya Bay Collaboration) *Observation of electron-antineutrino disappearance at Daya Bay*, arXiv:1203.1669 v2, 2012
- [APS04] The American Physical Society *The Neutrino Matrix*, APS Multi-Divisional Neutrino Study, Nov 2004
- [Ard06] F. Ardellier et al. (Double Chooz Collaboration) *Double Chooz: A Search for the Neutrino Mixing Angle  $\theta_{13}$* , arXiv:hep-ex/0606025 v4, 2006
- [Arn89] W. D. Arnett et al. *Supernova 1987A*, Annu. Rev. Astron. Astrophys. (27), pp. 629-700, 1989
- [Ase11] V.N. Aseev et al. *An upper limit on electron antineutrino mass from Troitsk experiment*, arXiv:1108.5034 v3
- [Ash05] J. Ashie et al. (Super-Kamiokande Collaboration) *Measurement of atmospheric neutrino oscillation parameters by Super-Kamiokande I*, Phys. Rev. D (71), 112005, 2005
- [Bal06] M. Balata et al. (Borexino Collaboration) *Search for electron antineutrino interactions with the Borexino Counting Test Facility at Gran Sasso*, Eur. Phys. J. C (47), pp. 21-30, 2006
- [Bar00] V. Barger et al. *Long-Baseline Study of the Leading Neutrino Oscillation at a Neutrino Factory*, arXiv:hep-ph/9911524 v2
- [Bau11] S. Bauer *CKrS at the CPS*, KATRIN Internal Report Mar 2011
- [Bea80] G. Beamson et al. *The collimating and magnifying properties of a superconducting field photoelectron spectrometer*, J. Phys. E Sci. Instrum. (13), pp. 64-66, 1980
- [Bec72] K. Becker et al., Proc. Int. Cryog. Eng. Conf. (4), pp. 319-323, 1972
- [Ber10] K. Bergers et al. *Determination of Hydrogen in Steel by Thermal Desorption Mass Spectrometry*, Steel Research Int. (81), pp. 499-507, 2010
- [Bla06] K. Blaum *High-accuracy mass spectrometry with stored ions*, Phys. Rep. (425), pp. 1-78, 2006
- [Bod12] L. Bodine et al. *Tritium recoil-ion mass spectrometer*, Center for Experimental Nuclear Physics and Astrophysics, Annual Report 2012
- [Bon01] J. Bonn, B. Bornschein *Estimated limits on allowed tritium gasflow into the KATRIN spectrometer during standard operation*, KATRIN Internal Report, Jun 2001

- [Bon03] J. Bonn et al. *Tritium related parts of KATRIN: Basic Concepts and Key Requirements*, KATRIN Internal Report, Jan 2003
- [Bri07] S. Briske *Die Messung von Neutrinos aus Supernova-Explosionen bei Double Chooz*, Diploma Thesis, RWTH Aachen, May 2007
- [Bro86] L.S. Brown, G. Gabrielse *Geonium theory: Physics of a single electron or ion in a Penning trap*, Reviews of Modern Physics (58), pp. 233-311, 1986
- [Cow56] C. L. Cowan, Jr., F. Reines *Detection of the Free Neutrino: a Confirmation*, Science (124), pp.103-104, 1956
- [Cre10] O. Cremonesi *Neutrino masses and Neutrinoless Double Beta Decay: Status and expectations*, arXiv:1002.1437 v1
- [Dan01] P. Danielson *How To Use Getters and Getter Pumps*, Journal of Practical and Useful Vacuum Technology, 2001
- [Dav68] R. Davis et al. *Search for Neutrinos from the Sun*, Phys. Rev. Lett. (20), pp. 1205-1209, 1968
- [Day07] C. Day et al. *Determination of the sticking probability of a Zr-V-Fe nonevaporable getter strip*, J. Vac. Sci. Technol. A (25), pp. 824-830, 2007
- [Dem05a] W. Demtröder *Experimentalphysik 3 Atome, Moleküle und Festkörper*, 3. Auflage, Springer, 2005
- [Die03] U. Diebold *The surface science of titanium dioxide*, Surface Science Reports (48), pp. 53-229, 2003
- [Dob58] E.R. Dobbs et al. *Properties of Solid Argon*, Il Nuova Cimento (9 Sup1), pp. 32-35, 1958
- [Dor11] O. Dormicchi et al. *Manual for use and maintenance of DPS2-F magnetic system for KATRIN*, Delivery documentation, Apr 2011
- [Dor05] O. Dormicchi et al. *Report test a freddo secondo modulo Katrin DPS2-F superconduttivo*, Test documentation, Sep 2005
- [Dos06] N. Doss et al. *Molecular effects in investigations of tritium molecule  $\beta$  decay endpoint experiments*, Physical Review C (73), 2006
- [Dos08] N. Doss, J. Tennyson *Excitations to the electronic continuum of  $^3\text{HeT}^+$  in investigations of  $T_2$   $\beta$ -decay experiments*, J. Phys. B: At. Mol. Opt. Phys. (41) 125701, 2008
- [Dre12] G. Drexlin *private communication*

- [Dre11] G. Drexlin *Diodeneinbau* DPS2-F, KATRIN Internal Report, Aug 2011
- [Ear42] M. Earle *The Electrical Conductivity of Titanium Dioxide*, Phys. Review (61), pp. 56-62, 1942
- [Eic09] F. Eichelhardt *Measurement of the Tritium pumping properties of a 4.2 K Argon Condensate for the Cryogenic Pumping Section of KATRIN*, Dissertation, University of Karlsruhe, Jan 2009
- [Emm37] P.H. Emmett, S. Brunauer *The Use of Low Temperature van der Waals Adsorption Isotherms in Determining the Surface Area of Iron Synthetic Ammonia Catalysts*, J. Am. Chem. Soc. (59), pp. 1415-1582, 1937
- [Fin11] finetubes <http://www.finetubes.co.uk>
- [Fog11] G.L. Fogli et al. *Evidence of  $\theta_{13} > 0$  from global neutrino data analysis*, Phys. Rev. D (84), 053007, 2011
- [Fra08] Fraunhofer-Institut für Schicht und Oberflächentechnik IST *Jahresbericht 2008*
- [Gab89] G. Gabrielse, L. Haarsma, S. Rolston *Open-endcap Penning traps for high precision experiments*, Int. J. Mass Spectrom. (88), pp. 319-332, 1989
- [Gae13] W. Gaede *Die Molekularluftpumpe*, Annalen der Physik (41), pp. 337-380, 1913
- [Gal12] M. Galeazzi et al. *The Electron Capture Decay of  $^{163}\text{Ho}$  to Measure the Electron Neutrino Mass with sub-eV Accuracy (and Beyond)*, arXiv:1202.4763 v2 (to be published in Phys. Lett.)
- [Ger06] D. Meschede *Gerthsen Physik*, 23. Auflage, Springer, 2006
- [Gil12a] W. Gil *Status of Cryogenic Pumping Section*, KATRIN Internal Report, Mar 2012
- [Gil12b] W. Gil, A. Kosmider et al. *Status of the Magnets of the two Tritium Pumping Sections for KATRIN*, Accepted for publication in IEEE Transactions on Applied Superconductivity
- [Gil11] W. Gil *Comparison of Quenches of DPS2F*, KATRIN Internal Report Aug 2011
- [Glu10] F. Glück *Electrons and ions in KATRIN STS*, KATRIN Internal Report 2010

- [Goe10] S. Görhardt *Reduktion der durch Radon induzierten Untergrundprozesse in den KATRIN Spektrometern*, Diploma Thesis, KIT, Oct 2010
- [Gol58] M. Goldhaber et al. *Helicity of Neutrinos*, Phys. Rev. (109), pp. 1015-1017, 1958
- [Gum12] R. Gumbsheimer, internal calculations, private correspondence
- [Hae89] R. A. Haefer *Cryopumping - Theory and Practice*, Clarendon Press, Oxford, 1989
- [Han10] S. Hannestad *Neutrino physics from precision cosmology*, Prog. Part. Nucl. Phys. (65), pp. 185-208, 2010
- [Hir84a] T. Hirabayashi, M. Saeki *Sorption of gaseous tritium on the surface of type 316 stainless steel*, J. of Nuclear Materials (120), pp. 309-315, 1984
- [Hir84b] T. Hirabayashi et al. *A thermal distribution study of the surface interaction between tritium and type 316 stainless steel*, J. of Nuclear Materials (126), pp. 38-43, 1984
- [Hir91] K. S. Hirata et al. *Real-time, Directinal Measurements of B-8 Solar Neutrinos in the Kamiokande-II Detector* Phys. Rev. D (44), pp. 2241-2260, 1991
- [Ich84] K. Ichimura et al. *Absorption and desorption of hydrone, deuterium, and tritium for Zr-V-Fe getter*, J. Vac. Sci. Technol. A (2), pp. 1341-1347, 1984
- [Jan12] A. Jansen *Modellierung der Rotortemperatur von Turbomolekularpumpen in Magnetfeldern mit unterschiedlichen Gasflüssen*, Diploma thesis, KIT, Jan 2012
- [Jon99] S. Jonsell et al. *Neutrino-mass determination from tritium  $\beta$  decay: Corrections to and prospects of experimental verification of the final-state spectrum*, Physical Review C (60), 034601, 1999
- [Kae12] W. Käfer *Sensitivity studies for the KATRIN experiment*, Dissertation, KIT, Jan 2012
- [KAT04] The KATRIN Collaboration *KATRIN Design Report 2004*, Tech. Rep. Forschungszentrum Karlsruhe, 2004.
- [Kay05] B. Kayser *Neutrinos Get under your Skin*, SLAC lectures, Aug 2005
- [Kaz08] O.Kazachenko, F.Eichelhardt et al. *TRAP - a cryo-pump for pumping Tritium on pre-condensed Argon*, Nucl. Inst. and Meth. in Phys. Res. A (58), pp. 136-144, 2008

- [Ker09] R. Kersevana, J.-L. Pons *Introduction to MOLFLOW: New graphical processing unit-based Monte Carlo code for simulating molecular flows and for calculating angular coefficients in the compute unified device architecture environment*, J. Vac. Sci. Technol. A (27), pp. 1017-1023, 2009
- [Kit89] C. Kittel *Einführung in die Festkörperphysik*, 3. Auflage, Oldenbourg Verlag, 1973
- [Kla06] H. V. Klapdor-Kleingrothaus, I. V. Krivosheina *The Evidence for the Observation of  $0\nu\beta\beta$  Decay: The Identification of  $0\nu\beta\beta$  Events from the full Spectra*, Mod. Phys. Lett. A (21) pp. 1547-1566, 2006
- [Kle08] J. Kleinfeller et al. *Technical Specification - Cryogenic Pumping Section (CPS)*, KATRIN Internal, Rev.1, Jan 2008
- [Kom11] E. Komatsu et al. *Seven-Year Wilkinson Microwave Anisotropy Probe (WMAP) Observations: Cosmological Interpretation*, Accepted for Publication in Astrophys. J. Supp. Ser., 2011
- [Kos11b] A. Kosmider *DPS2-F Current Status - Diode Tests*, KATRIN Internal Report, Aug 2011
- [Kos11a] A. Kosmider *Magnetic Field Measurement - Position of the DPS Magnet System*, KATRIN Internal Report, Jan 2011
- [Kos10b] A. Kosmider & S. Lukić *Outgassing Analysis in the DPS2-F Beam Tube*, KATRIN Internal Report, Aug 2010
- [Kos10a] A. Kosmider & S. Lukić *First Results SLOW Experiment*, KATRIN Internal Report, Apr 2010
- [Kos09] A. Kosmider *Beschreibung SLOW-Experiment*, KATRIN Internal Report, Dec 2009
- [Kra05] C. Kraus et al. *Final results from phase II of the Mainz neutrino mass search in tritium  $\beta$  decay*, Eur. Phys. J. C (40), pp. 447-468, 2005
- [Kru83] P. Kruit, F. H. Read *Magnetic field paralleliser for  $2\pi$  electron spectrometer and electron-image magnifier*, J. Phys. E: Sci Instrum. (16), pp. 313-324, 1983
- [Lan95] P. Langacker *Implications of Neutrino Mass*, Lecture Scripts, University of Pennsylvania, 1995
- [LeC83] A. D. Le Claire *Permeation of Gases through Solids*, Defect and Diffusion Forum (33), pp. 1-66, 1983

- [Ley98] W. Umrath (comp.) *Fundamentals of vacuum technology*, Leybold Vacuum, 1998.
- [Lob85] V. M. Lobashev et al. *A Method for Measuring the Electron Antineutrino Restmass*, Nucl. Instr. and Meth. in Phys. Res. A (240), pp. 305-310, 1985
- [Lob03] V. M. Lobashev et al. *The search for the neutrino mass by direct method in the Tritium beta decay and perspectives of study in the project KATRIN*, Nuclear Physics A (719), pp. C153-C160, 2003
- [Lor02] T. J. Loredo, D. Q. Lamb *Bayesian analysis of neutrinos observed from supernova SN 1987A*, Phys. Rev. D (65), 063002, 2002
- [Lou75] M. R. Louthan, R.G. Derrick *Hydrogen transport in austenitic stainless steel*, Corrosion Science (15), pp. 565-577, (1975)
- [Luc00] L. L. Lucas, M.P. Unterweger *Comprehensive Review and Critical Evaluation of the Half-Life of Tritium*, J. Res. Natl. Inst. Stand. Technol. (105), pp. 541-549, 2000
- [Luk12] S. Lukić, A. Kosmider et al. *Measurement of the gas-flow reduction factor of the KATRIN DPS2-F differential pumping section*, Vacuum (86), pp. 1126-1133, 2012
- [Luk09a] S. Lukić et al. *Report on preparation phase for the gas-flow reduction measurements on DPS2-F for KATRIN*, KATRIN Internal Report, Aug 2009
- [Luk09b] S. Lukić *Vakuum-Testexperiment an DPS2-F von KATRIN - Sicherheitstechnische Beschreibung*, KATRIN Internal Report, Sep 2009
- [Luk11a] S. Lukić et al. *Ion source for tests of ion behavior in the Karlsruhe tritium neutrino experiment beam line*, Rev. Sci. Instrum. (82), 013303, 2011
- [Luk11b] S. Lukić & A. Kosmider *Gas-flow test experiment on the DPS2-F - Reduction factor measurement - Calibration of the vacuum sensors*, KATRIN Internal Report, Aug 2011
- [Luo08] X. Luo, C. Day *Test particle Monte Carlo study of the cryogenic pumping system of the Karlsruhe tritium neutrino experiment*, J. Vac. Sci. and Tech. A (26), pp. 1319-1325, 2008
- [Luo06b] X. Luo et al. *KATRIN DPS2-F Vacuum Monte Carlo Simulation*, FZKA Internal Report FE.5130.0052.0012/B, May 2004
- [Luo05] X. Luo, C. Day *Estimation of the vacuum performance of the KATRIN DPS1-F by Monte Carlo simulation*, KATRIN Internal Report, Apr 2005

- [Luo06a] X. Luo et al. *Monte Carlo simulations of the gas flow through the KATRIN DPS2-F differential pumping system*, Vacuum (80), pp. 864-869, 2006
- [Luo07] X. Luo et al. *KATRIN NEG pumping concept investigation*, Vacuum (81), pp. 777-781, 2007
- [Mak62] Z. Maki, M. Nakagawa, S. Sakata *Remarks on the Unified Model of Elementary Particles*, Prog. Theor. Phys. (28), pp. 870-880, 1962
- [Mal07] O. Malyshev *Characterisation of a turbo-molecular pump by a minimum of parameters*, Vacuum (81), pp. 752-758, 2007
- [Mal08] O. Malyshev et al. *Tritium gas flow dynamics through the source and transport system of the Karlsruhe tritium neutrino experiment*, J. Vac. Sci. Technol. A (27(1)), pp. 73-81, 2008
- [Mar98] A. Marshall, C. Hendrickson, G. Jackson *Fourier transform ion cyclotron resonance mass spectrometry: a primer*, Mass Spectrom. Rev. (17), pp. 1-35, 1998
- [McG79] J. Wm. McGowan et al. *Energy dependence of dissociative recombination below 0.08 eV Measured with (electron-ion) merged-beam technique*, Phys. Review Letters (42), pp. 373-375, 1979
- [Mer12] S. Mertens *Study of Background Processes in the Electrostatic Spectrometers of the KATRIN Experiment*, Dissertation, KIT, Feb 2012
- [Mik86] S. P. Mikheev, A. Yu. Smirnov *Neutrino oscillations in a variable-density medium and  $\nu$ -bursts due to the gravitational collapse of stars*, arXiv:0706.0454 v1
- [Min11] Y. Mine, T. Kimoto *Hydrogen uptake in austenitic stainless steels by exposure to gaseous hydrogen and its effect on tensile deformation*, Corrosion Science (53), pp. 2619-2629, 2011
- [Mit90] J. B. A. Mitchell *The Dissociative recombination of molecular ions*, Phys. Reports (186), pp. 215-248, 1990
- [Miz94] M. Mizuno et al. *Determination of Hydrogen Concentration in Austenitic Stainless Steels by Thermal Desorption Spectroscopy*, Materials Transactions (35), pp. 703-707, 1994
- [Moo95] B. C. Moore *Recombination limited outgassing of stainless steel*, J. Vac. Sci. Technol. A (13), pp. 545-548, 1995
- [Mor03] M. Moraw, H. Praso *Gas desorption from a stainless-steel surface in ultrahigh vacuum devices*, Vacuum (71), pp. 471-479, 2003



- [Mul08] K. Müller *Drawings to: Technical Specification - Cryogenic Pumping Section (CPS)*, KATRIN Internal, Rev.1, Jan 2008
- [Nep05] S. A. Nepijko et al. *Morphology of Frozen Rare-Gas Layers*, ChemPhysChem (6), pp. 235-238, 2005
- [Nuc10] A. Nucciotti et al. (MARE collaboration) *Neutrino mass calorimetric searches in the MARE experiment*, Nucl. Phys. B Proc. Supp. (00), pp. 1-5, 2010
- [Nuc02] A. Nucciotti et al. (MARE collaboration) *The Milano neutrino mass experiment with arrays of  $\text{AgReO}_4$  microcalorimeters*, APS CP605, Low Temperature Detectors, F. S. Porter et al. (ed.), 2002
- [Noe03] M. Noe et al. *Specifications for DPS2-F*, KATRIN Internal, Rev.1, Dec 2003
- [Ohm91] A. Ohmori et al. *Electrical Conductivity of Plasma-Sprayed Titanium Oxide (Rutile) Coatings*, Thin Solid Films (201), pp. 1-8, 1991
- [Ott06] E. W. Otten et al. *The Q-value of tritium  $\beta$ -decay and the neutrino mass*, Int. J. Mass Spec. (251), pp. 173-178, 2006
- [Pad87] R. Padma et al. *Electrical conductivity of thermally grown titanium oxide films*, J. of Mat. Sci. (22), pp. 2083-2086, 1987
- [Par11] S. Parodi et al. (ASG), KATRIN - DPS2-F - *Results of Acceptance tests at KIT*, KATRIN Internal Report, Apr 2011
- [Pas05] S. Pascoli et al. *The Absolute Neutrino Mass Scale, Neutrino Mass Spectrum, Majorana CP-Violation and Neutrinoless Double-Beta Decay*, arXiv:hep-ph/0505226 v2
- [PDG10] K. Nakamura et al. (Particle Data Group) *2011 Review of Particle Listings*, J.Phys. G (37) 075021, 2010
- [Pau95] W. Paul et al. *On the dynamics of the reaction of positive hydrogen cluster ions ( $H_5^+$  to  $H_{23}^+$ ) with para and normal hydrogen at 10 K*, International Journal of Mass Spectrometry and Ion Processes (149-150), pp. 373-387, 1995
- [Pav10] E. Pavlov *Bestimmung der Neutrino-Masse: Heidelberg Moskau Experiment und KATRIN*, lecture scripts, University Heidelberg, 2010
- [Per86] T-P. Perng, C.J. Alstetter *Effects of deformation on hydrogen permeation in austenitic stainless steels*, Acta Metall (34), pp. 1771-1781, 1986
- [Pes09] H. Pessard et al. (OPERA Collaboration) *Status of the OPERA neutrino experiment*, arXiv:0910.5701 v1

- [Pic92] A. Picard et al. *A solenoid retarding spectrometer with high resolution and transmission for keV electrons*, Nucl. Inst. Meth. Phys. Res. B (63), pp. 345-358, 1992
- [Pov08] B. Povh et al. *Teilchen und Kerne*, 8. edition, Springer, 2008
- [Poz96] A. Pozzo, C. Boffito, F. Mazza *Experience with the use of a turbomolecular pump combined with a NEG pump in UHV conditions*, Vacuum (47), pp. 783-786, 1996
- [Put11] S. Putselyk *Summary of first test results of differential pumping section (DPS) in the KATRIN experiment: cryogenics*, KATRIN Internal Report, Jan 2011
- [Rei09] S. Reimer *Ein elektrostatisches Dipolsystem zur Eliminierung von Ionen in der DPS2-F des KATRIN-Experiments*, Diploma Thesis, KIT, Nov 2009
- [Rob88] R. G. H. Robertson, D.A. Knapp *Direct Measurements of Neutrino Mass*, Ann. Rev. Nucl. Sci. (38), pp. 185-215, 1988
- [Rot90] A. Roth *vacuum technology*, north-holland, 1990
- [Ruj82] A. de Rújula, M. Lusignoli *Calorimetric measurements of  $^{163}\text{Ho}$  Holmium decay as Tools to determine the electron neutrino mass*, Phys. Lett. (118B), pp. 429-432, 1982
- [San05] C. San Marchi et al. *Permeability, Solubility and Diffusivity of Hydrogen Isotopes in Stainless Steels at High Gas Pressures*, WSRC-STI-2007-00579, 2005
- [San06] C. San Marchi et al. *Permeability, Solubility and Diffusivity of Hydrogen Isotopes in Stainless Steels at High Gas Pressures*, Int. J. of Hydrogen Energy (32), pp. 100-116, 2006
- [Sch71] W. Schulze, Dissertation, Technical University Berlin, 1971
- [Sch12] J. Schwarz *Focal Plane Detector System*, KATRIN Internal Report, Mar 2012
- [Sch10] J. Schwarz *Messungen der elektro-optischen Eigenschaften der differentiellen Pumpstrecke von KATRIN*, 74. annual summit DPG, Bonn, Mar 2010
- [Shu69] D. S. Shupe, R. E. Stickney *Thermodynamics of the Solubility and Permeation of Hydrogen in Metals at High Temperature and Low Pressure*, J. of Chem. Phys. (51), pp. 1620-1625, 1969

- [Sis04] M. Sisti et al. *New limits from the Milano neutrino mass experiment with thermal microcalorimeters*, Nucl. Instr. Meth. A (520), pp. 125-131, 2004
- [Smi66] C. G. Smith, G. Lewin *Free Molecular Conductance in a Cylindrical Tube with Wall Sorption*, J. Vac. Sci. Technol. (3), pp. 92-95, 1966
- [Smi10] B. Smirnov *Cluster Processes in Gases and Plasmas*, Wiley, 2010
- [Ste10] M. Steidl, J. Schwarz *Design Proposal for a  $^{83}\text{Rb}$  source for a beam alignment measurement at the DPS2-F*, KATRIN Internal Report, Feb 2010
- [Stu10] M. Sturm *Aufbau und Test des Inner-Loop-Systems der Tritiumquelle von KATRIN*, Dissertation, KIT, Jun 2010
- [Tem70] K. E. Tempelmeyer *Aerodynamic Dispersion Techniques*, AFATL-TR-70-123, 1970
- [Tem71] K. E. Tempelmeyer et al. *Sorption Pumping of Hydrogen by Carbon Dioxide Cryodeposits*, J. Vac. Sci. Technol. (8), pp. 575-581, 1971
- [Tit03] N. A. Titov *KATRIN Systematics*, KATRIN Internal Report, Jan 2003
- [Thu11] T. Thümmler for the KATRIN Collaboration *Direct Neutrino Mass Measurement*, Phy. of Part. and Nucl. (42), pp. 590-597, 2011
- [Ubi12] M. Ubieto-Diaz for the FT-ICR team Heidelberg, private correspondence
- [Ubi11] M. Ubieto-Diaz *Off-line commissioning of a non-destructive FT-ICR detection system for monitoring the ion concentration in the KATRIN beamline*, Dissertation, University Heidelberg, Dec 2011
- [Ubi09] M. Ubieto-Diaz et al. *A broad-band FT-ICR Penning trap system for KATRIN*, Int. J. of Mass Spec. (288), pp. 1-5, 2009
- [Vas93] G. Väsarru *Tritium Isotope Separation*, RCE Press, 1993
- [Wei03a] C. Weinheimer et al. *Violation of adiabaticity in the transport magnets of the KATRIN experiment*, KATRIN Internal Report, Jul 2003
- [Wei03b] C. Weinheimer *Neutrino Mass*, pp. 25-52, G. Altarelli and K. Winter, Ed., Springer (2003)
- [Wei93] C. Weinheimer et al. *Improved limit on the electron-antineutrino rest mass from tritium  $\beta$ -decay*, Physics Letters B (300), pp. 210-216, 1993

- [Wex59] S. Wexler *Dissociation of TH and T<sub>2</sub> by  $\beta$ -decay*, Journal of Inorganic and Nuclear Chemistry (10), pp. 8-16, 1959
- [Wik12] www.wikipedia.org, general references
- [Win11] A. Windberger *Berechnungen und Simulationen zum Verhalten von Ionen in der differentiellen Pumpstrecke des KATRIN-Experiments*, Diploma Thesis, KIT, Jan 2011
- [Win10] A. Windberger *Kalibrierung eines Restgas-Analysators für die Verwendung im DPS2-F Testexperiment*, KATRIN Internal Report, May 2010
- [Wol12] J. Wolf et al. *Vacuum calculations for radon and tritium in the KATRIN pre-spectrometer and main-spectrometer*, to be published, 2012
- [Wol09] J. Wolf for the KATRIN Collaboration *Size Matters: The vacuum System of the KATRIN Neutrino Experiment*, J. of the Vac. Soc. of Japan (52), pp. 22-28, 2009
- [Wur12] M. Wurm et al. (LENA Collaboration) *The next-generation liquid-scintillator neutrino observatory LENA*, arXiv:1104.5620 v3
- [Wut10] K. Jousten Wutz *Handbuch Vakuumtechnik*, 10. Auflage, Vieweg + Teubner, 2010
- [Xiu88] S. Xiukui et al. *Hydrogen Permeation Behaviour in Austenitic Stainless Steels*, Mat. Sci. and Engin. (A114), pp. 179-187, 1989
- [Zar79] A. Zarchy, R. Axtmann *Tritium permeation through 304 stainless steel at ultra-low pressures*, J. of Nuclear Materials (79), pp. 110-117, 1979
- [Zbo11] M. Zbořil *Feste Elektronenquellen für die Energieskalaüberwachung im KATRIN Experiment*, Dissertation, University of Münster, Aug 2011
- [Zol09] M. Zoll *Development of tools and methods for KATRIN DPS2-F test experiments*, Diploma Thesis, University of Karlsruhe, 2009

# Acknowledgment

I would like to express great gratitude towards Guido Drexlin and Christian Weinheimer. Not only for the supervision and appraisal of this work but also for years of support and mentoring at Münster and Karlsruhe.

Very special thanks is due to Strahinja Lukić for extensive work in preparation of the vacuum tests and manifold ways of support. I was very lucky to be able to learn a lot from him.

In this context, I would like to thank Alexander Windberger, whose Diploma thesis covered important aspects of the ion suppression system, for his valuable contributions, Joachim Wolf for numerous discussion and answers to vacuum related questions and Christian Day for clarifying my view on rarefied gas dynamics.

I thankfully acknowledge the help and input of the Heidelberg team, especially of Marta Ubieto-Diaz and Michael Heck.

I am also thankful that I had the opportunity to work with all the members of the DPS2-F team: L. Anselment, S. Bobien, B. Bornschein, L. Bornschein, A. Felden, R. Gehring, T. Höhn, S. Holzmann, S. Horn, M. Kaiser, N. Kernert, J. Kleinfeller, M. Knauer, P. Krämer, H. Krause, L. La Cascio, K. Metzger, R. Neeb, G. Prokott, H.-P. Schön, D. Stern, M. Sturm, M. Süßer, and the ASG staff around O. Dormicchi.

Among those I would like to extend special thanks to Beate, Jonny, Luisa, Lutz and Michael for valuable consult and guidance.

I thank all the colleagues at the Institute for Nuclear Physics for the creation of an inspiring and pleasant working environment. Dedz to the members KATRIN DiDo-Seminar in particular.

I would also like to thank Jochen Zimmer for the supply of aluminum coatings and fruitful discussions, the Fachschaft Physik at KIT for letting me work in their office late at night, and Moritz Ehrhard for supplying our office with a constant noise level.

Lastly I would like to thank my parents and my beautiful girlfriend Sabine for all the support.



## **Erklärung / Assertion**

Hiermit versichere ich, dass ich die vorliegende Arbeit selbständig und nur unter Verwendung der angegebenen Hilfsmittel und Quellen verfasst habe.

I hereby assert, that I have written this thesis autonomously using none but the denoted sources and aides.

Andreas Kosmider  
Karlsruhe, den 23. Mai 2012